DYNAMISCHE UNTERSUCHUNGEN BEI INTENSIVIERTER FISCHER-TROPSCH SYNTHESE

Zur Erlangung des akademischen Grades eines

DOKTORS DER INGENIEURSWISSENSCHAFTEN (DR.-ING.)

von der KIT-Fakultät für Chemieingenieurwesen und Verfahrenstechnik
des Karlsruher Instituts für Technologie (KIT)
genehmigte

DISSERTATION

von

Marcel Loewert
aus Rüsselsheim am Main

Tag der mündlichen Prüfung: 14.01.2021

Erstgutachter: Prof. Dr.-Ing. Peter Pfeifer (IMVT)

Zweitgutachter: Prof. Dr. Reinhard Rauch (EBI)

Danksagung

An dieser Stelle ergreife ich die Gelegenheit, den Menschen zu danken, die mich lange Jahre unterstützt, bereichert und geformt haben.

Zuallererst danke ich Prof. Dr.-Ing. Peter Pfeifer für seine Bemühungen, die heterogene Katalyse im Bereich der Energiewende voran zu treiben. Seine Weitsicht ermöglichte das Bearbeiten dieser interessanten Aufgabenstellung, welche sich gut mit der Motivation der Ingenieurinnen und Ingenieure in der Energiewende verzahnt.

Im Falle meiner Familie können Worte nicht ausdrücken, wie dankbar ich dafür bin, dass ich stets vollen Rückhalt und absolutes Vertrauen genoss.

Vieles habe ich Svenja zu verdanken, die mich lange Jahre in jeder Gemütslage erlebte und mich immer wieder motivierte und förderte.

Meine Freunde in allen Heimaten, die stets hinter mir standen, mich bereichert und inspiriert haben.

All den Kollegen, mit denen ich lernen, leiden und leisten durfte. Ebenso den fleißigen und begabten Studenten, die ich einen Teil ihres Weges begleiten durfte.

Abstract

Defossilization and the reduction of CO_2 emissions from anthropogenic actions are some of the big topics of this century. Being the largest contributor to the greenhouse effect, CO_2 emissions influence the global the carbon balance and thus the climate that makes this planet habitable. Renewable energy sources such as wind, solar and water power, as well as biomass, only play a secondary role in energy production. This needs to change in order to build up a sustainable energy system. A myriad of new applications and technologies emerged from that incentive. One of the most debated sectors is transportation and mobility which still relies mostly on fossil fuels and feedstock. The general consensus on new approaches to address this issue is the implementation of e-mobility and renewable fuels. The latter relies on chemical and process engineers to develop and produce synthetic alternatives to fossil refinery products. Those combine all advantages of traditional fuels with the property of carbon neutrality.

Significant technology readiness levels are reached for synthetic fuel production. Public acceptance of those fuels relies on an affordable price per energy unit, which in turn requires a high production efficiency. Process intensification is key to the highest possible efficiency to impact process economics. In this regard, microstructured reactors show outstanding reaction properties, especially for exothermic reactions that usually prove to be challenging. The system size of those reactors is well-suited for different scales of energy to be converted. The system intensification and the modularity makes those reactors important for decentralized plant-scales. Sector coupling will allow the well distributed processing of energy flows in the near future. Moreover, the system size allows a fast and safe change of process parameters. Dynamic synthesis has yet to find its way into industrial processes. Quickly changing process streams and parameters are feared to bring unpredictable effects to the catalyst and the reactor in use.

In the context of an increasing share of fluctuating primary energy coming from wind and solar plants, a constant supply of feed in the process is only possible by local energy storage. For standalone plant networks, this can be realized in the form of batteries or gas tanks. The amount of mass-related energy density of a battery is significantly smaller than the density of compressed hydrogen. For that reason, gas storage will play an important role as

buffer in synthesis processes. Since gas tanks are costly, an intelligent process control will contribute to reduce storage size significantly. In this regard, microstructured reactors are remarkably suited for fast process changes due to small internal dimensions and effective means to extract heat from or add heat to the system, for instance.

This work is devoted to shed light on different approaches to intensify catalytic processes in the field of renewable fuels with a high volumetric energy density. The Fischer-Tropsch reaction is investigated in microstructured fixed-bed reactors. These systems show exceptional reaction properties that intensify processes which makes them applicable in decentralized plants.

Two different system sizes of microstructured fixed-bed reactors for the Fischer-Tropsch synthesis were compared to evaluate the effectivity of a reactor scale-up. Both systems were tested on their versatility towards a range of different process parameters. The feedstock for the experiments comprised biomass-typical syngas with a high dilution and low syngas ratio. Both systems showed good catalytic performance despite challenging reaction parameters, resulting in 44 - 62 % of CO conversion. The respective influence of different process parameters was evaluated. The upscaled system had significantly more effective options to control the system parameters due to less important heat losses and the addition of evaporation cooling in the microstructured system.

Consequently, the larger system was used for dynamic synthesis. System dead times were determined prior to conducting periodic changes. Parameter changes were applied as dynamic feed gas supply and temperature manipulation, using the advantages of the scaled-up system. It was designed to produce up to 7 L of condensable product per day. Feed gas oscillation was performed by changing the syngas ratio in 30 and 8 minute cycles, respectively, without any disadvantages or decrease in synthesis performance. Temperature manipulation was carried out in 5 min-steps, by means of pressure ramping in the cooling water cycle. The results showed promising capability for dynamic applications.

Operational limitations needed to be determined. Insight about the highest possible load flexibility were found by using fluctuating input data derived from a 10 kW photovoltaic panel and a simulated electrolyzer. The setup resulted in a highly dynamic hydrogen flow that was fed to the system. It was assumed that all the electricity from the panel was converted instantaneously and given to the synthesis unit over the course of a day. Different assumptions for the carbon source were made, leading to two different experimental cases. Both were designed to put the system to its limits by either a high fluctuation in syngas ratio or residence time changes in the one minute-range. In a final experiment, temperature control was additionally added to control carbon monoxide conversion despite changes in syngas residence time and/ or syngas ratio. No limitation by the system could be determined for the applied time scale. The system was flexible and stable. Technical limitations did not allow to further shorten feed gas changes below one minute.

System modeling can reduce experimental effort, as well as forecast product characteristics and yields. Especially with volatile flows, the simulation environment should be as accurate as possible to describe the system at hand. In this context, a multi-level model for the description of relevant processes inside the test rig was developed. A residence time distribution sub-routine described flow and mixing behavior for the whole test rig in order to calculate time-dependand productivity. A program for vapor-liquid equilibrium calculation decided the state of the product fractions in each respective product condenser. A micro-kinetic model was developed and validated for the present system. Together, those three subroutines were capable of predicting time-resolved product and system characteristics only based on a few input parameters.

In order to have a look into the "catalytic black box", spectroscopic methods help to elaborate on changes happening on the catalyst's surface during reaction. The use of high-performance catalysts further improves intensified processes in microstructured reactors. Thus it is important to understand different reaction phenomena. During an experiment in the CAT-ACT beamline at the KIT synchrotron with time on stream for over 300 h, catalyst initiation phase was evaluated by *in situ* X-ray absorption spectroscopy (XAS) and X-ray diffraction (XRD) techniques. Experiments were carried out in a novel reaction cell suited for experimental conditions usually found in Fischer-Tropsch synthesis. Concurrent online product measurements made an *operando* setup possible. During reaction, a slight carburization of the active cobalt was observed. Wax fouling had a by far more pronounced influence on catalyst activity. After initiation phase, a forced hydrogen dropout caused further formation of cobalt carbides and poorly ordered graphites on the catalyst surface but no oxidation. An *ex situ* temperature-programmed hydrogenation and oxidation (TPH/TPO) analysis suggested a regeneration procedure applying both an oxidation and a reduction sequence.

The insight obtained by the different chapters of this work ultimately shows the potential this technology holds in respect to decentralized applications. Small- to medium-scale plants could contribute to the production of renewable fuels wherever a suitable carbon source is available. This will result in a positive impact on the production and consumption of fossil fuels and thus lower CO_2 emissions from the mobility sector.

Zusammenfassung

Die Defossilisierung und die Reduzierung der CO_2-Emissionen durch Gesellschaft und die Industrie sind dringliche Themen unserer Zeit. Es ist allgemein anerkannt, dass CO_2 als Treibhausgas das Klima beeinflusst und der Mensch den Klimawandel durch einen hohen CO_2-Ausstoß verstärkt. Die Umwelt muss mit geschützt werden, um die Grundlage für das Leben, wie wir es kennen, zu erhalten. Aktuell finden große Bemühungen statt, erneuerbare Energien als Primärenergie der Zukunft zu fördern. Dies geschieht durch die Nutzung von Wind-, Sonnen- und Wasserkraft, sowie Biomasse. Aus diesem Ansatz sind eine Vielzahl neuer Anwendungen und Technologien entstanden. Wir stehen vor einer Neuorientierung im Energiesektor, wodurch viele Herausforderungen entstehen und überwunden werden müssen. Einer der Sektoren mit der geringsten Veränderung ist der Verkehrssektor, welcher bis heute größtenteils auf fossile Brennstoffe und Rohstoffe zurück greift. Elektromobilität und erneuerbare Kraftstoffe sind wichtige Säulen für die Bewältigung der Energiewende. Synthetische Kraftstoffe besitzen dabei jegliche Vorteile fossiler Brennstoffe, zusammen mit der Eigenschaft der Klimaneutralität. Durch ihre hohe Energiedichte sind sie unverzichtbar in bestimmten Bereichen der Mobilität.

Synthetische Kraftstoffe mit hoher volumetrischer Energiedichte können in chemischen Anlagen produziert werden. Um die Eignung modernster Reaktortechnik für den großflächigen Einsatz dynamisch ausgelegter, erneuerbarer Umwandlungsprozesse zu untersuchen, wird in dieser Arbeit ein Ansatz zur Intensivierung des katalytischen Prozesses beleuchtet.

Konkret wird die Fischer-Tropsch-Reaktion in mikrostrukturierten Festbettreaktoren untersucht, die der modularen, dezentralen Sektorkopplung neue Ansätze bieten. Prozessintensivierung ist ein Schlüssel zu höchster Effizienz, die sich als signifikant für die Prozessökonomie erweist. Eine Modularität des Reaktorsystems ermöglicht die Handhabung unterschiedlichster Anwendungen und Integration in unterschiedliche Leistungsstufen.

Die dynamische chemische Synthese ist aufgrund der geringen Relevanz für industrielle Prozesse nur wenig untersucht. In etablierten Reaktionen wird befürchtet, dass schnell ändernde Prozessströme und Parameter unvorhersehbare Auswirkungen auf den eingesetzten Katalysator haben könnten. Vor dem Hintergrund eines zunehmenden Anteils schwankender Primärenergie aus Windkraft- und Solaranlagen ist eine konstante Versorgung mit

Feed nur mit lokalen Energiespeichern möglich. Für dezentrale Anlagennetzwerke könnten diese in Form von Batterien oder Gastanks realisiert werden. Speicher stellen allerdings einen beachtlichen Kostenfaktor dar. Somit wird eine intelligente und dynamische Prozesssteuerung dazu beitragen, Speicher, und damit Kosten, deutlich zu reduzieren. Mikrostrukturierte Reaktoren eignen sich aufgrund der geringen Abmessungen des Reaktionsraums und exzellenter Wärmeübertragungseigenschaften, hervorragend für schnelle Prozessänderungen.

Zwei unterschiedliche Systemgrößen für mikrostrukturierte Fischer-Tropsch-Festbettreaktoren wurden verglichen, um die Effektivität eines Reaktor-Scale-Ups von etwa 100 mL Flüssigprodukt pro Tag auf etwa 6 L zu bewerten. Der Fokus lag hierbei auf der Verwendung eines Cobalt-Katalysators für die Niedertemperatur-Fischer-Tropsch-Synthese.

Das skalierte System hatte aufgrund des geringen Einflusses von Wärmeverlusten und der Nutzung von Verdampfungskühlung in den Mikrostrukturen deutlich effizientere Möglichkeiten, Systemparameter zu steuern. Beide Systeme wurden auf ihre Vielseitigkeit gegenüber unterschiedlicher Prozessparametern getestet. Die durchgeführten Experimente umfassten biomassetypische Syntheseeigenschaften wie eine hohe Verdünnung und ein niedriges Synthesegasverhältnis. Beide Reaktoren zeigten trotz der herausfordernden Rahmenbedingungen zufriedenstellende Ergebnisse und der jeweilige Einfluss verschiedener Prozessparameter konnte bewertet werden. Das skalierte System zeigte vielversprechende Eigenschaften für zukünftige Anwendungen aufgrund größerer Möglichkeiten in der Prozesssteuerung.

Aus diesem Grund wurde nur das skalierte System für die Untersuchungen dynamischer Prozessführung verwendet. Die Totzeiten des Versuchsstandes mussten vor der Durchführung periodischer Änderungen ermittelt werden. Dynamische Feedgas- und Temperaturmanipulation wurde angewendet, wobei die oben erwähnten Vorteile des Scale-Ups genutzt wurden. Schwankungen im Feedgas wurden durch eine drastische Variation des Synthesegasverhältnisses in 30 min und 8 min-Zyklen durchgeführt, ohne Nachteile oder Einbußen in der Syntheseleistung festzustellen. Die Temperaturmanipulation wurde in 5-Minuten-Schritten getestet. Die Ergebnisse sprechen für die Eignung der Reaktortechnologie in dynamischen Anwendungen.

Die Systemgrenzen wurden noch intensiver untersucht. Erkenntnisse zur höchstmöglichen Lastflexibilität wurden durch die Verwendung eines Leistungsprofils für ein 10 kW Photovoltaikmodul und einem simulierten Elektrolyseur gewonnen. Errechnet wurde ein hochdynamischer Wasserstoffstrom: die im Laufe eines Tages gewonnene elektrische Energie wurde als instantan durch Wasser-Elektrolyse in Wasserstoff umgewandelt angenommen und entsprechend dem Tagesprofil der Syntheseeinheit zugeführt. Es wurden unterschiedliche Annahmen für die Kohlenstoffquelle getroffen, was zu zwei verschiedenen Hauptexperimenten führte. Beide wurden entwickelt, um die Grenzen des Systems zu ermitteln. So wurden im einminütigen Bereich das Synthesegasverhältnis oder die Feedmenge variiert. In einem abschließenden Experiment wurde zusätzlich eine manuelle Temperaturregelung hinzugefügt, um den Kohlenstoffmonoxidumsatz trotz Änderungen der Verweilzeit des Synthesegases oder das Synthesegasverhältnis zu steuern. Die Schlussfolgerung aus allen Experimenten war, dass der getesteten Zeitskala keine Limitierungen durch das System erkennbar waren. Technische Einschränkungen erlaubten es nicht, Zyklen auf unter eine Minute zu verkürzen.

Systemmodellierung kann den experimentellen Aufwand reduzieren und die Produkteigenschaften und -ausbeuten vorhersagen. Insbesondere bei volatilen Energieflüssen sollte die Simulationsumgebung so genau wie möglich sein. In diesem Zusammenhang wurde in MATLAB ein Multiskalenmodell zur Beschreibung relevanter Prozesse in der vorhandenen Anlage entwickelt. Ein Untermodell zur Verweilzeitverteilung beschrieb das Strömungs- und Mischverhalten für die gesamte Anlage, um die zeitabhängige Produktivität zu berechnen. Ein Programm zur Berechnung des Dampf-Flüssigkeit-Gleichgewichts bestimmte den Zustand der Produktfraktionen in den jeweiligen Kondensatoren. Ein Kinetikfit wurde entwickelt und für das bestehende System validiert. Zusammengenommen sind die drei Untermodelle in der Lage, zeitaufgelöste Produkt- und Systemeigenschaften, basierend auf wenigen Eingangsparametern, vorherzusagen.

Um einen Blick in den Reaktor als „katalytische Blackbox“ zu werfen, helfen spektroskopische Methoden, um Veränderungen am Katalysator während der Reaktion zu untersuchen. Der Einsatz von Hochleistungskatalysatoren verbessert die intensivierten Prozesse in mikrostrukturierten Reaktoren noch weiter. Daher ist es wichtig, unterschiedlichste Vorgänge auf der Katalysatoroberfläche zu untersuchen und verstehen. Während eines mehr als 300-

stündigen Experiments in der CAT-ACT-Beamline am KIT-Synchrotron wurde das Einlaufverhalten des Katalysators durch *in situ* Röntgenabsorptionsspektroskopie (XAS) und Röntgendiffraktion (XRD) in einer neuartigen Reaktionszelle ausgewertet, die zu experimentellen Bedingungen fähig ist, welche normalerweise in der Fischer-Tropsch-Synthese zu finden sind. Parallele Online-Produktmessungen ermöglichten ein *operando*-Setup. Während der Reaktion konnte eine leichte Carbidisierung des aktiven Cobalts beobachtet werden. Die Wachsablagerung hatte einen determinierenden Einfluss auf den Verlust von Katalysatoraktivität im beobachteten Zeitraum. Nach der Einlaufphase führte ein simulierter Wasserstoff-Dropout zur weiteren Bildung von Kobaltcarbiden und ungeordneten Graphiten auf der Katalysatoroberfläche, aber nicht zu Oxidation. Eine *ex situ* ausgeführte temperaturprogrammierte Hydrierung (TPH) und Oxidierung (TPO) deutete auf die Möglichkeit eines Regenerationsverfahren hin, das sowohl Oxidation als auch Reduktion beinhaltet.

Die Erkenntnisse aus den unterschiedlichen Kapiteln dieser Arbeit zeigen letztlich das Potenzial der Mikroverfahrenstechnik in Bezug auf dezentrale Anwendungen. Eine Vielzahl kleinerer Anlagen könnten zur Produktion nennenswerter Mengen erneuerbarer Kraftstoffe beitragen, solange eine geeignete Kohlenstoffquelle lokal verfügbar ist. Dies kann sich positiv auf die Produktionsmenge und den Verbrauch fossiler Ressourcen auswirken und damit die Emissionen des Mobilitätssektors senken.

Contents

List of publications

1. Microstructured Fischer–Tropsch Reactor Scale–up and Opportunities for Decentralized Application
   M. Loewert, J. Hoffmann, P. Piermartini, M. Selinsek, R. Dittmeyer and P. Pfeifer
   Chemical Engineering & Technology
   Published: 10th of July, 2019
   https://doi.org/10.1002/ceat.201900136
2. Dynamically Operated Fischer-Tropsch Synthesis in PtL-Part 1: System Response on Intermittent Feed
   M. Loewert and P. Pfeifer
   ChemEngineering
   Published: 28th of March, 2020
   https://doi.org/10.3390/chemengineering4020021
3. Dynamically Operated Fischer-Tropsch Synthesis in PtL-Part 2: Coping with Real PV Profiles
   M. Loewert, M. Riedinger and P. Pfeifer
   ChemEngineering
   Published: 13th of April, 2020
   https://doi.org/10.3390/chemengineering4020027
4. Coupling of Fischer-Tropsch reaction kinetics, enhanced vapor-liquid flash calculation and residence time distribution modeling for time-dependent product determination in load-flexible plants
   M. Loewert, V. Zaghini Francesconi, L. T. Brübach and P. Pfeifer
   Chemical Engineering Journal
   Accepted: 26th of June, 2020
   Forseeably published: 15th of December 2020
   https://doi.org/10.1016/j.cej.2020.126032
5. Bridging the gap between industry and synchrotron: an *operando* study at 30 bar over 300 h during Fischer-Tropsch synthesis
   M. Loewert, M.–A. Serrer, T. Carambia, M. Stehle, A. Zimina, K. Kalz, H. Lichtenberg, E. Saraci, P. Pfeifer and J.–D. Grunwaldt
   Reaction Chemistry & Engineering
   Published: 8th of April, 2020
   https://doi.org/10.1039/C9RE00493A

List of symbols and abbreviations

Symbols (latin)

Symbol	Unit [SI]	Description
a	$-$	Slope of a linear part of the ASF plot
$F(t)$	$-$	Residence time sum function
H	$J\,mol^{-1}$	Reaction enthalpy
m	kg	Mass
$\dot{m}$	$kg\,s^{-1}$	Mass flow
n	$-$	Number of reactors
P	$g\,h^{-1}$	Productivity
p	$g\,g^{-1}\,h^{-1}$	Specific productivity
p	bar	Pressure / partial pressure
S	$-$	Selectivity
T	$^\circ C,\ K$	Temperature
t	s	Time
TOS	h	Time on stream
$\dot{V}$	$m^3\,s^{-1}$	Volume flow
$WHSV$	$g\,g^{-1}\,s^{-1}$	Weight hourly space velocity
w	$-$	Mass fraction
X	$\%$	Conversion
y	$-$	Gas fraction

Symbols (greek)

Symbol	Unit [SI]	Description
α	$-$	Chain-growth probability
β	$-$	regression coefficients
ρ	$kg\,m^{-3}$	Density
τ	$kg\,s\,m^{-3}$	Modified residence time

Abbreviations

Abbreviation	Description
ASF	Anderson-Schulz-Flory
$BATEC$	Battery Technical Center
BtL	Biomass-to-Liquid
CNT	Carbon nanotubes
CS_2	Carbondisulfite
$CSTR$	Continuous stirred-tank reactor
CT	Cold trap
CtL	Coal-to-Liquid
DAC	CO_2 direct air capture
DME	Dimethyl ether
EOS	Equation of state
$EXAFS$	Extended X-ray absorption fine structure
FID	Flame ionization detector
FT	Fischer-Tropsch
FTS	Fischer-Tropsch synthesis
GC	Gas chromatograph / chromatography
GHG	Greenhouse gas
GNS	Graphene nanosheets
GtL	Gas-to-Liquid
HC	Hydrocarbon
HT	Hot trap
$IMVT$	Institute for Micro process Engineering
KIT	Karlsruhe Institute of Technology
$LTFT$	low-temperature Fischer-Tropsch synthesis
$MeOH$	Methanol
MFC	Mass flow controller
MFI	Mass flow meter
MS	Mass spectrometer / spectrometry
MtG	Methanol-to-gasoline

NO_X	Nitrogen oxides
$OECD$	Organization for Economic Co-operation and Development
OME	Oxymethylene dimethyl ether
$PBtL$	Power-and-Biomass-to-Liquid
PFR	Plug-flow reactor
PtL	Power-to-Liquid
PV	Photovoltaic
QS	Quick-sample
$RWGS$	Reverse water-gas shift
SEM	Scanning electron microscope
TC	Thermocouple
TCD	Thermal conductivity detector
TEM	Transmission electron microscope
TIS	Tanks-in-series
$TG-MS$	Thermo-gravimetric measurement using a mass spectrometer
TPH	Temperature-programmed hydrogenation
TPO	Temperature-programmed oxidation
TPR	Temperature-programmed reduction
VLE	Vapor-liquid equilibrium
$VTPR$	Volume-Translated Peng-Robinson method
WGS	Water-gas shift
$XANES$	X-ray absorption near-edge spectroscopy
XAS	X-ray absorption spectroscopy
XRD	X-ray diffraction spectroscopy

Sub- and superscripts

Script	Description
0	Standard state
Ci	Carbon chain with length i
$feed$	Gases at the reactor entry
h	CO or H_2

i	Carbon number
j	Hydrogen number, associated to the carbon number of a hydrocarbon
k	Product water, oil or wax
mod	Modified
N	Normal
$product$	Gases at the reactor exit
R	Reaction
STP	Standard temperature and pressure
$total$	All product phases

1 Introduction

It is recognized that humanity plays a crucial role in global warming. The most prominent anthropogenic greenhouse gas (GHG) is CO_2 [1], having the largest effect of all GHG with a share of 65.9 % (2018) over CH_4 (17 %) and N_2O (6 %) [2].

GHG in general are important for the current climate. Without them, Earth would be a planet with an average temperature of -18 °C [3]. This unstable system is quite susceptible to changes in gas concentrations, however. While there is a consensus about trying to limit the average atmospheric temperature increase to 2 °C compared to pre-industrial levels, the transition in energy consumption is evolving slowly [4–6].

CO_2 is emitted as a waste product from many technical processes that use fossil resources as energy carriers, such as industrial manufacturing, transport, heating and power generation. We already possess the technology to convert energy and obtain chemical intermediates from renewable sources. However, it is frequently stated that either the price per unit of energy is too high as of today or the established infrastructure is critically challenged by structural changes that a new energy system would bring [6, 7]. In contrast, some studies show that a fully renewable energy system would not be more expensive than existing structures, making "the energy transition not a question of technical feasibility or economic viability, but one of political will", as the Energy Watch group stated [7, 8].

Liquid energy carriers or fuels possess the highest volumetric energy density at atmospheric pressure and room temperature of any energy-related substance [9, 10]. Thus, a number of energy-related applications is difficult to electrify, even in the future [6, 10–12]. The high energy density of liquid energy carriers is especially relevant for long-distance transportation. This condensed form of energy can be effectively stored and transported while being easy to handle.

Renewable energy can be used to produce synthetic fuels that are CO_2 neutral and possess the same or even better combustion characteristics in terms of soot formation and nitrogen oxide (NO_X) emissions than fossil fuels [13–15]. The production of synthetic fuels is a multistep, energy-intensive process. Efficiency losses with every step of production make a renewable product more costly compared to their fossil counterparts [16, 17]. Studies show that such production could nevertheless be feasible if e.g. existing electrical propulsion subsidies were applied on those alternative technologies as well [17–20]. In countries like Switzerland this is already in practice [21]. Additionally, fuel standards sometimes hinder the use of a hundred percent synthetic fuel [15], which needs to be overcome.

The chemical storage of energy could be a solution to neutralize power peaks that will occur with a rising share of renewable but fluctuating electricity generation provided by wind, solar and water power [7, 22–24]. However, this asks for full process control and smart energy handling which is currently not a standardized procedure, placing high demands on process engineering.

In order to improve process control, microstructured reactors and devices intensify process properties and could potentially allow fast changes while being in full control of the process. To what extent this is possible and what potential use emerges from it was investigated in this thesis.

In the scope of this work, beyond state-of-the-art reaction environments for the decentralized production of renewable fuels will be introduced. Those microstructured systems allow an intensified process control and are well suited to handle complex catalytic chemical reactions such as the Fischer-Tropsch synthesis. From carbon monoxide and hydrogen, this catalytic reaction forms hydrocarbons of variable chain lengths to produce a combination of gaseous, liquid and solid products. Those are needed in different industries and applications. The mixture of produced hydrocarbons, syncrude, can be separated into target fractions. Decentralized small-scale plants could be erected wherever a fitting feedstock is available, making efficient energy conversion available for many scales and types of applications. This, however, presupposes that the reaction system is fully applicable to follow every change change in feed. Changes could occur in dependency of fluctuation of renewable energy and applied intermittent storage infrastructure. The aim of this work is the deep understanding if microstructured reactor technology could be helpful to improve reaction manipulation under dynamic conditions.

A process parameter study for two microstructured reactors is provided in this thesis. Dynamic or load-flexible process control, as well as possible limits of the reactor system are presented. In that regard, a highly dynamic hydrogen input is tested for the first time in a pilot-scale reactor. To describe the complex system, a reaction kinetics model is coupled with a vapor-liquid equilibrium model to determine properties of the liquid products. A residence time distribution model for all system elements allows a time-dependent product and synthesis evaluation. In order to investigate catalyst performance during reaction and eventual causes of deactivation, spectroscopic methods are used in *operando* analysis.

This work is devoted to enable future decentralized PtL and sector coupling applications by giving ideas of possibilities and limitations that such systems might possess. Future energy systems might profit from findings presented in several publications.

2 Theoretical background

In this chapter, an introduction to current energy consumption is given. Next, the Fischer-Tropsch synthesis (FTS), a polymerization reaction to convert syngas into hydrocarbons, as well as product processing and current plant concepts are presented. The potential of a load-flexible or transient operation is explained. Deactivation and regeneration of the catalyst are explained and methods to investigate catalyst behavior in *operando* are elaborated.

2.1 Energy

With an increase in population and the general pursuit of prosperity, the need for energy is naturally rising. This leads to two main challenges: the total amount of energy needed to sustain everyday life must be generated and available when and where it is needed. Additionally, energy must be generated sustainably if we want to preserve our environment and limit long-term damages to this planet. Table 2.1 shows the potential of renewable fuels in our current energy system. As of 2018, less than 5 % of energy used for mobility came from renewable sources such as bio-fuels and renewable electricity [25, 26].

Even amidst the energy transition, crude oil products make up more than 970 TWh of energy used in Germany, which amounts to 37.4 % of the final energy consumption [26]. Globally, the mobility sector accounts for 25 % of fossil energy demand [32]. Germany was able to substitute its nuclear energy share with renewable energy, while the fossil share was barely changed in the last 15 years [25, 31]. There will always be a need for liquid fuels due to heavy duty transport and long-distance air travel. Those applications rely on the high energy density of the fuel, its availability and reliability. Thus, the potential to increase the share of renewable fuels in an existing infrastructure are given. Several reports urge to take political

Table 2.1: Share of renewable, fossil and nuclear energy with regard to different energy sectors for members of the Organization for Economic Co-operation and Development (OECD) and Germany for 2018 [25–31]

OECD	Residential*	Mobility	Electricity	Industry
Fossil	70.4 %	95.5 %	56.0 %	81.4 %
Renewable	22.4 %	4.4 %	26.0 %	14.3 %
Nuclear	7.2 %	0.1 %	18.0 %	4.3 %
Germany	Residential*	Mobility	Electricity	Industry
Fossil	74.6 %	95.3 %	53.0 %	75.2 %
Renewable	22.1 %	4.5 %	35.0 %	20.4 %
Nuclear	3.2 %	0.2 %	12.0 %	4.5 %

*Residential = Municipal heat + electricity

action and innovative steps towards a market entry of "e-fuels" [8, 33–35].

Battery material has drastically increased in cost over the last few years. The price of cobalt went up more than 100 % from 2016 to 2017 and lithium carbonate cost increased by 37 % in the same period [35]. Additionally, the largest portion of those resources are located in development countries that are known to suffer from economic pressure and struggle to keep up labor standards and ecological standards in return. Despite first triumphs in electrical mobility, this technology is not solely advantageous today [10, 23, 36–39].

There will be forms of mobility that need a high energy density, most prominently air travel and heavy-duty transport. If we aim to be CO_2-neutral in those areas, renewable fuels are the only solution as of today. Fossil energy carriers are cheaper than other energy sources and might always be but certainly bring disadvantages with their use. Crude oil quality is decreasing with each emptied drilling field [40]. The cost and availability are unpredictable due to geopolitical decisions and unreliable distributors [25]. Carbon stored underground for millions of years is slowly changing our geosphere by the evolution of CO_2 from combustion [5].

The use of renewable instead of fossil energy is part of the energy transition. In the best possible future, sun, wind and water energy will be harnessed and converted to electrical energy to satisfy 100 % of our energy demand. If the current production is higher than the demand, energy must be stored. Similarly, a deficit must be compensated. In both cases, a reliable energy storage is asked for.

In terms of storage efficiency, batteries are the obvious choice for storing electrical energy. Since electricity is not the only form of energy that is needed in daily life, energy conversion is inevitable. Mechanical energy and heat are just as important as electrical energy. In this regard, energy carriers are both needed as storage and medium. Chemical energy within molecules can be released when- and wherever needed.

In whatever form, energy will always deal with a number of challenges, for instance storage and transportation of energy with an acceptable technical efficiency. Liquid fuels omit most of those concerns and stand out due to their high volumetric energy density compared to gases (approx. 35 MJ L^{-1} vs. 9 MJ L^{-1} for methane at 0 °C and 250 bar) [10]. In order to promote sustainability in the fuel sector, chemical conversion processes from low volumetric energy density gaseous products are discussed. Based on the carbon source, these conversion processes are called "power-to-liquid" (PtL), "gas-to-liquid" (GtL) or, depending on the definition, "biomass-to-liquid" (BtL) processes. While the multi-step production of renewable fuels is not a simple task, it might be realistic to produce those fuels for 1 - 2 Euro per liter [25]. Depending on the study, e-fuels or powerfuels could cover a demand of 200 to 900 TWh in 2050 in Germany. They have the potential to save up to 70 % of CO_2 of German traffic emissions today [41].

In table 2.2, those process routes are sketched in principle. If natural gas, methane or biogas are the feedstock, a multitude of their volumetric energy density is gained from liquefaction. The above mentioned storability and transportability are thus given. Liquefaction of syngas can be realized by different technologies, depending on the product. Fischer-Tropsch synthesis, methanol (MeOH) synthesis, methanol-to-gasoline (MtG), dimethylene ether (DME) synthesis with DME compression, oxymethylene dimethyl ether (OME) synthesis and other routes can be chosen to produce a liquid intermediate.

2.2 Fischer-Tropsch synthesis

A pathway from synthesis gas to renewable liquid fuels is given by the FTS. Carbon monoxide is hydrogenated to gaseous, liquid and solid hydrocarbons (HC) of a variable carbon

Table 2.2: Process routes from various carbon feedstocks, carbon processing, syngas conditioning and additional technology steps

Process route	Carbon source	Carbon processing	Hydrogen supply	Syngas conditioning
PtL	CO_2	Direct air capture (DAC); CO_2 sequestration from industrial or biomass application	Electrolysis	Reverse water-gas shift (RWGS); co-electrolysis; CO_2 electrolysis
GtL	Biogas	Partial oxidation		Gas cleaning, purification
	Natural gas	Dry/wet reforming		Gas cleaning
BtL	Biomass	Gasification		Gas cleaning and cooling; reformation
	Municipal waste			

chain length. The reaction is promoted on a metallic catalyst surface, in most industrial processes iron or cobalt [42–44], making it a heterogeneously catalyzed reaction. Due to the nature of chain propagation, the reaction is considered a polymerization type synthesis. The discovery of the reaction was almost 100 years ago [45, 46]. The reaction equations from syngas are given in equation 2.1.

$$n\mathrm{CO} + 2n\mathrm{H_2} \rightleftharpoons -(\mathrm{CH_2})_n- + n\mathrm{H_2O} \quad \Delta H_R^0 = -158.5\ \mathrm{kJ\,mol^{-1}}$$

$$\begin{aligned} \text{Alkanes and Iso-alkanes: } n\mathrm{CO} + (2n+1)\mathrm{H_2} &\rightleftharpoons \mathrm{C}_n\mathrm{H}_{2n+2} + n\mathrm{H_2O} \\ \text{Alkenes: } n\mathrm{CO} + 2n\mathrm{H_2} &\rightleftharpoons \mathrm{C}_n\mathrm{H}_{2n} + n\mathrm{H_2O} \\ \text{Alcohols: } n\mathrm{CO} + 2n\mathrm{H_2} &\rightleftharpoons \mathrm{C}_n\mathrm{H}_{2n+1}\mathrm{OH} + (n-1)\mathrm{H_2O} \end{aligned} \tag{2.1}$$

The process works with elevated pressure ($\geq$ 20 bar) and temperature ($\geq$ 200 °C). The pressure is necessary to increase the yield of long-chained products and reduce the selectivity towards gaseous HCs [40, 47, 48]. The temperature is needed for kinetic reasons, since catalyst activity is usually low below 200 °C [42, 49]. Since H_2 and CO monomers build up hydrocarbon chains on the catalyst surface, the chain growth probability heavily influences the type and distribution of the HC products.

In figure 2.1, the typical product distribution as a function of the chain growth probability during reaction is depicted. The mathematical background is elaborated in section 3.3.4. The chain growth probability can be strongly influenced by various process parameters. The product always is a mixture of many different molecules and chain lengths.

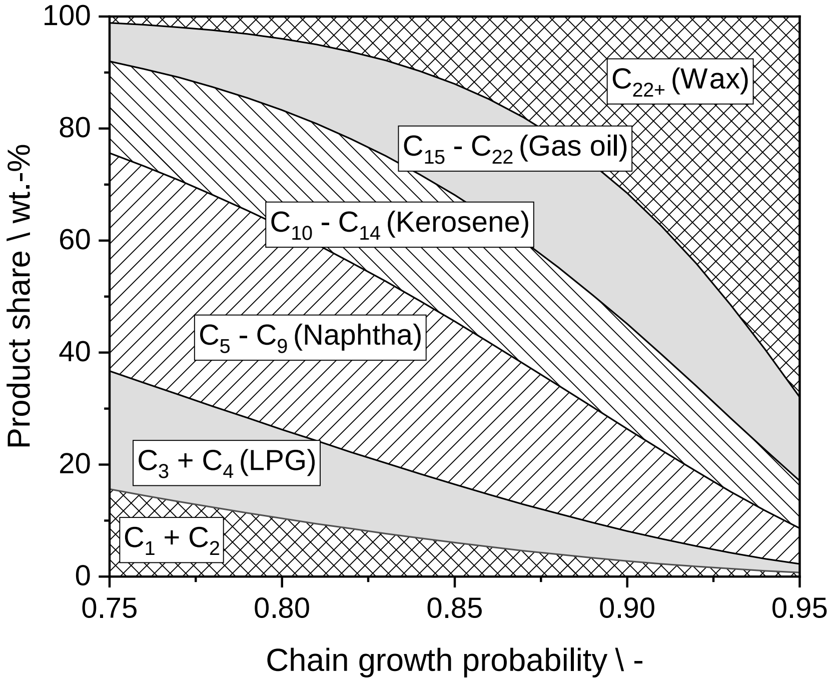

Figure 2.1: Share of different product fractions over the chain growth probability, data representation after [50].

2.2.1 Product processing

Since hundreds of different products spread over four different product phases (including water), all of those phases need to be properly processed in order to separate the molecules used for different applications. Short, gaseous HCs can be used as heating gas or fuel gas or can be reconverted to syngas in a process loop. Ethylene is a valuable intermediate for the chemical industry [42, 51, 52]. The liquid syncrude fraction must be processed to fulfill current fuel standards. Distillation and hydroprocessing are important and necessary steps towards drop-in fuels [42, 53, 54]. Depending on the catalyst system, more or less alkenes and iso-alkanes are formed [49, 55–57]. The share of those product classes can be adjusted, depending on the target application. Gasoline, diesel or kerosene have different, specific fuel standards. The chain length, octane or cetane number, as well as cold flow properties and densities are only a few criteria that must be adjusted to existing norms and regulations [54, 58, 59]. Additionally, new fuel standards could be helpful to adapt to changing fuel systems. Compared to its fossil counterparts, FTS products show distinct advantages in soot formation and NO_X emissions upon combustion [13–15].

The long-chained wax fraction can be used as coating material or in the cosmetics industry [60]. Alternatively, waxes can be hydro-cracked to increase the yield of fuels [43, 61]. The FTS can produce high-end, customer-specific products with a flexible carbon-range. The increasing scarcity of fossil raw materials can thus be counteracted technologically. Still, processing of the products is necessary due to the number of different products.

2.2.2 Feed gas production for the Fischer-Tropsch synthesis

For the FTS, quality and quantity of the synthesis gas is essential. Solid carbon sources such as coal or biomass can be gasified in an oxygen-poor environment [62, 63]. Gaseous feedstock such as biogas or natural gas can be partially oxidized or reformed [64, 65]. In order to adjust the ratio of hydrogen to carbon monoxide, gas conditioning can be applied. The water-gas shift reaction (WGS) can be used to adjust the syngas ratio (H_2/CO). The reaction is shown in equation 2.2.

$$\mathrm{CO} + \mathrm{H_2O} \leftrightharpoons \mathrm{CO_2} + \mathrm{H_2} \quad \Delta H_R^0 = -41.2\ \mathrm{kJ\,mol^{-1}} \tag{2.2}$$

By shifting the reaction equilibrium, the RWGS is used to activate rather inert CO_2, reducing it to CO. The target syngas ratio for conditioning is somewhere between 1.7 and 2.15 to pay respect to reaction stoichiometry and suitable carbon chain propagation while suppressing excessive methane formation [49].

Using the RWGS or co-electrolysis, CO_2 can be used as the carbon feedstock for syngas and consecutive reaction steps such as the FTS. This technology then allows the production of CO_2-neutral fuels, given a high carbon efficiency.

2.2.3 Industrial Fischer-Tropsch process

Industrially, the FTS is only used for fossil feedstock (coal or natural gas). The technology developed in the past was mostly driven by independency of specific countries and the Great Depression (massive crude oil price increase), leading to large reactor industry and enormous process flows [49, 66].

Challenges in the process traditionally come from complex, space- and cost-intensive installations. Reactors are large in diameter, so reaction heat can only dissipate slowly [67, 68]. In the case of slurry reactors, the start-up phase of the reactor, as well as the separation of the product from the catalyst pose a challenge, next to the need of abrasive-resistant catalyst design and low per-pass conversion [42, 58, 59, 69].

2.2.4 Decentralized plant concepts for local energy conversion

Recognizing the need to convert significantly smaller amounts of energy in decentralized, sustainable applications, a number of companies offer solutions to convert stranded gas, offshore gas, associated gas, biogas or concentrated CO_2 into high-value products. Those operations are offered by INFRA, EFT, Greyrock, CompactGTL, Velocys or INERATEC, to only name a few [38, 54, 70–75].

Lower throughput in decentralized plants and size requirements ask for even better process control to increase conversion efficiency. Microstructured reactors may offer the needed level of control by process intensification. Reaction heat can be extracted from the system effectively and isothermally while achieving a high syngas conversion. The contact between reacting agents and the catalyst is increased. Especially surface phenomena are intensified in those systems. The modularity of microstructured packed-bed reactors can be used to number-up reactors in order to scale to the throughput. After all, an efficient process for decentralized application is realized in high-performance reactors. [71, 73–91]

2.2.5 Power-to-liquid – pathway of the future?

As CO_2 is a greenhouse gas and waste product for most carbon-based processes, its use as feedstock is of great importance for the energy transition. Electrical energy will be available and cheap in future energy systems [17, 23, 92, 93]. Using efficient technologies such as the FTS in microstructured reactors might result in a sustainable way to produce renewable, CO_2-neutral fuels in relevant amounts in the future. The key is numbering up small, efficient processes instead of scaling up centralized existing industries.

Nevertheless, the downside of a multi-stage liquifaction process is the efficiency loss with every reaction step. Table 2.3 compares the relative efficiency of overall chemical liquefaction processes per feedstock.

Table 2.3: Efficiency from feedstock to product for various process paths, including coal-to-liquid (CtL) and combined power-and-biomass-to-liquid (PBtL) [16, 20, 58, 59, 94, 95]

Process route	Overall process efficiency
PtL	39.2 - 50.6 % [16, 20]
GtL (CH_4)	60 % [58, 59]
CtL	45 - 50 % [59, 94, 95]
PBtL	51.5 % [20]
BtL	36.3 - 39 % [20, 95]

Despite conversion losses, the final product price for renewable fuels is estimated to be 0.85 - 3 € L^{-1} within the next 20 years, depending on location, plant size and production pathway [12, 18, 20, 95, 96].

2.2.6 Load-flexible or dynamic operation

Innovation and smart grids will allow decentralized plant networks to store excess electrical energy [10, 12, 34–36, 97–100]. This option asks for an emphasized load flexibility of several process steps with according demands on the technology. The potential of dynamic process properties is notably high. An internal study conducted alongside this thesis in cooperation with the Ruhruni Bochum concluded that over 90 % of the needed gas storage tanks could be reduced just from a smart process control for a PtL plant. Energy flows were calculated over the course of a year with a mixture of wind and solar power as an island solution scenario [101]. This conclusion has a significant influence on installation cost of a plant network. Standby times of the FTS plant could be completely avoided or significantly reduced.

Historically, there never was much interest in industrial "dynamic catalysis", since stationary production in most processes relies only on a fixed combination of parameters from economic optimization. In this safe environment, the influence of changing parameters in catalysis are unknown for most systems, leaving principal questions unanswered. Still, there is a high potential for transient operation [102].

In the history of dynamic operation, researchers always hoped to overpass the boundaries of steady-state synthesis reactions [103–119]. It was realized that potential advantages in selectivity from forced feed cycling must thereby overcome additional cost and complexity brought into the system [111, 113, 118]. In the context of PtL applications, the reduction of hydrogen storage is a hands-on improvement enabled by dynamic operation [111, 113, 120]. Only a small number of publications investigated potential effects from dynamic synthesis on the FTS, mostly before the 1990s [118, 119]. It was observed that iron-based catalysts produce more methane under forced feed cycling. When repeated for a cobalt-based catalyst, a "hydrocarbon formation overshoot" for the C1 - C7 species, compared to steady-state, was observed [119]. It should be noted that such effects might be strictly linked to one specific catalyst alone. In a review by Silveston from 1995, a generally increased catalyst activity or performance was described for multiple systems [118]. Other observations are worth mentioning, such as that steady-state kinetics are unable to predict dynamic behavior and that forced feed-cycling was the only practicable way to induce dynamic behavior to the system.

Temperature cycles were thus not much looked into at this point. Only the work of Gonzalez and Eilers picked up that topic 20 years later [111, 113, 117]. PtX technologies became increasingly interesting for process engineers, so new findings for Fischer-Tropsch catalysts were discovered. For both iron and cobalt-based catalysts, no improvement in activity or selectivity could be found. Still, no down-sides from forced feed cycling could be observed. Thus, steady-state kinetics were applied for unsteady-operation. A final validation of the actual dynamic context with regard to electrolysis, storages and general sector coupling could not be concluded, since no system with sufficiently short response time was present at the time of publication.

A deeper look into dynamic synthesis was taken in the form of the methanation reaction [103–110, 114–116]. The need for flexibility in an ever-changing energy system was recognized and researched intensively in that field. From simplified assumptions in his model, Güttel concluded that oscillation brings no improvement in the reaction rate compared to steady-state [112]. A high-frequency oscillation showed an equal quality to the steady-state product gas composition with worse results, the longer oscillation cycles were taking. Unsteady-state kinetics were likely missing for more reliable simulation results. Reactor temperature is an unresolved issue that needs to be closer looked on. On paper, the methanation reaction seems simpler in terms of reaction kinetics, compared to the FTS. At the same time, catalyst deactivation and moving of the reactor hot spot is a much bigger issue, compared to most Fischer-Tropsch experiments [104, 106, 109]. Reaction stability opened up a new degree of uncertainty in dynamic methanation. Since, multiple models were developed to simulate product properties and system stability with dynamic operation. Some of them focus on thermal stability and synthesis improvement [103, 105–110] while practical approaches often lack a sufficient feedback loop or monitoring options [103, 105, 107]. There are mixed reports about the decline of reaction rate by oscillation experiments. While few advantages from oscillation are reported [103, 104], there seems to be close to no negative effect on catalyst lifetime with relatively better performance the smaller the cycles become [104, 114, 115]. Both the isothermal and adiabatic reactor approach have advantages and disadvantages, while the latter seems to be better suited for load-flexible operation [103]. Thanks to microstructured fixed bed reactors, many of the above-mentioned challenges do not apply to this research, as shown in our work [120]. Hot spots can be controlled, while ensuring high per-pass conversion. There seemed to be no advantage or disadvantage from dynamic oscillation experiments and steady-state kinetics are assumed to be valid for unsteady-states as well. This all lead up to the next step of research: high-frequency oscillation following the power profile of an electrolysis [121].

Start-up and shut-down phases of reactions might behave differently. Changes in the feed gas or other system impacts must be counteracted instantaneously, at best. That sets a number of requirements on the catalyst system and the reactor itself. Well-controlled systems such as microstructured reactors help in that regard.

2.2.7 Catalyst deactivation

The longevity of catalysts is of utmost importance with regard to the economics of the process. This means to avoid unexpected shut-downs and cost due to catalyst degradation [49, 122]. Extraction of catalyst from reactors with a pronounced liquid phase is technically complex and regeneration cycles take up important process time. The degree of catalyst deactivation is strongly dependent on the preparation of the catalyst and can be controlled by process parameters during synthesis. The main reasons for deactivation differ drastically depending on the materials used.

A number of effects are expected to have a high impact on catalyst activity. Overviews for cobalt catalysts applied in this thesis are given in the mini-review from Rytter et al., the review from Tsakoumis et al. and the report from Saib et al. [123–125].

According to literature, the following mechanisms are the main reason for deactivation:

- Poisoning
- Oxidation
- Catalyst-support-interactions
- Sintering
- Surface reconstruction
- Carbon deposition

- Attrition

According to Saib et al., the reasons for deactivation after a literature research of 133 papers are distributed after figure 2.2. It is noticeable that oxidation is named in over 50 % of publications as the main reason for deactivation.

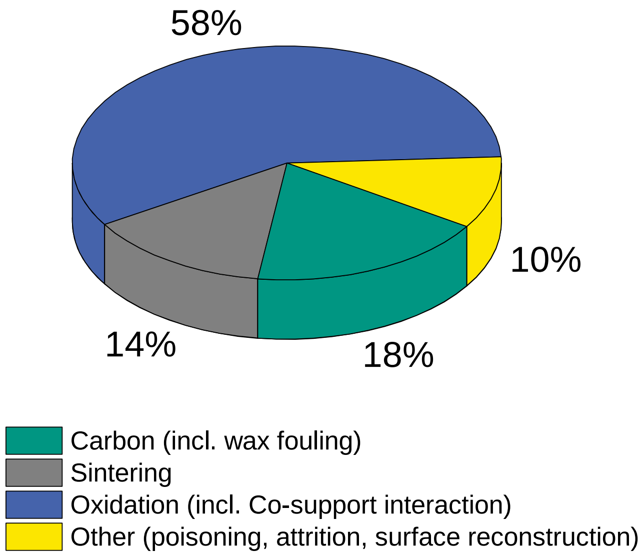

Figure 2.2: Results from a literature research for the deactivation of cobalt catalysts based on articles published between 1995 and 2009, reconstructed from [125].

Poisoning

As with all catalysts, cobalt can be influenced by contaminants. Known catalyst poisons are sulfur- or nitrogen-containing substances that are formed during synthesis gas generation (in most CtL and BtL applications). By gas purification, hazards from these components can be ruled out in almost all cases [125]. Ammonia and acetonitrile are reported to cause an irreversible deactivation by forming cobalt nitrides at 50 ppb upwards [126, 127]. Many fundamental insights on the effect of N-containing agents are still locked due to patent reasons [124].

With an increase in sulfur content of the syngas, the activity and C_{5+} selectivity decrease, alkenes are better hydrated to alkanes, however [128]. It is assumed that sulfur forms rather physical blockades at active sites than influencing the electron distribution in the surrounding system [42]. The concentration of sulfur nowadays is strictly regulated and thus far below the hazardous amount stated in early reports from the 70s [49, 129].

Additional poisons were reported to have an effect at around 400 ppm with an inhibiting effect decreasing in the following order [130].

$$\mathrm{Na} > \mathrm{Ca} > \mathrm{K} > \mathrm{Mg} > \mathrm{P}$$

Mn, Fe and Cl had showed almost no effect. Chloride is known to reduce the chemisorption of H_2 significantly but still showed very weak effect as a poison [123]. Alkali and alkaline earth metals influence the dissociation of CO on the catalyst surface with its strong electronegativity [131]. Critical concentrations are yet to be determined [124]. With sufficient gas purity, no poisoning should occur in the regular FTS. In contrast to PtL applications, BtL are more hazardous in that regard.

Oxidation

In the past, oxidation counted as one of the main reasons for rapid deactivation of cobalt crystallites [132–135]. Only in the last 10 - 15 years, publications gave different statements on that topic [136]. Modern spectroscopic analysis showed that cobalt oxides form independent from time on stream and sometimes not at all (see section 2.3). This implies the reasons for oxidation to be found in the catalyst preparation or in unusual process properties. There are many different statements for each support, promoter and crystallite size distribution the catalyst [125, 136]. Thermodynamically, the formation of cobalt oxides is unfavorable to impossible [125, 137]. The smaller the crystallites, the more vulnerable they are to oxidation. The critical crystallite size in regards to different deactivation effects is reported to lie between 2 and 6 nm [125, 138].

The effect of water is especially interesting with regard to oxidation since a high conversion increases its partial pressure significantly [132]. Findings vary for different support and promoter materials, partially increasing catalyst activity for certain promoters. There is no hard line from which the ratio of partial pressures becomes a problem. Since the absolute par-

tial pressure of water P_{H_2O} also plays a role, CO conversion is an indicator for deactivation as well. The higher the conversion level, the higher the water partial pressure [123, 132].
In catalyst preparation, the metal crystallite size distribution should be adjusted carefully. In industrial applications, the water partial pressure and the ratio of water to hydrogen partial pressures should be regulated so no oxidation may be caused. In practice, this can be achieved by conversion level control, e.g. in back-mixed slurry type reactors.

Cobalt-support interaction

Cobalt-support interactions are kinetically limited under regular FTS conditions [125]. They are primarily determined by system temperature and thus much more critical in high-temperature FTS. If interactions occur in low-temperature FTS at all, they do not contribute significantly to deactivation [125]. Rytter et al. described the effect of the support on the reaction product rather than on the catalyst itself, influencing the selectivity towards longer carbon chains ($S_{C_{5+}}$) [123].

Sintering

There is a consensus about the effect of small Co crystallites sintering, thus causing deactivation in the first phase of the reaction. Argyle et al. report 30 % loss of activity within the first 14 days of time on stream (TOS) from sintering alone [139]. Kistamurthy et al. could prove the loss of crystallites smaller than four nanometers using a transmission electron microscope (TEM) [138]. Especially with a high conversion and associated local hot spots, local sintering is promoted. Temperature is by far the most important factor. Still, surface conditions and the catalyst pore structure, as well as the support also play a role [140]. Sintering reduces the number of active sites by crystallite migration which increases the average crystallite size significantly. This causes surface and activity loss.
Sintering is either caused by Ostwald ripening or migration and coalescence under certain conditions (high temperature, weakly binding support, gas composition; e.g. water and CO content) [124, 141]. Ostwald ripening seems to be the more pronounced cause at lower temperature [124, 138, 141]. Physically, single crystallites aim to minimize their surface energy [124], where smaller crystallites have a higher mobility. The migration of crystallites

can be influenced by the support, e.g. Al_2O_3 is considered to be a strongly interacting carrier material. Other, thermally unstable carrier materials such as SiO_2 are partly susceptible to sintering themselves, but only under high temperature conditions with a high water partial pressure [142]. Experiments on carbon nanotube (CNT) supports have shown how strongly the extent of sintering can depend on the support [124, 143]. A better application of carbon-based substrates, related to sintering, could be applied by Karimi et al. in the form of graphene nanosheets (GNS) [144].

There is a series of precursors for sintering which, with the correct catalyst preparation and a good reactor and experiment design, can lead to a short deactivation time in the first few hours [145]. According to Holmen et al., one prevention of sintering in reactor engineering is the use of microstructured reactors which exhibit excellent heat dissipation [146].

Surface reconstruction

Only for a few years, the phenomenon of surfaces reconstruction is described [136]. The restructuring of the crystallite surface is a dynamic process that results in a "roughening" of the surface which increases its surface energy. A second effect is the formation of planar areas which cause a reduction of the surface energy [125, 145]. The presence of carbon seems to play an important role here. Overall, the effect of surface reconstruction is not considered to make a major contribution to deactivation, in some cases the transformation can even be beneficial for the activity of the catalyst [123, 125].

Carbon deposition

The deposition of carbon (C) species is the deactivation cause with the highest proportion of conversion loss over a longer period of time for syntheses with Co catalysts [123–125, 138, 139, 145, 147, 148]. Especially with CNT carriers, carbon deposits are described as the main reason for deactivation [143]. Argyle et al. observed a gradual deactivation by C deposits after initial sintering [139]. Carbon is deposited on the catalyst in the form of polymers, waxes or cobalt carbides, which have a deactivating effect even in small amounts [125]. Some of the deposits are irreversible. Especially C deposits below the surface (subsurface carbon) become a problem, since they weaken C-O-bands and thus complicate the

adsorption and desorption of intermediates. Coke formation is rather unlikely, as intermediates react kinetically preferred to HCs. C-settlements on the surface are also stoichiometrically difficult, since many HC species are present [124]. Methods like temperature-programmed reduction (TPR) are suitable for the analysis of deposits. According to de Smiz et al., carbide formation in Co catalysts is 10^5-times smaller than in Fe catalysts, but still takes place [149]. This happens mainly at the surface of the catalyst. Waxes on the surface cause a retarding effect during mass transport and can block catalyst pores. Precious metal components seem to prevent C deposits [150, 151]. Other approaches to prevent deactivation include the use of super-critical fluids with outstanding mass transfer or functional catalysts with cracking properties to prevent wax clogging [152, 153].
Kistamurthy et al. found out that oxygenates function as precursors for atomic C deposits [154]. Keyvanloo et al. found that the observed deactivation is triggered by polymeric C deposits and the associated reduced CO uptake. Stable polymers are formed by a low ratio of H_2/CO and a high CO conversion. Pt promoters noticeably reduce polymer formation [145]. Furthermore, five cases of carbon influences on the catalyst could be observed;

1. carbon binds irreversibly as a kind of catalyst poison to the catalyst surface and thus destroys active sites
2. mesopores are blocked and the accessibility of active sites is limited to the gas phase
3. solid cobalt carbides form and reduce activity
4. deposits below the surface reduce the activity by reducing the electron availability
5. a positive or negative surface reconstruction takes place.

In case 2, activity could be restored on a Co-zeolite catalyst after extraction and high-temperature H_2 treatment. Case 3 could be quickly reverted by normal FT operation. The effect on catalyst deactivation must be correspondingly small.
Several groups dealt more profoundly with the effect of noble metal promoters on the carburization of catalysts. For Pt and Ru it was found that C-H bonds are supported and C-C bonds are blocked, which does not prevent carbon migration below the surface, however. More complex C structures have been shown to be destabilized by promoters, with Pt having a greater effect than Ru. [148, 155]

In their report, Rytter et al. state that the number of depositions can be well adjusted by temperature control [123]. Claeys et al. dealt with the carbidization of catalysts, which is favored by a low H_2/CO ratio and a high temperature [147]. Those carbides are mechanically stable, but degrade under H_2 treatment at 150 °C and above. According to their work, cobalt carbides are a negligible phenomenon with regard to deactivation.

Attrition

Attrition is not relevant for fixed bed catalyst systems but must be regarded in fluidized bed reactors.

Deactivation summary

In conclusion, the importance of a deactivation mechanism for the FTS must be investigated for each process and catalyst. In general, for cobalt it can be said that oxidation, poisoning of any kind and Co-support-interactions are negligible for long-term deactivation. Structural surface changes are either not a problem in most reports or can even have a positive effect on catalyst activity. Sintering and carbon deposition, on the other hand, are significant disruptive factors in a system that relies on the longevity of a catalyst. A summary of the relevance of all identified deactivation mechanisms is given in table 2.4.

2.2.8 Regeneration of spent catalyst

The countermeasure to deactivation is regeneration of the catalyst. The procedure is different in each publication, but usually works with the same list of tools in different combinations. Many regeneration processes have been developed specifically for a particular catalyst-promoter-support combination and cannot be fully applied to similar combinations [156]. The configuration is often not mentioned in detail since many new processes have been patented [123]. In the conclusion of the work by Arcuri and LeViness, there is realization that there can be no universal process for catalyst reactivation in general [156].

The toolbox at hand usually includes oxidation, reduction, a combination of both, reduction in water-gas, elevated temperatures and physical methods such as solvent extraction.

Table 2.4: Deactivation mechanisms and their importance in the FTS process with Co catalysts, recreated from [125]

Mechanism	Degree of deactivation	Importance	Remarks
Poisoning from S species	high	negligible	species can be removed from syngas
Poisoning from N species	medium	negligible	species can be removed from syngas
Oxidation	none	negligible	improbable to occur
Co-support interaction	none	negligible	formed from non-reduced Co oxides
Sintering	high	relevant	can cause up to 30 % loss of activity
C deposition	high	relevant	gradual deposition of larger polymers with increasing TOS
Surface reconstruction	medium	might be relevant	initiated by the presence of C, could play a role in the formation of highly active sites

These methods are still used today in improved or modified form for *in situ* or *ex situ* regeneration.

Pour et al. dealt with regeneration mechanisms and their effectiveness in relation to the removal of C deposits, as this was identified as the main mechanism of deactivation. A high temperature treatment with H_2 (reduction) proved to be the most effective method of regeneration, followed by a reduction coupled with combustion in air. Combustion showed the lowest improvement in activity. [143]

Vogel et al. combined an oxidation to burn elemental carbon and oxidize the cobalt with a reduction to reactivate the cobalt fraction [122].

Keyvanloo et al. were able to completely regenerate a CoPt/AlSi catalyst after 3 h at 350 °C under H_2 fumigation. By measuring the CO uptake and by spectrometric methods the main cause of long-term deactivation could be traced back to the deposition of C polymers. The reduction temperature should have no effect on the degree of dispersion of the catalyst, since it was already calcined at 450 °C during preparation. [145]

Saib et al. used a three-stage *ex situ* regeneration - (1) de-waxing by heptane washing, (2) oxidation (calcination) and (3) reduction. They reported that this sequence was able to reverse sintering, C deposition and surface reconstruction.
Heptane washing was carried out at 100 °C, oxidation in a calcination unit with a liquid bed using an air/N_2 mixture at up to 300 °C, with slowly increased O_2 content. The reduction was carried out in pure hydrogen in a liquid bed reactor at up to 425 °C. Potential poisoning by sulfur could not be regenerated with this method, in contrast to those caused by nitrogen compounds, since those were easily reversible with a H_2 treatment.
Much of the deposited carbon could be removed between 200 and 350 °C in TPO. To remove the rest of the carbon, it was necessary to operate at temperatures where cobalt oxide formation is common. The subsequent reduction resulted in the re-dispersion of the Co crystallites using the Kirkendall effect. This was confirmed by TEM images. Finally, the importance of both oxidation and reduction in reversing the most important deactivation effects is emphasized. [125]

Rytter and Holmen report on industrial regeneration processes as carried out by Shell and Sasol [123]:

Sasol regenerates part of the catalyst, which they remove from a slurry reactor. This ensures continuous operation of the low-temperature FTS. Regeneration takes place in several steps, starting with de-waxing by hydrolysis (2 h, 220 °C) and reduction (2 h, 350 °C) [157]. This is followed by passivization with CO_2 and oxidation in air in a liquid bed calcining unit (6 h, 250 °C, 10 bar). The final reduction takes place at 425 °C and regenerates the catalyst to 98 % of its initial activity. Again, the Kirkendall effect is used to re-disperse oxidized particles.

Shell regularly regenerates the catalyst, but it is not known whether *in* or *ex situ*. A process from the Bintulu plant in Malaysia also includes de-waxing (using cyclohexane/n-heptane), hydrogenation (atmospheric) and oxidation/calcination. There is evidence of a process that subsequently works with concentrated ammonia solution and CO_2 to produce cobalt amine carbonate complexes needed for re-dispersion [158]. Based on the data, hydrogenation itself seems to have little or no effect on regeneration, as opposed to burning the C residues on the catalyst.

Exxon published a regeneration method with hydrogen fumigation under atmospheric conditions [159]. The regenerated catalyst was a $Co/Ru/TiO_2$ catalyst, which was used at low-temperature FTS conditions between 200 and 230 °C. The role of the promoter is also of great importance in preventing C deposition [155]. Different approaches have been realized in later patents, for example the addition of active metal particles after oxidation or hydrogenation to low-temperature FTS conditions (200 °C, 20 bar) [160].

Further approaches use water vapor (Nippon Oil [161], ConocoPhillips [162]) or nitrogen (Syntroleum [163]) for regeneration.

For microstructured reactors, Rytter and Holmen formulate a number of options; *in situ* and *ex situ* methods by removing the catalyst or several reaction channels for regeneration.

Oxford Catalyst/Velocys compensates for the deactivation of their catalyst by increasing the process temperature from 205 to 232 °C, which also increases CO conversion and selectivity to short-chain products [71]. Activity and selectivity are fully restored by *in situ* hydrogenation, oxidation/calcination and reduction. Hydrogenation performed under low-temperature FTS conditions is believed to reduce smaller Co crystallites and partially remove waxes and residues from the catalyst. The removal of persistent C deposits will not be possible under these conditions, based on research in conventional reactors.

In slurry reactor systems, it is possible to continuously discharge part of the catalyst and regenerate *ex situ*. In fixed-bed reactors, which also include microstructured systems, a method should be implemented in which de-waxing and burning of residues and thus temperature development can be controlled. According to patent literature, *ex situ* procedures seem to be the standard.

Information on the long-term performance of regenerated catalysts is difficult to find. However, the range of regeneration methods in literature is wide. The list of dependencies on the degree of regeneration is almost as long. However, the number of available tools is limited, so that the development of a regeneration method for a specific plant system can be carried out with small effort.

2.3 *In situ* analysis

In order to get a glimpse inside the catalytic black box that is the reactor, *in situ* and *operando* techniques can be applied. Spectroscopy is an effective tool for identifying relationships between structural changes in the catalyst under reaction conditions and the reactor performance for a given system [164]. *Operando* spectroscopy combines time-resolved *in situ* spectroscopy methods with simultaneous online product analysis. *In situ* spectroscopy for the characterization of heterogeneous catalysts in defined environments has been practiced for over 60 years [165], whereby a wide range of spectroscopic methods is available today. The term "*operando*" was first used in 2002 in catalysis literature, and the number of publications on this topic has been steadily increasing since [165–167]. There are also publications with the same underlying methodology that appeared before the term was coined [168–170]. An essential prerequisite for contributing to the understanding of a reaction system by means of *operando* experiments is process observation under relevant reaction conditions. The model reactors and measuring cells used may have to be able to withstand high temperatures and pressures, which also poses great challenges for *in situ* analysis. For *operando* studies in the FTS, certain requirements must therefore be met both for the reaction cell and for the measurement technology used. Ideally, the measurement cell used should show similar properties to the reactor, in which the catalyst is used in practice.

Most of the described reaction cells for such applications are designed for high-temperature but not for high-pressure applications. Therefore, the application of new cells that can bridge or close this "pressure gap" holds an enormous potential [171]. Only a number of publications deal with high-pressure *in situ* FTS characterization, which has been investigated in the range of 10 bar [172–174] to a maximum of 20 bar [175–177]. In addition, long-term studies far beyond the first 5-6 hours reaction time are necessary to understand the reasons for the original deactivation during the initial phase of the Fischer-Tropsch reaction [175]. There is a small number of reaction cells that would be suitable for high-pressure *in situ* application with X-rays [178, 179]. At present, there is no publication on the topic of continuous *in situ* FTS above 20 bar, let alone using *operando* techniques, i.e. the combination of *in situ* catalyst and online product analysis. Furthermore, there are no long-term *operando* measurements at a synchrotron to investigate the deactivation processes of the catalyst in the start-up phase, beyond six hours of TOS.

Synchrotron-based methods such as XAS, XRD or special applications such as magnetometers are ideally suited for characterization *in situ* or *operando* [164]. In the interaction of X-rays with matter, various effects occur that can contribute in different ways to the elucidation of chemical and structural changes. While XRD can be used to obtain information about crystalline and ordered regions of a solid, XAS allows the characterization of amorphous structures [176].

For online analysis of gaseous reaction products, mass spectrometers (MS) or micro gas chromatographs (μGC) are suitable, depending on the application. Due to the high temporal resolution, changes in the catalyst can be correlated with corresponding changes in the product mixture.

3 Experimental

3.1 Reaction system

The reaction volume limits the mass of catalyst that can be introduced into the reactor as a powder. This in turn has an effect on the maximum total enthalpy of reaction and thus on the heat flow to be removed in the system. Furthermore, the mass of catalyst in the reactor determines the amount of gas volume flow that can be introduced into the system under reaction conditions with the highest possible conversion, expressed by the weight hourly space velocity (WHSV) in equation 3.1, for instance.

$$WHSV = \frac{\dot{m}_{feed}}{m_{catalyst}} \tag{3.1}$$

3.1.1 Catalyst

For all featured experiments, a commercial cobalt catalyst with 20 wt.-% Co and 0.5 wt.-% Re on optimized γ-Alumina support was used. Cobalt is the preferred catalyst for low-temperature FTS (LTFT) if saturated compounds are targeted. It shows high selectivity towards linear alkanes, a high activity at low temperature as well as a negligible WGS activity compared to iron catalysts [40, 49, 180]. The particle size distribution was adjusted to 50 - 200 μm for the fixed bed inside the microstructures. Approximately 120 g of catalyst were placed inside the pilot reactor. Figure 3.1 shows a scanning electron microscope (SEM) picture of a commercial Co catalyst.

The fresh catalyst was first reduced *in situ*. The needed temperature was applied with either heating oil (lab-scale reactor) or with heat cartridges placed on the reactor surface (pilot-

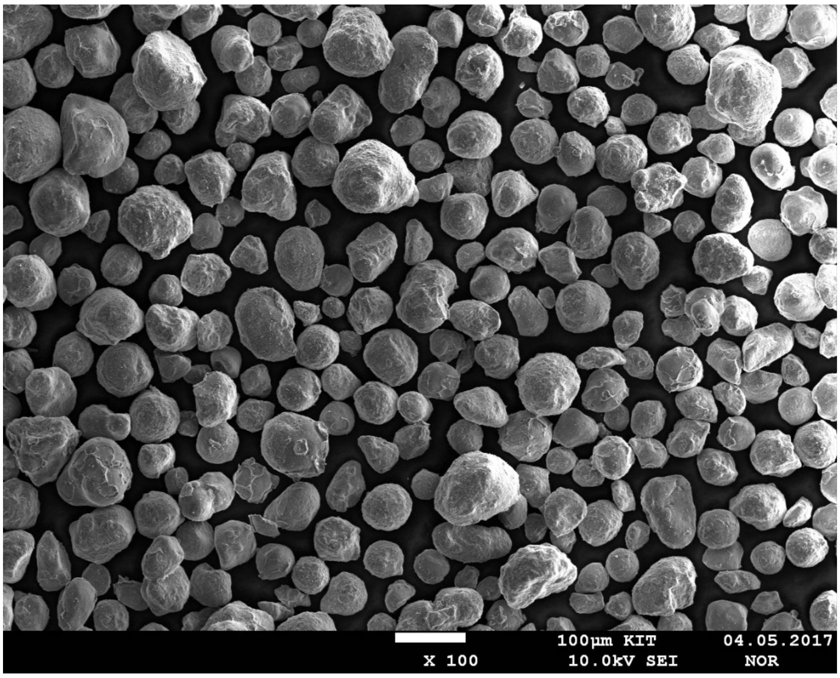

Figure 3.1: SEM image of a commercial Co catalyst. Sieve fraction: 100 - 200 µm.

scale reactor). The reduction procedure was carried out at ambient pressure. A temperature ramp for the reactor was applied starting from room temperature to 350 °C with 1 K min^{-1}. For that ramp, a gas mixture of 5 % H_2 and 95 % N_2 was given to the reactor. The final temperature was held for 16 h. Once the temperature maximum was reached, 100 % H_2 was fed into the reactor for the residual time of the reduction. After 16 h, the reactor was cooled down to 170 °C. From that temperature the different reaction parameters and gas flows were adjusted.

3.1.2 Test rig infrastructure

The small lab scale test rig was previously described in literature, as well as in the first publication of this thesis [73, 75, 82]. The following section describes the pilot scale reactor that was used for all five publications included in this thesis.

Feed gas supply was regulated by mass flow controllers (MFCs; model 5850S, Brooks) and monitored by a mass flow meter (MFM; model 5860S, Brooks). The gas mixture was fed through the house pipe via connected gas cylinders (bundles). Each gas pressure was adjusted via a respective pressure reducer. The pressure in the system had to be slightly above the reaction pressure. The MFCs were controlled via LabView (National Instruments). The gas quantity required for the reaction was specified with relation to standard conditions and had to be calibrated at the gas outlet via a bubble column. All tubing material and system components such as valves and pressure regulators were made from stainless steel. This material meets the respective requirements regarding operating pressure and temperature and shows negligable interaction with the reactants. The products from the reactor outlet were heated to keep longer HC in liquid state. Those products were first collected in a hot trap (HT), which is a pressure resistant container with a volume of about 4 L. It was electrically heated to 170 - 180 °C so that higher hydrocarbons, so called waxes, can condense in this vessel and stay liquid. The subsequent cold trap (CT) was held at low temperature to collect the at ambient conditions liquid product fraction. This vessel is the largest system component with about 20 L of total volume which is kept at around 10 °C by a stainless steel cooling coil of about 2 m length inside the vessel. Liquefied product accumulated in the respective trap system for offline sampling while the gaseous fraction of the product was led to an online gas chromatograph (GC, Agilent 7890B) to determine the conversion and selectivity towards gaseous components. System pressure was held by a back-pressure regulator valve. A permanent bypass with about 2 % of the total flow was adjusted with a fine needle valve to measure the feed gas composition. All system components and pipes were insulated according to the respective local temperature. The entire plant was tested for leaks with a portable gas detector under a hydrogen stream. The system is shown in figure 3.2.

In both separators it was possible to take samples via a needle valve and ball valve-system. Water condensed to a large extent in the cold trap. After the micro heat exchanger, another sampling spot was installed. This location was important for dynamic experiments mentioned in section 4.2.

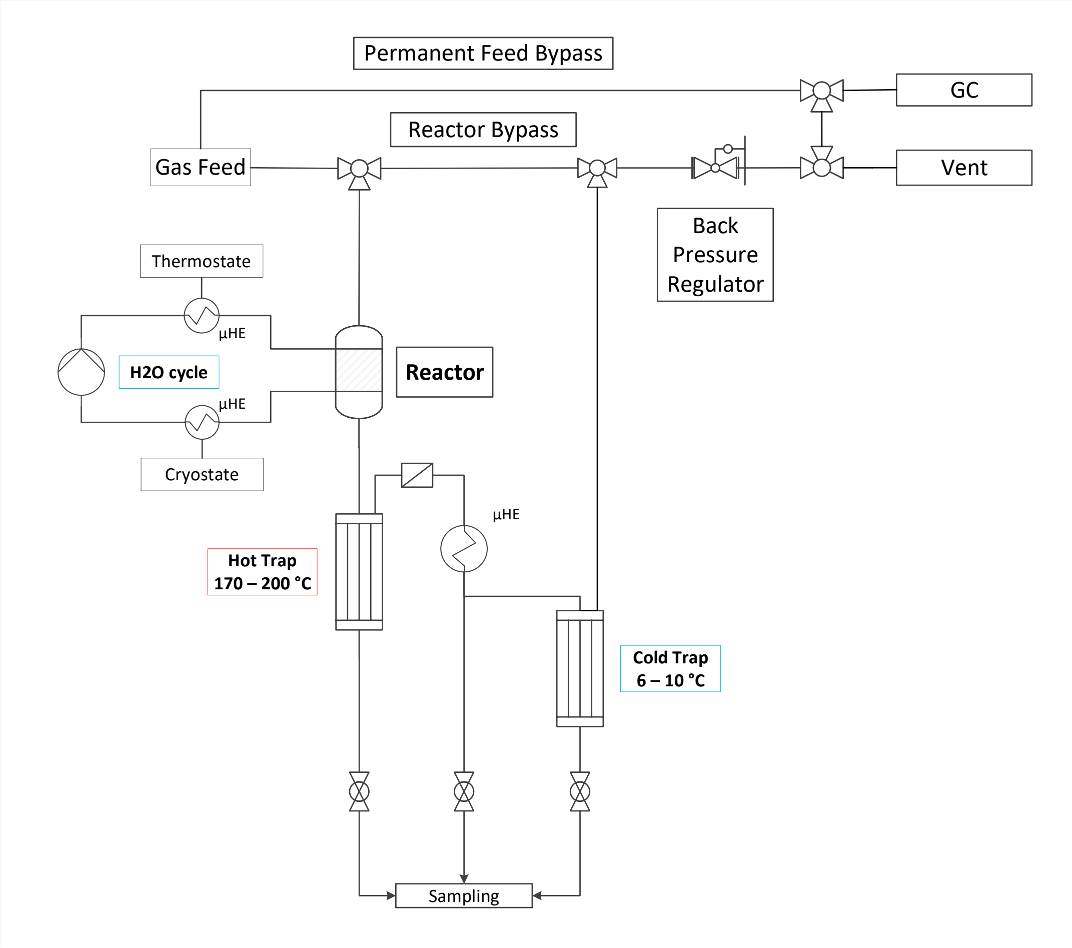

Figure 3.2: Pilot scale test rig in the lab at KIT for a production of up to 7 L of liquid and solid product per day.

3.1.3 Microstructured reactor

The small lab scale reactor was previously described in literature, as well as in the first publication of this thesis [73, 75, 82].

The pilot scale reactor described in this work uses a stack of microstructured steel plates (foils), working after the same principle introduced before [82]. The foils were redesigned and optimized to fit the larger outer dimensions. The reaction volume amounted to approx. 163.4 cm^3 and yielded about 6 - 7 L of liquid and solid product per day, depending on the process conditions. Additionally, patented channels with special cooling structures [181] were integrated for water entering at nearly boiling temperature. Evaporation cooling should keep the reaction temperature isothermal. Evaporation cooling was feasible for this reactor size due to the absolute reaction enthalpy emitted from the reaction. The catalyst mass was high enough to keep the reactor at isothermal set points without electrical heating, enabling an autothermal operation. Access channels for the integration of thermocouples (TC) were integrated in the main body to monitor the temperature inside the reactor. Frits at both ends of the reaction chamber prevented the catalyst from exiting the system, see figure 3.3.

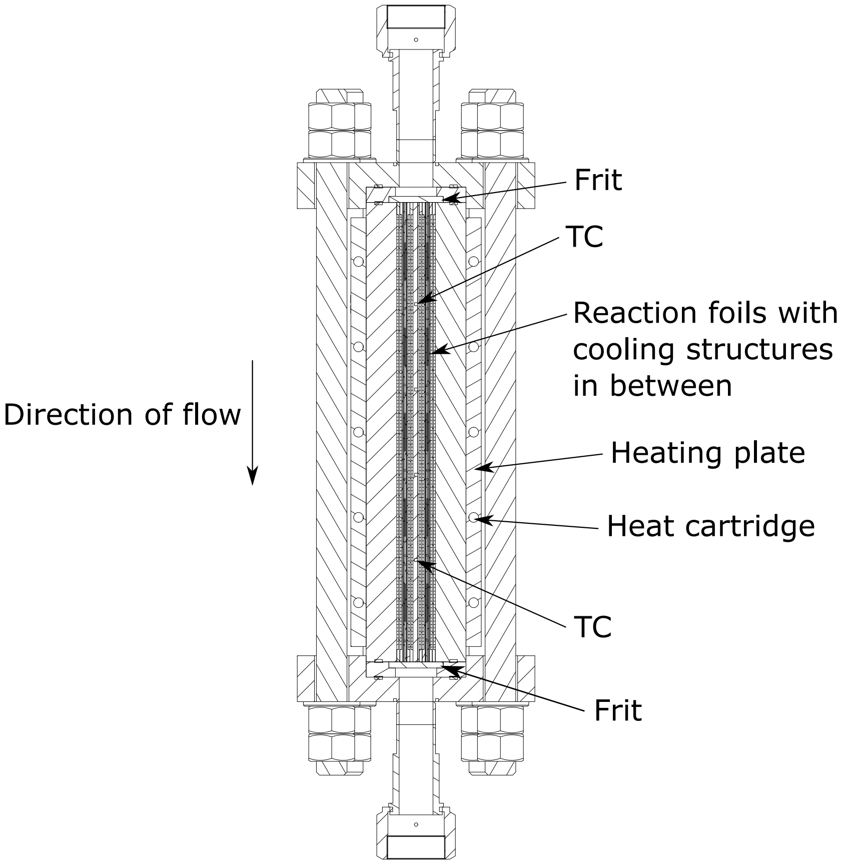

Figure 3.3: Pilot scale FTS reactor for a production of up to 7 L of liquid and solid product per day.

3.2 Process parameters

As literature implied [58, 182], there are four main process parameters having the most influence on the outcome of the reaction: system pressure, the H_2/CO-ratio, temperature and the residence time of the gas. Apart from that, many different materials such as catalyst, support, promoter, active metal, size distributions, composition etc. may be further mentioned at this point.

3.2.1 Temperature

Syngas conversion is strongly related to the reaction temperature. However, it may also severely influence the chain length so a parameter set should represent conditions where an acceptable low methane selectivity and sufficient CO conversion can be found. Up to around 250 °C, many sources describe the process as LTFT that may use iron or cobalt as an active component [183, 184]. Under those conditions, the usage of a cobalt containing catalyst is possible since oxidation may be a negligible factor for long-term activity. A high temperature would lead to shorter hydrocarbon chains, since chain termination is promoted through hydrogenation and other effects [185]. A high temperature would also enhance deactivating effects such as coking, sintering or wax fouling [123, 124]. Experiments in the test rig were thus executed using temperatures between 213 and 246 °C.

3.2.2 Pressure

The total system pressure may influence operation cost [186]. Especially in solid feedstock applications, e.g. direct biomass gasification, a higher pressure may be disadvantageous. To investigate a certain flexibility towards syngas generation, different total pressures were tested. According to literature, the total pressure has no clear trend on the synthesis outcome [187, 188]. It may be more important to look at the partial pressure of the components, especially for gases whose presence favor deactivation [43, 49, 188]. Most of the experiments were executed at 30 bar to maximize the product yield of long-chained hydrocarbons. Experiments at 25 and 20 bar were executed occasionally.

3.2.3 Syngas ratio and gas dilution

The syngas or H_2/CO ratio determines the stoichiometric availability of hydrogen to form hydrocarbons with CO monomers. In biomass applications, a variety of different syngas ratios are reported depending on the gasification conditions and oxidation ratio (oxygen/air and steam content). To highlight the versatility of microstructured reactors, different syngas ratios were tested in the present system. Many mechanisms on how to perform the FTS polymerization reaction have been published in the past [43, 189, 190]. In the end, the availability of hydrogen in the catalyst bed determines whether or not chain progression can be initiated, influencing the average length of the product's hydrocarbon chain. The stoichiometric feed ratio for maximum conversion nevertheless accounts to 2.15 [49]. A ratio of 1.8 significantly reduces the selectivity towards methane. Ratios between 1.38 and 2.80 were fed to the reactor in various experiments.

The syngas was diluted between 1.89 and 55.23 %. A small amount of nitrogen is necessary to determine the conversion as internal standard due to volume reduction. The higher the dilution, the smaller the average residence time in the catalyst bed. Also, the partial pressure of the active feed gas components is reduced due to inert gas.

3.2.4 Residence time

The flow rate of the gaseous feed determines the contact time with the catalyst surface. Thus the possibility of syngas conversion and chain growth will decrease with increasing WHSV since it relates the feed's mass flow with the mass of catalyst inside the reactor, as indicated in equation 3.1. Since the WHSV increases with inert dilution, the syngas ratio and the degree of syngas dilution are complementary information.

3.3 Product analysis

Every product phase demands a separate method of analysis, all of which needed to be carried out in different GC systems. Products formed are gaseous or liquid at reaction conditions. The wax fraction removed from the hot trap under liquid conditions needed to be melted and dissolved in carbondisulfite (CS_2) after sample solidification. A liquid oil fraction accumulated inside the cold trap with accompanying water. The water was separated from the non-polar phase before analysis. Liquid products were analyzed with a 7820 GC (Agilent) in a DB-2887 column (Agilent), while the solid fraction was analyzed using a cooled injection system and a high-temperature simulated distillation column. All samples were taken few hours after parameters were changed and after emptying the traps in between setup changes to avoid instationary conditions influencing the product composition. The GC columns used and products analyzed per column and detector are listed in Table 3.1.

Table 3.1: List of GC systems, columns, detectors and detected products for each phase

GC	Columns	Detectors	Analyzed species
7890B (online)	HayesepQ + MS5A	TCD + FID	O_2, N_2, H_2, CO, CH_4
	Plot Q	TCD + FID	CO_2, hydrocarbons from $C_{1\text{-}7}$
7820 (offline)	DB-2887	FID	Hydrocarbons from $C_{4\text{-}30}$
G1530A (offline)	MXT-HT1	FID	Hydrocarbons from $C_{9\text{-}100+}$

3.3.1 Gas phase analysis

For the permanent gas analysis, different GC columns and detectors were applied within the unit (Agilent 7890B). Hydrocarbon species were analyzed in a flame ionization detector (FID), while two thermal conductivity detectors (TCDs) were used to measure H_2, N_2, O_2, CO, and CO_2 as well as hydrocarbons up to heptane. Two HayesepQ columns (Agilent) first separated hydrocarbons from CH_4 to C_7H_{14}, as well as CO_2 from the rest of the permanent gases. Two Molsieve 5A columns (Agilent) were used to split the retained CO, N_2 and H_2, while a PoraPlot Q column (Agilent) separated hydrocarbons and CO_2. By measuring a feed bypass, the present H_2/CO-ratio could be calculated via the gas fraction y_i according equation 3.2.

$$H_2/CO = \frac{y_{H_2\,feed}}{y_{CO_{feed}}} \tag{3.2}$$

Syngas conversion X_h was determined using nitrogen as internal standard to correlate the flow before and after the reaction, since there is considerable volume reduction from the reaction. The conversion can be calculated according to equation 3.3.

$$X_h = \frac{\frac{y_{h_{feed}}}{y_{N_2\,feed}} - \frac{y_{h_{product}}}{y_{N_2\,product}}}{\frac{y_{h_{feed}}}{y_{N_2\,feed}}} \tag{3.3}$$

h = CO or H_2.

The selectivity of hydrocarbon components $S_{C_iH_j}$ was determined by using a FID detector. N_2 is only detected on the TCD. Since CH_4 was measured on both detectors, the relation of its signal between FID and TCD was used as an additional factor, see equation 3.4. i is the carbon number and j the equivalent number of hydrogen atoms of the observed hydrocarbon.

$$S_{C_iH_j} = \frac{i \cdot \frac{y_{C_iH_j\ FID}}{y_{N_2\ product}} \cdot \frac{y_{CH_4\ TCD}}{y_{CH_4\ FID}}}{\frac{y_{CO\ feed}}{y_{N_2\ feed}} - \frac{y_{CO\ product}}{y_{N_2\ product}}} \tag{3.4}$$

3.3.2 Liquid phase analysis

The selectivity towards products with carbon chain lengths of five and higher (fuel range) was determined by subtracting the selectivity towards gaseous components from 1, see equation 3.5.

$$S_{C_{5+}} = 1 - \sum_{i=1}^{4} S_{C_iH_j} \tag{3.5}$$

The, at ambient conditions, liquid phase from the cold trap consists of a lower water phase and a HC phase. Many different species of molecules are present in this mixture, ranging from linear alkanes over double bonded alkenes to branched iso-alkanes and alcohols. A GC method was used to separate the species in the HC phase. Since calibration of all components is not possible due to missing standards, the correlation between the GC signal area and the number of -CH_2- monomers per molecule was used to calculate the concentration of higher hydrocarbons. Correction factors for the FID signal were applied if product molecules differ from the alkane form C_iH_{2i+2} [191].

The specific productivity p_k was calculated for each liquid (water, hydrocarbons) and solid product. It was measured gravimetrically after an experiment via the weighed product mass

m_k with k being water, oil or wax, respectively, see equation 3.6.

$$p_k = \frac{m_k}{\Delta t \cdot m_{catalyst}} \tag{3.6}$$

3.3.3 Solid phase analysis

Analysis of high density hydrocarbons with low solubility is not a simple task [192]. A method with carbon disulphide (CS_2) was applied, which showed sufficient solvent characteristics [193] and was used for analysis despite its high toxicity and low boiling and ignition point. Additionally, a separately heated injection module (Gerstel KAS 4 with C506 controller) was used on an Agilent G1530A GC with a column that was specifically suitable for simulated distillation (Restek MXT-1HT).

3.3.4 Total product distribution

After weighing and analyzing all fractions, the total amount of a chosen compound with given carbon number w_i is determined in dependence of the respective mass flows $\dot{m}_i$, gas fractions y_i, volume flows $\dot{V}_i$, productivity P_k and densities ρ_i using equations 3.7 and 3.8.

$$w_i = \frac{\dot{m}_i}{\dot{m}_{total}} = \frac{y_i \cdot P_k \cdot m_{catalyst}}{\dot{m}_{gas} + \dot{m}_{liquid} + \dot{m}_{solid}} \text{ for solids / liquids} \tag{3.7}$$

$$w_i = \frac{y_i \cdot \dot{V}_{feed} \cdot \rho_{i,STP}}{\dot{m}_{total}} \text{ for gases} \tag{3.8}$$

The Anderson-Schulz-Flory (ASF) distribution was originally developed by Schulz and Flory and is widely used for FTS analysis [48]. Through equation 3.9, the chain-growth probability α can be determined in the range from zero to one. It can be used to reflect the tendency of the catalyst to produce longer hydrocarbon chains.

$$\alpha_{n-m} = \exp\{-\alpha_{n-m}\} = \exp\{-\frac{w_n/i_n}{w_m/i_m}\} \tag{3.9}$$

with n > m; m, n = carbon chain numbers
α = chain-growth probability
w = mass fraction of a certain chain length
i = carbon number within a certain chain length.

4 Findings

4.1 Paper I – "Microstructured reactors on the test bench"

4.1.1 Introduction

The heterogeneously catalyzed Fischer-Tropsch synthesis was discovered over 90years ago [45] to produce synthetic fuels out of syngas, CO, and H_2. Coming from coal gasification (coal-to-liquid, CtL), the FTS nowadays experiences renewed interest with novel process paths towards syngas. It offers the possibility to change the present fuel consumption while using renewables to produce synthetic fuels with distinct advantages compared to its fossil counterparts. This technology could help to lower the anthropogenic carbon footprint in the transport sector due to multiple available feedstocks. Conversion technologies range from natural gas or biogas liquefaction (GtL) to applications using electricity, water and CO_2 (PtL) or organic sources like biomass (BtL).

In this work, influences from the feedstock on product properties are highlighted for the LTFT. A previously introduced microstructured fixed-bed reactor is used [82, 194]. Different microstructured layouts are tested and optimized towards their effect on product properties in pure syngas before [75]. There, the high surface area of the reaction foils has been found to be very effective in removing the reaction heat. Thermal stability under severe conditions has also been demonstrated before [82]. The present study details the influence of different partial and total pressure levels, as well as H_2/CO ratios. A thorough analysis of all product fractions is executed. Furthermore, a scaled-up pilot reactor is tested which allows comparison of results with the much smaller lab-scale reactor at varying system temperature and WHSV. Due to autothermal behavior within this reactor scale, evaporation cooling

Table 4.1: Process conditions tested in the presented work for both reactor scales. In the sample declaration 1 stands for the smaller reactor size, while 2 represents experiments in the upscaled reactor

Sample	H_2 vol-%	CO vol-%	N_2 vol-%	CO_2 vol-%	H_2/CO ratio	Total flow $mL_N\ min^{-1}$	WHSV $g\ g^{-1}\ h^{-1}$	p_{total} bar	T °C
1A	27.77	16.13	43.28	12.82	1.72	640	20.80	30	240
1B	29.44	16.70	42.56	11.30	1.76	640	20.18	20	235
1C	27.69	16.55	42.34	13.42	1.67	640	20.90	15	240
1D	27.77	16.13	43.28	12.82	1.72	640	20.80	30	240
2A	29.46	15.41	43.47	11.76	1.91	38,147	20.08	30	223
2B	29.46	15.41	43.47	11.76	1.91	38,166	20.09	28	229
2C	29.46	15.41	43.47	11.76	1.91	38,166	20.09	28	238
2D	31.08	15.47	42.02	11.44	2.01	38,134	19.65	30	226
2E	31.08	15.47	42.02	11.44	2.01	26,407	13.61	30	224

is introduced as the method of choice to extract the released reaction enthalpy from the system and to efficiently change the system temperature. Similar process conditions are tested for both reactor scales to evaluate possible effects from feed gas dilution in order to simulate syngas from BtL applications.

4.1.2 Experimental methods

Both reactor scales were compared under similar conditions, namely a high inert gas dilution and variable process parameters. This was applied to show that both reactor scales are equally capable to convert syngas from various sources and under different process conditions. An emphasis on BtL scenarios was chosen, as those are more challenging in terms of syngas quality and level of dilution.

Finally, both reactor sizes were compared to each other by applying similar process conditions to determine if any disadvantages or performance losses emerged from the upscale. In table 4.1, all tested process conditions are listed.

Similar to section 3.3, fundamental methods of product analysis for the various phases and GC systems were reported in publication 1.

4.1.3 Results and discussion

Despite the high dilution, CO conversion was satisfactorily high with $\geq$ 44 % in all experiments. While the total specific productivity was varying strongly with the different setups A - E, the mass ratio of produced oil to wax was always quite constant with 4:1. Also, the ratio between the different product classes alkanes, alkenes and iso-alkanes was quite constant with 75:10:15 and 80:10:10 for the different reactor sizes, respectively. Both reactors operated isothermal with only 2 °C temperature difference between the thermocouples. The temperature difference was even smaller in the larger setup due to evaporation cooling.

Evaporation cooling proved to be a very effective tool to determine the average system temperature and prevent reaction runaway at the same time. By applying this technology, fast changes within the cooling mechanism can be realized. The observed reaction temperature of the reactor was responding effectively on a water pressure between 15 and 35 bar.

Pressure

With an increase of the total pressure, longer hydrocarbons could be synthesized in average. Also, the CO conversion increased. At lower pressure, the methane selectivity increased.

Syngas ratio

With a smaller syngas ratio, averagely longer synthesis products were generated. The high dilution of the syngas likely superimposed the effect of the low stoichiometric syngas ratio. A high inert gas content lowers the partial pressure of reactants but also decreases the contact time of the reactive syngas with active sites.

Temperature

The products were better hydrated in general with increasing temperature, resulting in less alkenes. Also the average chain length decreased with higher temperature, as it was reported in literature.

Residence time

Since the WHSV was relatively high in all observed experiments, differences between different set points were much less pronounced. The high inert dilution is likely responsible for the small differences. At a lower WHSV, other parameters would have a much larger impact on the average maximum chain length and conversion.

Upscale

From the reactor upscale, no apparent disadvantages could be observed. Similar process conditions were tested in both systems. Besides assumed issues during sampling, all products were of similar composition. In pilot scale however, longer total chain lengths could be observed. After all, there were no concerns for even further reactor scale-up. Different syngas sources can be utilized, even for BtL applications. Comparable system properties can be observed in figure 4.1

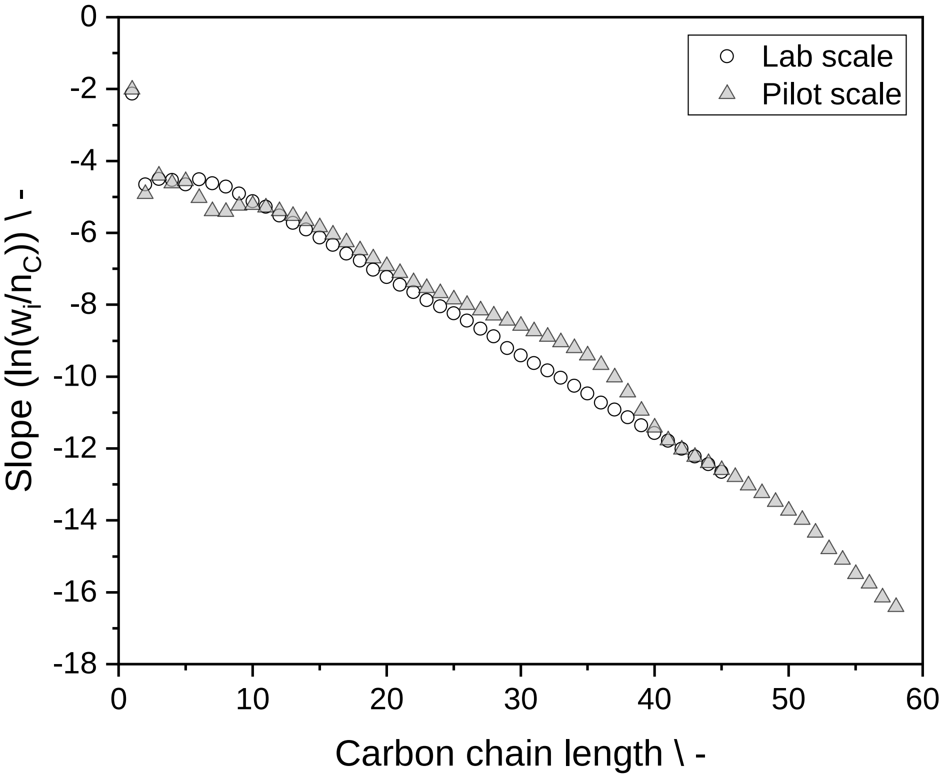

Figure 4.1: ASF plots for two comparable setups in both reactor scales.

4.1.4 Summary

Two reactor sizes were tested individually towards their versatility in terms of process parameter settings. The smaller reactor size was presented in previous work [75, 195]. There it could be proven that the special foil design for reaction and cooling was very suitable for the targeted process intensification in FTS. CO conversion of up to 91 % could be achieved and temperature control was excellent for the specific size of reactor internal structures. In this work, a 60-times larger reactor upscale should prove the effectiveness of microstructured FTS reactors even after a significant increase of reactor outer dimensions. With the increase in overall size and catalyst loading, the system was capable of sustaining autothermal operation starting from specific throughput accompanied with mid-level conversion, while maintaining isothermal properties. Due to the increase of total reaction heat, evaporation cooling served as an effective mechanism to cool down the reaction while producing high-pressure steam at the reactor outlet that can be used in other reaction steps in a decentralized plant network.

After the successful scale-up and the verification of its potential, the aspect of decentralized application with quickly changing process parameters must be elaborated. There should be pronounced focus on the system response time and possible effects on the reaction output.

4.2 Papers II + III – "First-of-its-kind dynamic FTS - performance and limits?"

4.2.1 Introduction

In the framework of decentralized applications, fuel synthesis must be able to cope with dynamics due to fluctuating energy flows [102]. Since renewable primary energy flows will only be exploitable under specific conditions such as time of day and weather, a long-term storage is necessary to distribute energy over time and distance [17, 27, 93, 196–200]. To reduce size and cost of intermittent storage which may come in many different forms such as batteries or gas tanks, a dynamic synthesis could show significant potential to improve overall process economics. Intermittent storages are costly but necessary for decentralized processes [23, 92, 93, 200]. In the end, with increasing use of renewable electricity as primary energy, the overall fluctuation of energy flows endangers grid stability and the grid may not be capable to support the current power demand at all times.

The work first compares different forms of energy and their potential for long-term storage. It is concluded that liquid fuels with a high energy density will play a leading role in the coming energy system. Thus, existing infrastructure can be further used and supported with a large number of transport vessels simply adapting to the new fuel.

In order to develop a new system of CO_2 utilization, decentralized PtL plants are an interesting but demanding concept to start with. Figure 4.2 shows one example flow sheet from CO_2, water and electricity.

Technology like microstructured reactors enable intense contact of reactants and catalyst. Small system dimensions significantly increase the surface area and local heat transfer. Higher reaction performance may be applied without harming the catalyst. Furthermore, concentration and temperature changes can be quickly applied because of short overall distances and advanced tools like evaporation cooling [65, 201–203]. This allows high-pressure steam to be produced from the FTS reaction enthalpy that holds the opportunity to enhance the thermal efficiency of a system network. Additionally, the small internal dimensions of microstructured devices enable operation of the overall process in a regime that is not ac-

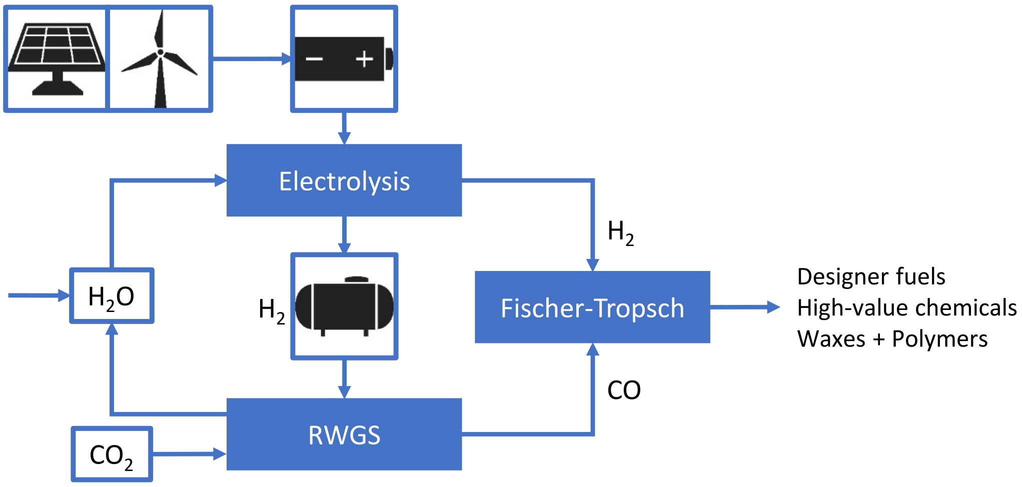

Figure 4.2: Example of a PtL approach based on renewable electricity, water and CO_2. Intermediate process steps include an electrolysis, a RWGS unit and the FTS. Possible products include designer fuels, waxes and other high-value chemicals. Also, storage systems for electricity and hydrogen are shown, which are needed to tackle the intermittency problem of future electricity systems.

cessible with industrial solutions. Thus they can help in the framework of decentralized small-scale applications to reduce the overall cost and plant sizes of process chains. Microstructured reactors may even be advantageous in island solutions for local energy conversion.

Open questions remain for decentralized plant networks and much effort is put into the understanding of those concepts. One of the largest research infrastructures in the 200 kW-range is the Energy Lab 2.0 [204], which looks into the real-time behavior of energy producers, converters and consumers in a plant network. A PtL approach suffers most prominently by fluctuating energy flows from PV panel or wind turbine power profiles. The synthesis must be compliant with this circumstance. Different pieces of the puzzle can either be connected by a significant gas buffer storage or by smart flow control in the minute-scale. However, this which might put the respective catalysts into unknown kinetic regimes. In this work, the pilot scale FTS reactor is used to investigate process parameter changes for a prospective PtL application with dynamic input changes.

Unresolved questions that needed answering include:

- What knowledge is needed for controlling a dynamic process in small to medium size?
- Can all different process steps be aligned in dynamic operation? What are their general limitations?
- What is the potential to reduce storages through dynamic synthesis?
- What are considerable dynamic time periods and ramping scenarios that plants need to tolerate?
- Can the prerequisites from "dynamic time periods" be met by reactors and/or plants?
- How is overall higher efficiency correlated to values of buffer reduction?

In the scope of publication part one and the following part two, most of the above questions are addressed from the point of view of a microstructured FT reactor. However, to fully answer these questions, information from other steps, i.e. from hydrogen generation to syngas production, need to be included.

In the second part of this work, a deeper look into the load flexibility of microstructured Fischer-Tropsch synthesis reactors aims to determine possible limits of dynamic operation. Fluctuating input data is calculated from a 10 kW photovoltaic system and an electrolyzer, from which a highly dynamic H_2 volume flow can be derived. The CO flow was either mimicking a constant biomass gasification (BtL case) or a direct air capture that produces CO_2 which is dynamically converted in a RWGS reactor into syngas with a desired syngas ratio (PtL case, depicted in figure 4.2). In both cases, the input is a constantly changing syngas ratio and/or residence time to determine the limits of the given system. The first trials tested harsh experimentation conditions in a controlled environment. Furthermore, a coupled temperature-conversion relationship model is developed for quickly-changing feed conditions to keep the conversion and product distribution constant despite highly dynamic operation.

4.2.2 Experimental methods

Dynamic feed gas and temperature changes in a pilot scale Fischer-Tropsch synthesis unit were applied to investigate the general versatility of microstructured reactors. Operating conditions were adjusted by hand and evaluated by online GC and MS. The MS is a valuable tool to determine changes with a high temporal resolution.

In part 1 of the work, the dead time of several system components was determined with the help of the MS. Due to immense back-mixing in the larger vessels of the test rig, signal delays of over 80 min were discovered. In order to evaluate product concentrations in a relevant time span, a quick sampling site (QS) was installed between the HT and the CT. The signal delay was still 17.5 min which could not be shortened due to product flow temperatures and a risk of condensation in the measurement units.

Two setups were chosen to switch between in order to test oscillating gas feed changes. Only the syngas concentration was changed between both setups, with the residence time being the same. A change between a syngas ratio of 1.95 and 1.38 showed significant differences in the synthesis products.

After the dead time of 17.5 min was determined both in standby and reaction mode, oscillation cycles of 30 min (approx. two times the dead time) and of 8 min (approx. half the dead time) were chosen for the experiments. The syngas ratio was switched multiple times for each experiment.

Finally, the speed of water pressure changes for evaporation cooling was tested. Water pressure was ramped down and up again between 30 and 24 bar during reaction. Changes in system temperature were observed.

In the second part, the limits of the given system were explored. A real-time power profile for a 10 kW photovoltaic (PV) table was provided by KIT's Battery Technical Center (BATEC). This data was used to develop experimental campaigns. The PV table consists of polycrystalline solar modules. The tilt angle was adjusted to 30° facing south, which is considered optimal for the given location (N 49.1 E 8.4). This allowed the theoretical maximum of 10 kW to be reached in practice. In this work, a favorable 24 h profile for a sunny spring day in 2015 was used. It was confirmed by BATEC that this profile is a representative average for time and location of data gathering. The average net output was favorable for dynamic testing. A proportional hydrogen flow was calculated from the assumption of a specific conversion energy. A discretization of the signal was conducted by hand to limit the total amount of

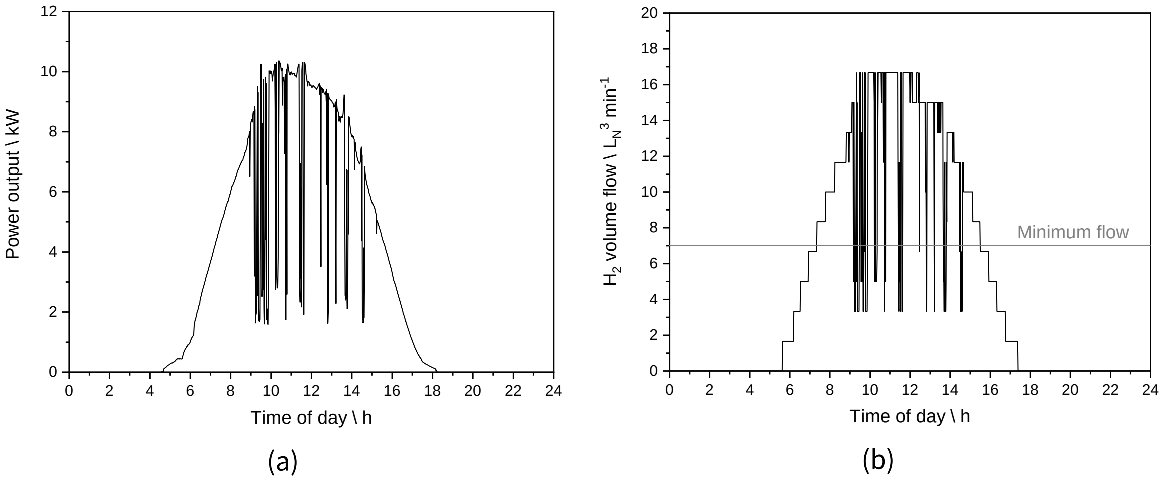

Figure 4.3: Experimental input signals based on the data from KIT's Battery Technical Center (BATEC). (a) Power output profile of a 10 kW PV table for a sunny spring day in 2015; (b) Discretized hydrogen flow assuming a specific conversion energy. A total number of ten different setup steps was chosen and changes are held for at least one minute.

different flow levels to ten. Also, the time frame of a change lasted at least one minute so new syngas flows could be typed in the software. Also, a minimum hydrogen flow needed to be guaranteed in order to keep the reaction running isothermally by emitting sufficient total reaction enthalpy. This way, the reactor was guaranteed to run autothermal. The total released enthalpy is a function of the reactor size and total mass of catalyst in the system as well as the conversion and was estimated based on previous steady-state experiments. The discretized input signal for the reaction is depicted in figure 4.3. After cutting the set points beneath the minimum flow, seven different experimental setup steps remain. A continuation of step-change experiments from part 1 in preparation of the PV panel profile experiments was executed beforehand.

In order to apply the hydrogen profile, different scenarios were chosen to gather first insights into process suitability. Figure 4.4 shows simple potential pathways for either PtL or BtL approaches including the FTS unit. For both cases, the PV panel and electrolysis unit deliver the hydrogen needed for the FTS. The carbon source is either CO_2 or biomass. For the BtL pathway, a steady biomass gasification is assumed so that a constant flow of synthesis gas is gathered. This syngas typically offers an unfavorable, syngas ratio lower than 2 [205]. If the fluctuating hydrogen flow from the electrolysis is added to the constant syngas flow from the gasification, a varying H_2/CO ratio in the FTS reactor is applied with every step change of the experiment. This is accompanied by a strongly fluctuating residence time of the gas mixture. Varying two system parameters at the same time promotes unpredictable effects on the performance of the synthesis. In the second process route, a CO_2 storage can be depleted on demand. It is assumed that a RWGS unit can be operated with fixed gas mixtures for changing total flows. In this scenario, a fixed H_2/CO ratio of 2 is led to the FTS reactor. A dilution of the feed gas from the RWGS output is not regarded in this approach. Normally, larger amounts of CO_2 and CH_4 would accompany the syngas. Water is extracted before entering the FTS.

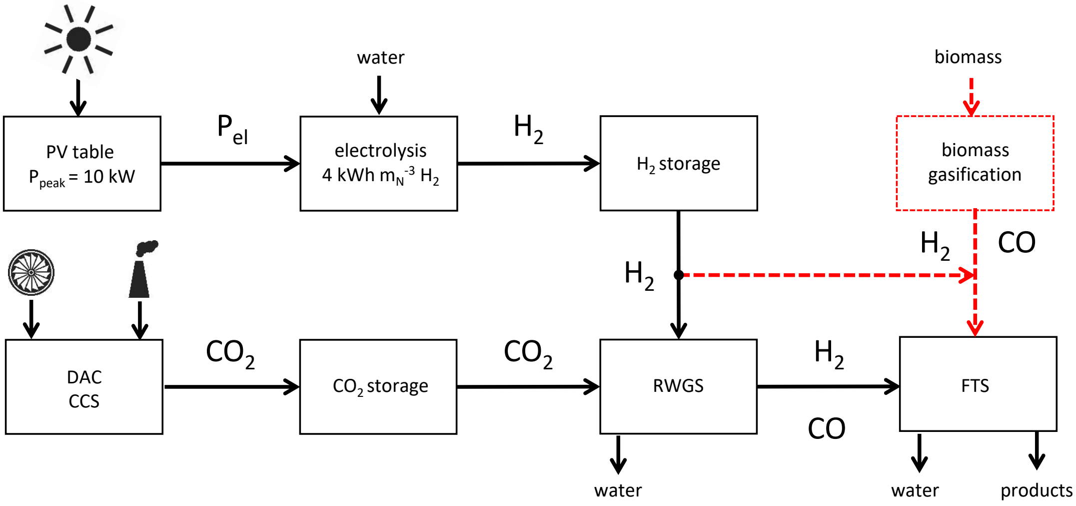

Figure 4.4: Potential PtL (black solid lines) and BtL (red dotted lines) pathways to produce syngas for the microstructured FTS reactor are showcased. Both pathways include a PV panel and electrolyzer, as well as a hydrogen buffer storage. The PtL pathway takes CO_2 as carbon source which needs to be converted into syngas in a RWGS unit. A CO_2 buffer storage is assumed. The BtL pathway uses syngas from biomass gasification to be mixed with electrolysis hydrogen as feed gas for the FTS.

In order to approximate conversion levels despite fast process changes, a linear regression model was developed, based on a database of 20 sets of process parameters that were tested experimentally. The modified residence time τ_{mod}, the syngas ratio and the temperature have a significant influence on CO conversion. Because of different gas densities between all gas feed species, the density-independent parameter τ_{mod} was chosen over the

WHSV and calculated via the following relation:

$$\tau_{mod} = \gamma_{feed}\, WHSV^{-1}, \tag{4.1}$$

with γ_{feed} being the respective density of the feed gas mixture. The correlation of the individual values can be described by the linear regression model. The base model is described in equation 4.2. The regression coefficients β_k are linearly related.

$$X_{CO} = \beta_0 + \beta_1 X_{\tau_{mod}} + \beta_2 X_{H2/CO} + \beta_3 X_{T_{reactor}} \tag{4.2}$$

Based on the equation, the CO conversion could be calculated from step changes and temperature measurements, despite the short time spans.

4.2.3 Results and discussion

The system was stable even after shortening periodic cycles from 30 to 8 min. Product characteristics such as composition and flow-rate oscillated harmonically as expected of results from stationary experiments. The liquid phase during the shorter cycles suffered due to a resolution problem, since liquid sampling took a good portion of one step change, thus integrating the signal. Neither of the periodic changes showed negative effects on process performance. On the contrary, the findings suggest the capability of this technology for effective, small- to medium scale applications, even with periodically changing process parameters.

Evaporation cooling is a very effective tool to quickly control system temperature. Temperature instantly correlates with the applied cooling cycle pressure. Tools like evaporation cooling help to control quick system changes by impacting reaction temperature as a function of water pressure. In the current setup, quick temperature changes via pressure regulation needed to be applied by hand, which could be automated for better process control and response time.

In order to decrease complex storage systems, a dynamic operation might lower size and cost of those operations. As a proof of concept, dead time determination and consecutive oscillation cycles were carried out in the presented setup. Although there is a misalignment between observable catalytic effects and their detection speed, the reactor answers to changes in an appropriate timely manner, based on the interpretation of obtained signals.

To answer the questions posted in Section 4.2.1, new findings hint at the advantageous technical possibilities of this reactor system. Questions regarding applications in a realistic dynamic context could not be answered at this point. The findings of the first part of the papers will strongly contribute to PtL projects like PowerFuel, where a dynamic synthesis is part of the research schedule [206]. The presented results are demonstrating the advantages of microstructures. They were intensively tested in dynamic application, considering challenges coming from the test rig size and eventually making use of them for advanced process control. Future energy related operations will include PtL technology, some of which will make use of the pathway presented here for effective energy storage. The results may allow further applications that might require even more intense process control, such as highly dynamic applications. A conversion dependent increase or decrease of temperature could easily be developed and automated.

In the second part of the papers, a deeper look into the load flexibility of microstructured Fischer-Tropsch synthesis reactors aimed to determine possible limits of dynamic operation. First trials tested harsh experimentation conditions in a controlled environment. Even with oscillation of syngas ratio and residence time, the reaction behaved similar to stationary experiments.

Concerning the BtL and PtL cases derived from the PV profile, a good overall system performance was observed. A varying temperature along the experiment was observed for the BtL case which decreased in the PtL experiment. Methane production was lowered significantly from fast changes in the lower min-regime and benefits from a steady syngas ratio. Liquid product properties strongly benefit from a constant syngas ratio in the PtL case. The stability of liquid product quality was very promising for future upgrading steps necessary for drop-in fuels.

Conversion changes can be countered with temperature manipulation. A linear regression equation (equation 4.3) was developed for the system and used to calculate the conversion for each step change in the PtL case based on the temperature. Figure 4.5 shows a contour plot as an exemplary diagram to calculate the conversion based on the process parameters.

$$X_{CO} = 19.51 + 25.26\, X_{\tau_{mod}} + 13.20\, X_{H2/CO} + 29.34\, X_{T_{reactor}} \tag{4.3}$$

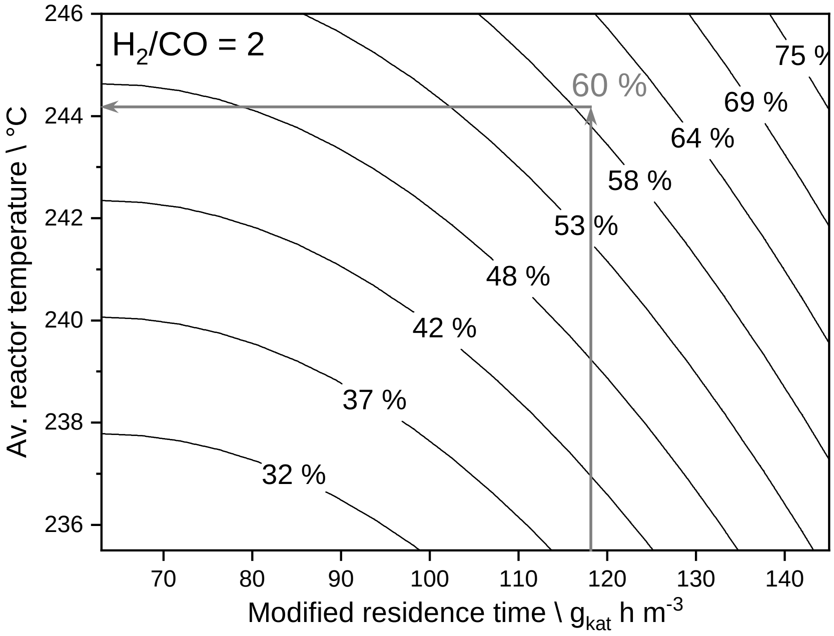

Figure 4.5: Contour plot derived from equation 4.3 with characteristic curves for different CO conversion levels ranging from 32 to 75 %. The syngas ratio is 2 for this plot. For a changing modified residence time with each step change, the corresponding reactor temperature can be determined. An example for 60 % target CO conversion is given.

The equation was developed to calculate the temperature needed to keep the conversion and product distribution constant despite highly dynamic operations. Above sixty percent of conversion could be realized throughout the experiment even without temperature manipulation. Seventy percent of CO conversion could almost always be established by temperature control except when the reaction heat was limited by a low gas flow. Methane concentration was lower and more stable with temperature control.

Evaporation cooling proved as an effective tool to change the system temperature when sufficient reaction heat can be extracted. Thus conversion can be adapted at varying syngas flow accordingly.

Those findings demonstrate the possibility of the given microstructures to react to changes quickly. Intermediate reaction states last shortly and changes quickly resulted in a stationary state in the reactor. This makes the use of stationary reaction kinetics for operational estimations applicable. Limiting operational modes still need to be investigated.

4.2.4 Summary

To answer the questions posted in Section 4.2.1, the findings hint for the advantageous properties of the applied reactor system.

It could be proven that highly dynamic, load flexible operation in microstructured FT reactors with multi-parameter changes in the one-minute regime are feasible and fully controllable. Quick changes in the feed gas concentration could be applied in the reactor without obvious influence on its operation. Intermediate reaction states did not influence the product distribution. This allows the use of stationary reaction kinetics for operational estimations in conjunction with residence time models. No runaway or blowout was found during fast changes of experimental conditions.

The development of a regression model for adapting the reactor temperature without the need for measuring the product composition, i.e. only on basis of the knowledge of syngas ratio and residence time, led to almost even product quality. Constant product quality is important for product post-processing such as distillation and hydrotreating and highlights the importance of such methods. Keeping the CO conversion level by temperature manipulation seems to be a suitable approach for PtL plants as determined in this study. With a fixed H_2/CO ratio, reaching the goal of a target conversion of 70 % by temperature manipulation via the pressure in the evaporating cooling cycle was experimentally verified as good strategy. Due to the fact of relatively small total flows in the pilot scale FTS test rig, it was difficult to increase system temperature on demand from all starting points. This observation would improve with larger reactors. Consequently, autothermal operation will be possible with even lower relative loads leading to more hours of operation without considerable hydrogen storage. Changes in the test rig were done manually, which can be optimized.

Last but not least, no apparent signs of catalyst damage were found through dynamic experiments. Nevertheless, *operando* technology would enable a deeper look onto the active catalyst sites to determine if the applied process caused negative effects on long-term activity.

4.2.5 Further investigation on deactivation

Quick changes in the feed gas concentration could be applied in the reactor without measurable negative effects to the process, as observable in figure 4.6. Not much information concerning potential harm to the catalyst could be gathered over the course of the experiments. A reference setup was regularly chosen for conversion and selectivity checks. No immediate deactivation from harsh dynamic experimentation could be found. An initial deactivation phase of the catalyst is probably the reason for conversion loss during the first period of dynamic experiments. Nevertheless, selectivity towards liquid fuels and methane were constant.

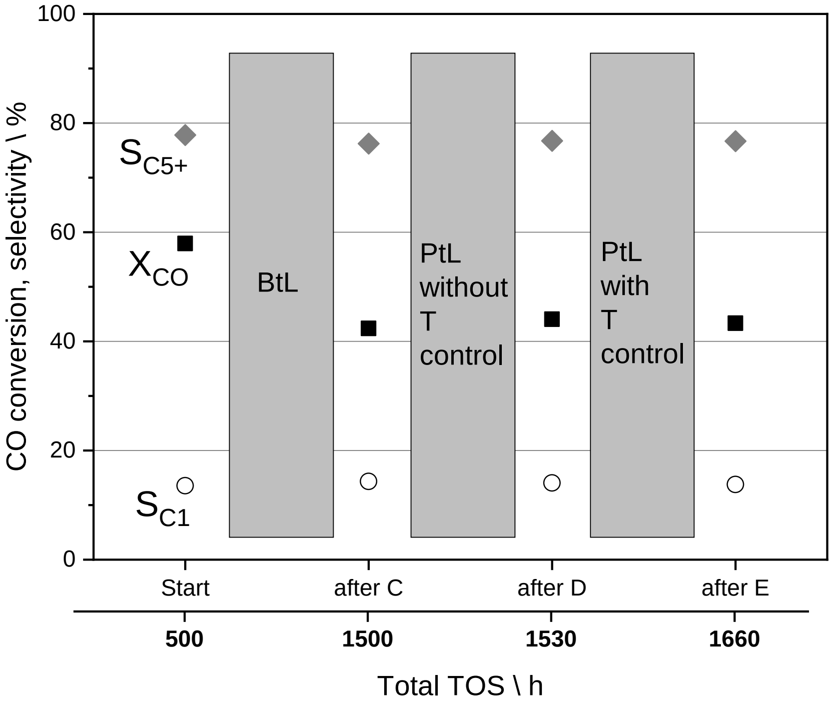

Figure 4.6: CO conversion and selectivity towards methane (S_{C1}) and liquid products (S_{C5+}) over total experimental TOS. A reference setup is tested at each given TOS. Grey areas mark the experimental campaigns presented in this work.

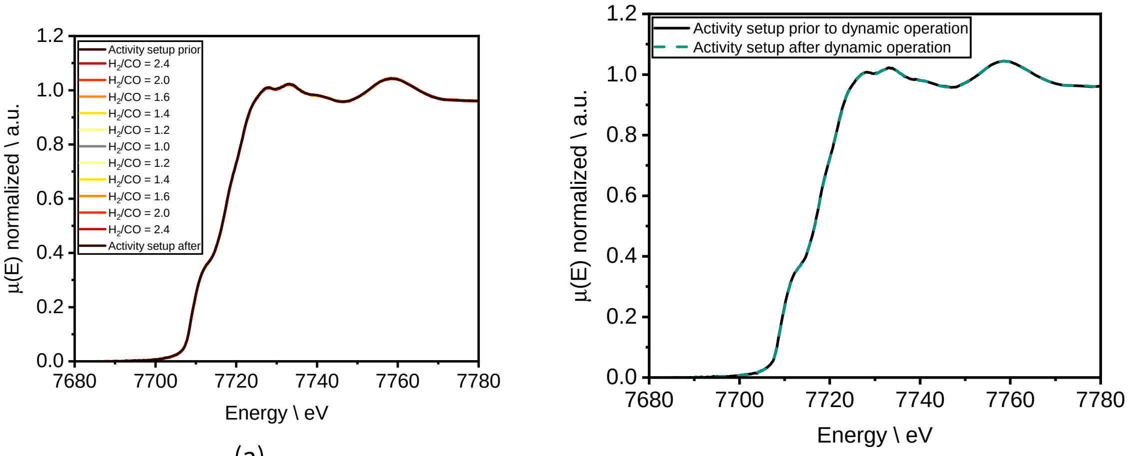

(a)

(b)

Figure 4.7: XANES spectra taken continuously during a synchrotron beamtime campaign. (a) XANES spectra near the cobalt edge taken for different syngas ratios in a step-change experiment; (b) XANES spectra near the cobalt edge taken before and after dynamic experiments.

In situ-techniques are appropriate to determine effects on the catalyst bed if changes are applied quickly. While FTS conditions are challenging for *in situ*-environments, some applications were used in the past for similar processes [102, 165, 171, 177, 207, 208].

In order to undertand surface effects, *in situ* or *operando* measurements are necessary. For the FTS, this is not a simple analysis to perform. Elevated pressure and temperature are usually rough conditions for the measurement equipment. Many reaction cells are designed to withstand the required temperature but are vulnerable to pressure buildup. A complementary analysis of the metal surface and the reaction products allows for a more accurate interpretation of the observed phenomena. The methods of choice for *operando* analysis would be XAS, XRD and a coupled GC-MS analysis [102, 175–177].

In a setup described in publication number 5 (see sections 4.4 and 5), the effect of varying syngas ratios was tested in a reaction cell capable of performing *in situ* X-ray absorption near-edge spectroscopy (XANES) measurements, as one of many tools. The results are presented in figure 4.7a. Every syngas ratio step was held for one hour. Also, the same dynamic setup displayed in figure 4.3 was tested in the reaction cell with XANES spectra taken continuously. Figure 4.7b shows the results for XANES spectra taken for various syngas ratios, as well as before and after a dynamic run of ten hours, similar to the ones described in this section.

The findings from the synchrotron experiments support previous observations. There is no imminent deactivation from a low syngas ratio. Also, concurrently changing residence time and syngas ratio shows no change in the structural cobalt properties of the used catalyst.

4.3 Paper IV – "Holistic system description by kinetic modeling"

4.3.1 Introduction

For economical and safe operation, knowledge about conversion and selectivity in the reactor as well as heat integration and material flows in the plant are required information. Dynamic process simulation is able to calculate species distribution, heat flows and product composition at any time at any location inside the plant. In the case of the complex Fischer-Tropsch product composition, the species distribution is hardly to assess experimentally; lots of effort is required to determine the product composition every minute [120, 121]. One issue is a suitable kinetic model for chemical synthesis for the prediction, design and optimization of microstructured reactor behavior. Furthermore, residence time distribution and correct description of the phase equilibria in the two-phase flow of the FT product at product condensation traps are required for description of plants.

This publication is devoted to deliver the three major elements: kinetics, residence time distribution and the strategy for phase description - all experimentally verified from a pilot scale test rig. The strategy could be applied to larger FT plants to derive the mean composition of the product depending on the input, i.e. wind or solar energy and their respective location. From an economic point of view, it has already been verified in previous contributions that at constant H_2/CO ratio a constant conversion manipulated by the reactor temperature could lead to rather constant product distribution over a real-time photovoltaics energy profile [120, 121]. Heat flows are not yet considered but may be addressed in upcoming further publications.

4.3.2 Experimental methods and simulation

Based on 20 experimental setups for ranges given in table 4.2, a valid model for reaction kinetics was developed.

Table 4.2: Ranges of 20 process conditions used to develop a micro-kinetic model.

	Temperature °C	Total pressure bar	Syngas ratio -	WHSV $g\,g^{-1}\,h^{-1}$	Dilution %
Minimum value	225	20	1.48	4.37	1.89
Maximum value	245.5	30	2.20	7.74	20.00

Reaction kinetics and reactor model

Various assumptions were made before developing the reaction model, since there is not a single mechanism capable of describing the complex reaction network of the FTS [209]. Still, the formation of CH_2 monomers mark the beginning of chain propagation [210]. Elementary steps of the FTS can be summarized as follows:

1. Adsorption and dissociation of the educts
2. Chain start by formation of a CH_2 monomer at the surface
3. Chain growth
4. Chain termination
5. Desorption of the products e.g. by hydrogenation or dehydrogenation

A micro-kinetic model, based on the alkyl mechanism [210–218], was developed by Kwack et al. [210]. It was used in this work to simulate the reaction properties of the present system. Some kinetic parameters were adapted for the applied catalyst.

The microstructured fixed-bed reactor mentioned and presented in sections 3.1.3 and 4.2 was described as a quasi-homogeneous stationary reactor model based on initial calculations according to the criteria of Mears and Weisz-Prater [219–221]. The reactor was isothermal and isobaric, as pressure losses in the catalyst bed were negligible. An ideal plug-flow reactor (PFR) with continuous flow was assumed, without radial gradients and axial mixing. A cell model was implemented which discretized the reactor. Each cell corresponded to a differential volume element. Temperature, pressure and volume flow of the reactants were read in as input variables. The kinetics were solved for each individual cell in a loop, whereby the result was always used for updating the material properties and as input for the calculation of the next cell. To calculate grid-independent kinetic results, the cell size was adjusted. The differentially calculated conversion in each step and the difference between the mole flows for H_2 and CO of the input and output of a cell might not exceed a certain threshold value. The cell size was reduced until the differential H_2 and CO conversion was at most 1 % and the difference of the molar flows for both gases was at most 10 -12 mol s^{-1}. Upon calculation, the respective product streams and compositions as well as conversion levels and each selectivity were given. The program flowchart is given in figure 4.8.

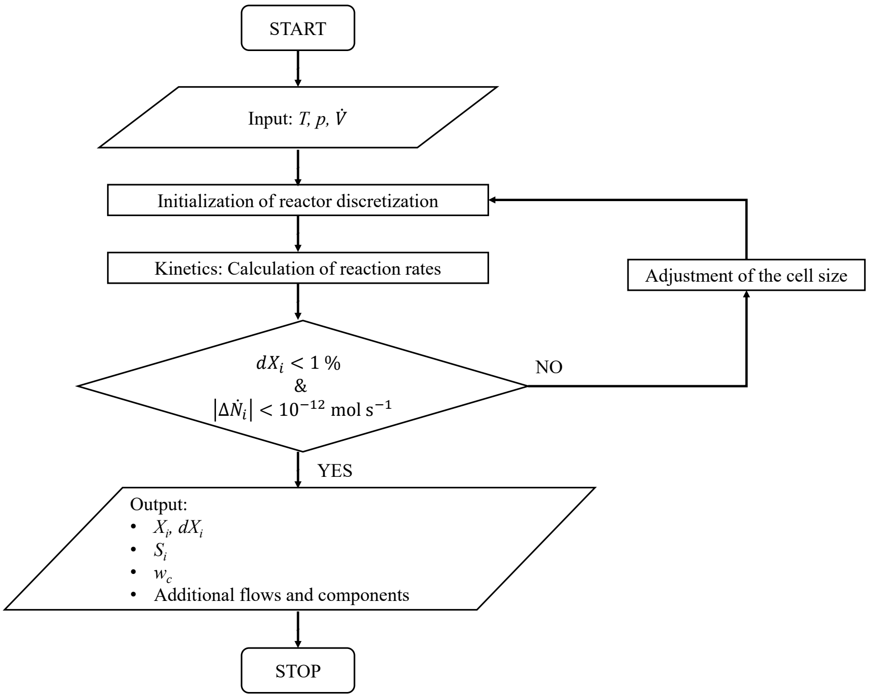

Figure 4.8: Program flowchart for calculating the reactor output in the reactor model.

Vapor-liquid equilibrium to forecast the respective product compositions

A cubic equation of state (EOS) using the Volume-Translated Peng-Robinson (VTPR) method was used to describe the vapor-liquid equilibrium (VLE) for all product phases in both product separators [222]. Various parameters and pure substance data were required, such as critical temperature and pressure, acyclic factor and group contribution parameters [223, 224]. The necessary data for the calculations was taken from Ahlers et al. [225–227].

In the HT, a liquid phase (wax) and a gaseous phase were formed, so a two-phase flash was implemented. In the CT, an oil, water and permanent gas phase were formed, so a three-phase flash was developed. The algorithm for the two-phase flash used the Wilson equation [228] to determine initial values for the VLE. The flash calculation was solved with the Rachford-Rice algorithm [229]. Iterations were used to determine the molar gas and liquid phase fraction in the VLE. If the convergence of a mole fraction is not reached, real phase behavior via an EOS was taken into account for the calculation of a new distribution coefficient.

The three-phase flash worked analogously to the two-phase flash. An advanced Rachford-Rice flash algorithm was used. Since two liquid phases were taken into account, the initialization of the distribution coefficients for the oil phase was done with the Wilson equation [228]. For the water phase, a distribution coefficient was additionally calculated [230].

System dead times and residence time

Initially, the dead times of all system components were determined by tracer experiments executed with the help of the MS mentioned in section 4.2.2. Based on this data, residence time sum functions F(t) were determined for multiple system components. Those functions were modeled by assuming a cascade of continuously stirred tank reactors (CSTR) called tanks-in-series (TIS) [231]. The more CSTR are assumed serially, the more a cascade behaves like a PFR. For a number of reactors $n \rightarrow \infty$, the design equation for the PFR is obtained.

In table 4.3, the obtained numbers of CSTR in series are provided to describe the tracer experiments for the reactor and both separators.

Table 4.3: Number of CSTR in a row needed to model the reactor and both product separators.

	Reactor	Hot trap	Cold trap
n_{CSTR} in a cascade	50	2	1

With the determination of the F-curves for the separators, a time-dependency of the product formation could be implemented. A change between two predetermined reaction set points could then be performed. For each set point, the reaction kinetics first determined product quality and output parameters in the form of conversion levels and selectivity. The phase equilibrium calculated the share of each product chain-length in liquid or gaseous form depending on temperature and pressure level given inside each separator. Finally, the time a product gas needed to flow through the infrastructure was by the F-curves of each system component.

4.3.3 Results and discussion

Model application in MATLAB

The kinetic parameters were determined assuming a reactor without mass transfer limitations. The differential equations were solved with the *ode45* solver. The optimization algorithm *lsqnonlin*, suitable for nonlinear problems, was used for fitting some of the parameters of the kinetic model to the experimental data. The kinetic model contains two activation energies and seven rate or adsorption coefficients. The *sobolset* function was used to avoid a trial and error procedure for determining the initial values during parameter optimization.

Only process variables such as temperature, pressure and volume flow of the reactants were used as input for the combined model. Time-dependent product concentrations and properties such as conversion, selectivity, product formation in different fractions and their mass distribution are predicted. Figure 4 gives a schematic representation of the multi-level model for the plant.

For the prediction of mixing states, two options were implemented. The first option was to choose a fixed mixing ratio of two different feeds to calculate resulting product properties for each respective product trap. The second option was to decide on respective mixing times for both feeds.

Model evaluation and limits

A certain inaccuracy could be observed for the estimation of short-chained hydrocarbons as it was described by Kwack et al. [210]. The largest deviation from the actual mass distribution could be observed here.

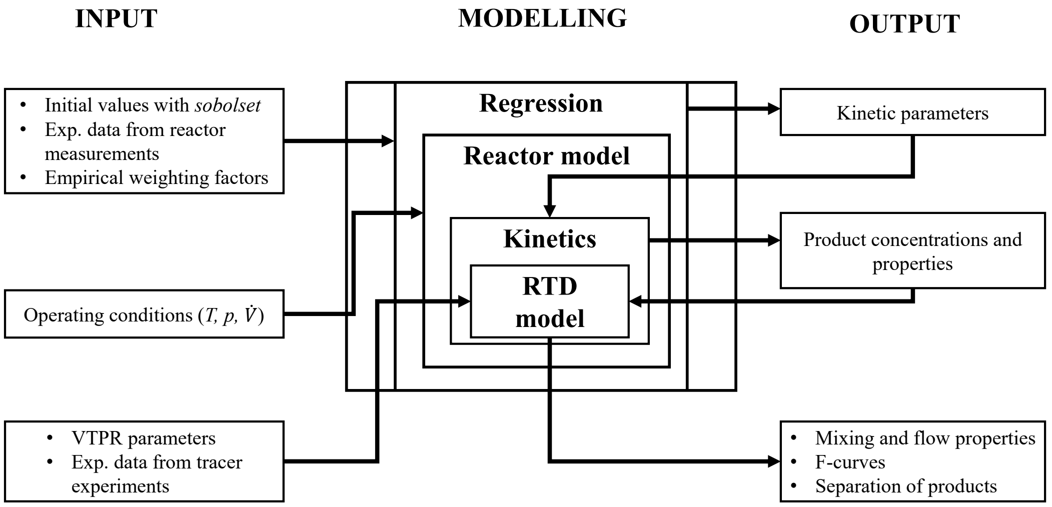

Figure 4.9: Overview of the modeling structure. Kinetic parameters are determined by non-linear regression. These parameters and desired operating conditions are input for the program and serve as a basis for the simulation of the reaction kinetics. The results of this calculation, as well as additional data (e.g. VTPR parameters of the EOS) are transferred to the F-curve model to calculate product separation, mixing and flow properties.

Only hydrocarbons up to a chain length of 50 were considered for the model, since the mass fraction of longer molecules was usually less than two percent. Substance data on iso-alkanes and alkenes could not be obtained and were thus not considered for this model.

Selectivity calculations and conversion levels were in good agreement with experimental data. Figure 4.10 shows two parity plots for the selectivity towards higher hydrocarbons (S_{C5+}) and the CO conversion. The average deviation between simulated and experimental values was usually below 10 - 15 %, which implicates a sufficient model accuracy.

The influence of each process parameter on the reaction is very different [73]. The tested range of each parameter in the initial experiments was limited, which effects the reliability of the simulation concerning the range of validity. If the following combination of operating conditions occured, conversion levels are usually overestimated:

- high temperature ($T > 240$ °C)

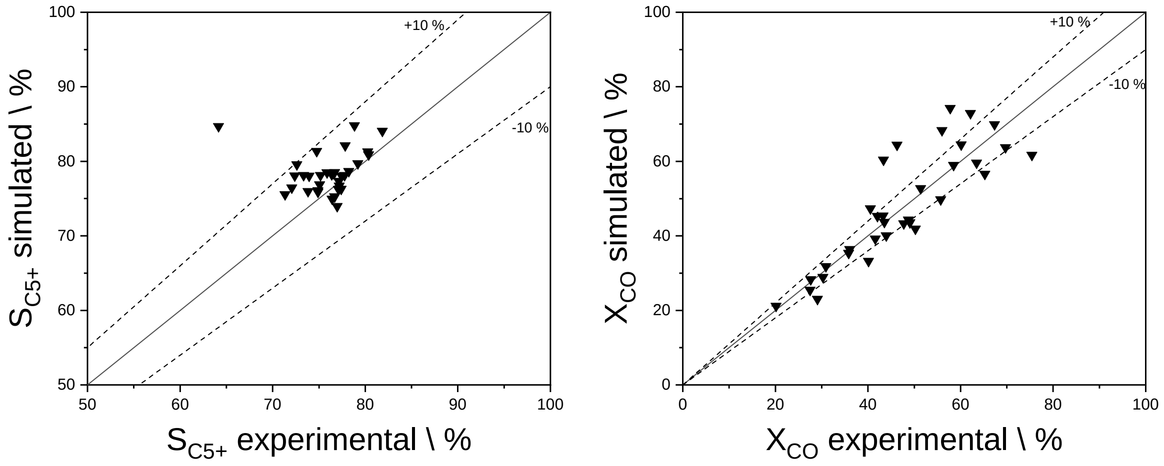

(a) (b)

Figure 4.10: Parity plots to display model accuracy. (a) Parity plot for the selectivity towards higher hydrocarbons (S_{C5+}); (b) parity plot for the CO conversion (X_{CO}).

- low syngas ratio ($H_2/CO < 1.8$)
- low feed flow ($\dot{V} < 14$ L min^{-1}).

With a broader range of each parameter, a better kinetic fit could be achieved. The model is sensitive to extrapolation, especially for conversion levels.

The VLE using the EOS showed significant improvements over an ideal flash separation [232]. Figure 4.11a shows a comparison of experimental data with a calculated mass distribution of the liquid product in the cold trap for both flash calculations. Besides beforementioned inaccuracies caused by the bad representation of the short-chained hydrocarbons by the kinetic model, additional inaccuracies can be caused by a faulty temperature determination of the HT. Since the responsible thermocouple was installed at the outside of the tank, the precise inner temperature of the vessel is unknown, which falsifies assumptions for the flash model.

Figure 4.11b shows the mixing state of two reaction conditions after certain mixing times. One set of conditions is stationary before mixing with the product from the other set. Mixing between two sets of conditions takes the volume flow of the individual operating conditions into account. The mixture is calculated by multiplying the mixing ratio by operating condition A and multiplying the complementary value by operating condition B and vice

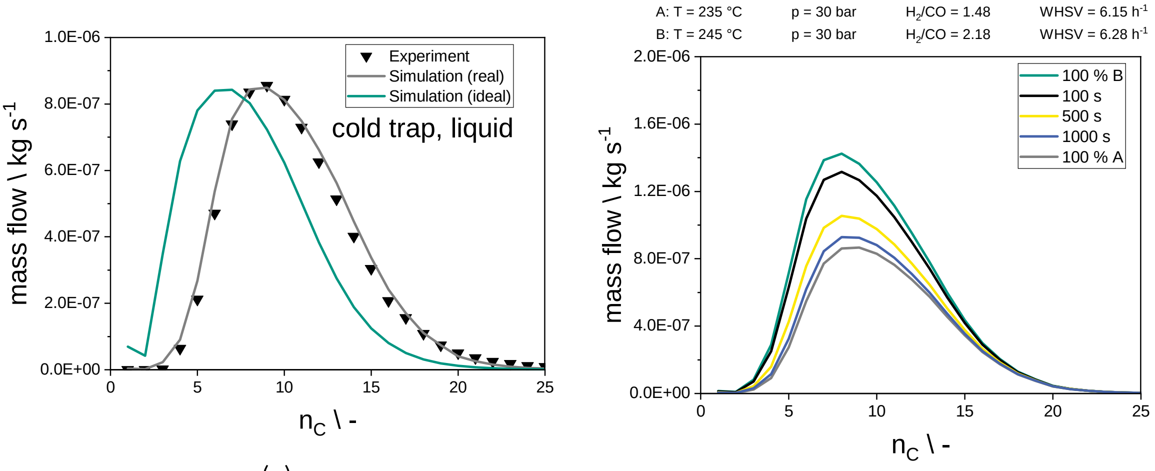

(a)

(b)

Figure 4.11: Cold trap liquid sample mass distribution. (a) Experimental data compared to both an ideal flash and calculations using the EOS; (b) Two sets of reaction conditions switched between with respect to the mass distribution for the liquid product in the CT according to specific mixing times. The operating conditions switched between are shown above the figure.

versa. The mixing time calculated from the volume flow indicates how much time elapses for a mixture to form in the respective part of the system after the gas composition at the reactor inlet changes. This mixing state is calculated individually for mass, volume and molar flows. The presented model assumes instantaneous phase formation upon vessel entry. The CT needs at least 6,000 s to apply new operating conditions in the product spectrum of the gas phase. According to tracer tests, the mean residence time of the gas phase in the CT is approximately 5,000 s. The simulation can thus describe the mixing behavior with sufficient accuracy. Due to the large volume of the tank, an emphasized back-mixing and thus system inertia is to be expected.

4.3.4 Results and discussion

Within this work, a reactor model for a pilot scale microstructured fixed-bed reactor was developed. Reaction kinetics were fitted with MATLAB. With the help of ad nonlinear regression, kinetic parameters could be determined in good agreement with literature. Furthermore, a residence time model was developed from tracer experiments. Accurate representations of the total residence time function (F-curve) for each system component were developed. This enabled time-resolved calculations of product distribution of each respective phase. With an equation of state, a significantly more reliable prediction of the phase equilibrium could be achieved, compared to ideal phase behavior assumptions.

By specifying input variables such as temperature, pressure and volume flow of the reactants, the prediction of reaction products, F-curves, fractional product separation, as well as flow and mixing properties could be calculated. The reaction kinetics subroutine provides a satisfactory representation of experimental results. There is still potential for improvement in the description of the kinetics, especially in the prediction of H_2 and CO conversion. Here, the error accounts to a maximum of 10 % for about 70 % of the data. The kinetic model could be extended by implementing the formation of alkenes and iso-alkanes as well as by increasing the chain length range of the products. Various mechanistic processes, such as alkene re-adsorption, could also be added to the model. However, it should be considered whether these improvements have technical relevance.

A further step towards the simulation of load-flexible, dynamic operation would be the representation of a time-resolved product separation so that the quantity of products in the hot and cold trap can be determined at any time by varying the operating conditions. This requires the consideration of a phase equilibrium for each time frame within each vessel, as well as a new reactor model that considers liquid and gas phase buildup.

All in all, the developed simulation provides satisfactory results and can be used as a first basis for controlling dynamic operation of the FTS system in microstructured reactors. A transferability to other systems is easily possible by adaptation of boundary conditions. The simulation of mixing conditions made it possible to predict the basic behavior of product separation in the most important system components. This pays respect to the complex nature of the synthesis and its diverse products. Both experimentally and from simulation, a reliable system was represented, which should be able to meet the challenges of a decentralized PtL application with regard to future volatile energy flows.

4.3.5 Summary

Flexibility of synthesis plants will be a necessary asset in future applications. It is time and money consuming to experimentally test different setups, especially in larger scales. In order to make product predictions quicker and more feasible, system modeling and performance simulation are indispensable tools in process design. The development of a kinetic model for chemical synthesis is essential for the prediction and optimization of reactors and catalyst behavior. The assessment and description of the flexibility of the reactor during dynamic operation must also be considered in order to develop an adaptable control system for varying operating conditions. In this work, a multi-level model for the description of relevant processes inside a pilot scale Fischer-Tropsch reactor and the associated plant infrastructure is presented. Flow and mixing behavior can be described by a residence time distribution designed for different system components. Time and temperature-dependent product concentration can be determined by a vapor-liquid-equilibrium applied to the product condensers. Furthermore, phase equilibria models with ideal and real phase behavior assumptions were compared. A micro-kinetic model was validated in good agreement with a variety of experimental data. When coupled, the three separate MATLAB models are able to predict time-resolved online product characteristics, based on process and feed properties only. Future small-scale synthesis units will make use of the synergy between highly efficient microstructured reactors and their mathematical description in simulation.

4.4 Paper V – "*operando* analysis of catalyst behavior in the synchrotron – a look behind the curtain"

4.4.1 Introduction

The FTS nowadays is still subject to mechanistic research, despite its age of almost 100 years since discovery [210, 212–217]. During reaction, e.g. surface species are reported to form carbides or oxides that can decrease the catalytic activity [233, 234]. Adsorbing species or reconstruction are known to change the way a catalyst behaves up to the point where its activity is lowered significantly.

In order to understand surface and bulk chemistry, advanced analysis methods are required to shed light on the catalytic black box. Synchrotron-based methods are optimal tools to investigate catalysts and to monitor their changes during operation [102, 175]. Therefore, Fischer-Tropsch catalysts have been thoroughly investigated using methods like XAS or XRD or a combination of both to get complementary information on the changes of the amorphous and crystalline phases and to connect them to observed deactivation phenomena.

However, compromises between industrial conditions and synchrotron Fischer-Tropsch studies had to be made due to the challenging reaction conditions of e.g. 250 °C and 30 bar. Synchrotron experiments under an elevated pressure of up to 18 bar [175, 235] have been performed in micro quartz capillary reactors that lacked a suitable temperature profile as well as an sufficient amount of catalyst in the bed. The low amount of catalyst in these kind of reactors results in WHSV far from industrial conditions and makes it impossible to produce analyzable amounts of liquid FTS products at the synchrotron. Furthermore, catalysts have only been characterized *in situ* for 48 h TOS. Due to the lack of *in situ* or *operando* reaction cells for combined XAS and XRD at a pressure of up to 50 bar combined with temperatures of up to 450 °C [236], a new cell was designed for these harsh conditions. Studies with combined XAS and XRD on a commercial Co-Ni-Re/Al_2O_3 catalyst over 310 h TOS during the FT reaction were performed. The information gathered during the long-term FTS synchrotron studies will support future applications, especially for small-scale plants that rely on a steady catalyst activity [73, 237, 238].

Furthermore, the newly designed *operando* cell for combined XAS and XRD opens room to new realistic studies for further applications under elevated pressure e.g. methanol synthesis.

4.4.2 Experimental methods

Catalyst, cell and test rig

The same commercial Co-based catalyst mentioned before was again tested in this work. 83.8 mg of this catalyst, after diluting it 1:4 with γ-Al_2O_3 and adjusting the sieve fraction to 100 - 200 μm, was filled into the novel reaction cell, shown in figure 4.12.

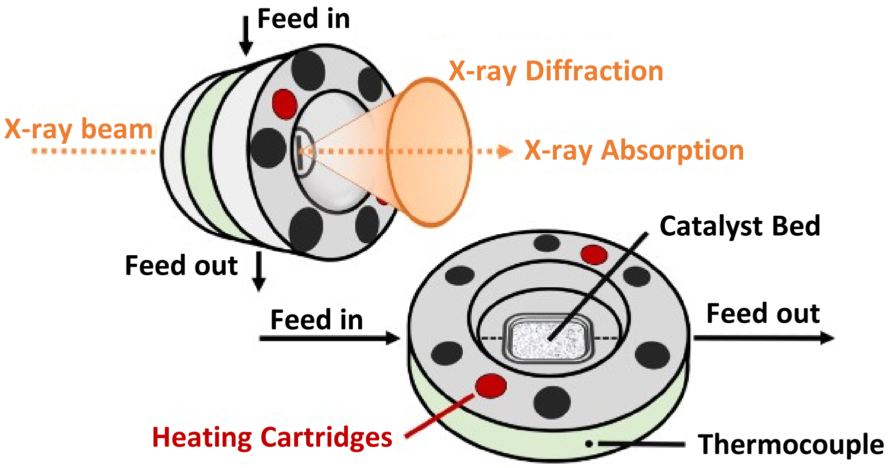

Figure 4.12: Novel designed high-pressure cell for combined XAS and XRD at temperatures up to 450 °C and pressure of up to 50 bar.

The high-pressure cell offers simultaneous measurements of X-ray absorption and -diffraction. The cell was tested up to 450 °C and 50 bar (He). The catalyst bed is fixed from both sites with 1.5 mm PF-60 beryllium foils by Materion and sealed with graphite foils. The X-ray beam can penetrate through a 10 x 2 mm slit cut in both outer parts of the cell. The position of the slit enables spatially resolved measurements (e.g. inlet, middle, outlet). The reactive gases are passed through the cell from top to bottom to assist the outflow of the liquid products. In front of the catalyst bed the gases are equally distributed by an additional inlay to ensure a homogeneous gas distribution over the whole catalyst bed. The cell was heated by two 160 W heating cartridges (HORST) and controlled by a thermocouple mounted close to the reactor bed inside the stainless steel main body. The whole cell was secured in a newly designed safety-box equipped with polyimide windows that was flushed continuously with nitrogen. The gases were filtered at the outlet to prevent any contamination of the environment due to beryllium in the event of a break or bursting of the beryllium foils.

The test rig infrastructure was derived from iterations installed at the IMVT, as presented in publication 1 (sections 4.1 and 5). The test rig was miniaturized to fit into the beamline setting.

Analysis

A micro-GC was able to measure the online gas composition of the product gas for inert gases, and hydrocarbons up to C_4 species. The offline-GC mentioned in section 3.3 enabled the analysis of liquid hydrocarbons.

The synchrotron beam was capable of entering and exiting the measurement cell and the safety box. XAS spectra were taken at the Co-K edge. XANES was taken continuously with 2.5 min per spectrum, while one extended X-ray absorption fine structure (EXAFS) measurement was taking about 30 min. Co references of different oxidized states were compared to the results. XRD could be measured in 10 min.

Experimental campaign

The catalyst was activated by TPR in pure hydrogen and kept at 380 °C for five hours. The initiation phase for the catalyst was executed at around 250°C with 10 mL min^{-1} of H_2 and 5 mL min^{-1} CO for 310 h TOS. Afterwards, a hydrogen dropout was carried out to purposely oxidize or carburize the catalyst in pure CO.

Post mortem *ex situ* analysis included XRD, Raman spectroscopy and a thermo-gravimetric measurement using a mass spectrometer (TG-MS).

4.4.3 Results and discussion

in situ **results**

Linear combination analysis (LCA) showed that the fresh catalyst was nearly completely oxidized (ca. 91 %) before the initial TPR. After reduction, EXAFS spectra showed a nearly completely reduced Co catalyst (ca. 94 %). XRD measurements supported the observation.

During initiation phase, changes on the catalyst were very small, as seen in taken XAS spectra. Over 310 h TOS, a slight decrease of the Co-K edge whiteline features at 7715 eV and 7726 eV accompanied by an increase at 7719 eV, 7731 eV and 7742 eV was observed. The findings hint towards the formation of small amounts of either oxidized cobalt species or Co_2C, while the signals do not fit a single reference completely. The most significant changes happened between 60 and 310 h of TOS, yet the peaks found in EXAFS are within the error of the signal to noise ratio, being them hints rather than evidence. The comparison of the first derivatives to the carburized and oxidized catalyst provided information that neither Co_2C nor CoO was formed during the first 310 h TOS in the FTS. The formation of a peak at 7717 eV was also observed in previous studies by Rønning et al. [175, 239], where it was assigned to the formation of $CoAl_2O_3$ species.

The observed changes during initiation phase could not explain the rapid deactivation observed during online GC measurements. During the first eight hours TOS a fast drop from 80 - 90 % to 66 % CO conversion was observed (see figure 4.13a). The changes must be due to the formation of a wax phase and a thereby declined pore diffusion. The formation of liquid species/waxes was also confirmed by a low C-balance of the gaseous products, which is also an indicator for the formation of liquid/solid products during the first hours of initiation phase. This fast deactivation was also observed in previous studies and assigned to a "reversible deactivation" [240]. After eight hours, the rate of deactivation significantly declined to a quasi-stationary state at the end of the experiment. The CO conversion dropped from 66 % to 38 %. The observed deactivation during this time period is assigned as "non-reversible deactivation" [240] and might be due to irreversible changes of the catalyst or the formation of different carbon species [234]. Product selectivity could further support those assumptions (see figure 4.13b). It was rather constant in the observed time period, after the catalyst got wetted in the first 80 h by increasing wax formation along the bed.

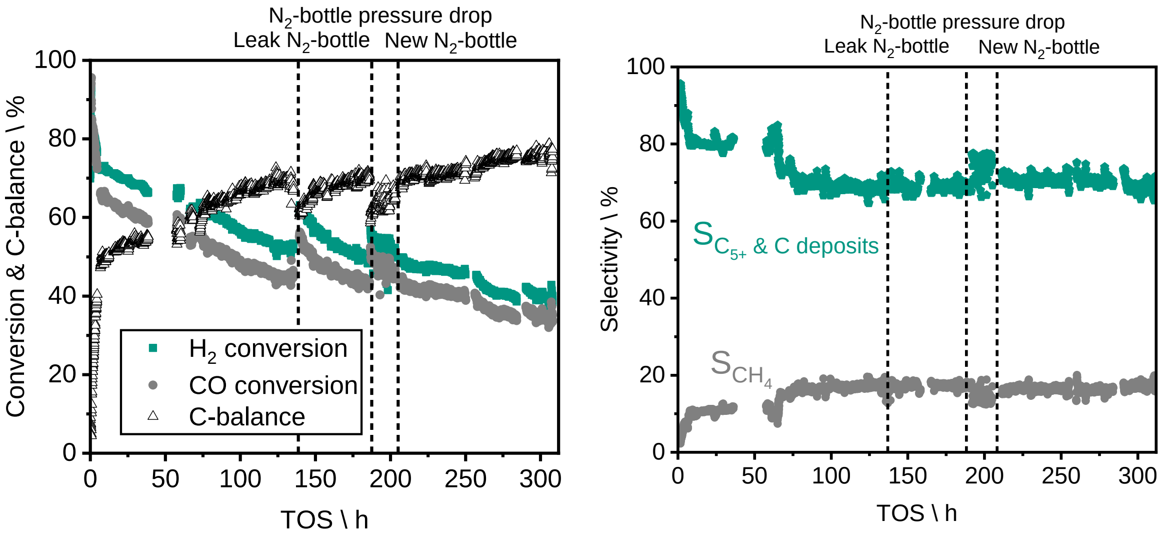

(a) (b)

Figure 4.13: Experimental results from the 310 h initiation phase. (a) Conversion of the syngas molecules and the carbon balance in the gas phase; (b) selectivity to gaseous products as derived from the product gas phase.

A significant rise of the selectivity to CH_4 occurredin this time phase. From that point on, the selectivity data is constant, besides a signal jittering caused by the back-pressure valve or product sampling. The low conversion levels and C_{5+} selectivity are caused by the very low residence time compared to previous lab-scale studies [73, 75]. Since not all of the observed deactivation phenomena could be explained by the applied *operando* methods, the catalyst was further analyzed *ex situ* after the long-term experiment.

***ex situ* results**

Ex situ XRD analysis showed no oxidic cobalt species, despite the catalyst being extracted from the reaction cell in an oxygen-rich atmosphere. This might be due to the formation of a protecting wax phase on the catalyst surface. A significant formation of cobalt carbides was also excluded, as no reflections for Co_2C have been found in the XRD.

However, Raman spectroscopy showed the formation of three peaks assigned to the D4 (1170 cm^{-1}), D1 (1319 cm^{-1}) and G (1603 cm^{-1}) bands. According to Sadezky et al. [241], the D4 and D1 bands originate from disordered graphitic lattice and/or from the graphitic lattice. The G band originates from ideal graphitic lattice. The absence of D2 bands indicate that mainly poorly ordered structures of graphite were formed [242]. This was confirmed by the relatively broad shapes of the D1 and the G bands that are sensitive to the extent of two-dimensional graphitic ordering and might be a hint for a large degree of interstitial disorder along the c-axis between the in-plane direction [243]. Microcrystalline planar size analysis further supports that statement by providing evidence on a large degree of disorder suggesting the presence of a very poorly graphitized structure [244].

The amount and types of carbon and wax depositions were characterized by H_2-TPR and a subsequent O_2-TPO coupled with MS-analysis. The H_2-TPR provided the formation of two significant methane peaks at 280 °C and 650 °C. The first peak corresponded to a loss of 3 % of total mass and could be assigned to the hydration of atomic carbon, surface carbides and hydrocarbons. The second peak with a total mass-loss of 2 % was likely caused by the hydration of graphitic carbon deposits [245]. The peak formation of H_2O at around 100 °C was due to desorption of surface H_2O, while the second rise of the H_2O signal at around 475 °C could be caused by the reduction of oxidized cobalt species. In total, around 10 % of the sample mass was lost due to hydration, with about half due to hydration of carbonaceous species and half due to water evaporation and reduction of oxidized cobalt species.

The consecutive O_2-TPO showed one distinct CO_2 peak at the reference line around 350 °C. This peak formation is due to hydrogen-resistant carbonaceous species. It provides evidence that a reactivation procedure simply by H_2-TPR is not enough to completely reactivate the catalyst [233]. The mass loss of the catalyst due to oxidation of the hydrogen-resistant carbonaceous species was not determined in this case, as the mass-increase due to re-oxidation of the catalyst was overlapping with the mass-loss of the oxidized carbonaceous species. The progressive loss of the mass with the temperature above 550 °C without formation of a CO_2 signal might be due to an ongoing $CoAl_2O_4$ formation. This would be in a good agreement to the blue color of the catalyst after the TPH/TPO experiment.

4.4.4 Summary

This operando XAS and XRD study on the Fischer-Tropsch synthesis over more than 300 h TOS at 250 °C and 30 bar on a commercial catalyst for FTS provides an important step forward to bridge the gap between fundamental studies at synchrotron radiation sources and industrial reaction conditions. Furthermore, these results demonstrate that by using spectroscopic reactors that allow to perform operando studies with an adequate amount of catalyst and realistic space velocities, the catalytic performance can be well derived directly at a synchrotron radiation facility. This opens new possibilities for the clarification of structure-activity relationships not only in the Fischer-Tropsch synthesis, but also in other industrial reactions requiring high pressure and temperature.

5 Summary and Outlook

In the course of this work, a deep understanding of the functionality of microstructured pilot scale reactors for use in exothermal, heterogeneously catalyzed Fischer-Tropsch synthesis was developed. The LTFT proved to be a great example for the technology's advantages. The pathway to produce sustainable, renewable fuels in decentralized plants is supported through this work.

The potential and advantages of a microstructured reactor scale-up and the list of tools available for its process control has been elaborated. A demanding BtL setup with high inert dilution was chosen to evaluate the influence of different process conditions such as temperature, pressure, residence time and gas properties both in a lab and a pilot scale reactor. While a broad range of conditions is applicable in both fixed-bed reactors, the larger system showed even more advantages by offering process control by evaporation cooling. High conversion levels could be achieved, at which the reaction could be operated isothermally while still controllable. Further reactor scale-ups or numbering-ups may thus help to increase productivity, with regard to decentralized, small-scale BtL and PtL applications.

Possibilities from fast and efficient process control were evaluated in two consecutive publications, both investigating dynamic operation of the given pilot scale system. The main focus was set on changes in the feed gas composition and -flows, as well as the change of reaction temperature. After initial tests and an introduction to the general reaction periphery and measurement devices, parameter changes were carefully applied and steadily developed to shorter time scale. Since the system suffered from a certain signal delay caused by dead times of the product condensation vessels, the evaluation of dynamic effects below that time span was challenging. Still, step-changes were shortened to the minute-range. In order to test restrictions for changes in a challenging reaction system, a real photovoltaic power output profile was discretized into a volatile hydrogen flow experiment to fit the reaction system at hand. In multiple campaigns, despite looking for potential restrictions in the rate of parameter changes, the versatility and reliance of microstructured reactors with evaporation cooling was proven. Overall, the process could be improved by fast dynamic operation, in terms of methane selectivity and product quality. A more unfavorable BtL case with changing syngas ratio, residence time and temperature under the assumption of a stationary CO feed was executable by the pilot scale FT reactor. The PtL case study exhibited very stable and better controllable conversion at constant product quality. Within the framework of the PtL campaign, 70 % of CO conversion was targeted and in most situations achieved, despite a fluctuation in gas feed and temperature. Only the start-up and down-ramping phases were challenging, since there was not enough total available reaction enthalpy to keep the reactor operating in autothermal mode.

From this work it can be assumed that fast dynamic changes performed in the FTS within microstructured reactors have no influence on long-term catalyst activity and stability. This was shown by regular determination of the conversion level for a reference setup. Still, as the reactor is a black box, sophisticated methods must be applied to get a glimpse of effects happening on catalyst level. For that reason, spectroscopic methods were chosen to inspect different process effects on the catalyst surface and bulk in a run with over 300 h of operation at the KIT synchrotron. Methods to investigate effects included XAS and XRD measurements with concurrent product evaluation via a micro GC and a mass spectrometer. Liquid products were analyzed *ex situ* in an offline-GC. During initiation phase, carburization was assumed to occur from regular reaction. Since the formation of those species was not sufficient to explain the drastic drop in conversion levels during that time on stream, the formation of long-chained, immobile hydrocarbons was assumed to be the main cause of the decrease. Feed gas changes were applied in that reaction setup and proved that no imminent deactivation occurs from fast gas concentration changes, going as low as a hydrogen to carbon monoxide ratio of 1. Reducing the ratio to 0 during a hydrogen dropout was found to deactivate the catalyst even further boy carburizing and not oxidizing it. Deactivation of the catalyst was evaluated as being partially reversible and irreversible. The catalyst needed to be reactivated and a combination of oxidation and reduction is proposed to get rid of the carbides visible in *ex situ* analysis. Catalyst lifetime is an important topic, especially with valuable materials such as cobalt.

A microkinetic model of the reaction was adapted to predict productivity and product quality. When coupled with a vapor-liquid equilibrium and a residence time model, real-time separation of the diverse Fischer-Tropsch product phases was established in a multi-level model. The microkinetic model, based on 20 experimental setups, showed a good performance in terms of accuracy. Phase calculations for product condensation were developed based on a volume-translated Peng-Robinson equation of state. The residence time model of the system was described based on a tanks-in-series model. Data to fit the model parameters was based on dead time experiments. The layout of the model was ultimately focusing on a fast switch between two experimental setups and the influence on the products during the change of process conditions.

If further developed, the model can be used to forecast productivity and product properties in dynamic process campaigns. Improvements in product characteristics could include the extension of the highest product chain length from 50 carbon atoms to a higher value and the addition of iso-alkanes and alkenes as product compounds. Model validity can be further improved by incorporating more experimental setups with a broader range of process parameters.

All sections in this work focus on one or more system characteristics under the general assumption that microstructured Fischer-Tropsch fixed-bed reactors are well suited for decentralized BtL and PtL plants. The efficient microstructure technology with its intensified heat and mass transport properties allowed manageable control regarding changing process conditions and a constant process performance under these dynamic conditions that large-scale industrial reactors lack.

Dynamic synthesis will be a valuable piece in the future of process engineering. Smart flow and process control will become increasingly important and this work gives important insights into relevant system properties, challenges and opportunities. The use of microstructured reactors might be one of the most promising paths to follow to flexibly produce storable high-quality energy carriers from renewable energy.

Bibliography

[1] H. Rodhe, "A Comparison of the Contribution of Various Gases to the Greenhouse Effect," *Science*, vol. 248, no. 4960, pp. 1217 – 1219, 1990.

[2] NOAA Earth System Research Laboratory, "The NOAA annual greenhouse gas index (AGGI)." `http://www.esrl.noaa.gov/gmd/ccgg/aggi.html`, updated Spring 2019. Accessed: 25.08.2019.

[3] Q. Ma, "Greenhouse Gases: Refining the Role of Carbon Dioxide," *NASA Science Briefs*, 1998.

[4] UN Climate Change, "Historic Paris Agreement on Climate Change: 195 Nations Set Path to Keep Temperature Rise Well Below 2 Degrees Celsius." `http://newsroom.unfccc.int/unfccc-newsroom/finale-cop21/`. Accessed: 03.04.2018.

[5] C. Le Quéré, R. M. Andrew, P. Friedlingstein, S. Sitch, J. Hauck, J. Pongratz, P. A. Pickers, J. I. Korsbakken, G. P. Peters, J. G. Canadell, A. Arneth, V. K. Arora, L. Barbero, A. Bastos, L. Bopp, F. Chevallier, L. P. Chini, P. Ciais, S. C. Doney, T. Gkritzalis, D. S. Goll, I. Harris, V. Haverd, F. M. Hoffman, M. Hoppema, R. A. Houghton, G. Hurtt, T. Ilyina, A. K. Jain, T. Johannessen, C. d. Jones, E. Kato, R. F. Keeling, K. K. Goldewijk, P. Landschützer, N. Lefèvre, S. Lienert, Z. Liu, D. Lombardozzi, N. Metzl, D. R. Munro, J. E. M. S. Nabel, S.-i. Nakaoka, C. Neill, A. Olsen, T. Ono, P. Patra, A. Peregon, W. Peters, P. Peylin, B. Pfeil, D. Pierrot, B. Poulter, G. Rehder, L. Resplandy, E. Robertson, M. Rocher, C. Rödenbeck, U. Schuster, J. Schwinger, R. Séférian, I. Skjelvan, T. Steinhoff, A. Sutton, P. P. Tans, H. Tian, B. Tilbrook, F. N. Tubiello, I. T. van der Laan-Luijkx, G. R. van der Werf, N. Viovy, A. P. Walker, A. J. Wiltshire, R. Wright, S. Zaehle, and B. Zheng, "Global Carbon Budget 2018," *Earth System Science Data*, vol. 10, no. 4, pp. 2141–2194, 2018.

[6] T. Bründlinger, J. Elizalde-König, O. Frank, D. Gründig, C. Jugel, P. Kraft, O. Krieger, S. Mischinger, P. Prein, H. Seidl, S. Siegemund, C. Stolte, M. Teichmann, J. Willke, and M. Wolke, "Integrated Energy Transition." Deutsche Energie-Agentur, a study, 2018.

[7] M. Z. Jacobson, M. A. Delucchi, M. A. Cameron, and B. A. Frew, "Low-cost solution to the grid reliability problem with 100% penetration of intermittent wind, water, and solar for all purposes," *Proceedings of the National Academy of Sciences of the United States of America*, vol. 112, no. 49, pp. 15060–15065, 2015.

[8] M. Ram, D. Bogdanov, A. Aghahosseini, A. Gulagi, A. S. Oyewo, M. Child, U. Caldera, K. Sadovskaia, J. Farfan, L. Barbosa, M. Fasihi, S. Khalili, H.-J. Fell, and C. Breyer, "Global Energy System based on 100 % Renewable Energy: Energy Transition in Europe Across Power, Heat, Transport and Desalination Sectors." LUT University and Energy Watch Group, a report, 2018.

[9] A. Bisio, *Encyclopedia of energy technology and the environment*. A Wiley-Interscience publication, New York: Wiley, 1995.

[10] M. Sterner, "Notwendigkeit und Chancen für Power-to-X-Technologien - Energiewirtschaftliches Kurzgutachten." a report, 2017.

[11] M. Sterner, N. Gerhardt, M. Jentsch, Y.-M. Saint-Drenan, C. Pape, J. Schmid, M. Specht, U. Zuberbühler, and B. Stürmer, "Speichertechnologien als Lösungsbaustein einer intelligenten Energieversorgung - Fokus Strom-Gasnetzkopplung." presented at E-World energy & water, 09.02.2011.

[12] J. Hobohm, A. Auf der Maur, H. Dambeck, A. Kemmler, S. Koziel, S. Kreidelmeyer, Piégsa, P. Wendring, B. Meyer, A. Apfelbacher, M. Dotzauer, and K. Zech, "Status und Perspektiven flüssiger Energieträger in der Energiewende." Prognos AG, a report, 2018.

[13] A. Abu-Jrai, A. Tsolakis, K. Theinnoi, R. Cracknell, A. Megaritis, M. L. Wyszynski, and S. E. Golunski, "Effect of gas-to-liquid diesel fuels on combustion characteristics, engine emissions, and exhaust gas fuel reforming. Comparative study," *Energy and Fuels*, vol. 20, no. 6, pp. 2377–2384, 2006.

[14] S. S. Gill, A. Tsolakis, K. D. Dearn, and J. Rodríguez-Fernández, “Combustion characteristics and emissions of Fischer-Tropsch diesel fuels in IC engines,” *Progress in Energy and Combustion Science*, vol. 37, no. 4, pp. 503–523, 2011.

[15] E. Corporan, M. J. DeWitt, V. Belovich, R. Pawlik, A. C. Lynch, J. R. Gord, and T. R. Meyer, “Emissions characteristics of a turbine engine and research combustor burning a fischer- tropsch jet fuel,” *Energy & fuels*, vol. 21, no. 5, pp. 2615–2626, 2007.

[16] K. Wagemann and F. Ausfelder, “WhitePaper: E-Fuels - Mehr als eine Option.” Dechema - Gesellschaft für Chemische Technik und Biotechnologie e.V., a study, 2017.

[17] S. Brynolf, M. Taljegard, M. Grahn, and J. Hansson, “Electrofuels for the transport sector: A review of production costs,” *Renewable and Sustainable Energy Reviews*, vol. 81, pp. 1887–1905, 2018.

[18] S. Schemme, R. C. Samsun, R. Peters, and D. Stolten, “Power-to-fuel as a key to sustainable transport systems – An analysis of diesel fuels produced from CO_2 and renewable electricity,” *Fuel*, vol. 205, pp. 198–221, 2017.

[19] S. Horvath, M. Fasihi, and C. Breyer, “Techno-economic analysis of a decarbonized shipping sector: Technology suggestions for a fleet in 2030 and 2040,” *Energy Conversion and Management*, vol. 164, pp. 230–241, 2018.

[20] F. G. Albrecht, D. H. König, N. Baucks, and R.-u. Dietrich, “A standardized methodology for the techno-economic evaluation of alternative fuels – A case study,” *Fuel*, vol. 194, pp. 511–526, 2017.

[21] energate, “E-fuels sollen CO_2-Flottenregulierung ergänzen.” `https://www.energate-messenger.ch/news/184570/e-fuels-sollen-co2-flottenregulierung-ergaenzen`, 2018. Accessed: 25.08.2019.

[22] D. H. Koenig, M. Freiberg, R. U. Dietrich, and A. Woerner, “Techno-economic study of the storage of fluctuating renewable energy in liquid hydrocarbons,” *Fuel*, vol. 159, pp. 289–297, 2015.

[23] G. Leonard, V. Francois-Lavet, D. Ernst, C. J. Meinrenken, and K. S. Lackner, “Electricity

storage with liquid fuels in a zone powered by 100 % variable renewables." presented at the International Conference on the European Energy Market, EEM, 2015.

[24] A. Tremel, *Electricity-based Fuels*. Berlin: Springer International Publishing, 2018.

[25] H.-W. Schiffer, R. Höher, F. Jakob, N. Kaim-Albers, and C. Menzel, "Energie für Deutschland - Faktien, Perspektiven und Positionen im globalen Kontext." World Energy Council, a report, 2019.

[26] Umweltbundesamt, Arbeitsgemeinschaft Energiebilanzen, "Endenergieverbrauch 2018 nach Sektoren und Energieträgern." `https://www.umweltbundesamt.de/bild/endenergieverbrauch-2018-nach-sektoren`, 2018. Accessed: 04.08.2020.

[27] International Energy Agency, "CO_2 emissions from fuel combustion - Highlights." a report, 2018.

[28] International Energy Agency, "World energy balances: overview." a report, 2018.

[29] World Energy Council, "Innovation Insights Brief - Energy Infrastructure." a report, 2019.

[30] IHS Markit, "Global Renewable Power Market Outlook." a study, 2019.

[31] Enerdata, "Global Energy Statistical Yearbook 2020." `https://yearbook.enerdata.net/total-energy/world-consumption-statistics.html`, a report. Accessed: 02.08.2020.

[32] J.-P. Rodrigue, C. Comtois, and B. Slack, *The geography of transport systems*. London and New York: Routledge Taylor & Francis Group, 4th edition ed., 2017.

[33] D. Bothe, M. Fritsch, A. Lövenich, J. Perner, and T. Schaefer, "Synthetische Energieträger - Perspektiven für die deutsche Wirtschaft und den internationalen Handel." Institut der deutschen Wirtschaft, a study, 2018.

[34] K. Crone, S. Fasbender, C. Jugel, M. Klebe, S. Löchle, H. Schumacher, H. Seidl, S. Shanmugam, and B. Stuntz, "Powerfuels : A missing link to a successful global energy transition," 2019.

[35] Fuels Europe, "Statistical report 2019." a report, 2019.

[36] F. Ausfelder and H. E. Dura, "1. Roadmap des Kopernikus-Projektes "Power-to-X": Flexible Nutzung erneuerbarer Ressourcen (P2X)." Dechema - Gesellschaft für Chemische Technik und Biotechnologie e.V., a report, 2018.

[37] A. Varone and M. Ferrari, "Power to liquid and power to gas: An option for the German Energiewende," *Renewable and Sustainable Energy Reviews*, vol. 45, pp. 207–218, 2015.

[38] F. Vidal, J. Koponen, V. Ruuskanen, C. Bajamundi, A. Kosonen, P. Simell, J. Ahola, C. Frilund, J. Elfving, M. Reinikainen, N. Heikkinen, J. Kauppinen, P. Piermartini, and F. V. Vázquez, "Power-to-X technology using renewable electricity and carbon dioxide from ambient air : SOLETAIR proof-of-concept and improved process concept," *Journal of CO2 Utilization*, vol. 28, no. August, pp. 235–246, 2018.

[39] P. Schmidt, V. Batteiger, A. Roth, W. Weindorf, and T. Raksha, "Power-to-Liquids as Renewable Fuel Option for Aviation: A Review," *Chemie-Ingenieur-Technik*, vol. 90, no. 1, pp. 127–140, 2018.

[40] P. M. Maitlis and A. de Klerk, *Greener Fischer-Tropsch Processes for Fuels and Feedstocks*. Weinheim: Wiley VCH, 2013.

[41] Bundesverband der Deutschen Industrie, "Positionspapier der deutschen Industrie zum Aufbau von Rahmenbedingungen für die e-fuels-Technologien." a study, 2018.

[42] C. H. Bartholomew and R. J. Farrauto, *Fundamentals of industrial catalytic processes*, vol. 20. Hoboken: John Wiley & Sons, 2011.

[43] M. E. Dry, "Catalytic aspects of industrial Fischer–Tropsch synthesis," *Journal of Molecular Catalysis*, vol. 17, no. 2-3, pp. 133–144, 1982.

[44] J. van de Loosdrecht, F. Botes, I. Ciobica, A. Ferreira, P. Gibson, D. Moodley, A. Saib, J. Visagie, C. Weststrate, and J. Niemantsverdriet, "7.20 - fischer-tropsch synthesis: Catalysts and chemistry," in *Comprehensive Inorganic Chemistry II (Second Edition)* (J. Reedijk and K. Poeppelmeier, eds.), pp. 525 – 557, Amsterdam: Elsevier, second ed., 2013.

[45] F. Fischer and H. Tropsch, “The preparation of synthetic oil mixtures (synthol) from carbon monoxide and hydrogen,” *Brennstoff-Chemie*, vol. 4, pp. 276–285, 1923.

[46] F. Fischer and H. Tropsch, “Über die direkte synthese von erdöl-kohlenwasserstoffen bei gewöhnlichem druck. (erste mitteilung,” *Berichte der deutschen chemischen Gesellschaft (A and B Series)*, vol. 59, no. 4, pp. 830–831, 1926.

[47] S. R. Craxford, “The Fischer-Tropsch synthesis with cobalt catalysts,” *Journal of the Society of Chemical Industry*, vol. 66, no. 12, pp. 440–444, 1947.

[48] J. Yang, W. Ma, D. Chen, A. Holmen, and B. H. Davis, “Fischer-Tropsch synthesis: A review of the effect of CO conversion on methane selectivity,” *Applied Catalysis A: General*, vol. 470, no. 3-4, pp. 250–260, 2014.

[49] M. E. Dry, “The Fischer-Tropsch process: 1950-2000,” *Catalysis Today*, vol. 71, no. 3-4, pp. 227–241, 2002.

[50] V. van Wechem and M. Senden, “Conversion of Natural Gas to Transportation Fuels Via the Shell Middle Distillate Synthesis Process (SMDS),” in *Natural Gas Conversion II* (H. Curry-Hyde and R. Howe, eds.), vol. 81 of *Studies in Surface Science and Catalysis*, pp. 43 – 71, Elsevier, 1994.

[51] E. Alper and O. Yuksel Orhan, “CO_2 utilization: Developments in conversion processes,” *Petroleum*, vol. 3, no. 1, pp. 109–126, 2017.

[52] G. Petersen, D. Viviani, K. Magrini-Bair, S. Kelley, L. Moens, P. Shepherd, and D. DuBois, “Nongovernmental valorization of carbon dioxide,” *Science of the Total Environment*, vol. 338, no. 3, pp. 159–182, 2005.

[53] A. C. Vosloo, “Fischer-Tropsch: A futuristic view,” *Fuel Processing Technology*, vol. 71, no. 1-3, pp. 149–155, 2001.

[54] S. Jürgens, P. Oßwald, M. Selinsek, P. Piermartini, J. Schwab, P. Pfeifer, U. Bauder, S. Ruoff, B. Rauch, and M. Köhler, “Assessment of combustion properties of non-hydroprocessed Fischer-Tropsch fuels for aviation,” *Fuel Processing Technology*, vol. 193, no. December 2018, pp. 232–243, 2019.

[55] J. Patzlaff, Y. Liu, C. Graffmann, and J. Gaube, “Interpretation and kinetic modeling of

product distributions of cobalt catalyzed Fischer-Tropsch synthesis," *Catalysis Today*, vol. 71, no. 3-4, pp. 381–394, 2002.

[56] S. T. Sie and R. Krishna, "Fundamentals and selection of advanced Fischer–Tropsch reactors," *Applied Catalysis A: General*, vol. 186, no. 1-2, pp. 55–70, 1999.

[57] Y. Lu and T. Lee, "Influence of the Feed Gas Composition on the Fischer-Tropsch Synthesis in Commercial Operations," *Journal of Natural Gas Chemistry*, vol. 16, no. 4, pp. 329–341, 2007.

[58] A. Steynberg and M. Dry, "Fischer–Tropsch Technology," *Applied Catalysis A: General*, vol. 152, 2004.

[59] A. de Klerk, *Fischer-Tropsch Refining*. Weinheim: Wiley-VCH, first ed., 2011.

[60] K. L. Jensen, R. J. Menard, and B. C. English, "Market Analysis for Fischer-Tropsch Waxes." Department of Agriculture and Resource Economics, Institute of Agriculture, University of Tennessee, a report, 2013.

[61] S. Sie, M. Senden, and H. V. Wechem, "Conversion of natural gas to transportation fuels via the shell middle distillate synthesis process (smds)," *Catalysis Today*, vol. 8, no. 3, pp. 371 – 394, 1991.

[62] K. Im-orb and A. Arpornwichanop, "Techno-environmental analysis of the biomass gasification and Fischer-Tropsch integrated process for the co-production of bio-fuel and power," *Energy*, vol. 112, pp. 121–132, 2016.

[63] A. S. Snehesh, H. S. Mukunda, S. Mahapatra, and S. Dasappa, "Fischer-Tropsch route for the conversion of biomass to liquid fuels - Technical and economic analysis," *Energy*, vol. 130, pp. 182–191, 2017.

[64] L. Schulz, M. Selinsek, C. Wild, P. Pfeifer, and T. Böltken, "Influence of reaction conditions on the conversion of methane rich gases to Fischer-Tropsch products," *Chemical Engineering & Technology*, 2019.

[65] A. Delparish and A. K. Avci, "Intensified catalytic reactors for Fischer-Tropsch synthesis and for reforming of renewable fuels to hydrogen and synthesis gas," *Fuel Processing Technology*, vol. 151, pp. 72–100, 2016.

[66] A. de Klerk, “Gas-to-liquids conversion.” Presented at tge Natural gas conversion technologies workshop of ARPA-E, US Department of Energy, 13 January 2012, 2012.

[67] B. H. Davis, “Fischer–Tropsch synthesis: relationship between iron catalyst composition and process variables,” *Catalysis Today*, vol. 84, no. 1, pp. 83–98, 2003.

[68] M. E. Dry, “Practical and theoretical aspects of the catalytic Fischer-Tropsch process,” *Applied Catalysis A: General*, vol. 138, no. 2, pp. 319–344, 1996.

[69] B. H. Davis and M. L. Occelli, “A History of the Fischer-Tropsch Synthesis in Germany 1926- 45,” *Studies in Surface Science and Catalysis*, pp. 1–28, 2007.

[70] T. Fleisch, “Associated Gas Monetization via miniGTL; Conversion of flared gas into liquid fuels & chemicals.” World Bank, a report, 2014.

[71] S. LeViness, S. R. Deshmukh, L. A. Richard, and H. J. Robota, “Velocys Fischer–Tropsch Synthesis Technology—New Advances on State-of-the-Art,” *Topics in Catalysis*, vol. 57, no. 6-9, pp. 518–525, 2014.

[72] M. van Sint Annaland, “Editorial overview: Process intensification in reaction engineering: intensified efforts to boost intensification,” *Current Opinion in Chemical Engineering*, vol. 17, 2017.

[73] M. Loewert, J. Hoffmann, P. Piermartini, M. Selinsek, R. Dittmeyer, and P. Pfeifer, “Microstructured Fischer–Tropsch Reactor Scale–up and Opportunities for Decentralized Application,” *Chemical Engineering & Technology*, no. 10, 2019.

[74] R. Dittmeyer, T. Boeltken, P. Piermartini, M. Selinsek, M. Loewert, F. Dallmann, H. Kreuder, M. Cholewa, A. Wunsch, M. Belimov, S. Farsi, and P. Pfeifer, “Micro and micro membrane reactors for advanced applications in chemical energy conversion,” *Current Opinion in Chemical Engineering*, vol. 17, pp. 108–125, 2017.

[75] P. Piermartini, T. Boeltken, M. Selinsek, and P. Pfeifer, “Influence of channel geometry on Fischer-Tropsch synthesis in microstructured reactors,” *Chemical Engineering Journal*, vol. 313, pp. 328–335, 2017.

[76] K. F. Jensen, “Microreaction engineering-is small better?,” *Chemical Engineering Science*, vol. 56, no. 2, pp. 293–303, 2001.

[77] W. Ehrfeld, V. Hessel, and H. Löwe, *Microreactors - New Technology for Modern Chemistry*, vol. 5. Weinheim: Wiley-VCH, 2001.

[78] A. Tonkovich, T. Mazanec, and K. Jarosch, “Improved Fischer-Tropsch catalysts,” *Focus on Catalysts*, vol. 2004, no. 2, p. 7, 2004.

[79] E. Klemm, H. Doering, A. Geisselmann, and S. Schirrmeister, “Microstructured reactors in heterogenous catalysis,” *Chemical Engineering & Technology*, vol. 30, no. 12, pp. 1615–1621, 2007.

[80] R. Guettel, U. Kunz, and T. Turek, “Reactors for Fischer-Tropsch synthesis,” *Chemical Engineering and Technology*, vol. 31, no. 5, pp. 746–754, 2008.

[81] N. Kockmann, *Transport phenomena in micro process engineering*. Springer Science & Business Media, 2007.

[82] R. Myrstad, S. Eri, P. Pfeifer, E. Rytter, and A. Holmen, “Fischer-Tropsch synthesis in a microstructured reactor,” *Catalysis Today*, vol. 147, pp. 301–304, 2009.

[83] J. Knochen, R. Güttel, C. Knobloch, and T. Turek, “Fischer-Tropsch synthesis in millistructured fixed-bed reactors: Experimental study and scale-up considerations,” *Chemical Engineering and Processing: Process Intensification*, vol. 49, no. 9, pp. 958–964, 2010.

[84] L. C. Almeida, F. J. Echave, O. Sanz, M. A. Centeno, G. Arzamendi, L. M. Gandía, E. F. Sousa-Aguiar, J. A. Odriozola, and M. Montes, “Fischer-Tropsch synthesis in microchannels,” *Chemical Engineering Journal*, vol. 167, no. 2-3, pp. 536–544, 2011.

[85] T. Turek, “Fischer–Tropsch-Synthese in Mikro-Festbettreaktoren,” *Dechema Fachbericht im Rahmen der Max-Buchner-Forschungsstiftung, MBFSt. Kennziffer 2820*, 2011.

[86] A. Holmen, H. J. Venvik, R. Myrstad, J. Zhu, and D. Chen, “Monolithic, microchannel and carbon nanofibers/carbon felt reactors for syngas conversion by Fischer-Tropsch synthesis,” *Catalysis Today*, vol. 216, pp. 150–157, 2013.

[87] G. Kolb, “Review: Microstructured reactors for distributed and renewable production of fuels and electrical energy,” *Chemical Engineering and Processing: Process Intensification*, vol. 65, pp. 1–44, 2013.

[88] C. Knobloch, R. Güttel, and T. Turek, “Holdup and pressure drop in micro packed-bed reactors for fischer-tropsch synthesis,” *Chemie-Ingenieur-Technik*, vol. 85, no. 4, pp. 455–460, 2013.

[89] S. Park, I. Jung, Y. Lee, K. S. Kshetrimayum, J. Na, S. Park, S. Shin, D. Ha, Y. Lee, J. Chung, C.-J. Lee, and C. Han, “Design of microchannel Fischer–Tropsch reactor using cell-coupling method: Effect of flow configurations and distribution,” *Chemical Engineering Science*, vol. 143, pp. 63–75, 2016.

[90] A. P. Steynberg, S. R. Deshmukh, and H. J. Robota, “Fischer-Tropsch catalyst deactivation in commercial microchannel reactor operation,” *Catalysis Today*, 2017.

[91] A. Wunsch, M. Mohr, and P. Pfeifer, “Intensified LOHC-Dehydrogenation Using Multi-Stage Microstructures and Pd-Based Membranes,” *Membranes*, 2018.

[92] G. Pleßmann, M. Erdmann, M. Hlusiak, and C. Breyer, “Global energy storage demand for a 100% renewable electricity supply,” *Energy Procedia*, vol. 46, pp. 22–31, 2014.

[93] L. Kotzur, P. Markewitz, M. Robinius, and D. Stolten, “Time series aggregation for energy system design: Modeling seasonal storage,” *Applied Energy*, vol. 213, pp. 123–135, 2018.

[94] A. N. Stranges, “A history of the fischer-tropsch synthesis in Germany 1926-45,” *Studies in Surface Science and Catalysis*, vol. 163, pp. 1–27, 2007.

[95] F. Trippe, M. Fröhling, F. Schultmann, R. Stahl, E. Henrich, and A. Dalai, “Comprehensive techno-economic assessment of dimethyl ether (DME) synthesis and Fischer-Tropsch synthesis as alternative process steps within biomass-to-liquid production,” *Fuel Processing Technology*, vol. 106, pp. 577–586, 2013.

[96] K. Im-orb, L. Simasatitkul, and A. Arpornwichanop, “Techno-economic analysis of the biomass gasification and Fischer-Tropsch integrated process with off-gas recirculation,” *Energy*, vol. 94, pp. 483–496, 2016.

[97] G. Schiller, “Überblick über die Verfahren der Wasserelektrolyse und Forschungsergebnisse sowie Forschungsbedarf bei der alkalischen Elektrolyse.” presented at DLR, 2012.

[98] P. Allianz, “Eckpunktepapier Für Ein Markteinführungsprogramm Von Power-To-X-Technologien - Vorschlag Für Ein Innovations-Förderprogramm Mit Fokus Auf Ptx-Anwendungen Im Mobilitätssektor.” `https://www.uniper.energy/storage/sites/default/files/2017-12/2017_okt_eckpunktepapier_power_to_x_allianz.pdf`, `astudy`, 2017. Accessed: 04.08.2020.

[99] Siemens, “Siemens Position zur Dekarbonisierung und Energiewende Deutschland.” https://assets.new.siemens.com/siemens/assets/api/uuid:2ef07c318e3d2de3450e85bc8d236c9b31 position-dekarbonisierung-energiewende-2017.pdf, a study, 2017. Accessed: 04.08.2020.

[100] G. Fuchs, B. Lunz, M. Leuthold, and D. U. Sauer, “Technology Overview on Electricity Storage Overview on the potential and on the deployment perspectives of electricity storage technologies Smart Energy for Europe Platform GmbH (SEFEP).” Smart Energy For Europe Platform GmbH (SEFEP), `http://www.sefep.eu/activities/projects-studies/120628_Technology_Overview_Electricity_Storage_SEFEP_ISEA.pdf`, a report, 2012. Accessed: 04.08.2020.

[101] M. Loewert, D. Rudolf, and P. Pfeifer, “unpublished internal study,” 2019. Institute for Micro Process Engineering (IMVT).

[102] K. F. Kalz, R. Kraehnert, M. Dvoyashkin, R. Dittmeyer, R. Gläser, U. Krewer, K. Reuter, and J. D. Grunwaldt, “Future Challenges in Heterogeneous Catalysis: Understanding Catalysts under Dynamic Reaction Conditions,” *ChemCatChem*, vol. 9, no. 1, pp. 17–29, 2017.

[103] S. Theurich, *Unsteady-state operation of a fixed-bed recycle reactor for the methanation of carbon dioxide*. Dissertation, Shaker Verlag and Shaker Verlag GmbH, Düren, 2019.

[104] S. Theurich, S. Rönsch, and R. Güttel, “Transient Flow Rate Ramps for Methanation of Carbon Dioxide in an Adiabatic Fixed–Bed Recycle Reactor,” *Energy Technology*, vol. 8, no. 3, p. 1901116, 2020.

[105] J. Bremer, K. H. G. Rätze, and K. Sundmacher, “CO_2 methanation: Optimal start-up

control of a fixed-bed reactor for power-to-gas applications," *AIChE Journal*, vol. 63, no. 1, pp. 23–31, 2017.

[106] J. Bremer and K. Sundmacher, "Operation range extension via hot-spot control for catalytic CO 2 methanation reactors," *Reaction Chemistry & Engineering*, vol. 4, no. 6, pp. 1019–1037, 2019.

[107] A. Fache and F. Marias, "Dynamic operation of fixed-bed methanation reactors: Yield control by catalyst dilution profile and magnetic induction," *Renewable Energy*, vol. 151, pp. 865–886, 2020.

[108] A. Fache, F. Marias, and B. Chaudret, "Catalytic reactors for highly exothermic reactions: Steady-state stability enhancement by magnetic induction," *Chemical Engineering Journal*, vol. 390, p. 124531, 2020.

[109] A. Fache, F. Marias, V. Guerré, and S. Palmade, "Optimization of fixed-bed methanation reactors: Safe and efficient operation under transient and steady-state conditions," *Chemical Engineering Science*, vol. 192, pp. 1124–1137, 2018.

[110] A. Fache, F. Marias, V. Guerré, and S. Palmade, "Intermittent Operation of Fixed-Bed Methanation Reactors: A Simple Relation Between Start-Up Time and Idle State Duration," *Waste and Biomass Valorization*, vol. 11, no. 2, pp. 447–463, 2020.

[111] M. I. González and G. Schaub, "Fischer-Tropsch synthesis with H2/CO2-catalyst behavior under transient conditions," *Chemie-Ingenieur-Technik*, vol. 87, no. 6, pp. 848–854, 2015.

[112] R. Güttel, "Study of Unsteady-State Operation of Methanation by Modeling and Simulation," *Chemical Engineering and Technology*, vol. 83, no. 11, 2013.

[113] M. Iglesias Gonzalez, *Gaseous Hydrocarbon Synfuels from H2/CO2 based on Renewable Electricity Kinetics, Selectivity and Fundamentals of Fixed-Bed Reactor Design for Flexible Operation*. Dissertation, Verlag Dr. Hut, München, 2016.

[114] B. Kreitz, J. Friedland, R. Güttel, G. D. Wehinger, and T. Turek, "Dynamic Methanation of CO_2 – Effect of Concentration Forcing," *Chemie Ingenieur Technik*, vol. 91, no. 5, pp. 576–582, 2019.

[115] B. Kreitz, G. D. Wehinger, and T. Turek, “Dynamic simulation of the CO_2 methanation in a micro-structured fixed-bed reactor,” *Chemical Engineering Science*, vol. 195, pp. 541–552, 2019.

[116] G. Tauer, C. Kern, and A. Jess, “Transient Effects during Dynamic Operation of a Wall–Cooled Fixed–Bed Reactor for CO_2 Methanation,” *Chemical Engineering and Technology*, vol. 42, no. 11, pp. 2401–2409, 2019.

[117] H. Eilers, M. I. González, and G. Schaub, “Lab-scale experimental studies of Fischer-Tropsch kinetics in a three-phase slurry reactor under transient reaction conditions,” *Catalysis Today*, vol. 275, pp. 164–171, 2016.

[118] P. Silveston, R. R. Hudgins, and A. Renken, “Periodic operation of catalytic reactors-introduction and overview,” *Catalysis Today*, vol. 25, no. 2, pp. 91–112, 1995.

[119] A. A. Adesina, P. L. Silveston, and R. R. Hudgins, “A Comparison of Forced Feed Cycling of the Fischer-Tropsch Synthesis Over Iron and Cobalt Catalysts,” *Studies in Surface Science and Catalysis*, vol. 19, 1984.

[120] M. Loewert and P. Pfeifer, “Dynamically Operated Fischer-Tropsch Synthesis in PtL-Part 1: System Response on Intermittent Feed,” *ChemEngineering*, vol. 4, no. 2, 2020.

[121] M. Loewert, M. Riedinger, and P. Pfeifer, “Dynamically Operated Fischer-Tropsch Synthesis in PtL-Part 2: Coping with Real PV Profiles,” *ChemEngineering*, vol. 4, no. 2, 2020.

[122] A. P. Vogel, B. Van Dyk, and A. M. Saib, “GTL using efficient cobalt Fischer-Tropsch catalysts,” *Catalysis Today*, vol. 259, pp. 323–330, 2015.

[123] E. Rytter and A. Holmen, “Deactivation and regeneration of commercial type Fischer-Tropsch Co-catalysts - A mini-review,” *Catalysts*, vol. 5, no. 2, pp. 478–499, 2015.

[124] N. E. Tsakoumis, M. Rønning, Ø. Borg, E. Rytter, and A. Holmen, “Deactivation of cobalt based Fischer-Tropsch catalysts: A review,” *Catalysis Today*, vol. 154, no. 3-4, pp. 162–182, 2010.

[125] A. M. Saib, D. J. Moodley, I. M. Ciobîc, M. M. Hauman, B. H. Sigwebela, C. J. Weststrate, J. W. Niemantsverdriet, and J. Van De Loosdrecht, “Fundamental understanding of

deactivation and regeneration of cobalt Fischer-Tropsch synthesis catalysts," *Catalysis Today*, vol. 154, no. 3-4, pp. 271–282, 2010.

[126] V. V. Ordomsky, A. Carvalho, B. Legras, S. Paul, M. Virginie, V. L. Sushkevich, and A. Y. Khodakov, "Effects of co-feeding with nitrogen-containing compounds on the performance of supported cobalt and iron catalysts in Fischer–Tropsch synthesis," *Catalysis Today*, 2016.

[127] W. Behrmann, S. Hsia, S. Leviness, C. Mart, and D. Neskora, "Slurry hydrocarbon synthesis process with increased catalyst life," November 12 1998. WO Patent App. PCT/US1998/008,687 `https://encrypted.google.com/patents/WO1998050487A1?cl=zh`.

[128] J. Barrientos, V. Montes, M. Boutonnet, and S. Järås, "Further insights into the effect of sulfur on the activity and selectivity of cobalt-based Fischer–Tropsch catalysts," *Catalysis Today*, 2015.

[129] R. J. Madon and H. Seaw, "Effect of Sulfur on the Fischer-Tropsch Synthesis," *Catalysis Reviews*, vol. 15, no. 1, pp. 69–106, 1977.

[130] Ø. Borg, N. Hammer, B. C. Enger, R. Myrstad, O. A. Lindvåg, S. Eri, T. H. Skagseth, and E. Rytter, "Effect of biomass-derived synthesis gas impurity elements on cobalt Fischer-Tropsch catalyst performance including in situ sulphur and nitrogen addition," *Journal of Catalysis*, vol. 279, no. 1, pp. 163–173, 2011.

[131] C. M. Balonek, A. H. Lillebø, S. Rane, E. Rytter, L. D. Schmidt, and A. Holmen, "Effect of alkali metal impurities on Co-Re catalysts for Fischer–Tropsch synthesis from biomass-derived syngas," *Catalysis Letters*, vol. 138, no. 1-2, pp. 8–13, 2010.

[132] S. Storsæter, Borg, E. A. Blekkan, and A. Holmen, "Study of the effect of water on Fischer-Tropsch synthesis over supported cobalt catalysts," *Journal of Catalysis*, vol. 231, no. 2, pp. 405–419, 2005.

[133] A. Hilmen, D. Schanke, K. Hanssen, and A. Holmen, "Study of the effect of water on alumina supported cobalt Fischer–Tropsch catalysts," *Applied Catalysis A: General*, vol. 186, pp. 169–188, oct 1999.

[134] G. Jacobs, T. K. Das, P. M. Patterson, J. Li, L. Sanchez, and B. H. Davis, “Fischer–Tropsch synthesis XAFS,” *Applied Catalysis A: General*, vol. 247, no. 2, pp. 335–343, 2003.

[135] P. van Berge, J. van de Loosdrecht, S. Barradas, and A. van der Kraan, “Oxidation of cobalt based Fischer–Tropsch catalysts as a deactivation mechanism,” *Catalysis Today*, vol. 58, no. 4, pp. 321–334, 2000.

[136] J. van de Loosdrecht, B. Balzhinimaev, J. A. Dalmon, J. W. Niemantsverdriet, S. V. Tsybulya, A. M. Saib, P. J. van Berge, and J. L. Visagie, “Cobalt Fischer-Tropsch synthesis: Deactivation by oxidation?,” *Catalysis Today*, vol. 123, no. 1-4, pp. 293–302, 2007.

[137] E. Van Steen, M. Claeys, M. E. Dry, J. Van De Loosdrecht, E. L. Viljoen, and J. L. Visagie, “Stability of nanocrystals: Thermodynamic analysis of oxidation and re-reduction of cobalt in water/hydrogen mixtures,” *Journal of Physical Chemistry B*, vol. 109, no. 8, pp. 3575–3577, 2005.

[138] D. Kistamurthy, A. M. Saib, D. J. Moodley, J. W. Niemantsverdriet, and C. J. Weststrate, “Ostwald ripening on a planar Co/Silica catalyst exposed to model Fischer-Tropsch synthesis conditions,” *Journal of Catalysis*, vol. 328, pp. 123–129, 2015.

[139] M. D. Argyle, T. S. Frost, and C. H. Bartholomew, “Cobalt fischer-tropsch catalyst deactivation modeled using generalized power law expressions,” *Topics in Catalysis*, vol. 57, no. 6-9, pp. 415–429, 2014.

[140] J. A. Moulijn, A. E. Van Diepen, and F. Kapteijn, “Catalyst deactivation: Is it predictable? What to do?,” *Applied Catalysis A: General*, vol. 212, no. 1-2, pp. 3–16, 2001.

[141] M. Claeys, M. E. Dry, E. Van Steen, P. J. Van Berge, S. Booyens, R. Crous, P. Van Helden, J. Labuschagne, D. J. Moodley, and A. M. Saib, “Impact of process conditions on the sintering behavior of an alumina-supported cobalt Fischer-Tropsch catalyst studied with an in situ magnetometer,” *ACS Catalysis*, vol. 5, no. 2, pp. 841–852, 2015.

[142] G.-Z. Bian, N. Fujishita, T. Mochizuki, W.-S. Ning, and M. Yamada, “Investigations on the structural changes of two co/sio2 catalysts by performing fischer–tropsch synthesis,” *Applied Catalysis A: General*, vol. 252, no. 2, pp. 251 – 260, 2003.

[143] A. Nakhaei Pour, S. A. Taheri, S. Anahid, B. Hatami, and A. Tavasoli, “Deactivation stud-

ies of Co/CNTs catalyst in Fischer-Tropsch synthesis," *Journal of Natural Gas Science and Engineering*, vol. 18, pp. 104–111, 2014.

[144] S. Karimi, A. Tavasoli, Y. Mortazavi, and A. Karimi, "Enhancement of cobalt catalyst stability in Fischer–Tropsch synthesis using graphene nanosheets as catalyst support," *Chemical Engineering Research and Design*, vol. 104, pp. 713–722, 2015.

[145] K. Keyvanloo, M. J. Fisher, W. C. Hecker, R. J. Lancee, G. Jacobs, and C. H. Bartholomew, "Kinetics of deactivation by carbon of a cobalt Fischer-Tropsch catalyst: Effects of CO and H2 partial pressures," *Journal of Catalysis*, vol. 327, pp. 33–47, 2015.

[146] A. Holmen, H. J. Venvik, R. Myrstad, J. Zhu, and D. Chen, "Monolithic, microchannel and carbon nanofibers/carbon felt reactors for syngas conversion by Fischer-Tropsch synthesis," *Catalysis Today*, vol. 216, pp. 150–157, 2013.

[147] M. Claeys, M. E. Dry, E. Van Steen, E. Du Plessis, P. J. Van Berge, A. M. Saib, and D. J. Moodley, "In situ magnetometer study on the formation and stability of cobalt carbide in Fischer-Tropsch synthesis," *Journal of Catalysis*, vol. 318, pp. 193–202, 2014.

[148] N. Balakrishnan, B. Joseph, and V. R. Bhethanabotla, "Effect of Pt and Ru promoters on deactivation of Co catalysts by C deposition during Fischer-Tropsch synthesis: A DFT study," *Applied Catalysis A: General*, vol. 462-463, pp. 107–115, 2013.

[149] E. de Smit and B. M. Weckhuysen, "The renaissance of iron-based fischer-tropsch synthesis: on the multifaceted catalyst deactivation behaviour," *Chemical Society Reviews*, vol. 37, pp. 2758–2781, 2008.

[150] E. Iglesia, S. L. Soled, R. A. Fiato, and G. H. Via, "Dispersion, support, and bimetallic effects in fischer-tropsch synthesis on cobalt catalysts," in *Natural Gas Conversion II* (H. Curry-Hyde and R. Howe, eds.), vol. 81 of *Studies in Surface Science and Catalysis*, pp. 433 – 442, Elsevier, 1994.

[151] R. M. Bowman and C. H. Bartholomew, "Deactivation by carbon of Ru/Al_2O_3 during CO hydrogenation," *Applied Catalysis*, vol. 7, no. 2, pp. 179 – 187, 1983.

[152] C. Sun, *Direct syngas-to-fuel: integration of Fischer-Tropsch synthesis and hydrocrack-*

ing in micro-structured reactors. Dissertation, Karlsruher Institut für Technologie, 15.12.2017.

[153] C. Sun, T. Zhan, P. Pfeifer, and R. Dittmeyer, “Influence of Fischer-Tropsch synthesis (FTS) and hydrocracking (HC) conditions on the product distribution of an integrated FTS-HC process,” *Chemical Engineering Journal*, vol. 310, pp. 272–281, 2017.

[154] D. Kistamurthy, A. M. Saib, D. J. Moodley, H. Preston, I. M. Ciobîca, W. J. van Rensburg, J. W. Niemantsverdriet, and C. J. Weststrate, “The role of carboxylic acid in cobalt Fischer-Tropsch synthesis catalyst deactivation,” *Catalysis Today*, 2015.

[155] E. Iglesia, “Bimetallic Synergy in Cobalt Ruthenium Fischer-Tropsch Synthesis Catalysts,” *Journal of Catalysis*, vol. 143, no. 2, pp. 345–368, 1993.

[156] K. B. Arcuri and S. C. LeViness, “The Regeneration of Hydrocarbon Synthesis Catalyst - A Partial Review of the Related Art Published during 1930 to 1952.” Presented at AIChE Spring National Meeting, 2003.

[157] J. Van de Loosdrecht and M. Saib, “Wipo patent application wo/2008/139407,” 2008. WO Patent WO/2008/139407 `http://www.freepatentsonline.com/WO2008139407.html`.

[158] C. M. Lok, S. Bailey, and G. Gray, “Method for the production of cobalt catalysts supported on silicon dioxide and their use,” 2003. US Patent 6,534,436.

[159] E. Iglesia, S. L. Soled, and R. A. Fiato, “Cobalt-ruthenium catalysts for fischer-tropsch synthesis and process for their preparation,” April 19 1988. US Patent 4,738,948.

[160] M. Daage, R. Koveal, and M. Chang, “Catalyst regeneration,” July 31 2003. US Patent App. 10/059,926 `http://www.google.ch/patents/US20030144366`.

[161] H. Ono, Y. Nagayasu, and K. Hayasaka, “Method for manufacturing a regenerated fischer-tropsch synthesis catalyst, and hydrocarbon manufacturing method,” Ocotber 13 2013. US Patent 8,557,725 `https://www.google.com/patents/US8557725`.

[162] H. A. Wright, A. P. Raje, and R. L. Espinoza, “Pressure swing catalyst regeneration procedure for fischer-tropsch catalyst,” December 26 2002. US Patent 20,020,198,096.

[163] J. Huang, K. Agee, K. Arcuri, and P. Schubert, "Process for regenerating a slurry fischer-tropsch catalyst," November 2 2004. US Patent 6,812,179 `https://www.google.com/patents/US6812179`.

[164] M. Wolf, B. K. Mutuma, N. J. Coville, N. Fischer, and M. Claeys, "Role of CO in the Water-Induced Formation of Cobalt Oxide in a High Conversion Fischer–Tropsch Environment," *ACS Catalysis*, pp. 3985–3989, 2018.

[165] A. Chakrabarti, M. E. Ford, D. Gregory, R. Hu, C. J. Keturakis, S. Lwin, Y. Tang, Z. Yang, M. Zhu, M. A. Bañares, and I. E. Wachs, "A decade+ of operando spectroscopy studies," *Catalysis Today*, vol. 283, pp. 27–53, 2017.

[166] M. A. Bañares, M. O. Guerrero-Pérez, J. L. G. Fierro, and G. G. Cortez, "Raman spectroscopy during catalytic operations with on-line activity measurement (operando spectroscopy): a method for understanding the active centres of cations supported on porous materials," *Journal of Material Chemistry*, vol. 12, pp. 3337–3342, 2002.

[167] M. O. Guerrero-Pérez and M. A. Bañares, "Operando Raman study of alumina-supported Sb-V-O catalyst during propane ammoxidation to acrylonitrile with on-line activity measurement," *Chemical Communications*, pp. 1292–1293, 2002.

[168] B. Clausen, G. Steffensen, B. Fabius, J. Villadsen, R. Feidenhans, and H. Topsœ, "In situ cell for combined XRD and on-line catalysis tests: Studies of Cu-based water gas shift and methanol catalysts," *Journal of Catalysis*, vol. 132, no. 2, pp. 524 – 535, 1991.

[169] S. Woo and C. Hill, "Raman study of dicobalt octacarbonyl covalently attached to a phosphinated silica," *Journal of Molecular Catalysis*, vol. 15, no. 3, pp. 309 – 325, 1982.

[170] J. W. Ward, "The nature of active sites on zeolites: V. In situ spectroscopic observations of hydrogen Y zeolite during cumene cracking," *Journal of Catalysis*, vol. 11, no. 3, pp. 259 – 273, 1968.

[171] G. Jacobs, W. Ma, P. Gao, B. Todic, T. Bhatelia, D. B. Bukur, and B. H. Davis, "The application of synchrotron methods in characterizing iron and cobalt Fischer-Tropsch synthesis catalysts," *Catalysis Today*, vol. 214, pp. 100–139, 2013.

[172] J. Paterson, M. Peacock, E. Ferguson, R. Purves, and M. Ojeda, "In Situ Diffrac-

tion of Fischer–Tropsch Catalysts: Cobalt Reduction and Carbide Formation," *ChemCatChem*, vol. 9, no. 18, pp. 3463–3469, 2017.

[173] N. Fischer, B. Clapham, T. Feltes, E. Van Steen, and M. Claeys, "Size-dependent phase transformation of catalytically active nanoparticles captured in situ," *Angewandte Chemie - International Edition*, vol. 53, no. 5, pp. 1342–1345, 2014.

[174] E. de Smit, F. Cinquini, A. M. Beale, O. V. Safonova, W. van Beek, P. Sautet, B. M. Weckhuysen, N. Supe, R. J. Horowitz, and F.-G. Cedex, "Stability and Reactivity of E-X-θ Iron Carbide Catalyst Phases in Fischer - Tropsch Synthesis: Controlling μC," *Journal of the American Chemical Society*, no. 5, pp. 14928–14941, 2010.

[175] M. Rønning, N. E. Tsakoumis, A. Voronov, R. E. Johnsen, P. Norby, W. Van Beek, Ø. Borg, E. Rytter, and A. Holmen, "Combined XRD and XANES studies of a Re-promoted Co-Al_2O_3 catalyst at Fischer-Tropsch synthesis conditions," *Catalysis Today*, vol. 155, no. 3-4, pp. 289–295, 2010.

[176] J. D. Grunwaldt and B. S. Clausen, "Combining XRD and EXAFS with on-line catalytic studies for in situ characterization of catalysts," *Topics in Catalysis*, vol. 18, no. 1-2, pp. 37–43, 2002.

[177] A. Rochet, V. Moizan, C. Pichon, F. Diehl, A. Berliet, and V. Briois, "In situ and operando structural characterisation of a Fischer-Tropsch supported cobalt catalyst," *Catalysis Today*, vol. 171, no. 1, pp. 186–191, 2011.

[178] J.-D. Grunwaldt, M. Caravati, and A. Baiker, "In situ extended X-ray absorption fine structure study during selective alcohol oxidation over Pd/Al_2O_3 in supercritical carbon dioxide," *Journal of Physical Chemistry B*, vol. 110, no. 20, pp. 9916–9922, 2006.

[179] M. Rohr, M. Günther, F. Jutz, J.-D. Grunwaldt, H. Emerich, W. van beek, and A. Baiker, "Evaluation of strategies for the immobilization of bidentate ruthenium-phosphine complexes used for the reductive amination of carbon," *Applied Catalysis A: General*, vol. 296, pp. 238–250, 12 2005.

[180] Ø. Borg, S. Eri, E. A. Blekkan, S. Storsæter, H. Wigum, E. Rytter, and A. Holmen,

"Fischer-Tropsch synthesis over γ-alumina-supported cobalt catalysts: Effect of support variables," *Brennstoff Chemie*, vol. 248, no. 1, pp. 89–100, 2007.

[181] P. Pfeifer, P. Piermartini, and A. Wenka, "Mikrostrukturreaktor zur durchführung exothermer, heterogen katalysierter reaktionen mit effizienter verdampfungskühlung," 2015. Patent number DE102015111614A1 `https://patents.google.com/patent/DE102015111614A1/nl`.

[182] A. de Klerk and E. Furimsky, *Catalysis in the Refining of Fischer-Tropsch Syncrude*. Cambridge: Royal Society of Chemistry, 2010.

[183] B. H. Davis, ed., *Fischer-Tropsch synthesis, catalysts and catalysis*, vol. 163 of *Studies in Surface Science and Catalysis*. Amsterdam, Netherlands: Elsevier, 1. ed., 2007.

[184] C. G. Visconti and M. Mascellaro, "Calculating the product yields and the vapor-liquid equilibrium in the low-temperature Fischer–Tropsch synthesis," *Catalysis Today*, vol. 214, pp. 61–73, 2013.

[185] G. P. Van Der Laan and A. Beenackers, "Kinetics and selectivity of the Fischer–Tropsch synthesis: a literature review," *Catalysis Reviews*, vol. 41, no. 3-4, pp. 255–318, 1999.

[186] M. J. Tijmensen, A. P. Faaij, C. N. Hamelinck, and M. R. Van Hardeveld, "Exploration of the possibilities for production of Fischer Tropsch liquids and power via biomass gasification," *Biomass and Bioenergy*, vol. 23, no. 2, pp. 129–152, 2002.

[187] M. A. Agee, "Convert natural gas into clean transportation fuels," *Fuel Technology amd Management*, vol. 7, no. 2, 1997.

[188] J. van de Loosdrecht, B. Balzhinimaev, J.-A. Dalmon, J. W. Niemantsverdriet, S. V. Tsybulya, a.M. Saib, P. J. van Berge, and J. L. Visagie, "Cobalt Fischer-Tropsch synthesis: Deactivation by oxidation?," *Catalysis Today*, vol. 123, no. 1-4, pp. 293–302, 2007.

[189] C. G. Visconti, E. Tronconi, L. Lietti, P. Forzatti, S. Rossini, and R. Zennaro, "Detailed Kinetics of the Fischer–Tropsch Synthesis on Cobalt Catalysts Based on H-Assisted CO Activation," *Topics in Catalysis*, vol. 54, no. 13, p. 786, 2011.

[190] A. A. Adesina, "Hydrocarbon synthesis via Fischer–Tropsch reaction: Travails and triumphs," *Applied Catalysis A: General*, vol. 138, no. 2, pp. 345–367, 1996.

[191] J. T. Scanlon and D. E. Willis, “Calculation of Flame Ionization Detector Relative Response Factors Using the Effective Carbon Number Concept,” *Journal of Chromatographic Science*, vol. 23, pp. 333–340, 1985.

[192] Restek Corporation, “Hydrocarbon ranges of polywax reference standards.” `http://blog.restek.com/?p=10846`, 2015. Accessed: 06.10.2015.

[193] G. E. Totten, Westbrook, and R. J. Shah, “Fuels and lubricants handbook: technology, properties, performance, and testing,” *Training*, vol. 2007, pp. 08–21, 2003.

[194] F. Dadgar, H. J. Venvik, and P. Pfeifer, “Application of hot-wire anemometry for experimental investigation of flow distribution in micro-packed bed reactors for synthesis gas conversion,” *Chemical Engineering Science*, vol. 177, pp. 110–121, 2018.

[195] R. Myrstad, S. Eri, P. Pfeifer, E. Rytter, and A. Holmen, “Fischer–Tropsch synthesis in a microstructured reactor,” *Catalysis Today*, vol. 147, pp. S301–S304, 2009.

[196] Schlögl, Robert and Abanades, Carlos and Aresta, Michele and Azapagic, Adisa and Blekkan, Edd Anders and Cantat, Thibault and Centi, Gabriele and Duic, Neven and El Khamlichi, Aïcha, G. Hutchings, M. Mazzotti, U. Olsbye, and H. Mikulcic, “Novel carbon capture and utilisation technologies - Research and climate aspects.” SAPEA - Science Advice for Policy by European Academics `https://www.sapea.info/wp-content/uploads/CCU-report-May2018-3.pdf`, a study, 2018.

[197] K. Vaillancourt, O. Bahn, P. O. Roy, and V. Patreau, “Is there a future for new hydrocarbon projects in a decarbonizing energy system? A case study for Quebec (Canada),” *Applied Energy*, vol. 218, pp. 114–130, 2018.

[198] I. Ridjan, B. V. Mathiesen, and D. Connolly, “Terminology used for renewable liquid and gaseous fuels based on the conversion of electricity: A review,” *Journal of Cleaner Production*, vol. 112, pp. 3709–3720, 2016.

[199] W. Li, H. Wang, X. Jiang, J. Zhu, Z. Liu, X. Guo, and C. Song, “A short review of recent advances in CO_2 hydrogenation to hydrocarbons over heterogeneous catalysts,” *RSC Advances*, vol. 8, no. 14, pp. 7651–7669, 2018.

[200] M. Reuß, T. Grube, M. Robinius, P. Preuster, P. Wasserscheid, and D. Stolten, “Seasonal

storage and alternative carriers: A flexible hydrogen supply chain model," *Applied Energy*, vol. 200, pp. 290–302, 2017.

[201] K. S. Kshetrimayum, I. Jung, J. Na, S. Park, Y. Lee, S. Park, C. J. Lee, and C. Han, "CFD Simulation of Microchannel Reactor Block for Fischer-Tropsch Synthesis: Effect of Coolant Type and Wall Boiling Condition on Reactor Temperature," *Industrial and Engineering Chemistry Research*, vol. 55, no. 3, pp. 543–554, 2016.

[202] L. C. Almeida, O. Sanz, J. D'Olhaberriague, S. Yunes, and M. Montes, "Microchannel reactor for Fischer-Tropsch synthesis: Adaptation of a commercial unit for testing microchannel blocks," *Fuel*, vol. 110, pp. 171–177, 2013.

[203] G. Arzamendi, P. M. Diéguez, M. Montes, J. A. Odriozola, E. F. Sousa-Aguiar, and L. M. Gandía, "Computational fluid dynamics study of heat transfer in a microchannel reactor for low-temperature Fischer-Tropsch synthesis," *Chemical Engineering Journal*, vol. 160, no. 3, pp. 915–922, 2010.

[204] Karlsruhe Institute of Technology (KIT), "EnergyLab 2.0." `https://www.elab2.kit.edu/`. Accessed: 25.03.2019.

[205] F. Monaco, A. Lanzini, and M. Santarelli, "Making synthetic fuels for the road transportation sector via solid oxide electrolysis and catalytic upgrade using recovered carbon dioxide and residual biomass," *Journal of Cleaner Production*, vol. 170, pp. 160–173, 2018.

[206] "PowerFuel - Fuels for Climate-neutral Airplanes." `https://www.kit.edu/kit/english/pi_2018_165_fuels-for-climate-neutral-airplanes.php`. Accessed: 09.05.2019.

[207] H. Topsøe, "Developments in operando studies and in situ characterization of heterogeneous catalysts," *Brennstoff Chemie*, vol. 216, no. 1-2, pp. 155–164, 2003.

[208] Y. Zhang, D. Fu, X. Xu, Y. Sheng, J. Xu, and Y. F. Han, "Application of operando spectroscopy on catalytic reactions," *Current Opinion in Chemical Engineering*, vol. 12, pp. 1–7, 2016.

[209] C. Sun, *Direct syngas-to-fuel: integration of Fischer-Tropsch synthesis and hydrocrack-*

ing in micro-structured reactors. Dissertation, Karlsruhe Institute of Technology (KIT), Institute for Micro Process Engineering (IMVT), Karlsruhe, 2018.

[210] S. H. Kwack, M. J. Park, J. W. Bae, K. S. Ha, and K. W. Jun, “Development of a kinetic model of the Fischer-Tropsch synthesis reaction with a cobalt-based catalyst,” *Reaction Kinetics, Mechanisms and Catalysis*, vol. 104, no. 2, pp. 483–502, 2011.

[211] H. Eilers, *Flexibler Betrieb der Fischer-Tropsch-Synthese - Katalysator- und Reaktorverhalten mit Co in der 3-Phasen-Blasensäule*. Dissertation, Karlsruhe Institute of Technology (KIT), Engler-Bunte Institute, Fuel Technology, Karlsruhe, 2018.

[212] H. Pichler and H. Schulz, “Neuere Erkenntnisse auf dem Gebiet der Synthese von Kohlenwasserstoffen aus CO und H_2,” *Chemie Ingenieur Technik*, vol. 42, no. 18, pp. 1162–1174, 1970.

[213] R. C. Brady and R. Pettit, “Mechanism of the Fischer-Tropsch reaction. The chain propagation step,” *Journal of the American Chemical Society*, vol. 103, no. 5, pp. 1287–1289, 1981.

[214] W. Chen, I. A. Filot, R. Pestman, and E. J. Hensen, “Mechanism of Cobalt-Catalyzed CO Hydrogenation: 2. Fischer-Tropsch Synthesis,” *ACS Catalysis*, vol. 7, no. 12, pp. 8061–8071, 2017.

[215] M. Zhuo, K. F. Tan, A. Borgna, and M. Saeys, “Density Functional Theory Study of the CO Insertion Mechanism for Fischer—Tropsch Synthesis over Co Catalysts,” *The Journal of Physical Chemistry C*, vol. 113, no. 19, pp. 8357–8365, 2009.

[216] J. Schweicher, A. Bundhoo, and N. Kruse, “Hydrocarbon chain lengthening in catalytic CO hydrogenation: evidence for a CO-insertion mechanism,” *Journal of the American Chemical Society*, vol. 134, no. 39, pp. 16135–16138, 2012.

[217] P. H. Emmet, J. T. Kummer, H. H. Podgurski, and W. B. Spencer, “Mechanism Studies of the Fischer-Tropsch Synthesis. The Addition of Radioactive Alcohol,” *Journal of the American Chemical Society*, pp. 564–569, 1951.

[218] P. H. Emmett and J. T. Kummer, “Fischer-Tropsch Synthesis Mechanism Studies. The

Addition of Radioactive Alcohols to the Synthesis Gas," *Journal of the American Chemical Society*, pp. 5177–5183, 1953.

[219] D. E. Mears, "Diagnostic criteria for heat transport limitations in fixed bed reactors," *Journal of Catalysis*, vol. 20, no. 2, pp. 127–131, 1971.

[220] D. E. Mears, "Tests for Transport Limitations in Experimental Catalytic Reactors," *Industrial & Engineering Chemistry Process Design and Development*, vol. 10, no. 4, pp. 541–547, 1971.

[221] H. Hofmann, *Chemical Reactor Analysis and Design*, vol. 63. New York - Chichester: John Wiley & Sons, second ed., 1991.

[222] D.-Y. Peng and D. B. Robinson, "Two and three phase equilibrium calculations for systems containing water," *The Canadian Journal of Chemical Engineering*, vol. 54, no. 5, pp. 595–599, 1976.

[223] J. Gmehling, B. Kolbe, M. Kleiber, and J. R. Rarey, *Chemical thermodynamics for process simulation*. Weinheim: Wiley-VCH-Verl., 2012.

[224] B. Schmid, A. Schedemann, and J. Gmehling, "Extension of the VTPR Group Contribution Equation of State: Group Interaction Parameters for Additional 192 Group Combinations and Typical Results," *Industrial & Engineering Chemistry Research*, vol. 53, no. 8, pp. 3393–3405, 2014.

[225] J. Ahlers and J. Gmehling, "Development of an universal group contribution equation of state I. Prediction of liquid densities for pure compounds with a volume translated Peng-Robinson equation of state," *Fluid Phase Equilibria*, vol. 191, 2001.

[226] J. Ahlers and J. Gmehling, "Development of a Universal Group Contribution Equation of State. 2. Prediction of Vapor—Liquid Equilibria for Asymmetric Systems: Industrial & Engineering Chemistry Research," *Industrial & Engineering Chemistry Research*, vol. 41, no. 14, pp. 3489–3498, 2002.

[227] J. Ahlers and J. Gmehling, "Development of a Universal Group Contribution Equation of State III. Prediction of Vapor—Liquid Equilibria, Excess Enthalpies, and Activity Coefficients at Infinite Dilution with the VTPR Model: Industrial & Engineering Chemistry

Research," *Industrial & Engineering Chemistry Research*, vol. 41, no. 23, pp. 5890–5899, 2002.

[228] R. D. Gray, N. H. Rent, and D. Zudkevitch, "A modified Redlich-Kwong equation of state," *AIChE Journal*, vol. 16, no. 6, pp. 991–998, 1970.

[229] H. H. Rachford and J. D. Rice, "Procedure for Use of Electronic Digital Computers in Calculating Flash Vaporization Hydrocarbon Equilibrium," *Journal of Petroleum Technology*, vol. 4, no. 10, pp. 19–3, 1952.

[230] S. Mokhatab, "Three-Phase Flash Calculation for Hydrocarbon Systems Containing Water," *Theoretical Foundations of Chemical Engineering*, vol. 37, no. 3, pp. 291–294, 2003.

[231] O. Levenspiel, *Tracer technology: Modeling the flow of fluids*, vol. v.96 of *Fluid mechanics and its applications*. New York, NY: Springer and Springer New York and Imprint: Springer, 2012.

[232] C. Sun, Z. Luo, A. Choudhary, P. Pfeifer, and R. Dittmeyer, "Influence of the Condensable Hydrocarbons on an Integrated Fischer-Tropsch Synthesis and Hydrocracking Process: Simulation and Experimental Validation," *Industrial and Engineering Chemistry Research*, vol. 56, no. 45, pp. 13075–13085, 2017.

[233] E. Rytter and A. Holmen, "Deactivation and regeneration of commercial type Fischer-Tropsch Co-catalysts - A mini-review," *Catalysts*, vol. 5, no. 2, pp. 478–499, 2015.

[234] N. E. Tsakoumis, M. Rønning, Ø. Borg, E. Rytter, and A. Holmen, "Deactivation of cobalt based Fischer-Tropsch catalysts: A review," *Catalysis Today*, vol. 154, no. 3-4, pp. 162–182, 2010.

[235] N. E. Tsakoumis, A. Voronov, M. Rønning, W. van Beek, Ø. Borg, E. Rytter, and A. Holmen, "Fischer-Tropsch synthesis: An XAS/XRPD combined in situ study from catalyst activation to deactivation," *Journal of Catalysis*, vol. 291, pp. 138–148, jul 2012.

[236] D. E. Doronkin, H. Lichtenberg, and J.-D. Grunwaldt, *Cell Designs for In Situ and Operando Studies*, ch. 3, pp. 75–89. Cham: Springer International Publishing, 2017.

[237] M. Decker, F. Schorn, R. C. Samsun, R. Peters, and D. Stolten, "Off-Grid Power-to-Fuel

Systems for a Merket Launch Scenario - A Techno-Economic Assessment," *Applied Energy*, vol. 250, pp. 1099 – 1109, 2019.

[238] J. Guilera, T. Andreu, N. Basset, T. Boeltken, F. Timm, I. Mallol, and J. R. Morante, "Synthetic natural gas production from biogas in a waste water treatment plant," *Renewable Energy*, vol. 146, pp. 1301–1308, 2020.

[239] N. E. Tsakoumis, J. C. Walmsley, M. Rønning, W. van Beek, E. Rytter, and A. Holmen, "Evaluation of Reoxidation Thresholds for γ-Al_2O_3-Supported Cobalt Catalysts under Fischer-Tropsch Synthesis Conditions," *Journal of the American Chemical Society*, vol. 139, no. 10, pp. 3706–3715, 2017. PMID: 28191967.

[240] P. J. van Berge and R. C. Everson, "Cobalt as an alternative Fischer-Tropsch catalyst to iron for the production of middle distillates," *Studies in Surface Science and Catalysis*, vol. 107, pp. 207–212, 1997.

[241] A. Sadezky, H. Muckenhuber, H. Grothe, R. Niessner, and U. Pöschl, "Raman Microspectroscopy of Soot and Related Carbonaceous Materials: Spectral Analysis and Structural Information," *Carbon*, vol. 43, pp. 1731–1742, 2005.

[242] K. H. Cats, J. C. Andrews, O. Stéphan, K. March, C. Karunakaran, F. Meirer, F. M. F. de Groot, and B. M. Weckhuysen, "Active phase distribution changes within a catalyst particle during Fischer-Tropsch synthesis as revealed by multi-scale microscopy," *Catalysis Science and Technology*, vol. 6, pp. 4438–4449, 2016.

[243] J. Llorca, N. Homs, J. Sales, and P. R. de la Piscina, "Efficient Production of Hydrogen over Supported Cobalt Catalysts from Ethanol Steam Reforming," *Journal of Catalysis*, vol. 209, no. 2, pp. 306 – 317, 2002.

[244] F. Tuinstra and J. L. Koenig, "Raman Spectrum of Graphite," *The Journal of Chemical Physics*, vol. 53, no. 3, pp. 1126–1130, 1970.

[245] D. J. Moodley, J. van de Loosdrecht, A. M. Saib, M. J. Overett, A. K. Datye, and J. W. Niemantsverdriet, "Carbon deposition as a deactivation mechanism of cobalt-based Fischer–Tropsch synthesis catalysts under realistic conditions," *Applied Catalysis A: General*, vol. 354, no. 1-2, pp. 102–110, 2009.

PAPER I

MICROSTRUCTURED FISCHER-TROPSCH REACTOR SCALE-UP AND OPPORTUNITIES FOR DECENTRALIZED APPLICATION

Published in Chemical Engineering & Technology, 10.07.2019

`https://doi.org/10.1002/ceat.201900136`

Paper I

Chemical & Engineering Technology Research Article 2202

Marcel Loewert[1,*]
Julian Hoffmann[2]
Paolo Piermartini[2]
Manuel Selinsek[2]
Roland Dittmeyer[1]
Peter Pfeifer[1,2]

Microstructured Fischer-Tropsch Reactor Scale-up and Opportunities for Decentralized Application

Current projects focusing on the energy transition in traffic will rely on a high-level technology mix for their commissioning. One of those technologies is the Fischer-Tropsch synthesis (FTS) that converts synthesis gas into hydrocarbons of different chain lengths. A microstructured packed-bed reactor for low-temperature FTS is tested towards its versatility for biomass-based syngas with a high inert gas dilution. Investigations include overall productivity, conversion, and product selectivity. A 60-times larger pilot-scale reactor is further tested. Evaporation cooling is introduced which allows to increase the available energy extraction from the system. From that scale on, an autothermal operation at elevated conversion levels is applicable.

Keywords: Biomass-to-liquid, Compact reactor technology, Fischer-Tropsch synthesis, Microstructured reactor, Renewable fuels

Received: February 26, 2019; *revised:* April 15, 2019; *accepted:* July 09, 2019

DOI: 10.1002/ceat.201900136

1 Introduction

The heterogeneously catalyzed Fischer-Tropsch synthesis (FTS) was discovered over 90 years ago [1] to produce synthetic fuels out of syngas, CO, and H_2. Coming from coal gasification (coal-to-liquid, CtL), the FTS nowadays experiences renewed interest with novel process paths towards syngas. It offers the possibility to change the present fuel consumption while using renewables to produce synthetic fuels with distinct advantages compared to its fossil counterparts. This technology could help to lower the anthropogenic carbon footprint in the transport sector due to multiple available feedstocks (X-to-liquid, XtL). Conversion technologies range from natural gas or biogas liquefaction (gas-to-liquid, GtL) to applications using electricity, water and CO_2 (power-to-liquid, PtL) or organic sources like biomass (biomass-to-liquid, BtL).

The route from syngas to synthetic fuel (synfuel) according to a simplified reaction equation for the FTS is:

$$n\mathrm{CO} + 2n\mathrm{H_2} \rightarrow -(\mathrm{CH_2})-_n + n\mathrm{H_2O} \quad \Delta H_\mathrm{R}^0 = -158\ \mathrm{kJ\ mol^{-1}} \tag{1}$$

Humanity will still rely on liquid fuels in the next few decades due to a lack of alternatives in certain areas, e.g., aviation [2]. State-of-the-art fossil fuels have two problems: a limited availability of global reserves with slowly decreasing product quality [3] and the critical release of CO_2 from combustion that has been chemically stored underground for millions of years, which ultimately changes the global climate [4]. The use of alternative fuels offers an important possibility to reduce the anthropogenic greenhouse gas emissions while using an existing infrastructure. This has internationally been identified.

Several initiatives and projects investigate the improvement and application of advanced technologies to change energy sources and consumption. Examples are the World Bank's "Zero Routine Flaring by 2030" initiative [5] or Germany's "Kopernikus projects" [6]. Those operations aim to establish decentralized, on-site production units, may it be near an isolated gas or oil field or the executive support of a future power grid for optimized energy distribution via sector coupling.

The flexibility of the FTS is remarkable since many carbon feedstocks can be converted into syngas. Another stand-out feature is the high volumetric energy density of the liquid product, which ranges between 40 and 48 MJ kg^{-1} [7]. Compared to fossil counterparts [8, 9], improved overall combustion properties such as lowered soot and NO_x production can be achieved due to its paraffinic nature.

Thanks to subsidies from the German government, around 36.2 % of German electricity in 2017 was generated from renewable sources such as geothermal energy, solar and wind

---

[1] Marcel Loewert, Prof. Dr.-Ing. Roland Dittmeyer, Prof. Dr.-Ing. Peter Pfeifer
marcel.loewert@kit.edu
Karlsruhe Institute of Technology (KIT), Institute for Micro Process Engineering (IMVT), Hermann-von-Helmholtz-Platz 1, 76344 Eggenstein-Leopoldshafen, Germany.

[2] Julian Hoffmann, Dr. Paolo Piermartini, Manuel Selinsek, Prof. Dr.-Ing. Peter Pfeifer
INERATEC GmbH, Siemensallee 84, 76187 Karlsruhe, Germany.

power or biomass [10]. An important driver of that development changed recently when fixed subsidies per unit of produced electrical energy were changed into a competitive system. Now only the most developed technologies and plants with higher efficiency are supported. This aims to further increase technological advance, cost efficiency, and competition within the renewable sector [11]. However, for a good number of existing plants this poses an insecurity for a continuous economical operation.

Upgrade of biogas for the injection in the natural gas grid is less commonly applied compared to the direct use in decentralized combined heat and power (CHP) units for local energy supply, mainly due to the high investment cost for gas cleanup.

A promising option for biomass utilization is the conversion of the feedstock into liquid energy carriers for the use as fuels or platform chemicals. Potential process steps are biomass pretreatment, gasification, gas cleaning, and FTS with power generation from the gaseous FT byproducts and FT liquids [12]. Today, bioenergy contributes to approx. 50 % of all renewable energy that is consumed worldwide [13].

FTS in the framework of biomass conversion may be one important technology if the goals of the Paris agreement are to be kept by 2050. Besides FTS, BtL processes are able to produce different liquid energy carriers. Target products can include ethanol, methanol, dimethyl ether (DME), oxymethyl ether (OME), or methanol-to-gasoline (MTG) products. Already existing or soon to be commissioned BtL pilot-plant projects in Europe producing advanced biofuels include BioDME (DME synthesis, Chemrec, Sweden), Bioliq (methanol, DME, gasoline, KIT, Germany), Güssing FT (renewable diesel on gasifier side stream, Vienna University of Technology/BIOENERGY 2020+, Austria), and BioTfueL (biokerosene, a French industrial consortium, France). Another BtL application can be found in Canada (ethanol/methanol, Enerkem) [14].

For industrial application, there are a number of volatile variables that make investments in large plants risky: the final product price which strongly depends on the political framework and available supply chain, the feedstock capacity, but also the current metal price and all costs concerning the feed gas supply [15]. Reducing this complexity, intensifying the process by new technologies and markets rather than increasing centralized plant sizes can be a promising strategy [3, 16, 17].

The significance and the potential of small-scale applications has recently been acknowledged. PtL demonstration projects were formed, such as PowerFuel [18] or Soletair [19]. BtL projects such as COMSYN within the Horizon2020 frame by the European Commission [20] have also been introduced. Since the total carbon footprint from the transport sector has not changed since 1990, BtL and PtL will be an effective measure towards greenhouse gas (GHG) neutral transportation and boosting the bio-share quota of refineries while using an established infrastructure [21]. Car engines, fueling stations, and refineries can be further used.

A mixture of a few large plants and many decentrally applied technologies may reform the energy market of the future. Therefore, PtL/BtL plants are considerable building blocks for energy conversion. Different scenarios focus already on applications in the heavy transport sector, e.g., shipping and aviation [22, 23].

Due to the highly exothermic properties of the FTS, the conversion in common industrial reactors needs to be limited to avoid hot spots that would permanently harm the catalyst [24]. Because of this limited conversion, the product gas, which is rich in unconverted feed gas components, needs to be recycled in order to reach high carbon efficiency. This leads to increased cost [25]. Typical approaches to reduce hot spots are further dilution of the catalyst in the formed liquid phase in slurry-bed reactors or via egg-shell catalysts in tube-bundle reactors. Since it matters strongly how well the reaction heat can be taken out of a system, microstructured reactors show big advantages in this regard [26].

Heat removal from the catalyst and mass transfer from gas via the formed liquid phase to solid catalyst are intensified within microstructures, allowing to manage the active site temperature to stay isothermal even under challenging process conditions such as conversions around 80 % [27–29]. The possibility of a high conversion reduces or even omits gas recycling and thus simplifies the overall process. Due to intensified mass transfer, a very high space-time yield, which is nearly 100 times larger compared to conventional slurry-phase reactors, can be reached. A compact and modular plant design with small footprints can therefore be realized (see Tab. 1). This simplified, compact, and modular setup potentially enables decentralized application such as offshore or remote solutions [23, 30].

Previously inaccessible markets open up by utilizing locally available feedstocks [17]. Industrial application of microstructured reactors is often restrained due to less confidence in the technology. Scaling-up can be achieved by simple multiplication of microstructures [31]. In the area of FTS, advanced reactor technology is already bridging the gap between academia and industry [32–35].

Table 1. Comparison of intensified FTS technology in demonstration or industrial scale with conventional reactor systems, as well as catalyst activity from literature [36–38].

	Catalyst activity (C5+ per catalyst mass) [$g_{C5+}g_{cat}^{-1}h^{-1}$]	Space-time yield (C5+ per reactor volume) [$kg\,m^{-3}h^{-1}$]
INERATEC®	2.1	1785
Velocys	–	1600
Oryx GTL – Sasol	–	20.6
Literature review	1.4	–

Fischer-Tropsch products consist of linear and branched alkanes (paraffins, iso-paraffins), alkenes (olefins), and oxygenates. The products come in gaseous, liquid, and solid form under ambient conditions. The selectivity towards species and carbon chain length in the product mixture is strongly dependent on adjusted process conditions. Most important are temperature, residence time, partial pressures, and the catalyst system itself. Due to cleaned feed syngas from purification, the final fuels do not contain any organic sulfur or aromatics and have a cetane number well above 50 [24]. A high dilution with nitrogen is likely for any biomass-based feed from gasification or for biogas using air instead of oxygen for gas reformation [39].

In this work, influences from the feedstock on product properties are highlighted for the low-temperature FTS (LTFT). A previously introduced microstructured fixed-bed reactor is used [28, 40]. Different microstructured layouts are tested and optimized towards their effect on product properties in pure syngas before [29]. There, the high surface area of the reaction foils has been found to be very effective in removing the reaction heat. Thermal stability under severe conditions has also been demonstrated before [28].

The present study details the influence of different partial and total pressure levels, as well as H_2/CO ratios. A thorough analysis of all product fractions is executed. Furthermore, a scaled-up pilot reactor is tested which allows comparison of results with the much smaller lab-scale reactor at varying system temperature and weight hourly space velocity (*WHSV*). Due to autothermal behavior within this reactor scale, evaporation cooling is introduced as the method of choice to extract the released reaction enthalpy from the system and to efficiently change the system temperature. Similar process conditions are tested for both reactor scales to evaluate possible effects from feed gas dilution in order to simulate syngas from BtL applications.

2 Experimental

2.1 Catalyst

For all featured experiments, a commercial cobalt catalyst with 20 wt % Co and 0.5 wt % Re on an optimized γ-alumina support was used. Cobalt is the preferred catalyst for LTFT if saturated compounds are targeted. It shows high selectivity towards linear alkanes, a high activity at low temperature as well as a negligible water-gas shift (WGS) activity compared to iron catalysts [3, 41, 42]. The particle size distribution was adjusted to 50–200 μm for the fixed bed inside the microstructures.

Approximately 2 g and 120 g of catalyst were placed inside the lab and pilot reactor, respectively. The catalyst was first reduced in situ with either heat transfer oil flowing through the cooling channels or heat cartridges placed on top of the reactor surface. A temperature ramp for the reactor surface was applied starting from room temperature to 623 K with 1 K min^{-1}. For that ramp, a gas mixture of 5 % H_2 and 95 % N_2 was given to the reactor. The final temperature was held for 16 h. Once the temperature maximum was reached, 100 % H_2 was fed into the reactor for the rest of the reduction. After 16 h, the reactor was cooled down to 443 K. From that temperature the different reaction parameters and gas flows were adjusted.

2.2 Microstructured Reactors

2.2.1 Lab Scale

The reaction was carried out in a microstructured reactor that has been applied previously [28] and consecutively optimized regarding its structural properties [29]. The principal functionality has been elaborated. Negligible pressure drop in the reaction on the fixed bed was found due to appropriate particle sizes and reactor layout [43].

The reaction volume of the applied system was 2.71 cm^3 formed by eight diffusion bonded reaction foils containing micropillars with 0.75 mm height and 1.2 mm space between each other in face-to-face arrangement to form four reaction slits. Temperature control was ensured by five structured foils, which were stacked in between the reaction slits and where heating oil (Therminol 66, Fragol) was pumped through. The temperature at inlet and outlet of the reaction was measured with temperature sensors placed in the foil stack.

2.2.2 Pilot Scale

The larger pilot-scale reactor was designed with a scale-up factor of around 60 compared to the reactor described in Sect. 2.2.1 (Fig. 1). The foils were redesigned and optimized to fit the larger outer dimensions. The new development results in a reaction volume of ca. 163.4 cm^3 which was designed for at least 6 L of product per day, depending on process conditions. Additionally, channels with specially designed cooling structures were integrated for water entering at nearly boiling temperature. Evaporation cooling should keep the reaction temperature isothermal.

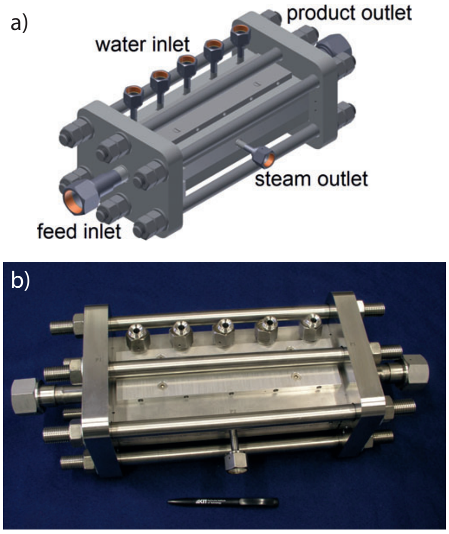

Figure 1. CAD sketch of the pilot-scale reactor (a) and a photo of the resulting design with a pen for size comparison (b).

2.3 Reaction Setup

The periphery of the smaller reaction setup was described earlier [29, 44]. The larger system showed the same structural properties but with associated bigger product traps and an evaporation cooling cycle under pressure (Fig. 2).

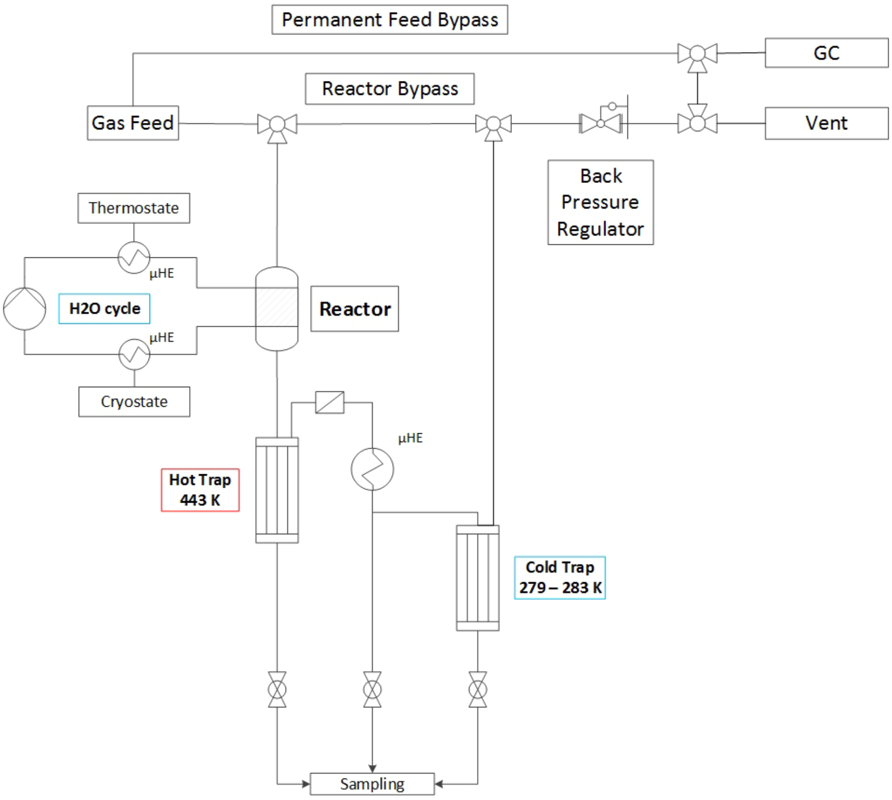

Figure 2. Overview of the pilot-scale reaction setup; a small amount of the gas mixture is bypassing the reactor to measure the feed (labeled Permanent Feed Bypass) via GC analysis. A micro heat exchanger (labeled µHE) is used to condense the liquids for the cold trap.

The feed gas supply was regulated by mass flow controllers (MFCs; model 5850S, Brooks) and monitored by a mass flow meter (MFM; model 5860S, Brooks). All tubing material and system components such as valves and pressure regulators were made from stainless steel. This material meets the respective requirements regarding operating pressure and temperature and shows no interaction with the reactants. Liquid products were first collected in a hot trap, which is a pressure resistant container with a volume of about 4 L. It was electrically heated to 443 K for that higher hydrocarbons, the so-called wax, can condense in this vessel. The subsequent cold trap was held at low temperature to collect the condensed and residual liquefiable product fraction from the micro heat exchanger. This vessel is the largest system component with about 20 L of total volume which is kept below 300 K by a stainless-steel cooling coil of about 2 m length inside the vessel.

The liquefied product accumulated in the respective trap system for offline sampling while the gaseous fraction of the product was led to an online GC system (Agilent 6890N) to determine the conversion and selectivity towards gaseous components. The system pressure was held by a back pressure regulator valve. A permanent bypass with a low flow was adjusted with a fine needle valve to measure the feed gas composition.

2.4 Product Analysis

All three product phases demanded their own method of analysis, all of which needed to be carried out in different GC systems. Products formed gaseous or liquid at reaction conditions. The wax fraction removed from the hot trap under liquid conditions needed to be melted and dissolved after sample solidification. A liquid "oil" fraction accumulated inside the cold trap with accompanying water. The water was separated from the upper, nonpolar phase before analysis. Liquid products were analyzed with a 7820 GC (Agilent) in a DB–2887 column (Agilent), while the solid fraction was analyzed using a cooled injection system and a high–temperature simulated distillation column (see Sect. 2.4.3). All samples were taken few hours after parameters were changed and after emptying the traps in between setups.

2.4.1 Gaseous Species

For gas analysis, different GC columns and detectors were applied within the unit (Agilent 7890B). Hydrocarbon species were analyzed in a flame ionization detector (FID), while a thermal conductivity detector (TCD) was used to measure H_2, N_2, O_2, CO, and CO_2 as well as hydrocarbons up to heptane. Two HayesepQ columns (Agilent) first separated hydrocarbons from CH_4 to C_7H_{14}, as well as CO_2 from the rest of the permanent gases. Two Molsieve 5A columns (Agilent) were used to split the retained CO, N_2, and H_2, while a PoraPlot Q column (Agilent) separated the hydrocarbons and CO_2.

By measuring a feed bypass, the present H_2/CO ratio could be calculated via the gas fraction y_i[1]:

$$\frac{H_2}{CO} = \frac{y_{H_2,\text{feed}}}{y_{CO,\text{feed}}} \tag{2}$$

Syngas conversion X_i was determined using nitrogen as internal standard to correlate the flow before and after the reaction, since there is considerable volume reduction from the reaction. The conversion can be calculated according to:

$$X_{CO} = \frac{\frac{y_{CO,\text{feed}}}{y_{N_2,\text{feed}}} - \frac{y_{CO,\text{product}}}{y_{N_2,\text{product}}}}{\frac{y_{CO,\text{feed}}}{y_{N_2,\text{feed}}}} \tag{3}$$

The selectivity of hydrocarbon components was determined by means of an FID detector. N_2 was only detected on the TCD. Since CH_4 was measured on both detectors, the relation of its signal between FID and TCD was taken as an additional factor:

$$S_{C_iH_x} = \frac{i\,\frac{y_{C_iH_x,\text{FID}}}{y_{N_2,\text{product}}}\,\frac{y_{CH_4,\text{TCD}}}{y_{CH_4,\text{FID}}}}{\frac{y_{CO,\text{feed}}}{y_{N_2,\text{feed}}} - \frac{y_{CO,\text{product}}}{y_{N_2,\text{product}}}} \tag{4}$$

with i being the carbon number and x being the equivalent number of hydrogen atoms of the observed hydrocarbon. The selectivity towards products with carbon chain lengths of five and higher ("fuel range") was determined by subtracting the selectivity towards gaseous components from 1:

$$S_{C_{5+}} = 1 - \sum_{i=1}^{4} S_{C_iH_x} \tag{5}$$

2.4.2 Liquid Product

Under ambient conditions, the liquid phase from the cold trap consists of a lower water phase and a hydrocarbon phase. Many different species of molecules are present in this mixture, ranging from linear alkanes over double-bonded alkenes to branched iso-alkanes and alcohols. A GC method was applied to separate the species. Since calibration of all components is not possible due to missing standards, the correlation between the GC signal area and the number of $-CH_2-$ monomers per molecule was employed to calculate the concentration of higher hydrocarbons.

The productivity P_X was calculated for each liquid (water, hydrocarbons) and solid product. It was measured gravimetrically after an experiment via the weighed product mass m_X, with X being water, oil or wax, respectively:

$$P_X = \frac{m_X}{\Delta t m_{\text{cat}}} \tag{6}$$

After weighing and analyzing a fraction, the total amount of a chosen compound with given carbon number w_i was determined in dependence of the respective mass flows $\dot{m}_i$, gas fractions, volume flows $\dot{V}_i$, productivities and densities ρ_i:

$$w_i = \frac{\dot{m}_i}{\dot{m}_{\text{total}}} = \frac{y_i P_X m_{\text{catalyst}}}{\dot{m}_{\text{gas}} + \dot{m}_{\text{liquid}} + \dot{m}_{\text{solid}}} \quad \text{for solids/liquids} \tag{7}$$

$$w_i = \frac{y_i \dot{V}_{\text{feed,STP}} \rho_{i,\text{STP}}}{\dot{m}_{\text{total}}} \quad \text{for gaseous species} \tag{8}$$

2.4.3 Solid Fraction

Analysis of hydrocarbons with a high density and low solubility is a difficult task [45]. A method with carbon disulfide (CS_2) was applied, which showed sufficient solvent characteristics [46] and was used for analysis despite its high toxicity and low boiling and ignition point. Additionally, a separately heated injection module (Gerstel KAS 4 with C506 controller) was employed on an Agilent G1530A GC with a column that was specifically suitable for simulated distillation (Restek MXT-1HT).

2.4.4 Anderson-Schulz-Flory (ASF) Distribution

The ASF chain length distribution was originally developed by Schulz and Flory and is widely applied for FTS analysis [64]. Through Eq. (9), the so-called chain-growth probability α can be determined in the range from 0 to 1. It can be used to reflect the tendency of the catalyst to produce longer hydrocarbon chains.

$$\alpha_{(j-i)} = \exp\{-a_{j-i}\} = \exp\left\{-\frac{w_j/C_j}{w_i/C_i}\right\} \tag{9}$$

with $j > i$; i, j being the carbon chain numbers, a the slope of a linear part of the ASF plot between $x = [i\ j]$, w_x the mass fraction of chain length x, and C_x the carbon number within chain length x.

2.5 Parameter Sets

As literature implied [47, 48], there are four main process parameters having the strongest influence on the outcome of the reaction: pressure, H_2/CO ratio, temperature, and residence time. Apart from that, many different materials such as support, promotor, active metal, distribution, composition etc. may be further mentioned.

---

[1] List of symbols at the end of the paper.

It was important to observe the system's behavior for different cases of gas composition, namely, a diluted syngas with high amounts of N_2 and or CO_2 as one would expect from biogas origins or from gasification without an air separation unit (ASU) [49].

Experiments concerning the addition of CO_2 in the feed were executed to confirm, apart from all other information, the influence of the WGS reaction on the cobal-based catalyst. This is generally reported to be negligible, depending on the catalyst system [50, 51]. Samples with running number "1" were carried out in the lab-scale reactor described in Sect. 2.2.1. Experiments with number "2" in front were carried out in the pilot-scale reactor described in Sect. 2.2.2.

The total system pressure may influence operation costs [12]. Especially in solid feedstock applications, e.g., direct biomass gasification, a higher pressure may be disadvantageous. To investigate a certain flexibility towards syngas generation, different total pressures were applied. According to literature, the total pressure exhibits no clear trend on the synthesis outcome [52, 53]. It is maybe more important to look on the partial pressure of the components, especially for gases whose presence favors deactivation [41, 53, 54]. In Tab. 2, three parameter sets regarding the pressure influence applied in the present study are listed.

The H_2/CO ratio determines the stoichiometric availability of hydrogen to form hydrocarbons with CO monomers. In biomass applications, a variety of different syngas ratios are reported depending on the gasification conditions and oxidation ratio (oxygen/air and steam content). To highlight the versatility of the reactors, different syngas ratios were tested.

Many mechanisms on how to perform the FTS "polymerization reaction" have been published in the past [54–56]. In the end, the availability of hydrogen in the catalyst bed determines whether or not chain progression can be initiated, influencing the average length of the product's hydrocarbon chain. The stoichiometric feed ratio for maximum conversion nevertheless accounts to ~ 2.15 [41].

Tab. 3 shows the two parameter sets for different H_2/CO ratios with rather unfavorable values, which may represent biomass gasification without syngas conditioning.

Table 2. Experiments 1A–1C for varying total pressure setups in the lab-scale reactor.

Sample	H_2 [vol %]	CO [vol %]	N_2 [vol %]	CO_2 [vol %]	H_2/CO ratio	Total flow [$mL_N min^{-1}$]	*WHSV* [$g g^{-1} h^{-1}$]	p_{total} [MPa]	*T* [K]
1A	27.77	16.13	43.28	12.82	1.72	640	20.80	3	513
1B	29.44	16.70	42.56	11.30	1.76	640	20.18	2	508
1C	27.69	16.55	42.34	13.42	1.67	640	20.90	1.5	513

Table 3. Experiments 1A and 1D for different syngas ratios in the lab-scale reactor.

Sample	H_2 [vol %]	CO [vol %]	N_2 [vol %]	CO_2 [vol %]	H_2/CO ratio	Total flow [$mL_N min^{-1}$]	*WHSV* [$g g^{-1} h^{-1}$]	p_{total} [MPa]	*T* [K]
1A	27.77	16.13	43.28	12.82	1.72	640	20.80	3	513
1D	25.56	16.68	44.55	13.22	1.53	690	23.50	3	513

Syngas conversion is strongly related to the reaction temperature. However, it may also severely influence the chain length, so a parameter set should represent conditions where an acceptable low methane selectivity and sufficient CO conversion can be found. The following experiments were chosen to further investigate evaporation cooling of the microstructures in pilot scale.

Up to around 523 K, many sources describe the process as LTFT that may use iron or cobalt as an active component [57, 58]. Under those conditions, the usage of a cobalt-containing catalyst is possible since oxidation is a negligible factor for long-term activity. A high temperature would lead to shorter hydrocarbon chains, since chain termination is promoted through hydrogenation and other effects [59]. A high temperature would also enhance deactivating effects such as coking, sintering, or wax fouling [51, 60]. Three different sets of parameters with different temperatures for the pilot-scale reactor were chosen for comparison between 493 K and 513 K, as summarized in Tab. 4.

The flow rate of the gaseous feed determines the contact time with the catalyst surface. Thus, the possibility of chain growth will decrease with increasing *WHSV* since it relates the feed's (mass) flow with the mass of catalyst inside the reactor.

$$WHSV = \frac{\dot{m}_{\text{feed}}}{m_{\text{catalyst}}} \quad (10)$$

To test the pilot-scale reactor in this regard, Tab. 5 gives an overview of the process parameters chosen for a comparison.

3 Results and Discussion

3.1 General Process Properties, Analysis Results, and Stability

CO conversion was typically above 50 % in the experiments, which were carried out under high dilution. A rather large number of set points was applied in a short time, so that long-term deactivation effects could be neglected in the observed time frame. Furthermore, an initiation phase was passed, after which natural deactivation was very low. The conversion change during initiation due to catalyst reshaping is known to appear in the course of the first few hundred hours of operation [61]; liquid hydrocarbons start to fill the catalyst pores and induce diffusion limitation until a stationary conversion level is reached [62].

The conversion over time-on-stream (TOS) for the lab reactor system is depicted in Fig. 3. At every point marked with an asterisk, a parameter change was applied. Gaps in the graph are caused by feed gas measurements

Table 4. Experiments 2A–2C for different temperatures adjusted within the pilot-scale reactor.

Sample	H_2 [vol %]	CO [vol %]	N_2 [vol %]	CO_2 [vol %]	H_2/CO ratio	Total flow [$mL_N min^{-1}$]	*WHSV* [$g g^{-1} h^{-1}$]	p_{total} [MPa]	*T* [K]
2A	29.46	15.41	43.47	11.76	1.91	38 147	20.08	3	496
2B	29.46	15.41	43.47	11.76	1.91	38 166	20.09	2.8	502
2C	29.46	15.41	43.47	11.76	1.91	38 166	20.09	2.8	511

Table 5. Experiments 2D and 2E with different *WHSV* in the pilot-scale reactor.

Sample	H_2 [vol %]	CO [vol %]	N_2 [vol %]	CO_2 [vol %]	H_2/CO ratio	Total flow [$mL_N min^{-1}$]	*WHSV* [$g g^{-1} h^{-1}$]	p_{total} [MPa]	*T* [K]
2D	31.08	15.47	42.02	11.44	2.01	38 134	19.65	3	499
2E	31.08	15.47	42.02	11.44	2.01	26 407	13.61	3	497

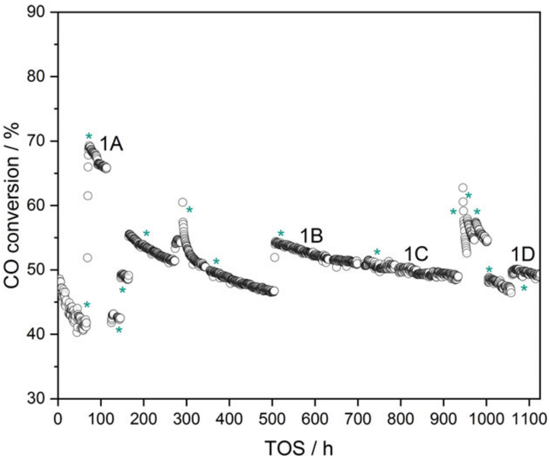

Figure 3. CO conversion over TOS for the course of over 1100 h for the lab-scale microstructured reactor with changing process parameters, each marked with an asterisk. All parameter sets described in this work are additionally labeled from 1A to 1D in the figure.

of the bypass instead of the product stream. The general negative slope is caused by the above-mentioned initiation of the reaction. The flattening of the conversion curve is observable after around 650 h TOS.

The lab-scale reactor behaved isothermal, meaning a temperature gradient of below 2 K, both in axial and radial length. This was observed with two thermocouples along the reactor's width and four thermocouples at the entrances and exits of both fluid streams, respectively. The efficiency of temperature regulation in this scale is very well adjustable with the use of heating oil.

In pilot scale, a maximum temperature gradient along the catalyst bed of 4 K maximum, in most cases around 1–2 K, is considered nearly isothermal. The possibility to cooling down and control the reaction temperature by evaporating water gave options to adjust temperatures in the process quickly and efficiently. The point from which the reaction behaved autothermal was reached around 35 % of CO conversion for most given flows.

In Fig. 4, CO conversion over TOS is depicted for around 250 h of experiments; an initiation phase as in the case of the lab reactor was not possible due to the considerable gas consumption of the system. Every change of parameters is marked with an asterisk. After around 155 h of TOS, several experiments without inert gas dilution were carried out, which led to an increase in CO conversion to around 80 %.

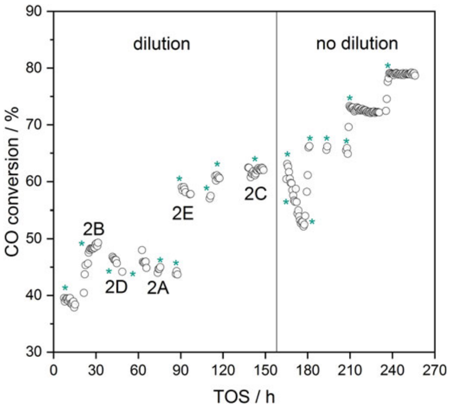

Figure 4. CO conversion over TOS of around 250 h for the pilot-scale microstructured reactor with changing process parameters, each marked with an asterisk. Setups 2A to 2E are additionally labeled within the figure. From around 155 h of TOS, experiments continued without inert gas dilution.

It is worth mentioning that no WGS activity was observed throughout the course of the presented experiments, as expected from cobalt systems without MnO support [63, 64]. No effect from water regarding reaction inhibition or permanent deactivation could be detected.

In Tab. 6, relevant results of all product phases are presented. CO conversion and product selectivity were calculated from the concentrations in gaseous phase averaged over TOS for each experiment.

Alkane, alkene, and iso-alkane contents were determined from the liquid product phase. The compound class spread for alkanes:alkenes:iso-alkanes was roughly 75:10:15 for lab scale and 80:10:10 for pilot scale, respectively, with ± 5 % deviation. The selectivity towards C_{5+} accounted between 66 and 83 mol %. With the given GC system, errors in the detection of alcohols might occur due to distinct overlapping with

Table 6. Overview of results for all experiments in both reactor scales.

Sample	X_{CO} [%]	P_{total} [g g^{-1}h^{-1}]	P_{wax} [g g^{-1}h^{-1}]	P_{oil} [g g^{-1}h^{-1}]	S_{C1} [mol %]	S_{C2} [mol %]	S_{C3} [mol %]	S_{C4} [mol %]	S_{C5+} [mol %]
1A	62.05	0.765	0.140	0.625	15.66	2.75	4.86	5.59	71.14
1B	58.66	1.103	0.223	0.880	14.63	2.45	4.56	5.50	72.86
1C	55.91	0.590	0.046	0.544	17.69	3.27	5.59	6.53	66.91
1D	50.86	0.739	0.119	0.620	10.84	2.85	3.99	0.19	82.13
2A	44.05	0.447	0.086	0.361	13.90	1.61	4.22	4.76	75.51
2B	47.17	0.541	0.103	0.438	14.14	1.66	4.31	4.69	75.20
2C	59.93	0.650	0.121	0.529	17.82	2.14	4.80	6.27	68.96
2D	48.87	0.494	0.094	0.400	17.10	2.08	4.84	6.95	69.02
2E	57.22	0.513	0.098	0.415	15.14	1.78	4.59	5.62	72.87

iso-alkane signals in the oil phase, making definitive identification difficult. Part of the detected iso-alkanes could therefore be alcohols.

3.2 Evaporation Cooling in Pilot Scale

The efficiency of the evaporation cooling structures was initially tested with heating oil replacing the reaction mixture in an even larger pilot reactor than presented (five times the width of the reaction zone). Preheated oil at 518 K (Therminol 66, Fragol) was put through the reactor from bottom to top to guarantee an even flow of the viscous liquid through the structures. Water was distributed from right to left inside the cooling channels by a pump with four horizontally movable thermocouples (position A–D in Fig. 5) measuring the local temperatures inside the structure. Four positions in width with even distribution were chosen (position 1–4). The observed temperature distribution is illustrated in Fig. 5 for the non-insulated reactor (a) and after insulation (b). Insulation lowered the maximum temperature gradient at the edges of the reactor at all positions, but also increased the average temperature inside the system. A gauge glass at the exit of the steam outlet was used to determine if water was fully evaporated upon leaving the reactor.

By establishing the cooling cycle with reaction media shown in Fig. 2, the system temperature was even better manipulated by the pressure of the liquid cooling medium. The relation between water pressure and boiling temperature opened a control window in which the fluid was sufficiently extracting reaction heat without extinction of the operation.

The pressure-dependent boiling temperature is held from the boiling point (saturated liquid) over the two-phase region of wet steam to the vapor region where water is fully evaporated and starts overheating. For best temperature control, the wet steam should not fully evaporate. The specific heat capacity of steam is more than 22 times lower compared to that of the liquid water. The gauge glass implied that water never evaporated completely and remained in the wet steam region. This was confirmed by temperature measurements at the steam outlet with regards to the applied water pressure. A pressure between 15 and 30 bar was adjusted to reach temperatures between 474 K and 514 K, in good agreement with the Antoine equation for water in that regime [65].

The possibility to use evaporation cooling is determined by the layout and dimensioning of the cooling channels. The

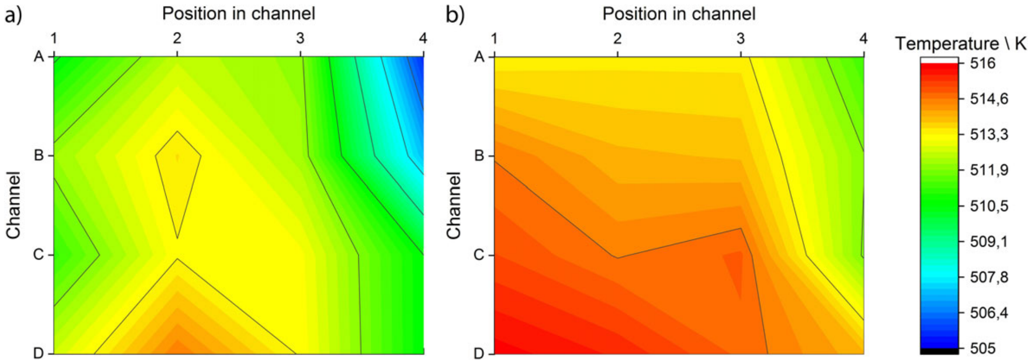

Figure 5. Temperature profile for 16 measurement spots in four thermocouple channels for a non-insulated (a) and an insulated microstructured pilot-scale FT reactor (b), as described in [26].

piping material determines the pressure that is applicable in a system. For the means of this experiment, 35 bar was chosen to be the highest applicable water pressure for which the piping was initially tested by pressure tests with nitrogen.

3.3 Total Pressure Variation in Lab Scale

As mentioned above, the effect of the total pressure on the outcome of FTS follows no certain tendency in literature. In Fig. 6, the ASF curves of three similar parameter sets at different total pressure are indicated. The total amount of methane is similar but has a trend to higher values at lower pressure. The clearest effect is on CO conversion, where the highest pressure could lead to the highest resulting value. The general forms of the ASF curves are similar except for the higher chain lengths from C_{35+} where a higher pressure is advantageous.

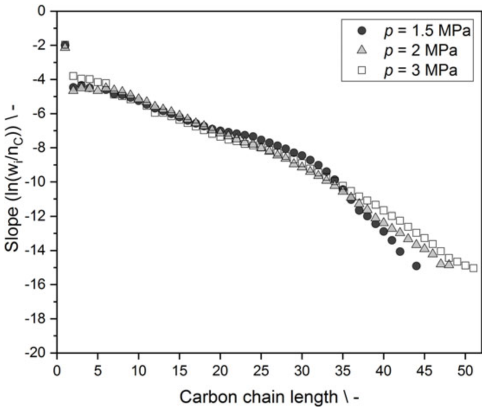

Figure 6. ASF plots for different absolute pressures and their effect on the product distribution from experiments 1A (3 MPa), 1B (2 MPa), and 1C (1.5 MPa).

3.4 H_2/CO Ratio Variation in Lab Scale

Investigations about the influence of the H_2/CO input ratio on the product distribution in regular plug-flow reactors show that the smaller the input ratio, the longer the average chain length becomes [47, 54, 66]. The expected change of chain growth probability, however, is not very distinct for the present experiments (Fig. 7). The effect of a higher dilution with nitrogen in the feed gas could have a more pronounced impact on chain termination than the available H_2/CO ratio. The chain growth probability for a H_2/CO ratio of 1.72 for C_{11} to C_{25} accounts to α_{11-25} (1A) = 82.5 %, whereas for a H_2/CO ratio of 1.53 the chain growth probability resulted in α_{11-25} (1D) = 84.0 %.

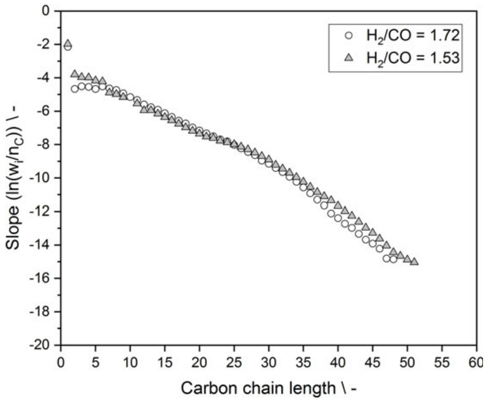

Figure 7. ASF plots with different syngas ratios from experiments 1A (H_2/CO = 1.72) and 1D (H_2/CO = 1.53).

3.5 Temperature Variation in Pilot Scale

The temperature plays an important role on reaction kinetics. It is also known to determine chain termination [47, 66, 67]. Keeping that in mind allows a certain controllability to the process by controlling the temperature [37]. At 473 K, very weak catalyst activity was observed. Thus, Fig. 8 presents the ASF plots for higher temperature obtained from increased water partial pressure in the cooling system. An enhanced production of alkanes between C_{10} and C_{20} at higher temperature and an average carbon chain length increase for lower temperatures in C_{21+} can be found. This trend is also confirmed by the gas phase, i.e., improved C_{5+} selectivity with decreasing temperature in Tab. 6.

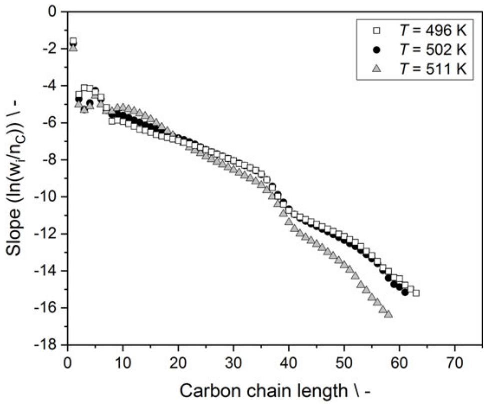

Figure 8. ASF plots at different reaction temperatures for experiments 2A–2C with respective temperatures of 496 K, 502 K, and 511 K in the pilot-scale reactor.

3.6 *WHSV* Variation in Pilot Scale

In Fig. 9, the *WHSV* influence is demonstrated for two different sets of parameters. The values of the *WHSV* were relatively high. Thus, the observable difference in the ASF plots is rather small. A lower *WHSV* value should increase the average chain length visibly. Interestingly, the maximum chain length seems not to be affected, again possibly due to high overall dilution.

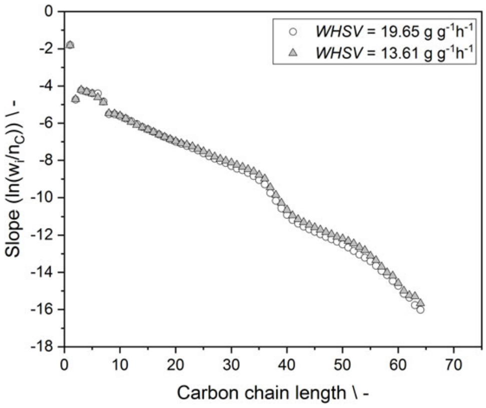

Figure 9. ASF plots with different *WHSV* from experiment 2D (*WHSV* = 19.7 g g^{-1}h^{-1}) and 2E (*WHSV* = 13.6 g g^{-1}h^{-1}) in the pilot-scale reactor.

In the end, a constant system performance and high load flexibility are apparent from these results, which is beneficial for any BtL application.

3.7 Success of Upscale

Experiments 1A and 2C enable a comparison of both reactor performances, since a similar temperature, residence time, and CO partial pressure was arranged. Only the syngas ratio differs with 1.91 vs. 1.72, because both setups were originally planned to compare parameters within the same reactor scale. Due to the high dilution, the effect of this difference on the reaction outcome should be limited, as discussed in Sect. 3.4. Regarding this, a comparison of both setups should be applicable.

In Fig. 10, the ASF plot for 1A (lab scale) and 2C (pilot scale) is displayed. While maintaining a similar CO conversion and productivity, the chain length of linear products in the larger reactor scale was observed. Between C_{10} and C_{25}, the form of the plots is similar. Differences in the curves between C_5 and C_{10} could be explained from variations in trap draining between the two reactor dimensions. Light hydrocarbons can potentially evaporate due to draining under ambient conditions. This was found in all experiments in pilot vs. lab scale. The means to cool down the sampling vessel while draining did not improve the lack of C_5 to C_{10}.

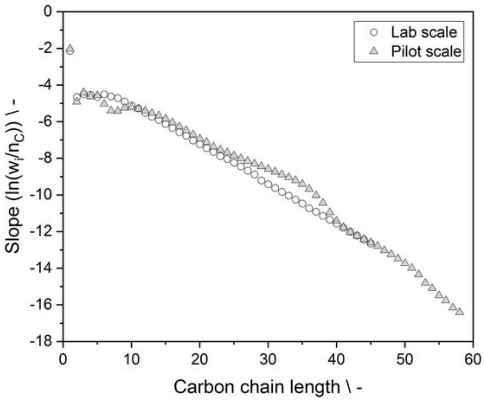

Figure 10. ASF plots for two comparable setups (1A and 2C) for both reactor scales.

Both reactors use a similar core technology. The distribution of the feed gas as well as the layout and the mechanism behind the cooling structures are quite different, though. Both showed near isothermal behavior and comparable product quality for many different applications despite versatile experimental parameters. In conclusion, the successful upscale considerably benefits from evaporation cooling as means for high-pressure steam export. This system can be utilized quite easily in larger reactor scales. No apparent downsides could be observed that might have been caused by the upscale.

4 Conclusions

Flexibility towards different sources of syngas is an important characteristic of process applicability. With significantly improved reactor concepts, it seems possible to produce high-performance synthetic fuels in a decentralized and renewable manner. The BtL route typically provides a more challenging syngas quality compared to other sources but its potential is too high to be neglected. To demonstrate the versatility of microstructured reactors for the Fischer-Tropsch synthesis in decentralized applications, a reactor upscale (scaling factor of about 60) was investigated with a number of experimental parameters adjusted to BtL application.

It could be demonstrated that both reactor sizes achieve comparable conversion levels, especially regarding the high dilution of up to 56 % representing gasification using air. The performance would increase with less dilution to reach even higher conversions. This could be shown for undiluted setups in pilot scale. The total productivity typically reached acceptable values of 0.5–0.75 g $g_{cat}^{-1}h^{-1}$, while the productivity ratio of "oil" to "wax" as a function of the respective condensation temperatures was quite constant at 4:1. Product selectivity ranged from 10 to 18 mol % for methane with a selectivity towards higher hydrocarbons of 66–83 mol %.

Regarding long-term stability, the commercial cobalt catalyst showed no signs of rapid deactivation within the course of 1000+ h of experiment. Isothermal properties of the lab reactor were satisfying with a maximum temperature gradient of 2 K over the reactor length. This isothermal behavior was successfully transferred into the pilot reactor with typically 1–2 K temperature gradient using evaporation of water in special cooling structures. The reaction temperature has been effectively manipulated by adjustment of the water pressure in all cases.

The quality of the liquid product (FT oil) was comparable in all experiments and both reactors with a typical ratio of 4:1:1 for alkanes:alkenes:iso-alkanes which is quite promising for decentralized fuel production and distribution. The maximum chain length detected in the FT wax was 65 C-atoms, which is limited by the high gas dilution.

FT synthesis in microstructured reactors has been proven as pressure-tolerant between 1.5 and 3 MPa. Also, the H_2/CO ratio under BtL-typical feed gas dilution showed no significant effect on the average chain length. Thus, the tradeoff between different types of syngas conditioning as well as gasification options can be weighed almost without consideration of the FT stage in case of a microstructured reactor.

The temperature increase in pilot scale followed a clear trend towards higher conversion at almost stable product distribution which is quite a singularity reached by the reactor design, as reported before [28, 29]. The low tendency towards deactivation at high conversion in highly diluted syngas raises hope towards a single-pass reactor operation in the FT process with satisfying results.

The comparison of microstructured FT reactors between lab scale and pilot scale has been investigated regarding the product quality. Insignificant changes from the scale-up in regard to product quality and reaction performance are evened out by improved controlling tools and operation mechanisms. This opens up scenarios for decentralized BtL or PtL applications. With an autothermal operation starting at a heat output only as low as 500 W allows quick temperature manipulation through water pressure adjustment which is a unique feature dedicated to PtL applications. Steam export enables the coupling of processes such as steam reforming, steam gasification, WGS, a steam turbine, or a steam electrolyzer to increase considerably the thermal efficiency of sector coupling.

Acknowledgment

The Vector Foundation is acknowledged for financial support of parts of this work within the DynSyn project. Additionally, parts of this work have been financially funded by the Young Innovators program ("Junge Innovatoren") of the Ministry of Science, Research and the Arts of the State of Baden-Wuerttemberg, Germany, as well as by the German Federal Ministry of Economy and Energy and the ESF (European Social Fund) Germany within the EXIST Business Start-up Grant ("EXIST Forschungstransfer", grant agreement No. 03EUGBW118). The authors like to thank the colleagues from KIT's Institute of Catalysis Research and Technology (IKFT) for enabling and supporting the wax analysis.

The authors have declared no conflict of interest.

Symbols used

a	[–]	slope of a linear curve
H	[kJ mol^{-1}]	enthalpy
m	[g]	mass
$\dot{m}$	[g h^{-1}]	mass flux
P	[g g$_{cat}^{-1}$h^{-1}]	specific productivity
p	[MPa]	pressure
S_{Ci}	[mol %]	selectivity towards species C_i
T	[K]	temperature
t	[h]	time
TOS	[h]	time-on-stream
$WHSV$	[g g$_{cat}^{-1}$h^{-1}]	weight hourly space velocity
w_i	[wt %]	mass fraction of species i
X_i	[vol %]	conversion of species i
y_i	[–]	gas fraction of species i

Greek letter

α	[%]	probability of chain growth

Sub- and superscripts

R	reaction
0	standard
C_{5+}	molecules with five carbon atoms or more
cat	catalyst
total	total amount

Abbreviations

ASF	Anderson-Schulz-Flory
ASU	air separation unit
BtL	biomass-to-liquid
CAD	computer-aided design
CHP	combined heat and power
CtL	coal-to-liquid
DME	dimethyl ether
FID	flame ionization detector
FTS	Fischer-Tropsch synthesis
GHG	greenhouse gas
GtL	gas-to-liquid
LTFT	low-temperature FT
MFC	mass flow controller
MFM	mass flow meter
MTG	methanol to gasoline
OME	oxymethylene ethers
PtL	power-to-liquid
SEM	scanning electron microscopy
TCD	thermal conductivity detector
WGS	water-gas shift
XtL	X-to-liquid

References

[1] F. Fischer, H. Tropsch, *Brennst. Chemie* **1923**, *4*, 276.

[2] M. Kousoulidou, L. Lonza, *Transp. Res. Part D* **2016**, *46*, 166. DOI: https://doi.org/10.1016/j.trd.2016.03.018

[3] *Greener Fischer-Tropsch Processes for Fuels and Feedstocks* (Eds: P. M. Maitlis, A. de Klerk), Wiley-VCH, Weinheim **2013**.

[4] S. Manabe, R. T. Wetherald, *J. Atmos. Sci.* **1967**, *24*, 241.

[5] http://www.worldbank.org/en/programs/zero-routine-flaring-by-2030 (Accessed on June 11, 2018)

[6] https://www.kopernikus-projekte.de/ (Accessed on June 11, 2018)

[7] A. Bisio, *Encyclopedia of Energy Technology and the Environment*, Wiley-Interscience, New York **1995**.

[8] A. Abu-Jrai, A. Tsolakis, K. Theinnoi, R. Cracknell, A. Megaritis, M. L. Wyszynski, S. E. Golunski, *Energy Fuels* **2006**, *20*, 2377.

[9] S. S. Gill, A. Tsolakis, K. D. Dearn, J. Rodríguez-Fernández, *Prog. Energy Combust. Sci.* **2011**, *37*, 503.

[10] https://www.umweltbundesamt.de/ (Accessed on July 03, 2018)

[11] https://www.bmwi.de/Redaktion/DE/Downloads/E/eeg-2017-fragen-und-antworten.pdf?__blob=publicationFile&v=20 (Accessed on February 12, 2019)

[12] M. J. A. Tijmensen, A. P. C. Faaij, C. N. Hamelinck, M. R. M. van Hardeveld, *Biomass Bioenergy* **2002**, *23 (2)*, 129. DOI: https://doi.org/10.1016/S0961-9534(02)00037-5.

[13] https://www.iea.org/renewables2018/ (Accessed on October 20, 2018)

[14] http://www.etipbioenergy.eu/images/EIBI-1-biomass-to-liquids.pdf (Accessed on October 20, 2018)

[15] R. Motal, Commercialization Considerations for Gas Conversion Technology Development, *ARPA-E Natural Gas Conversion Technologies Workshop*, Houston, TX, January **2012**.

[16] D. A. Wood, C. Nwaoha, B. F. Towler, *J. Nat. Gas Sci. Eng.* **2012**, *9*, 196.

[17] H. J. Venvik, J. Yang, *Catal. Today* **2017**, *285*, 135.

[18] http://www.chemie.de/news/1158952/treibstoff-fuer-klimaneutrales-fliegen.html (Accessed on February 20, 2019)

[19] https://soletair.fi/ (Accessed on June 11, 2018)

[20] https://www.comsynproject.eu/ (Accessed on June 11, 2018)

[21] C. N. Hamelinck, A. P. C. Faaij, H. den Uil, H. Boerrigter, *Energy* **2004**, *29*, 1743.

[22] S. Horvath, M. Fasihi, C. Breyer, *Energy Convers. Manage.* **2018**, *164*, 230.

[23] P. Schmidt, V. Batteiger, A. Roth, W. Weindorf, T. Raksha, *Chem. Ing. Tech.* **2018**, *90*, 127.

[24] *Fischer-Tropsch Technology* (Eds: A. Steynberg, M. Dry), Elsevier, Amsterdam **2004**.

[25] D. J. Wilhelm, D. R. Simbeck, A. D. Karp, R. L. Dickenson, *Fuel Process. Technol.* **2001**, *71*, 139.

[26] R. Dittmeyer, T. Boeltken, P. Piermartini, M. Selinsek, M. Loewert, F. Dallmann, H. Kreuder, M. Cholewa, A. Wunsch, M. Belimov, S. Farsi, P. Pfeifer, *Curr. Opin. Chem. Eng.* **2017**, *17*, 108. DOI: https://doi.org/10.1016/j.coche. 2017.08.001

[27] W. Bier, W. Keller, G. Linder, D. Seidel, K. Schubert, H. Martin, *Chem. Eng. Process. Process Intensif.* **1993**, *32*, 33.

[28] R. Myrstad, S. Eri, P. Pfeifer, E. Rytter, A. Holmen, *Catal. Today* **2009**, *147*, 301.

[29] P. Piermartini, T. Boeltken, M. Selinsek, P. Pfeifer, *Chem. Eng. J.* **2017**, *313*, 328. DOI: https://doi.org/10.1016/j.cej.2016.12.076

[30] C. Hopper, *J. Pet. Technol.* **2009**, *61*, 26.

[31] K. Ehrhardt, Micro Chemical Engineering – a fascinating journey from lab to industrial production, *IMRET 2018*, Karlsruhe, October **2018**.

[32] F. V. Vázquez, J. Koponen, V. Ruuskanen, C. Bajamundi, A. Kosonen, P. Simell, J. Ahola, C. Frilund, J. Elfving, M. Reinikainen, N. Heikkinen, J. Kauppinen, P. Piermartini, *J. CO2 Util.* **2018**, *28*, 235. DOI: https://doi.org/10.1016/j.jcou.2018.09.026

[33] S. LeViness, S. R. Deshmukh, L. A. Richard, H. J. Robota, *Top Catal.* **2014**, *57 (6–9)*, 518. DOI: https://doi.org/10.1007/s11244-013-0208-x

[34] The World Bank, *Mini-GTL Technology Bulletin*, The World Bank **2017**.

[35] http://www.neocarbonenergy.fi/ (Accessed on August 06, 2018)

[36] Velocys, *Presentation to analysts of the Oxford Catalysts Group* **2012**.

[37] S. LeViness, *Energy Frontiers International 2012*, Houston, TX, October **2012**.

[38] S. LeViness, *AIChE Spring Meeting*, San Antonio, TX, April/May **2013**.

[39] A. Faaij, B. Meuleman, R. van Ree, NOVEM Netherlands Agency for Energy and the Environment, *Long Term Perspectives of Biomass Integrated Gasification with Combined Cycle Technology: Costs and Efficiency and a Comparison with Combustion*, EWAB rapport, NOVEM **1998**.

[40] F. Dadgar, H. J. Venvik, P. Pfeifer, *Chem. Eng. Sci.* **2018**, *177*, 110. DOI: https://doi.org/10.1016/j.ces.2017.10.039

[41] M. E. Dry, *Catal. Today* **2002**, *71 (3–4)*, 227. DOI: https://doi.org/10.1016/S0920-5861(01)00453-9

[42] Ø. Borg, S. Eri, E. Blekkan, S. Storsater, H. Wigum, E. Rytter, A. Holmen, *J. Catal.* **2007**, *248 (1)*, 89. DOI: https://doi.org/10.1016/j.jcat.2007.03.008

[43] C. Knobloch, R. Güttel, T. Turek, *Chem. Ing. Tech.* **2013**, *85 (4)*, 455. DOI: https://doi.org/10.1002/cite.201200202

[44] C. Sun, T. Zhan, P. Pfeifer, R. Dittmeyer, *Chem. Eng. J.* **2017**, *310*, 272. DOI: https://doi.org/10.1016/j.cej.2016.10.118

[45] https://blog.restek.com/?p=10846 (Accessed on October 29, 2018)

[46] G. E. Totten, *Fuels and Lubricants Handbook: Technology, Properties, Performance, and Testing*, ASTM International, West Conshohocken, PA **2003**.

[47] *Fischer-Tropsch Technology* (Eds: A. Steynberg, M. Dry), Elsevier, Amsterdam **2004**.

[48] *Catalysis in the Refining of Fischer-Tropsch Syncrude* (Eds.: A. de Klerk, E. Furimsky), Royal Society of Chemistry, Cambridge **2010**.

[49] Deutsche Vereinigung des Gas- und Wasserfachs EV (DVGW), **2011**.

[50] A. Y. Khodakov, W. Chu, P. Fongarland, *Chem. Rev.* **2007**, *107 (5)*, 1692. DOI: https://doi.org/10.1021/cr050972v

[51] N. E. Tsakoumis, M. Rønning, Ø. Borg, E. Rytter, A. Holmen, *Catal. Today* **2010**, *154 (3–4)*, 162. DOI: https://doi.org/10.1016/j.cattod.2010.02.077

[52] M. Agee, *Fuel Technol. Manage.* **1997**, *7*, 69–72.

[53] J. van de Loosdrecht, B. Balzhinimaev, J.-A. Dalmon, J. W. Niemantsverdriet, S. V. Tsybulya, A. M. Saib, P. J. van Berge, J. L. Visagie, *Catal. Today* **2007**, *123 (1–4)*, 293. DOI: https://doi.org/10.1016/j.cattod.2007.02.032

[54] M. E. Dry, *J. Mol. Catal.* **1982**, *17 (2–3)*, 133. DOI: https://doi.org/10.1016/0304-5102(82)85025-6

[55] C. G. Visconti, E. Tronconi, L. Lietti, P. Forzatti, S. Rossini, R. Zennaro, *Top. Catal.* **2011**, *54 (13–15)*, 786. DOI: https://doi.org/10.1007/s11244-011-9700-3

[56] A. A. Adesina, *Appl. Catal., A* **1996**, *138 (2)*, 345. DOI: https://doi.org/10.1016/0926-860X(95)00307-X

[57] B. H. Davis, *Fischer-Tropsch Synthesis, Catalysts and Catalysis*, 1st ed., Studies in Surface Science and Catalysis, Vol. 163, Elsevier, Amsterdam **2007**.

[58] C. G. Visconti, M. Mascellaro, *Catal. Today* **2013**, *214*, 61. DOI: https://doi.org/10.1016/j.cattod.2012.10.016

[59] G. P. van der Laan, A. A. C. M. Beenackers, *Catal. Rev.* **1999**, *41 (3–4)*, 255. DOI: https://doi.org/10.1081/CR-100101170

[60] E. Rytter, A. Holmen, *Catalysts* **2015**, *5 (2)*, 478. DOI: https://doi.org/10.3390/catal5020478

[61] P. J. van Berge, R. C. Everson, in *Natural Gas Conversion IV*, 1st ed. (Eds: C. P. Nicolaides, M. D. Pontes, R. L. Espinoza), Studies in Surface Science and Catalysis, Vol. 107, Elsevier, Amsterdam **1997**.

[62] S. Rößler, C. Kern, A. Jess, *Chem. Ing. Tech.* **2018**, *90 (5)*, 634. DOI: https://doi.org/10.1002/cite.201700142

[63] T. Riedel, M. Claeys, H. Schulz, G. Schaub, S.-S. Nam, K.-W. Jun, M.-J. Choi, G. Kishan, K.-W. Lee, *Appl. Catal., A* **1999**, *186 (1–2)*, 201. DOI: https://doi.org/10.1016/S0926-860X(99)00173-8

[64] J. Yang, W. Ma, D. Chen, A. Holmen, B. H. Davis, *Appl. Catal., A* **2014**, *470*, 250. DOI: https://doi.org/10.1016/j.apcata.2013.10.061

[65] *VDI Heat Atlas*, V.D.I. VDI Gesellschaft Verfahrenstechnik und Ingenieurwesen, 2nd ed., Springer, Berlin **2010**.

[66] A. de Klerk, *Fischer-Tropsch Refining*, Wiley-VCH, Weinheim **2011**.

[67] H. Schulz, M. Claeys, *Appl. Catal., A* **1999**, *186 (1–2)*, 71. DOI: https://doi.org/10.1016/S0926-860X(99)00165-9

PAPER II

DYNAMICALLY OPERATED FISCHER-TROPSCH SYNTHESIS IN PTL-PART 1: SYSTEM RESPONSE ON INTERMITTENT FEED

Submitted to ChemEngineering, 15.02.2020

Published: 28.03.2020

`https://doi.org/10.3390/chemengineering4020021`

Paper II

chemengineering

MDPI

Article

Dynamically Operated Fischer-Tropsch Synthesis in PtL-Part 1: System Response on Intermittent Feed

Marcel Loewert [†] **and Peter Pfeifer** *

Institute of Micro Process Engineering (IMVT), Karlsruhe Institute of Technology (KIT), 76344 Eggenstein-Leopoldshafen, Baden-Württemberg, Germany; marcel.loewert@ineratec.de

[†] Current affiliation: INERATEC GmbH, Siemensallee 84, 76187 Karlsruhe, Baden-Württemberg, Germany

* Correspondence: peter.pfeifer@kit.edu; Tel.: +49-721-608-24767

Received: 15 February 2020; Accepted: 27 March 2020; Published: 28 March 2020

Abstract: Society is facing serious challenges to reduce CO_2 emissions. Effective change requires the use of advanced chemical catalyst and reactor systems to utilize renewable feedstocks. One pathway to long-term energy storage is its transformation into high quality, low-emission and CO_2-neutral fuels. Performance of technologies such as the Fischer-Tropsch reaction can be maximized using the inherent advantages of microstructured packed bed reactors. Advantages arise not only from high conversion and productivity, but from its capability to resolve the natural fluctuation of renewable sources. This work highlights and evaluates a system for dynamic feed gas and temperature changes in a pilot scale Fischer-Tropsch synthesis unit for up to 7 L of product per day. Dead times were determined for non-reactive and reactive mode at individual positions in the setup. Oscillating conditions were applied to investigate responses with regard to gaseous and liquid products. The system was stable at short cycle times of 8 min. Neither of the periodic changes showed negative effects on the process performance. Findings even suggest this technology's capability for effective, small-to-medium-scale applications with periodically changing process parameters. The second part of this work focuses on the application of a real-time photovoltaics profile to the given system.

Keywords: Fischer-Tropsch synthesis; microstructured reactors; dynamic processes; heterogeneous catalysis; decentralized application; compact reactor technology; PtX; PtL

---

1. Introduction

The Fischer-Tropsch synthesis (FTS) is a polymerization type reaction, which converts synthesis gas (hydrogen and carbon monoxide) into many different hydrocarbons; ranging from methane to carbon chains with over 100 carbon atoms. Those products can be distinguished as gases, liquids or solids under ambient conditions. Water is produced as a byproduct of the reaction. Synthesis products can be applied for many different applications in the energy, chemical and material industry. Middle distillate type hydrocarbons can be utilized as synthetic fuels for a multitude of vehicles and vessels that are designed for operation with fossil fuels. Specific metal surfaces are necessary to boost the reaction rate and to optimize the chain distribution, which makes the FTS a prominent example for heterogeneous catalysis. The reaction equation, based on synthesis gas to produce linear alkanes, is shown in Equation (1) [1–3]:

$$(2n + 1)H_2 + nCO \rightarrow C_nH_{2n+2} + nH_2O. \qquad (1)$$

This synthesis is influenced by a myriad of different process parameters such as the catalyst and support system, temperature, partial pressures, residence time and overall feed gas composition and dilution, as well as conversion levels [4–7]. All of those characteristics have been intensively investigated in the history of the FTS [2,6,8,9]. Investigations regarding process properties for the cobalt-based catalyst used in this work have been executed before [10–15]. Figure 1 shows a typical carbon chain length distribution of the FTS products. They mainly consist of linear alkanes, alkenes and iso-alkanes, as well as alcohols [2,16–19].

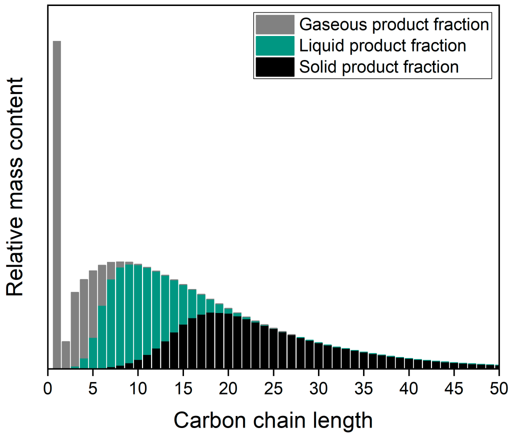

Figure 1. Exemplary mass distribution of a Fischer-Tropsch product from cobalt catalysts (own study).

1.1. Energy Transition and Technologies that May Be Required

In the context of energy transition, humanity aims to mitigate climate change, which is strongly influenced by the amount of anthropogenic CO_2 emissions [20]. In terms of efficiency, technological advances must help to achieve a reduction of energy demand per capita and overall consumption of goods [21–24]. While the world's CO_2 emission from crude oil utilization is almost constant over the past two decades, the transport sector has significantly increased its share from 22% in 1990 to 28% in 2016 [25]. Finding and applying sustainable alternatives is thus necessary.

Many different pathways to substitute fossil fuel with CO_2-neutral sources have opened up in recent years. Most of them rely on renewable electrical energy from wind, solar and hydropower. Whenever possible, the generated electricity should be directly used or can be converted into heat. It can also be used for transportation and manufacturing of materials, with given conversion losses [26,27]. Those technological pathways can be summarized as power-to-X (PtX) or, more specifically, power-to-liquid (PtL) and power-to-gas (PtG) processes. Generally, there will be a need for different energy storage technologies in a highly volatile and fluctuating renewable energy system [26,28–31]. A good share of the renewable energy will be exploitable under certain conditions. Energy from the sun can only be harvested at daytime and is best with good weather. Wind energy delivers more power when strong winds are present. Even hydropower from sea streams and rivers shows different performance profiles based on seasonal influences and water levels. In the end, with increasing use of renewable electricity, the overall fluctuation generates grid instabilities and the energy demand cannot be fulfilled at all times [32,33].

Thus, the two biggest challenges for the future energy grid are the storage of surplus energy and filling up the gaps in times of an undersupply. This is known as the intermittency problem [27,33–39]. The consequence is the need for storages that deplete in times of undersupply and can be filled in times of overproduction. Those storages need to work as a buffer system between the producer and the consumer. Storages come at a certain price [37,38,40,41].

In terms of batteries, the volumetric energy density is problematic on long distances and with heavier masses to be transported. They are thus less suitable for heavy duty or air transport [6,42,43]. The high demand for lithium and cobalt for a global supply and the limited capacity of batteries are further reasons not to completely rely on electric mobility as the predominant form of transportation [6].

Gaseous products offer a higher level of chemical availability from the respective molecule's inherent energy, but storage and product handling are quite difficult in terms of safety, cost and storage size [44–46]. Transportable gases need to be either condensed at low temperature or compressed, which adds cost to the overall process. Hydrogen is the most expensive to store due to its low density and condensation temperature. Still, it is necessary in most synthesis routes [45,46].

Liquid chemicals are a good energy storage due to their high volumetric energy density. This enables good transportability with low tank weight.

In order to cover the need for energy and materials, a full range of applicable technologies needs to be mixed and organized in an intelligent way. As one of many demonstration platforms in that regard, the "Energy Lab 2.0" was erected in the Helmholtz Association with funding of BMWi, BMBF and the State of Baden-Württemberg in Germany. This infrastructure looks into the real-time behavior of energy producers, converters and consumers [47]. The aim is to manage energy and to distribute it over many different pathways, such as power-to-heat (PtH), PtL and PtG. A number of different PtL projects use this platform to investigate sector coupling. Figure 2 is an example of a PtL-approach as a framework of the studies done in this work.

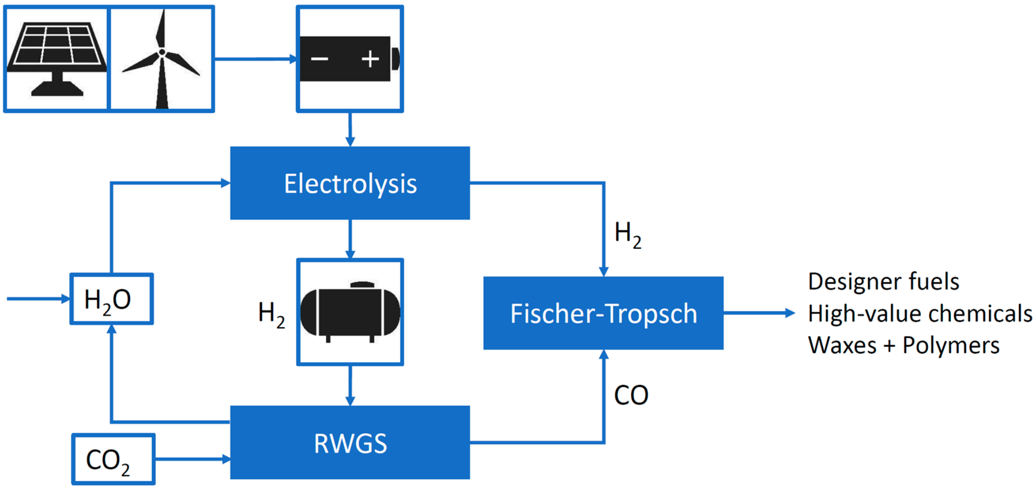

Figure 2. Example of a PtL approach based on renewable electricity, water and CO_2. Intermediate process steps include an electrolysis, a reverse water-gas shift reaction (RWGS) and the FTS. Possible products include designer fuels, waxes and other high-value chemicals. In addition, storage systems for electricity and hydrogen are shown, which might be needed to tackle the intermittency problem.

The Fischer-Tropsch reaction in the PtL pathway shows high potential to produce synthetic substitutes for fossil fuels in already existing, efficient engine systems [48,49]. Distribution would be possible without new infrastructure, since refineries and fueling stations could be used without much additional cost [3]. The liquid fuel shows better combustion properties in terms of soot and NO_x emissions and does not contain poisons, contaminants or aromatics, unlike fossil fuels [48–50].

Still, there are a number of reasons why this pathway has not been exploited yet. The most important one is the economic comparison between the costs of synthetic and fossil fuels. The synthetic pathway has always been considerably more expensive [51]. In times of ecological awareness and a changing energy system, this might easily change if CO_2 emission cost increase and synthetic fuels become recognized as carbon-neutral fuels [43,52,53].

The second main reason is technological limitation. The few technical plants installed worldwide operate with restricted reaction performance. Avoiding hot spots in the catalyst due to limited heat management or mass transfer limitation between reactants and catalysts are the main reasons [54]. Those compromises are evened out by economy of scale, for which a huge continuous feed is needed. This favors large installations as well as a large, centralized infrastructure [3,6]. Also, state-of-the-art technology would rely on large storage and buffer systems [46,55]. With advanced reactor systems, a broader application of this technology in smaller scale seems viable nowadays [54,56,57].

One idea to tackle the issues of buffer costs is to reduce their size by operating a dynamic synthesis with a flexible energy input. This may only be realized by advanced process control and modular approaches.

1.2. Microstructured Reactor Technology

In the last decade, the development of microstructured (packed bed) reactors enabled intensification of processes due to increased heat and mass transfer [10,11]. In regard to FTS, microstructured packed bed reactors constitute the most developed available technology to maximize the reaction output by overcoming state-of-the-art limitations and concerns [11,56,58–62]. Small interior dimensions drastically increase the surface area and local heat transfer. Higher conversion levels can be applied in the process without harming the catalyst. Furthermore, concentration and temperature changes may be quickly applied because of short overall distances and advanced tools like evaporation cooling [61,63–65]. This allows high-pressure steam production from the FTS reaction in order to enhance the thermal efficiency of a process network while enabling the control over the FTS reactor at the same time.

Additionally, the small interior dimensions of microstructured devices enable a broad scalability of the overall process that is not accessible with conventional solutions—decentralized small-scale applications become cost-competitive due to reduced transport distances. Advantages also include improved reaction safety through small reaction inventory [6,11,66].

Microstructured reactors have already been successfully implemented into the market for small-to-medium-scale applications [54,67,68]. They could also be used in additional processes (e.g., island solutions for local energy conversion).

Concluding, FT fuel may be a viable and competitive high-performance fuel besides obvious conversion losses that every multi-step synthesis must face. Microstructured packed bed reactors are advantageous for FT synthesis and may open up the possibility to operate the synthesis according to the fluctuating nature of renewable sources.

Nevertheless, unresolved technical questions need to be answered at this point. Those are:

- What knowledge is needed for controlling a dynamic process in small-to-medium-size businesses?
- Can all different process steps be aligned in dynamic operation? What are their general limitations?
- What is the potential to reduce storages through dynamic synthesis?
- What are considerable “dynamic time periods” and ramping scenarios that plants need to tolerate?
- Can the prerequisites from “dynamic time periods” be met by reactors and/or plants?
- How is overall higher efficiency correlated to values of buffer reduction?

In the scope of this manuscript and the following part two, most of the above questions will be addressed from the point of view of a microstructured FT reactor. However, to fully answer these questions, information from other steps, i.e., from hydrogen generation to syngas production, need to be included.

2. Materials and Methods

2.1. Analysis in Transient and Steady-State Operation

The steady-state analysis of the product phases, applied also in this study, is based on gas chromatography (GC) of the individual phases and the gravimetric measurement of liquid and solid phases. Details are explained in previous publications from our group [10–14]. Calculation of weight hourly space velocity (WHSV), the chain growth probability (α), conversion levels, selectivity, and productivity are described in detail there as well; those calculations do not differ from methods widely used in literature.

However, since regular GC analysis is too slow for analyzing transient experiments, a mass spectrometer (MS) was additionally used to measure gaseous products in intervals of several seconds, which is a justified time period for process changes below the minute-scale. The used device (V&F, Germany) applies standard electron impact ionization for hydrogen and chemical ionization to avoid fragmenting of larger molecules. It consists of three main parts:

1. A Diluter 004 that dilutes the sample with Ar to avoid detector overloading (below 500,000 counts s^{-1}). Measurements were performed at 1:20 up to 1:30 dilution. Pressure fluctuation from 0.02–0.5 MPa can be compensated.
2. An Airsense 2000 unit that can apply three different gases (or mixtures thereof) with different ionization energies: Hg (10 eV), Xe (12 eV) and Kr (14 eV); these gases can be switched within several milliseconds. Electron impact ionization is used to generate primary ions; those ions hit sample molecules and transfer their charge. A quadrupole high-frequency mass filter then separates gaseous molecules based on their mass number (0–500 amu) while the sample can be continuously measured with an impact detector using pulse counting electronics. Depending on the switching times of the quadrupole, the ionization gas and the required number of signals, the interval for a new measurement can range between < 1 s and several seconds. For detecting CO, CO_2, CH_4, and C_3H_8, approximately 3 s were needed to apply a mixture of Xe and Kr.
3. An H-Sense unit where the sample is ionized via electron impact ionization so the concentration of H_2 can be measured in response times below 300 ms.

2.2. Experimental Test Rig

The pilot scale test rig is detailed elsewhere [15]. In brief, it consists of

1) a gas feeding system with mass flow controllers (MFCs; Brooks, NL),
2) a microstructured pilot scale reactor with evaporation cooling in patented design (Figure 3) and a reaction volume of approx. 150 cm^3 designed to produce around 7 L of liquid product per day, depending on the process conditions; it was filled with 120 g commercial catalyst with 20 wt.% CO on optimized alumina,
3) a hot trap (HT) and cold trap (CT) to capture the different product phases; a micro-heat exchanger (μHE) cools down the stream between both traps (Figure 4).

Gaseous products are measured online via GC after a backpressure regulator. The setup is almost identical to previous publications [11,13,15] except for the Quick Sampling (QS) site (see Section 2.4). Setup, reactor and catalyst were operated for approx. 6500 h before the experiments in this work, mostly in standby mode but also several hundred hours of FTS reaction. In standby mode, small amounts of H_2 and N_2 were dosed at 170 °C reactor temperature to preserve the catalyst from oxidation.

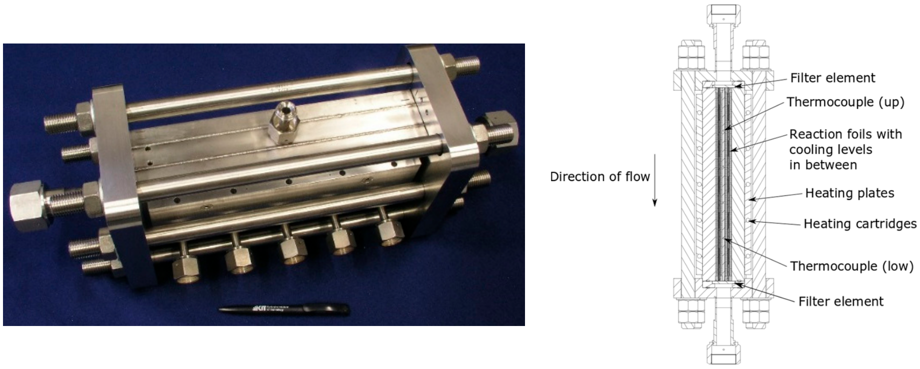

(**a**) (**b**)

Figure 3. (**a**) Picture of the micro-structured packed-bed reactor used in this study; (**b**) CAD scheme of the device in respect of the direction of flow and the position of different foil structures and thermocouples.

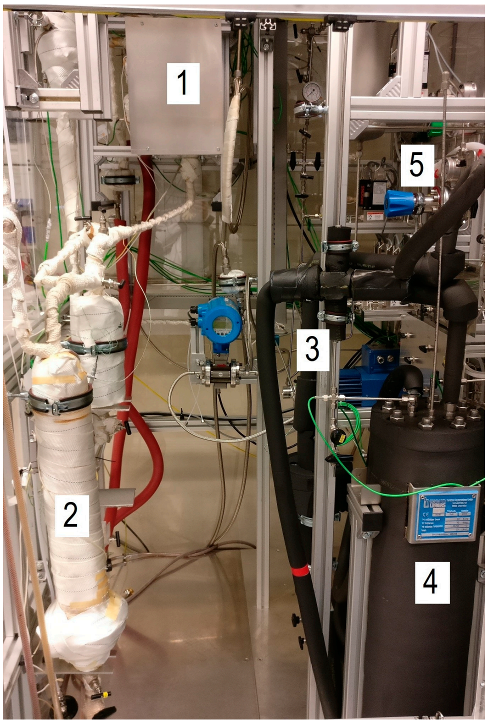

Figure 4. Photograph of the test rig used in this work. It contains the reactor in its insulation box (1), the HT (2), μHE (3), CT (4), and the back-pressure regulator (5).

2.3. Residence Time Distribution and Dead Time Measurements (Non-Reactive and Reactive Mode)

The determination of the residence time distribution (RTD) is an important criterion for the characterization and description of any chemical plant [69–73]. It indicates the average residence time and potential back-mixing of molecules in the reaction apparatus and system periphery. Knowledge of the RTD is of utmost importance in unsteady-state operation as back-mixing is taking additional influence on time-resolved product composition and on composition of recycle streams.

The RTD is influenced by molecular diffusion, shear forces and forced convection depending on laminar or turbulent conditions and on geometric designs of an apparatus. It is usually determined through tracer experiments. A marker substance is added to the inlet flow, which is then observed at the outlet. Two approaches are usually chosen to introduce a tracer; a pulse or a displacement marking. In this work, the latter strategy was the method of choice, since changes in the feed gas concentration are similar to displacement and can be described accordingly [74].

The sum function $F(t)$ indicates the share of the tracer that has already left the investigated system as a function of time t. It is directly accessible from a displacement marking. The common definition of the first momentum μ_1 is used according to Equation (2) to define the average residence time τ calculated from $F(t)$, [74]

$$\mu_1 = \tau = \int_0^1 t \, dF(t). \tag{2}$$

The MS was used to measure the F curve and a dead time without reaction (non-reactive) by adding CO_2, for details see below. The dead time is defined as the time where the signal approaches a constant value i.e., $F(t) = 1$. It was measured before the reactor and after each major system component, which includes the volume of tubing in between (see Figure 5).

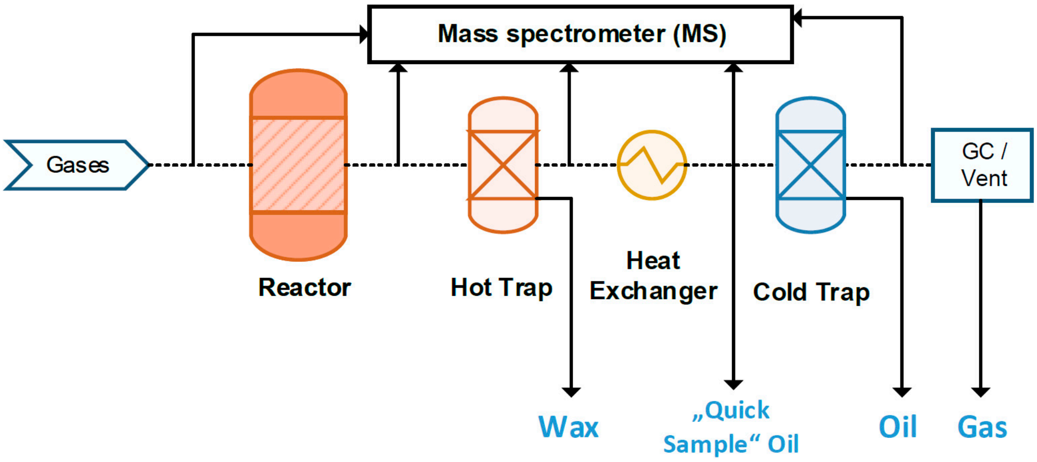

Figure 5. Basic flow scheme of the setup from feed gas dosing to product sampling. The MS was attached at the marked locations in non-reactive mode to investigate the dead time from gas dosage to the respective position.

The respective volumes between each location of measurement are listed in Table 1.

Table 1. List of volumes and applied temperature levels for the main components of the test rig.

System component	Volume (L)	Temperature (°C)
Reactor	0.15	220–250
HT/µHE	4.8	170
CT	25	10

Inert tracer experiments [75,76] were conducted with a total flow of 19 L min^{-1} hydrogen at 3 MPa; total flow and pressure are similar to values in reactive mode (see Table 3). To keep the total flow rate, an additional flow of 1 L min^{-1} of nitrogen was replaced by CO_2. After detecting 5 vol.% at the outlet, the gases were switched again. Three repetitions were carried out for each location in the test rig. Table 2 gives an overview over the adjusted parameters for RTD and dead time measurements in non-reactive mode. It also shows the threshold values of H_2/CO (“high” and “low” ratio), which were switched back and forth, in reaction experiments (reactive mode) to compare with results from non-reactive measurements (see also Section 2.5).

Table 2. List of parameters for response measurements in non-reactive and reactive mode.

Mode	Setup	Total gas flow (L min^{-1})	H_2 content (vol.%)	N_2 content (vol.%)	CO content (vol.%)	CO_2 content (vol.%)	Temperature (°C)	Pressure (MPa)	H_2/CO (-)
Non-reactive	CO_2 on/off	20	95	5/0	0	0/5	225	3	-
Reactive	H_2/CO high	17	50	25	25	0	238	3	1.95
Reactive	H_2/CO low	17	35	40	25	0	237	3	1.38

2.4. Quick Liquid and Gas Sampling (QS)

Since the CT is the largest vessel in the system with a volume of about 25 L, a quick liquid sampling (QS) was a prerequisite to avoid large back-mixing of gas as well as liquid in the vessel and to be able to detect gas phase changes in reaction experiments. Gas sampling before the hot trap would not have been possible due to potential damage of the MS from condensation of wax and liquid components inside the device. In Figure 6, the installation of the QS site is shown. Basically, it represents a glass vessel capable to collect a few milliliters of liquid in a minute-scale sampling time.

It could be connected via a needle valve to the effluent of the heat exchanger at a certain point in time. The accompanied gaseous products entering the QS were directed to the MS during the time when the liquid samples were captured. The needle valve was opened into a certain position to avoid pressure loss in the setup.

Figure 6. Photograph of the QS site that was installed to avoid gas and liquid back-mixing in the CT. Sampling included the collection of the liquids with the concurrent online-measurement of the gaseous product phase via MS. A minute-scale sampling time was needed to gather enough liquid for analysis.

2.5. Dynamic Profiles by Oscillation of Feed Concentration

For switching the gas composition under the reaction, two different parameter combinations were chosen, see also Table 3. The syngas ratio was significantly changed from 1.95 (“H_2/CO high”) to 1.38 (“H_2/CO low”) in those settings so that a measurable change in the product composition could be expected [6,76]. At this point, the ratio was not lowered further in order not to force deactivation of the catalyst by high hydrogen consumption at increasing CO partial pressure. The length of each oscillation cycle was selected based on the dead time experiments.

2.6. Evaporation Cooling as a Tool for Influencing the Reactor Temperature

Besides their potential ability to cope with quick changes of feed gas concentration due to a good plug flow type behavior in gaseous fluids, microstructured reactors further possess a high flexibility with regard to temperature changes due to the good heat transfer properties. This might be even more valid when evaporation cooling is applied since the reaction temperature could be manipulated with the evaporation conditions. Absolute pressure determines the boiling temperature in the water-steam system. The temperature is constant as long as both phases exist, thus, water is always fed in excess compared to the evolving reaction heat. Overheating of steam should be avoided due to the small specific heat capacity of steam [15,77]. Equation (3) shows the maximum amount of heat flux ($\Delta\dot{H}_{max}$) that liquid water may take up from starting temperature T_0 to boiling temperature T_b, over fully evaporating and overheating to temperature T_{end}.

$$\Delta\dot{H}_{max} = \dot{m}_{H_2O} \cdot c_{p,l} \cdot (T_b - T_0) + \dot{m}_{H_2O} \cdot \Delta h_v + \dot{m}_{H_2O} \cdot c_{p,g} \cdot (T_{end} - T_b) \quad (3)$$

with $\dot{m}_{H_2O}$ being the mass flow of water (g s^{-1}), $c_{p,l}$ being the specific heat capacity of liquid water (J g^{-1} K^{-1}), Δh_v being the specific evaporation enthalpy of water (J g^{-1}), and $c_{p,g}$ being the specific heat capacity of steam (J g^{-1} K^{-1}).

Figure 7 depicts the relationship between the pump’s water mass flow and the resulting enthalpy it could potentially take up. The theoretical vapor fraction is also shown, assuming the total reaction enthalpy is transferred to the water. An average reaction enthalpy from about 30 different experimental conditions is displayed for comparison. The reaction enthalpy ΔH_R (W) was calculated based on Equation (4) from the standard reaction enthalpy ΔH_R^0 (−158.5 kJ mol^{-1}), CO conversion X_{CO} (-) and the molar feed flow of CO, $\dot{n}_{CO,in}$ (mol s^{-1}).

$$\Delta H_R = \Delta H_R^0 \cdot \dot{n}_{CO,in} \cdot X_{CO}. \tag{4}$$

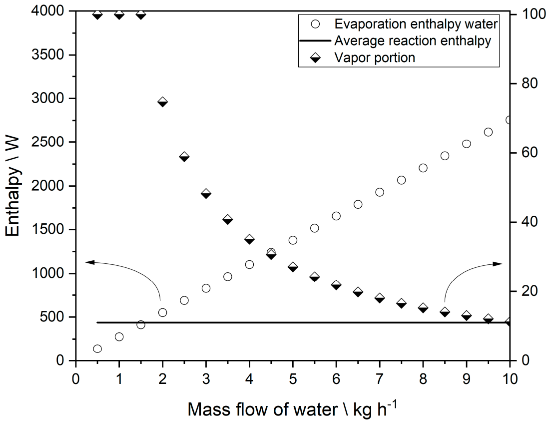

Figure 7. Enthalpy which water could take up (according to Equation (3)) if reaction heat released in the pilot scale reactor (according to Equation (4)) was fully transferred to the cooling medium as a function of the mass flow of water. The plotted vapor portion is calculated under consideration of a pre-heating from 223.6 °C up to the boiling point 233.6 °C at 3 MPa inside the reactor.

Experiments showing the system's cooling functionality have been conducted before [15]—a typical water mass flow, which has been set, ranged between three 3 and 4 kg/h.

Excess water, in an average operation case of the pilot scale reactor above a required minimum water mass flow of approximately 1.5 kg h^{-1}, can remove additional heat in a phase of cooling down the reactor. This heat is originating from the total heat capacity of the reactor. A strategy to reduce the reactor temperature could thus be to lower the pressure. Experiments to determine the reactor temperature response by changing water pressure have been carried out in this work. The water pressure was adjusted from 3 MPa to 2.4 MPa and back to 3 MPa by changing 0.1 MPa of pressure every 5 minutes while observing changes in the measured temperatures.

3. Results and Discussion

3.1. General Product Composition and Comparison to Quick Sampling

Product water is collected in the cold trap and is separated manually from the liquid FTS product (oil phase). There were several hydrocarbon species identified in this water. The average concentration of alcohols that could be analyzed from methanol to heptanol accounted for 21.78 g L^{-1} (±6.04 g L^{-1}) representing 18 randomly selected water samples. Table 3 gives an overview of the alcohol concentrations for calibrated species measured by GC applying the flame ionization detector (FID) signal. Residual 7.41% of the total signal area corresponds to uncalibrated peaks. Alcohol formation is strongly dependent on the process parameters, thus the large given average deviation.

Table 3. Average alcohol content in FTS water measured by GC-FID as an average of 18 randomly selected water samples. Residual uncalibrated signal areas are also given.

Species/property	Concentration
Methanol	14.19 ± 4.14 g L^{-1}
Ethanol	4.64 ± 1.44 g L^{-1}
Propanol	1.21 ± 0.32 g L^{-1}
Butanol	0.79 ± 0.27 g L^{-1}
Pentanol	0.66 ± 0.19 g L^{-1}
Hexanol	0.23 ± 0.06 g L^{-1}

Heptanol	0.07 ± 0.02 g L^{-1}
Total concentration	21.78 ± 6.04 g L^{-1}
Uncalibrated peaks	7.41 ± 2.10 %

Average product properties of 51 FT oil samples collected in the cold trap and the average chain growth probability, are listed in Table 4. Alcohols and iso-alkanes in the oil fraction could not be separated in the applied GC method. For that reason, those values are provided as sum.

Table 4. Average sample composition and chain growth probability α of FT oils determined from 51 samples collected in the CT.

Property	Content/value
Av. alkane content (oil)	78.18 ± 3.21 wt.%
Av. alkene content (oil)	14.14 ± 4.03 wt.%
Av. iso-alkane and alcohol content (oil)	7.69 ± 1.78 wt.%
Av. carbon chain length (oil)	10.71 ± 0.79 atoms
Av. probability of chain growth (α)	88.44 ± 1.53%

The detected alcohols are valuable products as they possess a high octane number, which is applicable for gasoline substitution [49]. It must be decided economically if the upgrading and separation process is viable at this point. Iso-alkenes are favorable for cold-flow properties of diesel and kerosene substitution; alkenes generally need to be converted by hydrogenation to reduce degradation effects in liquid storage or during distillation. N-alkanes and iso-alkanes possess good combustion properties with regard to low soot formation.

Previous to the cycling experiments it was checked in stationary reaction conditions whether the QS samples differ or not from the CT sample as a function of the QS sampling time. A certain discrepancy between the samples' characteristics could be observed (Table 5).

Table 5. Illustrative sample composition of FT oil from 5 min sampling at QS site and a sample taken at the CT. Stationary reaction conditions 245 °C, 3 MPa total pressure, a H_2/CO ratio of 1.96, and a WHSV of 4.37 h^{-1}.

Property	QS	CT
Alkane content (oil)	80.22 wt.%	75.77 wt.%
Alkene content (oil)	9.50 wt.%	17.70 wt.%
Iso-alkane and alcohol content (oil)	10.28 wt.%	6.53 wt.%
Carbon chain length (oil)	11.47 atoms	9.56 atoms

Around 5 minutes of sampling time at the QS site was required to obtain enough liquid sample for analysis. A longer sampling of e.g., 8 min showed no difference to 5 min samples, but pressure loss in the reaction setup occurred, which is not tolerable for the experiments. Thus, 5 min of sampling time was chosen for all experiments.

Additionally, cooling of the QS site was performed similar to the conditions at the CT (10 °C) to see if there is an effect of flashing temperature. However, the cooling had no effect on the composition of the sample. Thus the flashing pressure is most likely the reason for a shorter average chain length in the CT samples. While reducing the pressure in the QS site to around 0.1 MPa, the CT operates at 30 MPa in which the equilibrium conditions of the gas-liquid system are different. At lower total pressure, the partial pressure of all species is reduced; this lowers not only the overall liquid amount but also shifts the composition towards smaller molecules in the gas phase and consequently leads to a larger average chain length in the QS sample. Solubility effects may also play a role influenced by the equilibration time, which could explain the different alkene and isomer content. In the CT, the time for equilibration is much longer.

As mentioned in Section 2.1, online GC analysis of the product gas takes too long for a proper resolution in dynamic operation. Although resolution is enhanced by MS, the combination of species in the effluent gas and the typical drift of the MS system led us to the conclusion that a calibration of the individual signals is not straightforward. Instead, an analysis of the changes by MS during the change of reaction conditions was sufficient in all presented cases while exact gas compositions could be crosschecked by GC during stationary phases (see Section 3.2). The installed QS system was working properly with regards to parallel gas and liquid sampling.

3.2. Steady-State Compositions at Low and High H_2/CO Conditions

Under stationary conditions, the H_2/CO ratio is influencing the product composition; see Section 2.5. To know the steady-state composition and to be able to compare it to the transient composition, Table 6 shows the values obtained at the QS site in stationary conditions.

Table 6. Liquid product composition and average carbon chain length in stationary reaction experiments determined at the QS site as a function of the low and high H_2/CO threshold condition.

Setup	H_2 conversion (vol.%)	CO conversion (vol.%)	S_{C1} (mol.%)	S_{C5+} (mol.%)	Alkane content (wt.%)	Alkene content (wt.%)	Iso-alkane + alcohol content (wt.%)	Av. carbon chain length (-)
H_2/CO high	68.43	62.71	12.68	78.38	83.74	10.57	5.68	11.99
H_2/CO low	63.20	41.09	9.53	82.74	78.02	14.31	7.67	12.37

3.3. RTD Measurements—None-Reactive Mode

In Figure 8, the applied change in CO_2 concentration and the respective delay is plotted as the F curve for the individual positions inside the pilot scale test rig. The provided times are the determined dead times. The time $t = 0$ min represents the time when the new setpoints were adjusted in the MFCs.

Those experiments provide crucial information on the signal delay measured at different positions of the test rig. The signal delay from the MFCs to the MS already accounts for around 24 s. The microstructured reactor itself added about 60 s to the delay. Compared to the delay of all other system components, this is negligibly short. Dead times need to be considered in the interpretation of data, since the hot gaseous-liquid product mixture cannot be properly analyzed before the µHE.

The reactor signal indicates its general construction properties, i.e., that the inlet and outlet flanges are constructed as steep funnels, where the signal is disturbed. The signal should pass the reactor in 40 s according to the hydrodynamic residence time. Nevertheless, the first steep signal increase could indicate that the catalyst bed was not equally packed inside the microchannels as it occurs already at a similar time scale to the dead time from MFCs to analytics.

The increase in delay after the µHE of about 17.5 min is due to considerable back-mixing in the HT (see Table 2). The HT is located just in front of the µHE with only a small distance covered by tubes separating both elements. Thus, a similar curve was obtained after both the HT and the µHE due to almost identical average residence times.

A signal delay of over 82 min induced by the large volume of the CT vessel made product measuring at this position challenging. This proves the importance of the QS in order to reduce signal lag, implied by the multi-step condensation system, to 17.5 min. All consecutive measurements were carried out at the QS site after the µHE in reactive mode.

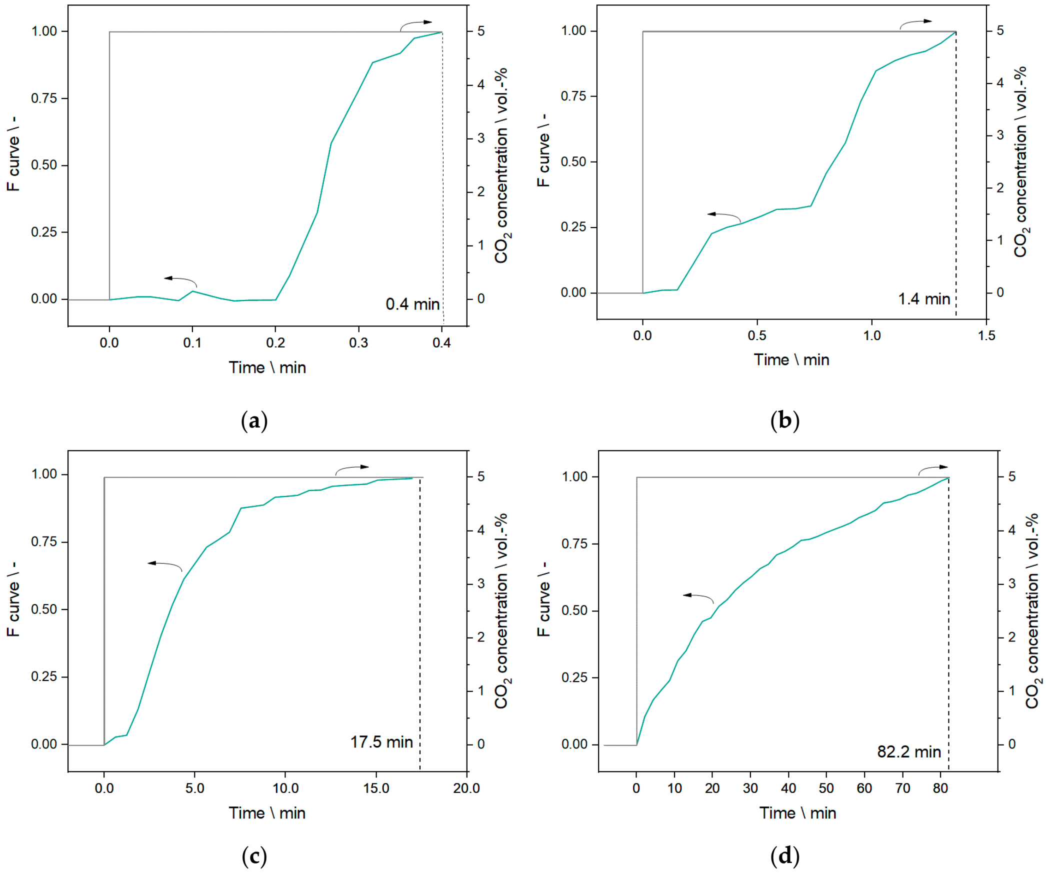

(**a**) (**b**)

(**c**) (**d**)

Figure 8. F curves determined in non-reactive mode. (**a**) F curve for the setup from MFCs directly to MS; (**b**) from MFCs to behind FT reactor; (**c**) from MFCs to behind the µHE; (**d**) from MFCs to behind the CT.

3.4. RTD Measurements—Reactive Mode

Figure 9 shows the response measured by MS and in the analyzed liquid sample collected at the QS site after switching from "H₂/CO low" to "H₂/CO high" at t = 0 min. Methane and propane are chosen as exemplary product molecules due to low signal noise in the MS.

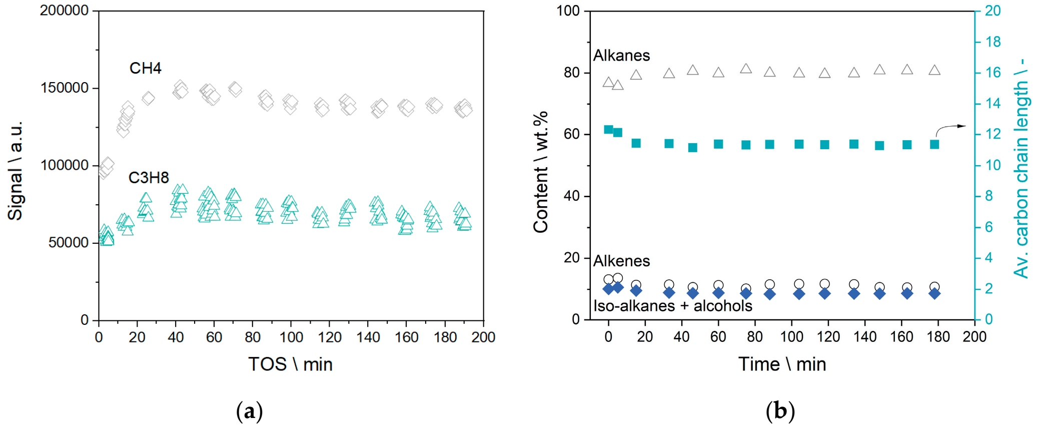

(**a**) (**b**)

Figure 9. Response measurements in reactive mode at the QS site during switching from "H_2/CO low" to "H_2/CO high". (**a**) Signals for methane and propane obtained by MS; (**b**) Product composition of the liquid FT oil with regard to contents of alkanes, alkenes and iso-alkanes + alcohols and the average carbon chain length of the liquid product.

The gas phase showed a rather constant signal after approx. 20 min, which is in line with the results from the non-reactive RTD measurement including the slight difference in total flow rate. The liquid phase showed stationary properties after 15–20 min, which is also in agreement with results from Section 3.3. No additional delay is found which could originate from processes on the catalyst. Changes on the catalyst and in the reactor obviously occur much faster, but measuring them in an appropriate time-resolved manner is impossible with wax molecules present in the product gas. A signal delay of 20 min always thus needs to be considered when measuring changes in transient operation.

3.5. Cycle Experiments—Concentration Switching

With obtained results from dead time measurements, a time period of 30 min was chosen for the first oscillation cycles. It was switched back and forth between "H_2/CO low" and "H_2/CO high". Eight minute oscillation cycles were further applied, representing a little bit less than half of the dead time in non-reactive mode, i.e., the gas and liquid composition may not be able to reach its threshold values obtained at "H_2/CO low" and "H_2/CO high" in stationary operation.

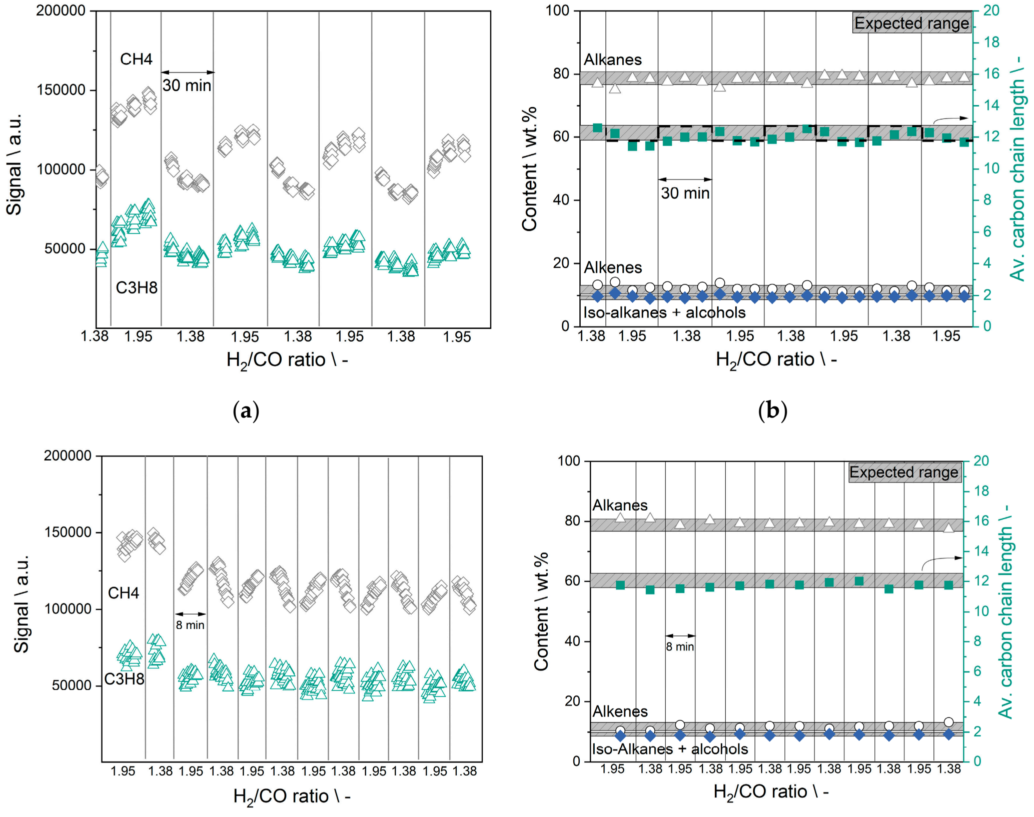

(**a**) (**b**)

(**c**) (**d**)

Figure 10. Product composition obtained at the QS site in reaction experiments as a function of the switching between "H_2/CO low" (H_2/CO = 1.38) and "H_2/CO high" (H_2/CO = 1.95) with different switching times. Vertical lines represent the switching actions and horizontal grey bars represent the expected value range for a certain species obtained from stationary reaction experiments. (**a** and **c**)

MS signals for methane and propane. (**b** and **d**) Product composition of the liquid FT oil samples regarding contents of alkanes, alkenes and iso-alkanes + alcohols as well as average carbon chain length of the liquid product. (**a** and **b**) 30 min switching time. (**c** and **d**) 8 min switching time.

Figure 10 shows the response measured by MS and in the analyzed liquid sample collected at the QS site from both experiments as a function of the setpoint of the H_2/CO ratio. The vertical lines represent the switching actions so that the abscissa is also representing a time axis. Horizontal grey bars represent the expected value range for a certain species obtained from stationary reaction experiments.

For cycles with switching times above the determined dead time (in this case 30 min), a good agreement between the liquid composition and the expected data from stationary experiments is obvious for the last data point in each segment. Also, the progression of the signal for methane (and also partially for propane) in the gaseous phase is settling towards a near constant value at the end of each segment from the second cycle on. Within 4 h of experiment, no deviation from the expected oscillation profile was determined.

In the case of the shorter cycles, i.e., 8 min each, a continuous steep increase or decrease of the gas concentrations is occurring throughout each switching segment, while the liquid phase seems to have reached a semi-steady state within the expected range. This is obviously a resolution problem, with 5 minutes of sampling in a 8-min time frame, integrating 62% of the whole sample.

Throughout the experiments, it could be demonstrated that the pilot scale test rig was able to cope with the changes in the feed gas concentration independently of the observed dead time of 20 min even at lower switching times. The microstructured reactor effectively compensated all changes without enhanced temperature differences in the bed. No clear drop of catalyst activity could be observed; a more detailed analysis will be provided in the second part of the study.

It is legitimate to assume that stationary reaction kinetics can be used to describe even the performed quick changes in reaction conditions. Intermediate reaction states seem to play a negligible role, considering back-mixing in product traps, and parameter changes always lead to the expected product characteristics. The application of stationary reaction kinetics in dynamic systems has been suggested by other groups [71,78] and seems also appropriate here.

3.6. Cycle Experiments—Temperature Switching

Temperature manipulation is especially interesting for applications with quickly changing feed gas flows or concentrations in order to control conversion levels at all times [79,80]. A special case in this regard is that catalyst degradation due to coke formation could occur if all hydrogen is consumed in the reaction. Experiments that investigated the temperature response of the reactor due to pressure changes in the water-cooling cycle are presented in Figure 11.

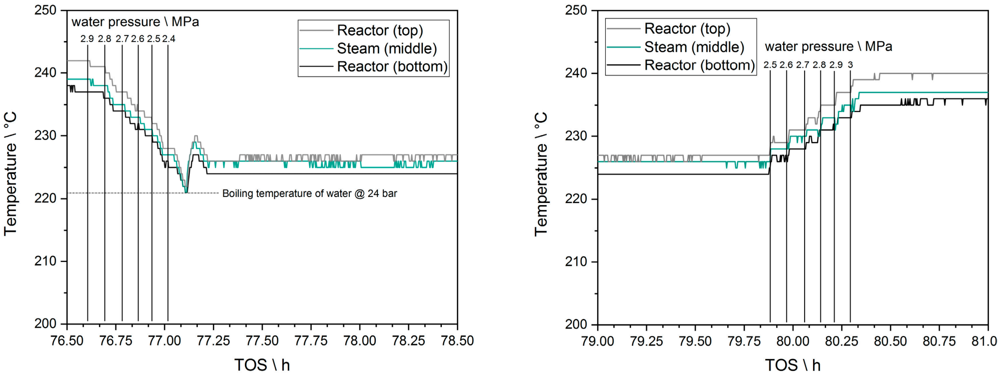

(**a**) (**b**)

Figure 11. Influence of changing the water pressure in the FT cooling cycle (**a**) from 3 to 2.4 MPa and (**b**) back to 3 MPa in 0.1 MPa steps every 5 minutes on the reactor temperatures as a function of time; steam outlet temperature and inlet (top) and outlet (bottom) temperature inside the metal plates of the reactor.

Changing the water pressure by 0.1 MPa every 5 minutes always resulted in a quick temperature response; the inlet and outlet temperature of the reactor (see Figure 3b) measured inside the metal plates followed the steam temperature immediately. Once the pressure was lowered from 2.5 to 2.4 MPa, a fluctuation in temperature by 2–3 °C occurred (Figure 11a). This effect did not occur when increasing the pressure back to 3 MPa (Figure 11b). Increasing the pressure shifts evaporation back in the liquid regime rather than favoring overheating of the steam, which might explain the temperature fluctuation while decreasing the pressure.

In sum, it was easy to change system temperature in both directions by adjusting the pressure and the reactor followed almost immediately under the applied conditions. No increasing temperature gradients were observed nor did a runaway occur. The applied temperature change of around 15 °C in 20 min corresponds to a considerable shift of the conversion levels. This highlights the enormous potential of the applied microreactor technology to cope with relative fast feed fluctuations.

4. Conclusions

A previously reported pilot scale test rig with microstructured packed bed reactor for FT synthesis cooled by evaporation of water was intensively tested in dynamic application. Challenges arising from the setup size, the multi-step condensation of the products, and required process control were discussed. Future energy systems may include PtX technology in a similar pathway as presented here in order to produce renewable, carbon neutral high-performance fuels with a high energy density. Those properties are needed for effective energy storage. In order to decrease buffer systems for intermediate gases, a dynamic operation might lower their demand, size and cost. As a proof of concept, residence time measurements as well as concentration and temperature cycles were carried out in the setup.

Dead times originating from the test rig, which were determined at multiple locations with an online mass spectrometer, are already considerably high compared to the applied reactor size. This is due to necessary two-step phase condensation. Nevertheless, changes in the catalyst bed occur much faster than they can be detected by the analysis. The reactor system answers to changes in a timely manner, based on the interpretation of the measured signals.

Evaporation cooling was proven to allow quick performance changes by immediately affecting the reaction temperature as a function of water pressure without spatial or temporal temperature gradients. In the current setup, quick temperature changes via pressure regulation were applied by hand, which could be automated for faster process control and response time in the future. This possibility opens up further applications that might require more intense process control, such as highly dynamic applications. A conversion-dependent increase or decrease of temperature could easily be developed and automated.

Quick changes in the feed gas concentration could be applied in the reactor without obvious influence on its operation. Intermediate reaction states did not influence the product distribution. This allows the use of stationary reaction kinetics for operational estimations in conjunction with residence time models.

In operando-techniques might be appropriate to determine what happens to the catalyst bed if changes are applied quickly. While FTS conditions are quite challenging for such analysis, some applications were used in the past for similar processes [55,81–85].

To answer the questions posted in Section 1.2, the findings hint for the advantageous properties of the applied reactor system. While questions regarding applications for a realistic "dynamic" context cannot be answered at this point, a second part of this work will provide more insight into technical system limits by applying even harsher process conditions. The findings of this work will strongly contribute to PtL projects like PowerFuel, where a dynamic synthesis is part of the research schedule [86].

Author Contributions: Conceptualization, M.L. and P.P.; Methodology, M.L.; Software, M.L.; Validation, M.L. and P.P.; Formal Analysis, M.L.; Investigation, M.L.; Resources, M.L. and P.P.; Data Curation, M.L.; Writing—Original Draft Preparation, M.L.; Writing—Review & Editing, M.L. and P.P.; Visualization, M.L.; Supervision, P.P.; Project Administration, M.L. and P.P.; Funding Acquisition, P.P. All authors have read and agreed to the published version of the manuscript.

Funding: We gratefully acknowledge funding from the Vector Stiftung under the project acronym DynSyn.

Acknowledgments: We kindly thank the Vector Stiftung for financial support of this work in the frame of the DynSyn project.

Conflicts of Interest: The authors declare no conflict of interest.

References

1. Fischer, F.; Tropsch, H. The preparation of synthetic oil mixtures (synthol) from carbon monoxide and hydrogen. *Brennst. Chem.* **1923**, 276–285.
2. Dry, M.E. The Fischer-Tropsch process: 1950–2000. *Catal. Today* **2002**, *71*, 227–241, doi:10.1016/S0920-5861(01)00453-9.
3. de Klerk, A. *Fischer-Tropsch Refining;* Wiley-VCH Verlag GmbH & Co. KGaA: Weinheim, Germany, 2011; ISBN 9783527635603.
4. Khorashadizadeh, M.; Atashi, H.; Mirzaei, A.A. Process conditions effects on Fischer-Tropsch product selectivity: Modeling and optimization through a time and cost-efficient scenario using a limited data size. *J. Taiwan Inst. Chem. Eng.* **2017**, 80, 709–719, doi:10.1016/j.jtice.2017.09.006.
5. Dry, M.E. Practical and theoretical aspects of the catalytic Fischer-Tropsch process. *Appl. Catal. A-Gen.* **1996**, *138*, 319–344, doi:10.1016/0926-860X(95)00306-1.
6. Maitlis, P.M.; de Klerk, A. *Greener Fischer-Tropsch Processes for Fuels and Feedstocks*; Wiley-VCH: Weinheim, Germany, 2013; ISBN 3527329455.
7. Lu, Y.; Lee, T. Influence of the Feed Gas Composition on the Fischer-Tropsch Synthesis in Commercial Operations. *J. Nat. Gas Chem.* **2007**, *16*, 329–341, doi:10.1016/S1003-9953(08)60001-8.
8. *Fundamentals of Industrial Catalytic Processes*, 2nd ed.; Bartholomew, C.H., Farrauto, R.J., Eds.; Wiley-Interscience: Hoboken, NJ, USA, 2010; ISBN 9780471730071.
9. Todic, B.; Nowicki, L.; Nikacevic, N.; Bukur, D.B. Fischer-Tropsch synthesis product selectivity over an industrial iron-based catalyst: Effect of process conditions. *Catal. Today* **2016**, *261*, 28–39, doi:10.1016/j.cattod.2015.09.005.
10. Myrstad, R.; Eri, S.; Pfeifer, P.; Rytter, E.; Holmen, A. Fischer-Tropsch synthesis in a microstructured reactor. *Catal. Today* **2009**, *147*, S301–S304.
11. Piermartini, P.; Boeltken, T.; Selinsek, M.; Pfeifer, P. Influence of channel geometry on Fischer-Tropsch synthesis in microstructured reactors. *Chem. Eng. J.* **2017**, *313*, 328–335, doi:10.1016/j.cej.2016.12.076.
12. Sun, C.; Luo, Z.; Choudhary, A.; Pfeifer, P.; Dittmeyer, R. Influence of the Condensable Hydrocarbons on an Integrated Fischer-Tropsch Synthesis and Hydrocracking Process: Simulation and Experimental Validation. *Ind. Eng. Chem. Res.* **2017**, *56*, 13075–13085, doi:10.1021/acs.iecr.7b01326.
13. Sun, C.; Zhan, T.; Pfeifer, P.; Dittmeyer, R. Influence of Fischer-Tropsch synthesis (FTS) and hydrocracking (HC) conditions on the product distribution of an integrated FTS-HC process. *Chem. Eng. J.* **2017**, *310*, 272–281, doi:10.1016/j.cej.2016.10.118.
14. Sun, C. Direct Syngas-to-Fuel: Integration of Fischer—Tropsch Synthesis and Hydrocracking in Micro—Structured Reactors. Ph.D. Thesis, Karlsruhe Institute of Technology, Karlsruhe, Germany, 2017.
15. Loewert, M.; Hoffmann, J.; Piermartini, P.; Selinsek, M.; Dittmeyer, R.; Pfeifer, P. Microstructured Fischer-Tropsch reactor scale-up and opportunities for decentralized application. *Chem. Eng. Technol.* **2019**, 2202–2214, doi:10.1002/ceat.201900136.
16. Adesina, A.A. Hydrocarbon synthesis via Fischer-Tropsch reaction: Travails and triumphs. *Appl. Catal. A-Gen.* **1996**, *138*, 345–367, doi:10.1016/0926-860X(95)00307-X.
17. Sousa, B.V.D.; Rodrigues, M.G.F.; Cano, L.A.; Cagnoli, M.V.; Bengoa, J.F.; Marchetti, S.G.; Pecchi, G. Study of the effect of cobalt content in obtaining olefins and paraffins using the Fischer-Tropsch reaction. *Catal. Today* **2011**, *172*, 152–157, doi:10.1016/j.cattod.2011.02.035.

18. Dry, M.E. Commercial conversion of carbon monoxide to fuels and chemicals. *J. Organomet. Chem.* **1989**, *372*, 117–128, doi:10.1016/0022-328X(89)87082-2.
19. Rausch, A.K.; Schubert, L.; Henkel, R.; van Steen, E.; Claeys, M.; Roessner, F. Enhanced olefin production in Fischer-Tropsch synthesis using ammonia containing synthesis gas feeds. *Catal. Today* **2016**, *275*, 94–99, doi:10.1016/j.cattod.2016.02.002.
20. Le Quéré, C.; Andrew, R.M.; Friedlingstein, P.; Sitch, S.; Hauck, J.; Pongratz, J.; Pickers, P.A.; Korsbakken, J.I.; Peters, G.P.; Canadell, J.G.; et al. Global Carbon Budget 2018. *Earth Syst. Sci. Data* **2018**, *10*, 2141–2194, doi:10.5194/essd-10-2141-2018.
21. Horvath, S.; Fasihi, M.; Breyer, C. Techno-economic analysis of a decarbonized shipping sector: Technology suggestions for a fleet in 2030 and 2040. *Energy Convers. Manag.* **2018**, *164*, 230–241, doi:10.1016/j.enconman.2018.02.098.
22. Kousoulidou, M.; Lonza, L. Biofuels in aviation: Fuel demand and CO_2 emissions evolution in Europe toward 2030. *Transport. Res. D* **2016**, *46*, 166–181, doi:10.1016/j.trd.2016.03.018.
23. Guandalini, G.; Robinius, M.; Grube, T.; Campanari, S.; Stolten, D. Long-term power-to-gas potential from wind and solar power: A country analysis for Italy. *Int. J. Hydrog. Energy* **2017**, *42*, 13389–13406, doi:10.1016/j.ijhydene.2017.03.081.
24. Vázquez, F.V.; Koponen, J.; Ruuskanen, V.; Bajamundi, C.; Kosonen, A.; Simell, P.; Ahola, J.; Frilund, C.; Elfving, J.; Reinikainen, M.; et al. Power-to-X technology using renewable electricity and carbon dioxide from ambient air: SOLETAIR proof-of-concept and improved process concept. *J. CO_2 Util.* **2018**, *28*, 235–246, doi:10.1016/j.jcou.2018.09.026.
25. International Energy Agency (IEA). *CO_2 Emissions from Fuel Combustion—Highlights*. Available online: https://www.iea.org/reports/co2-emissions-from-fuel-combustion-2019 (accessed on 27 March 2020).
26. Wagemann, K.; Ausfelder, F. *White Paper E-Fuels—Mehr Als Eine Option—Finale Version*; DECHEMA e.V.: Frankfurt a. M., Germany, 2017, SBN: 978-3-89746-198-7.
27. SAPEA—Science Advice for Policy by European Academies. *Novel Carbon Capture and Utilisation Technologies*; SAPEA: Berlin, Germany, 2018; ISBN 9789279820076.
28. Deutsche Energie-Argentur (DENA). *Study: Integrated Energy Transition*. Deutsche Energie-Agentur GmbH (dena): Berlin, Germany, 2018.
29. European University Association. Energy Transition and the Future of Energy Research, Innovation and Education: An Action Agenda for European Universities. *Int. J. Prod. Res.* **2017**, *53*, 59.
30. IRENA. Global Energy Transformation: A Roadmap to 2050. Available online: https://irena.org/publications/2018/Apr/Global-Energy-Transition-A-Roadmap-to-2050 (accessed on 27 March 2020).
31. IPCC. Global warming of 1.5 °C An IPCC Special Report on the impacts of global warming of 1.5 °C above pre-industrial levels and related global greenhouse gas emission pathways, in the context of strengthening the global response to the threat of climate change. Available online: https://www.ipcc.ch/sr15/ (accessed on 27 March 2020).
32. Tremel, A. *Electricity-Based Fuels;* Springer International Publishing: Basel, Switzerland, 2018; ISBN 9783319724584.
33. International Energy Agency (IEA). World Energy Outlook 2016. Available online: https://www.iea.org/reports/world-energy-outlook-2016 (accessed on 27 March 2020).
34. Vaillancourt, K.; Bahn, O.; Roy, P.O.; Patreau, V. Is there a future for new hydrocarbon projects in a decarbonizing energy system? A case study for Quebec (Canada). *Appl. Energy* **2018**, *218*, 114–130, doi:10.1016/j.apenergy.2018.02.171.
35. Ridjan, I.; Mathiesen, B.V.; Connolly, D. Terminology used for renewable liquid and gaseous fuels based on the conversion of electricity: A review. *J. Clean. Prod.* **2016**, *112*, 3709–3720, doi:10.1016/j.jclepro.2015.05.117.
36. Li, W.; Wang, H.; Jiang, X.; Zhu, J.; Liu, Z.; Guo, X.; Song, C. A short review of recent advances in CO 2 hydrogenation to hydrocarbons over heterogeneous catalysts. *RSC Adv.* **2018**, *8*, 7651–7669, doi:10.1039/C7RA13546G.
37. Reuß, M.; Grube, T.; Robinius, M.; Preuster, P.; Wasserscheid, P.; Stolten, D. Seasonal storage and alternative carriers: A flexible hydrogen supply chain model. *Appl. Energy* **2017**, *200*, 290–302, doi:10.1016/j.apenergy.2017.05.050.

38. Kotzur, L.; Markewitz, P.; Robinius, M.; Stolten, D. Time series aggregation for energy system design: Modeling seasonal storage. *Appl. Energy* **2018**, *213*, 123–135, doi:10.1016/j.apenergy.2018.01.023.
39. Brynolf, S.; Taljegard, M.; Grahn, M.; Hansson, J. Electrofuels for the transport sector: A review of production costs. *Renew. Sustain. Energy Rev.* **2018**, *81*, 1887–1905, doi:10.1016/j.rser.2017.05.288.
40. Leonard, G.; Francois-Lavet, V.; Ernst, D.; Meinrenken, C.J.; Lackner, K.S. Electricity storage with liquid fuels in a zone powered by 100% variable renewables. In Proceedings of the 12th International Conference on the European Energy Market-EEM15, Lisbon, Portugal, 19–22 May 2015.
41. Pleßmann, G.; Erdmann, M.; Hlusiak, M.; Breyer, C. Global Energy Storage Demand for a 100% Renewable Electricity Supply. *Energy Procedia* **2014**, *46*, 22–31, doi:10.1016/j.egypro.2014.01.154.
42. Kalghatgi, G. Is it really the end of internal combustion engines and petroleum in transport? *Appl. Energy* **2018**, *225*, 965–974, doi:10.1016/j.apenergy.2018.05.076.
43. Schemme, S.; Samsun, R.C.; Peters, R.; Stolten, D. Power-to-fuel as a key to sustainable transport systems—An analysis of diesel fuels produced from CO2and renewable electricity. *Fuel* **2017**, *205*, 198–221, doi:10.1016/j.fuel.2017.05.061.
44. Fuchs, G.; Lunz, B.; Leuthold, M.; Sauer, D.U. Technology Overview on Electricity Storage Overview on the Potential and on the Deployment Perspectives of Electricity Storage Technologies; Smart Energy for Europe Platform GmbH (SEFEP): Berlin, Germany, 2012.
45. Niaz, S.; Manzoor, T.; Pandith, A.H. Hydrogen storage: Materials, methods and perspectives. *Renew. Sustain. Energy Rev.* **2015**, *50*, 457–469, doi:10.1016/j.rser.2015.05.011.
46. Fuel Cell Technologies Office. Multi-Year Research, Development, and Demonstration Plan. Available online: https://www.energy.gov/eere/fuelcells/downloads/hydrogen-consortium-overview-part-2-3-electrolysis-webinar (accessed on 9 May 2019).
47. EnergyLab 2.0 Project Website. Available online: https://www.elab2.kit.edu/ (accessed on 25 March 2019).
48. Gill, S.S.; Tsolakis, A.; Dearn, K.D.; Rodríguez-Fernández, J. Combustion characteristics and emissions of Fischer-Tropsch diesel fuels in IC engines. *Prog. Energy Combust.* **2011**, *37*, 503–523, doi:10.1016/j.pecs.2010.09.001.
49. Tschann, P. Emission and Performance Studies of Alternative Fuels. Master's Thesis, Graz University of Technology, Graz, Austria, 2009.
50. Abu-Jrai, A.; Tsolakis, A.; Theinnoi, K.; Cracknell, R.; Megaritis, A.; Wyszynski, M.L.; Golunski, S.E. Effect of gas-to-liquid diesel fuels on combustion characteristics, engine emissions, and exhaust gas fuel reforming. Comparative study. *Energy Fuel* **2006**, 2377–2384.
51. *Fischer-Tropsch Synthesis: Catalysts and Chemistry*; van de Loosdrecht, J., Botes, F.G., Ciobica, I.M., Ferreira, A., Gibson, P., Moodley, D.J., Saib, A.M., Visagie, J.L., Weststrate, C.J., Niemantsverdriet, J.W., Eds.; Elsevier Ltd.: Amsterdam, The Netherlands, 2013; ISBN 9780080965291.
52. Albrecht, F.G.; König, D.H.; Baucks, N.; Dietrich, R.-U. A standardized methodology for the techno-economic evaluation of alternative fuels—A case study. *Fuel* **2017**, *194*, 511–526, doi:10.1016/j.fuel.2016.12.003.
53. Siegemund, S.; Trommler, M.; Kolb, O.; Zinnecker, V.; Schmidt, P.; Weindorf, W.; Zittel, W.; Raksha, T.; Zerhusen, J. *The Potential of Electricity-Based Fuels for Low-Emission Transport in the EU An Expertise by LBST and Dena*; Deutsche Energie-Agentur GmbH (dena): Berlin, Germany, 2017.
54. LeViness, S.; Deshmukh, S.R.; Richard, L.A.; Robota, H.J. Velocys Fischer-Tropsch Synthesis Technology—New Advances on State-of-the-Art. *Top. Catal.* **2014**, *57*, 518–525, doi:10.1007/s11244-013-0208-x.
55. Kalz, K.F.; Kraehnert, R.; Dvoyashkin, M.; Dittmeyer, R.; Gläser, R.; Krewer, U.; Reuter, K.; Grunwaldt, J.D. Future Challenges in Heterogeneous Catalysis: Understanding Catalysts under Dynamic Reaction Conditions. *ChemCatChem* **2017**, *9*, 17–29, doi:10.1002/cctc.201600996.
56. Venvik, H.J.; Yang, J. Catalysis in microstructured reactors: Short review on small-scale syngas production and further conversion into methanol, DME and Fischer-Tropsch products. *Catal. Today* **2017**, *285*, 135–146, doi:10.1016/j.cattod.2017.02.014.
57. Steynberg, A.P.; Deshmukh, S.R.; Robota, H.J. Fischer-Tropsch catalyst deactivation in commercial microchannel reactor operation. *Catal. Today* **2018**, *299*, 10–13, doi:10.1016/j.cattod.2017.05.064.
58. van Sint Annaland, M. Editorial overview: Process intensification in reaction engineering: Intensified efforts to boost intensification. *Curr. Opin. Chem. Eng.* **2017**, *17*, ii–iii, doi:10.1016/j.coche.2017.10.001.
59. Kolb, G. Review: Microstructured reactors for distributed and renewable production of fuels and electrical energy. *Chem. Eng. Process.* **2013**, *65*, 1–44, doi:10.1016/j.cep.2012.10.015.

60. Tonkovich, A.; Mazanec, T.; Jarosch, K. Improved Fischer-Tropsch catalysts. *Focus Catal.* **2004**, *2004*, 7, doi:10.1016/S1351-4180(04)00159-X.
61. Delparish, A.; Avci, A.K. Intensified catalytic reactors for Fischer-Tropsch synthesis and for reforming of renewable fuels to hydrogen and synthesis gas. *Fuel Process. Technol.* **2016**, *151*, 72–100, doi:10.1016/j.fuproc.2016.05.021.
62. Cao, C.; Hu, J.; Li, S.; Wilcox, W.; Wang, Y. Intensified Fischer-Tropsch synthesis process with microchannel catalytic reactors. *Catal. Today* **2009**, *140*, 149–156, doi:10.1016/j.cattod.2008.10.016.
63. Kshetrimayum, K.S.; Jung, I.; Na, J.; Park, S.; Lee, Y.; Park, S.; Lee, C.J.; Han, C. CFD Simulation of Microchannel Reactor Block for Fischer-Tropsch Synthesis: Effect of Coolant Type and Wall Boiling Condition on Reactor Temperature. *Ind. Eng. Chem.* **2016**, *55*, 543–554, doi:10.1021/acs.iecr.5b03283.
64. Almeida, L.C.; Sanz, O.; D'Olhaberriague, J.; Yunes, S.; Montes, M. Microchannel reactor for Fischer-Tropsch synthesis: Adaptation of a commercial unit for testing microchannel blocks. *Fuel* **2013**, *110*, 171–177, doi:10.1016/j.fuel.2012.09.063.
65. Arzamendi, G.; Diéguez, P.M.; Montes, M.; Odriozola, J.A.; Sousa-Aguiar, E.F.; Gandía, L.M. Computational fluid dynamics study of heat transfer in a microchannel reactor for low-temperature Fischer-Tropsch synthesis. *Chem. Eng. J.* **2010**, *160*, 915–922, doi:10.1016/j.cej.2009.12.028.
66. Dittmeyer, R.; Boeltken, T.; Piermartini, P.; Selinsek, M.; Loewert, M.; Dallmann, F.; Kreuder, H.; Cholewa, M.; Wunsch, A.; Belimov, M.; et al. Micro and micro membrane reactors for advanced applications in chemical energy conversion. *Curr. Opin. Chem. Eng.* **2017**, *17*, 108–125, doi:10.1016/j.coche.2017.08.001.
67. LeViness, S. Opportunities for modular GTL in North America; Presented at Energy Frontiers International, Gas-to-Market & Energy Conversion Forum, Houston, TX, USA, 22 October 2012.
68. LeViness, S. Velocys Fischer-Tropsch Synthesis Technology Comparison to Conventional FT Technologies; AIChE: Spring Meeting, San Antonio, TX, USA, 2013.
69. Zhang, J.; Xu, G. Scale-up of bubbling fluidized beds with continuous particle flow based on particle-residence-time distribution. *Particuology* **2015**, *19*, 155–163, doi:10.1016/j.partic.2014.04.019.
70. Sievers, D.A.; Kuhn, E.M.; Stickel, J.J.; Tucker, M.P.; Wolfrum, E.J. Online residence time distribution measurement of thermochemical biomass pretreatment reactors. *Chem. Eng. Sci.* **2016**, *140*, 330–336, doi:10.1016/j.ces.2015.10.031.
71. Eilers, H.; González, M.I.; Schaub, G. Lab-scale experimental studies of Fischer-Tropsch kinetics in a three-phase slurry reactor under transient reaction conditions. *Catal. Today* **2016**, *275*, 164–171, doi:10.1016/j.cattod.2015.11.011.
72. González, M.I.; Schaub, G. Fischer-Tropsch synthesis with H2/CO2-catalyst behavior under transient conditions. *Chem. Ing. Tech.* **2015**, *87*, 848–854, doi:10.1002/cite.201400137.
73. Schlosser, E.; Wolfrum, J.; Hildebrandt, L.; Seifert, H.; Oser, B.; Ebert, V. Diode laser based in situ detection of alkali atoms: Development of a new method for determination of residence-time distribution in combustion plants. *Appl. Phys. B* **2002**, *75*, 237–247, doi:10.1007/s00340-002-1001-x.
74. Levenspiel, O. *Tracer Technology*; Springer: New York, USA, 2012, ISBN 978-1-4419-8073-1.
75. van Steen, E.; Claeys, M.; Möller, K.P.; Nabaho, D. Comparing a cobalt-based catalyst with iron-based catalysts for the Fischer-Tropsch XTL-process operating at high conversion. *Appl. Catal. A-Gen.* **2018**, *549*, 51–59, doi:10.1016/j.apcata.2017.09.019.
76. *Fischer-Tropsch Technology;* Steynberg, A., Dry, M., Eds.; Elsevier: Amsterdam, The Netherlands, 2004; ISBN 9780444513540.
77. *VDI Heat Atlas*, 2nd ed.; VDI Gesellschaft Verfahrenstechnik und Ingenieurwesen, Ed.; Springer: Berlin/Heidelberg, Germany, 2010; ISBN 9783540799993.
78. Kreitz, B.; Wehinger, G. d.; Turek, T. Dynamic simulation of the CO_2 methanation in a micro-structured fixed-bed reactor. *Chem. Eng. Sci.* **2019**, *195*, 541–552, doi:10.1016/j.ces.2018.09.053.
79. *A Comparison of Forced Feed Cycling of the Fischer-Tropsch Synthesis over Iron and Cobalt Catalysts*; Adesina, A.A., Silveston, P.L., Hudgins, R.R., Eds.; S. Kaliaguine, A. Mahay: Amsterdam, Netherlands, 1984.
80. Silveston, P.; Hudgins, R.R.; Renken, A. Periodic operation of catalytic reactors-introduction and overview. *Catal. Today* **1995**, *25*, 91–112, doi:10.1016/0920-5861(95)00101-K.
81. Topsøe, H. Developments in operando studies and in situ characterization of heterogeneous catalysts. *J. Catal.* **2003**, *216*, 155–164, doi:10.1016/S0021-9517(02)00133-1.
82. Zhang, Y.; Fu, D.; Xu, X.; Sheng, Y.; Xu, J.; Han, Y.F. Application of operando spectroscopy on catalytic reactions. *Curr. Opin. Chem. Eng.* **2016**, *12*, 1–7, doi:10.1016/j.coche.2016.01.004.

83. Chakrabarti, A.; Ford, M.E.; Gregory, D.; Hu, R.; Keturakis, C.J.; Lwin, S.; Tang, Y.; Yang, Z.; Zhu, M.; Bañares, M.A.; et al. A decade+ of operando spectroscopy studies. *Catal. Today* **2017**, *283*, 27–53, doi:10.1016/j.cattod.2016.12.012.
84. Rochet, A.; Moizan, V.; Pichon, C.; Diehl, F.; Berliet, A.; Briois, V. In situ and operando structural characterisation of a Fischer-Tropsch supported cobalt catalyst. *Catal. Today* **2011**, *171*, 186–191, doi:10.1016/j.cattod.2011.03.079.
85. Jacobs, G.; Ma, W.; Gao, P.; Todic, B.; Bhatelia, T.; Bukur, D.B.; Davis, B.H. The application of synchrotron methods in characterizing iron and cobalt Fischer-Tropsch synthesis catalysts. *Catal. Today* **2013**, *214*, 100–139, doi:10.1016/j.cattod.2013.05.011.
86. Karlsruhe Institute of Technology (KIT). PowerFuel—Fuels for Climate-Neutral Airplanes. Available online: https://www.kit.edu/kit/english/pi_2018_165_fuels-for-climate-neutral-airplanes.php (accessed on 9 May 2019).

PAPER III

DYNAMICALLY OPERATED FISCHER-TROPSCH SYNTHESIS IN PTL-PART 2: COPING WITH REAL PV PROFILES

Submitted to ChemEngineering, 15.02.2020

Published: 13.04.2020

`https://doi.org/10.3390/chemengineering4020027`

Paper III

chemengineering

Article

Dynamically Operated Fischer–Tropsch Synthesis in PtL—Part 2: Coping with Real PV Profiles

Marcel Loewert [†], Michael Riedinger and Peter Pfeifer *

Institute of Micro Process Engineering (IMVT), Karlsruhe Institute of Technology (KIT),
76344 Eggenstein-Leopoldshafen, Baden-Württemberg, Germany; marcel.loewert@ineratec.de (M.L.);
michael.riedinger@kit.edu (M.R.)
* Correspondence: peter.pfeifer@kit.edu; Tel.: +49-721-608-24767
† Current affiliation: INERATEC GmbH, Siemensallee 84, 76187 Karlsruhe, Baden-Württemberg, Germany.

Received: 15 February 2020; Accepted: 9 April 2020; Published: 13 April 2020

Abstract: Climate change calls for a paradigm shift in the primary energy generation that comes with new challenges to store and transport energy. A decentralization of energy conversion can only be implemented with novel methods in process engineering. In the second part of our work, we took a deeper look into the load flexibility of microstructured Fischer–Tropsch synthesis reactors to elucidate possible limits of dynamic operation. Real data from a 10 kW photovoltaic system is used to calculate a dynamic H_2 feed flow, assuming that electrolysis is capable to react on power changes accordingly. The required CO flow for synthesis could either originate from a constantly operated biomass gasification or from a direct air capture that produces CO_2; the latter is assumed to be dynamically converted into synthesis gas with additional hydrogen. Thus two cases exist, the input is constantly changing in syngas ratio or flow rate. These input data were used to perform challenging experiments with the pilot scale setup. Both cases were compared. While it appeared that a fluctuating flow rate is tolerable for constant product composition, a coupled temperature-conversion relationship model was developed. It allows keeping the conversion and product distribution constant despite highly dynamic feed flow conditions.

Keywords: Fischer–Tropsch synthesis; microstructured reactors; dynamic processes; heterogeneous catalysis; decentralized application; compact reactor technology; PtX; BtL; PtL

1. Introduction

Anthropogenic greenhouse gas emissions must be reduced to limit global warming to less than 2 °C [1]. For this reason, the Climate Protection Plan 2050 was drawn up in Germany. In accordance with directives from the European Union (EU), the goal is to reduce greenhouse gas emissions by 80–95% by 2050 compared to 1990 [2]. Since CO_2 is one of the most emitted greenhouse gases [3], technologies that favor neutral or negative CO_2 emissions are becoming increasingly relevant. Renewable energy can be obtained from wind, solar power, or biomass. These sources offer the possibility to generate energy without affecting the fossil carbon cycle. It can be assumed that extensive implementation is tied to decentralized plants on a wide variety of free areas in order to produce energy where it is needed [4,5]. The share of biomass in the energy mix is considered to be limited, especially in Germany [6]. For this reason, wind and solar energy in particular need to be actively supported and will thus dominate the electricity market at a certain point in time. Due to seasonal effects as well as day and night cycles, a misalignment between energy generation and consumption exists. One of the biggest challenges is the storage of spatial and time-resolved excess energy and the compensation of energy gaps [7–10].

To store large amounts of energy over seasons or daytime, electrical energy must be converted into molecules with a high energy density that do not show losses even during long storage periods.

In power-to-liquid (PtL) processes, hydrogen is produced by water electrolysis and converted with carbon oxides into liquid hydrocarbons. Those processes are suitable to produce such molecules, i.e., chemical energy carriers. The storage of hydrogen itself is expensive and involves a number of risks, which makes its conversion to liquid hydrocarbons interesting [11–13]. The Fischer–Tropsch synthesis (FTS) is one of several pathways to produce a synthetic crude fuel from synthesis gas, a mixture of H_2 and CO. Pre-treated synthetic crude from the FTS can replace petroleum products without significantly changing existing infrastructure [14]. Carbon monoxide can be obtained from many carbon sources. To ensure CO_2 neutrality, the carbon source should be CO_2 from direct air capture (DAC) or biomass since plants utilize CO_2 to grow. Together with H_2 from electrolysis, CO_2 from the atmosphere can be converted into synthesis gas by reverse water–gas shift reaction (RWGS). Biomass gasification directly leads to synthesis gas but often lacks in hydrogen; thus, H_2 by electrolysis can be added to the produced gas stream to increase the efficiency of the biomass-to-liquid (BtL) process route.

Until recently, FTS has only been used in large-scale plants where large quantities of synthesis gas are processed [15]. In order to justify decentralized conversion of renewable energy sources, the applied reactor technology must be significantly improved in order to obtain similar efficiency without large internal recycling at small- to medium-scale installations. Within microstructured reactors, small dimensions and a large internal surface area can significantly improve both mass and heat transfer in many processes [4,16,17]. In addition, processes can be further intensified through evaporation cooling. Those advantages allow increasing of the reactors' space-time yield by a factor of 80 and enhancing the single pass conversion in FTS from 40% to above 60% [18]. That is a quantum leap for the generation of hydrocarbons and makes compact synthesis plants possible. To foster cost reduction in processes where hydrogen is required before the synthesis, expensive plant components such as a hydrogen buffer storage need to be minimized. This goal can be reached through dynamic process control, for instance [19]. Nevertheless, plant utilization needs to be maximized and the whole system must be assessed via an economic evaluation.

In the past, researchers always hoped to overcome the boundaries of steady-state synthesis reactions [20–37]. It is obvious that potential selectivity or conversion advantages from forced feed cycling or temperature swing or other types of unsteady-state operation must overcome additional cost and complexity brought into the system design [20,22,23]. In the context of PtL applications, the reduction of intermittent hydrogen storage is a clear reduction of capital costs enabled by dynamic operation [22–24,38]. Only a small number of publications investigated potential effects from dynamic operation on the FTS, mostly before the 1990s [20,37]. It was observed that iron-based catalysts produce more methane under forced feed cycling. When repeated for a cobalt-based catalyst, a "hydrocarbon formation overshoot" for the C1–C7 species, compared to steady-state, was observed [37]. It should be noted that such effects might be strictly linked to one specific catalyst compositions. In a review by Silveston from 1995, a generally increased catalyst activity or performance was described for multiple systems [20]. Other observations are worth mentioning, such as that steady-state kinetics are unable to predict benefits with regard to conversion or selectivity and that forced feed-cycling is so far the only practicable way to induce better process performance. Temperature cycles are not much investigated yet. Only the work of González and Eilers picked up that topic 20 years later [22–24]. PtX technologies became increasingly interesting for process engineers in the recent years. For the involved catalysts, mainly iron and cobalt-based, no improvement by dynamic operation in activity or selectivity could be found in these studies. However, no hint as to disadvantages from forced feed cycling have been reported to date. Thus, steady-state kinetics seem valid for unsteady-state operation. A final validation of a feasible dynamic operation in process combination with electrolysis is not possible, since no such systematic investigation is present up to now.

A deeper look into dynamic synthesis was performed for the methanation reaction [21,25–36]. The need for flexibility in the fast changing energy system was recognized and investigated. From simplified assumptions in his model, Güttel et al. concluded that oscillation brings no improvement in the reaction rate compared to steady-state [21]. Unsteady-state kinetics were likely unable to predict the experiments. Methanation reaction is probably simpler in terms of reaction kinetics, compared to the FTS. However, catalyst deactivation and a more severe and also moving hot spot is more difficult to describe in methanation, compared to Fischer–Tropsch synthesis [28,30,31]. Deactivation brings always uncertainty in kinetics descriptions and the description of methanation. Thus, multiple models were developed to simulate product properties and reactor performance in dynamic operation. Some of the investigations focus on thermal stability and synthesis improvement [28,31–36] while practical approaches often lack a sufficient feedback loop or monitoring options [34–36]. Mixed results are reported about the decline of reaction rate by oscillation experiments and only few advantages from oscillation are reported [30,36]. Almost no negative effect on catalyst lifetime is observed, while slightly better stability is found the shorter the cycles are [26,27,30]. Both the isothermal and adiabatic reactor approach have advantages and disadvantages, while the latter is reported to be better suited for load-flexible operation [36].

In microstructured fixed bed reactors, issues like hot-spot formation and associated deactivation do not apply ab initio, as shown in our previous work (Part 1) [38]. Hot spots are negligible and high per-pass conversion can be established without sintering effects. In addition, no advantage or disadvantage from oscillation experiments was found and description by steady-state kinetics seemed to be valid for unsteady-state experiments. As the time-scale was still in the minute-scale in Part 1, in this paper we will focus on a high-frequency oscillation following the power profile of an electrolysis by applying real photovoltaics data from a location in Baden–Württemberg to the setup. This analysis is performed under consideration of the two elaborated cases above, i.e., the variation of feed gas composition (assuming a constant biomass gasification with fluctuating hydrogen addition) and the variation of feed gas flow (assuming a CO_2-storage with dynamically operated RWGS). The paper will give insights in the reactor and setup response as well as possible limitations.

2. Materials and Methods

2.1. Experimental Setup and Process Analysis

The pilot scale setup for up to 7 L d^{-1} of liquid and solid product from previous publications was used for this work [18,38]. The microstructured fixed bed reactor using cobalt as active catalyst component was used as described elsewhere [16]. The catalyst was not exchanged in between part 1 and part 2 of the study.

Analysis consisted of an online gas chromatograph (GC) to determine conversion levels and selectivity, as well as two offline GC for liquid and solid product analysis. Details on data processing are detailed elsewhere [18,39,40]. Additionally, a mass spectrometer (MS) was introduced in part 1 for online measurement of the gas phase with better time resolution [38]. After some modifications on the MS, the gas phase concentration could be quantified in this work, in contrast to part 1. Three thermocouples enabled temperature measurement of the reaction. The top (feed inlet) and bottom (product outlet) temperatures of the microstructured reactor were measured with thermocouples inserted in between the plates of the microstructured packed bed. The steam outlet temperature was measured in the fluid. Calibrated mass flow controllers (MFCs) dosed the respective feed gases. A quick sampling (QS) site was previously installed for concurrent gas and liquid sampling [38].

It is important to point out that parameter changes affect the reaction performance much faster than they can be measured due to a signal delay of about 17.5 min (for both liquid and gas composition), as discussed in the previous work of Part 1.

In this part of the study, it must therefore be assumed that gas composition changes inside the catalyst bed appear fast, as the species residence time from the MFCs to the reactor exit is less than two minutes. Setpoint changes of reactor temperature can also be assumed to take effect almost instantaneously since internal temperature control via cooling water pressure manipulation is very effective and monitoring is performed by measuring the wall temperature inside the microstructured foil stack. Evaporation cooling is thus found to save response time in contrast to heating and cooling without phase change. As a result, the conversion inside the catalyst bed is subject to very fast changes.

2.2. Real Photovoltaic Profiles and Discretization of the Feed

Since a realistic context of an actual PtL process is not yet fully clear, testing the capabilities of the FTS step is straightforward to identify possible limits of future process chains. Stress on the catalyst can be applied in many ways. In the context of dynamic FTS, quickly fluctuating feeds are a good way to test system behavior under extreme conditions.

KIT's Battery Technical Center (BATEC) supplied different real-time profiles for a 10 kW photovoltaic (PV) table. This data was used to develop experimental campaigns. The PV table consists of polycrystalline solar modules. The tilt angle was adjusted to 30° facing south, which is considered optimal for the given location (N 49.1 E 8.4). This allowed reaching the theoretical peak power of 10 kW.

In this work, a daily profile for a sunny spring day in 2015 is used (see Figure 1a). It was confirmed by BATEC that this profile is a representative average for that period and location. A hydrogen flow of 4 kWh m_{N,H_2}^{-3} was calculated from the assumption of a conversion efficiency of 75% (based on the heating value). This is a typical value for industrial state-of-the-art PEM electrolysis as reported for Siemens Silyzer 200 and 300 systems, for instance [41,42]. Usually, we operate the reactor in steady state between 60 and 160 g_{cat} h m^{-3} of syngas mixture (see Table 2). This equals between 5 and 17.6 L_N min^{-1} of hydrogen. In order to achieve this, a downscaling factor of 2.5 was applied to fit the scale of H_2 production to the given reactor size and mass of catalyst. A discretization of the hydrogen volume flow was conducted to yield a maximum 10 steps during a ramp from the highest flow level to the lowest and vice versa. Furthermore, the time of a change between the different levels was expanded to minimum one minute so that new syngas flows could be established in the current test rig. A minimum flow of 7 L min^{-1} H_2 needed to be guaranteed from experience in order to keep the specific pilot scale reactor running autothermal by emitting sufficient reaction enthalpy. This is crucial in order to compensate the losses to the environment and the cooling cycle. This is an experimental limitation in the current setup as a function of the reactor size and total mass of catalyst in the system. A scale-up factor of 60 would fortunately reduce this lower limit to less than 20% of the upper value, which allows a wider flexibility of the reaction. An additional 3 h of operation time per day (phases of dawn and twilight) would be feasible then without including a hydrogen storage.

The discretized input signal for the reaction is depicted in Figure 1b. After cutting the graph along the minimum flow, seven different experimental conditions remained.

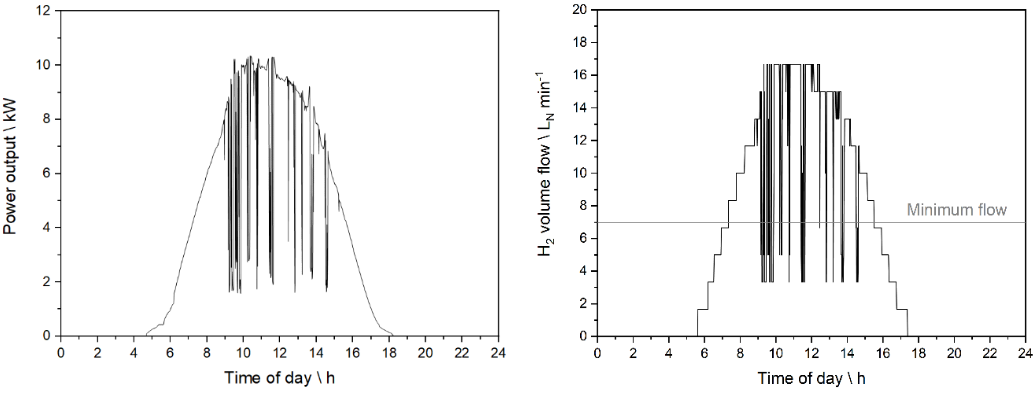

(**a**) (**b**)

Figure 1. Experimental input signals based on the data from KIT's Battery Technical Center (BATEC). (**a**) Power output profile for a 10 kW peak PV table for a sunny spring day in 2015; (**b**) Discretized hydrogen flow calculated from Figure 1a assuming a specific conversion energy of 4 kWh m_{N,H_2}^{-3} and applying a further downscaling factor of 2.5.

2.3. Experimental Base Cases

In order to apply the hydrogen profile presented in Section 2.2, the two different scenarios were chosen to gather first insights into the process stability and product quality. Figure 2 shows the potential pathways for either PtL or BtL approaches including an FTS unit in a simplified scheme. For both cases, the abovementioned PV panel and electrolysis unit deliver the hydrogen needed for the FTS. The carbon source is either CO_2 or biomass.

For Case 1, the BtL pathway, a steady biomass gasification is assumed so that a constant flow of CO-rich synthesis gas is gathered with a syngas ratio below 2 [43]. If the fluctuating hydrogen flow from the electrolysis is added to the constant flow of synthesis gas, a varying H_2/CO ratio in the FTS reactor and changing residence time of the gas mixture are the consequences. Varying two system parameters at the same time promotes unpredictable effects on the performance of the synthesis.

In Case 2, the PtL process route, a CO_2 storage can be depleted on demand. It is assumed that a RWGS unit can be operated with fixed gas mixtures and changing total flows In-line with the response time of the electrolysis. In this scenario, a fixed H_2/CO ratio of 2 is fed to the FTS reactor. A dilution of the feed gas with CO_2 or formed methane of the RWGS output is not considered in the current approach. Water is thought to be condensed before entering the FTS.

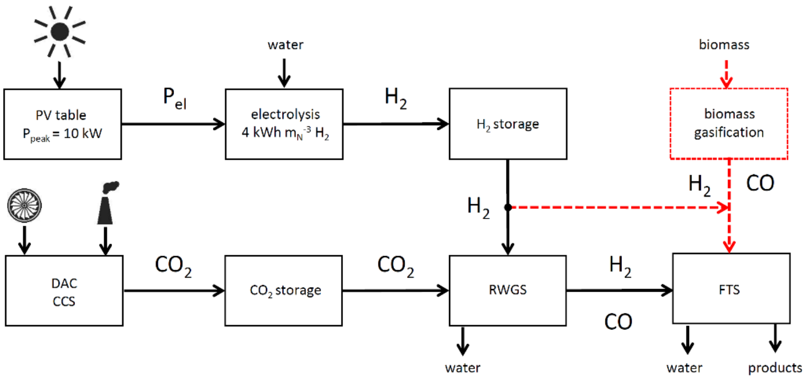

Figure 2. Potential PtL (black solid lines) and BtL (red dotted lines) pathways to produce syngas for the microstructured FTS reactor. Both pathways include a PV panel and electrolyzer; a hydrogen buffer storage of a certain size is optional. The PtL pathway utilizes CO_2 as carbon source exclusively, which needs to be converted into syngas in a RWGS unit. A CO_2 buffer storage is an assumed prerequisite here. The BtL pathway uses syngas from biomass gasification and hydrogen from electrolysis.

2.4. Calculation of Conversion Levels during Quick Process Changes

The actual CO conversion could not be determined in real time since both GC and MS analysis suffer from product back mixing with at least 17.5 min of signal delay, see part 1 of the study [38]. In order to approximate conversion levels during quick changes, a linear regression model was developed, based on a database of 19 sets of process parameters that were tested experimentally. Parameter ranges are listed in Table 1. Within these ranges, conversion estimations should be accurate.

Table 1. Overview of process parameters for linear regression data in a pilot scale FTS unit

	Temperature	**Syngas ratio**	τ_{mod}
	°C	**-**	g_{cat} **h** m^{-3}
Min. value	235.5	1.49	65.17
Max. value	246	2.20	158.02

The modified residence time (τ_{mod}), the syngas ratio and the temperature have a significant influence on CO conversion. Because of different gas densities between all gas feed species, the density-independent parameter τ_{mod} was chosen instead of the weight hourly space velocity (WHSV) and calculated via the relation $\tau_{mod} = \gamma_{feed}$ WHSV^{-1} with γ_{feed} being the respective density of the feed gas mixture.

The correlation of CO conversion from the individual values can be described with a linear regression model. The fundamental approach is described in Equation 1. The regression coefficients β_k are linearly related.

$$X_{CO} = \beta_0 + \beta_1 x_1 + \beta_2 x_2 + \cdots + \beta_k x_k, \tag{1}$$

with X_{CO} being the CO conversion, β_0 the base regression coefficient, β_k regression coefficients and x_k regression variables. The regression coefficients weigh the expected change in X_{CO} with changes in regression variables. The variables for this model are combinations of the modified residence time, the H_2/CO ratio and the temperature. The model was fitted using a systematic approach based on Equation 1 executed in a standard spreadsheet calculator program. A linear approach according to Equation 2 was chosen [44].

$$X_{CO} = \beta_0 + \beta_1 X_{\tau_{mod}} + \beta_2 X_{\frac{H_2}{CO}} + \beta_3 X_{T_{Reactor}}, \tag{2}$$

with X_i being the coefficients for the respective influence parameters mentioned above. $T_{Reactor}$ is the average temperature determined from two thermocouples in the foil stack next. These are placed along the bed length in the outer wall of the catalyst bed. The individual parameters from Equation 2 can be determined using the least squares method. In matrix notation, the measured values can be specified as shown in Equation 3.

$$\vec{x} = \mathrm{H} \cdot \vec{y}, \tag{3}$$

with $\vec{x}$ being the results matrix, H the matrix notation of the target equation and $\vec{y}$ the estimator and the coefficient matrix. The variables are defined in Equation 4

$$\vec{x} = \begin{pmatrix} X_{CO,1} \\ X_{CO,2} \\ \vdots \\ X_{CO,k} \end{pmatrix} \quad \mathrm{H} = \begin{pmatrix} 1 & X_{\tau_{mod},1} & X_{\frac{H_2}{CO},1} & X_{T_{Reactor},1} \\ 1 & X_{\tau_{mod},2} & X_{\frac{H_2}{CO},2} & X_{T_{Reactor},2} \\ \vdots & \vdots & \vdots & \vdots \\ 1 & X_{\tau_{mod},k} & X_{\frac{H_2}{CO},k} & X_{T_{Reactor},k} \end{pmatrix} \quad \vec{y} = \begin{pmatrix} \beta_1 \\ \beta_2 \\ \vdots \\ \beta_k \end{pmatrix}, \tag{4}$$

For the estimator of the least squares method $\vec{y}$, the relation in Equation 5 can be used [45]

$$\vec{y} = (\mathrm{H}^{\mathrm{T}}\mathrm{H})^{-1}\mathrm{H}^{\mathrm{T}} \cdot \vec{x}, \tag{5}$$

while matrix H must be of full rank for the inverse $(\mathrm{H}^{\mathrm{T}}\mathrm{H})^{-1}$ to exist. The residuals vector $\vec{e}$ can be determined from Equation 6

$$\vec{e} = \vec{x} - \mathrm{H} \cdot \vec{y}. \tag{6}$$

2.5. Step Change Experiments—Experimental Design

In order to test the system before PV profile experiments, step change experiments were conducted based on the seven remaining steps between minimum and maximum hydrogen flow, see Section 2.2. Reactor behavior was tested in accordance to Case 1 by manipulating the syngas ratio concurrently with the residence time of each step change. This was applied by giving a constant CO flow of 7 L_N min^{-1}, adding as much hydrogen as needed to reach certain H_2/CO ratios. The syngas ratio ranged consequently between 1.2 (very low) and 2.4 (over-stoichiometric) with 0.2-steps. The time between each step differed, starting with 10 min between each step (experiment A) to 5 min between each step (experiment B). A lower step time was unfavorable for the means of process observation since liquid sampling took 5 min. The initial syngas ratio was held overnight before each experiment. Two plateaus at minimum and maximum ratio were held for a prolonged time (60 min for experiment A, 30 min for experiment B) before ramping up or down again. Figure 3 shows the executed experiments.

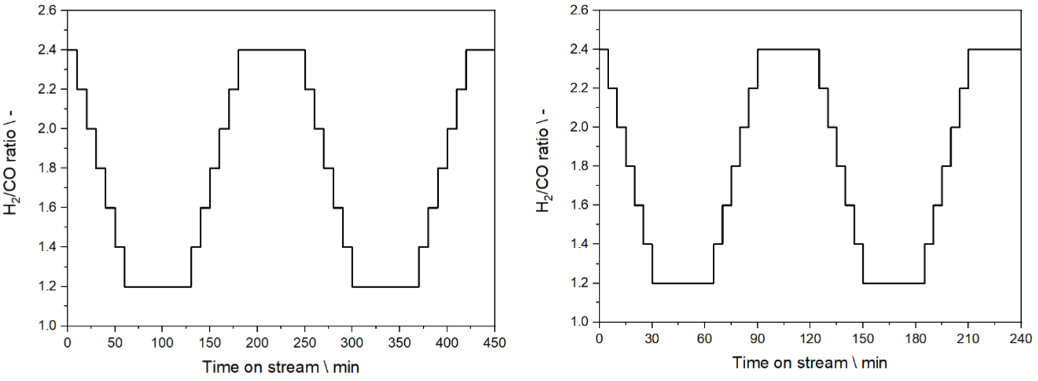

(**a**) (**b**)

Figure 3. Setpoints of H_2/CO ratio between 1.2 and 2.4 with two cycles of ramping it down and up as function of time in step change experiments. (**a**) Experimental profile for ten-minute steps with plateau times of 60 min (experiment A); (**b**) Experimental profile for five-minute steps with plateau times of 30 min (experiment B).

2.6. Experiments Based on the PV Profile

For the PV profile experiments, the BtL and the PtL case was covered experimentally. Figure 4 shows the FTS feed input data with regard to H_2 and CO flow adapted from the real PV profile. Figure 4a represents Case 1 (experiment C) and Figure 4b Case 2; Case 1 was conducted with a larger range of the syngas ratio (1.0–2.4) compared to the step change experiments. Case 2 was first conducted without external temperature control (experiment D) and repeated. The linear regression model introduced in Section 2.4 was used to calculate the necessary temperature, which is required to keep the CO conversion throughout the experiment (experiment E). The aim was to convert 70% of CO despite the changing residence time inside the reactor. Therefore, temperature data from experiment D was analyzed and temperature corrections applied by hand if the conversion was below 70%.

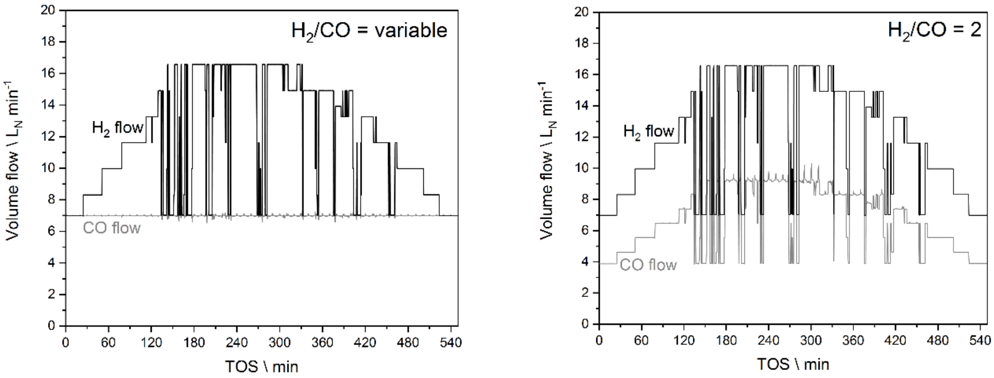

(**a**) (**b**)

Figure 4. Setpoints of CO an H_2 flow discretized from the PV profile as function of time. (**a**) Variable H_2/CO ratio and residence time (Case 1, experiment C); (**b**) Variable residence time with a fixed syngas ratio of 2 (Case 2, valid for experiments D and E).

3. Results and Discussion

3.1. Linear Regression Model

Using the regression described in Section 2.4, the linear approach from Equation 2 was systematically adapted to 19 data points with low inert gas dilution (<5%) using the least squares method. For the fit, the data from Table 2 were used. Before the fit, the variables were normalized to a range between 0 and 1 using the min-max transformation according to Equation 7 [46]. This minimizes the influence of larger numbers on the regression.

Table 2. Detailed overview of experimental data used for the linear regression model

Data	τ_{mod} g_{cat} h m^{-3}	H_2/CO -	*T* °C	τ_{norm} -	H_2/CO_{norm} -	T_{norm} -	X_{CO} %
1	93.91	1.98	245	0.3073	0.6855	0.9048	65.25
2	81.81	1.98	245	0.1779	0.6935	0.9048	55.72
3	72.74	2.11	244.5	0.0809	0.8757	0.8571	49.05
4	65.17	2.00	244.5	0.0000	0.7190	0.8571	41.58
5	65.27	2.00	235.5	0.0010	0.7214	0.0000	27.51
6	72.62	1.99	235.5	0.0797	0.7102	0.0000	27.61
7	81.74	1.99	235.5	0.1772	0.6993	0.0000	30.90
8	93.69	1.98	235.5	0.3050	0.6867	0.0000	36.06
9	158.02	1.94	235.5	0.9928	0.6295	0.0000	43.38
10	158.69	1.93	240	1.0000	0.6247	0.4286	57.79
11	141.32	1.49	244.5	0.8143	0.0000	0.8571	60.14
12	130.71	1.73	246	0.7008	0.3367	1.0000	62.14
13	121.26	1.96	244.5	0.5997	0.6593	0.8571	67.37
14	113.44	2.18	244.5	0.5161	0.9761	0.8571	71.34
15	94.22	2.19	241.5	0.3106	0.9875	0.5714	57.91
16	93.80	2.20	241	0.3061	0.9980	0.5238	42.37
17	94.69	2.20	240.5	0.3157	1.0000	0.4762	44.03
18	95.10	2.20	239	0.3200	0.9993	0.3333	43.29
19	107.33	1.96	238	0.4508	0.6658	0.2381	40.53

$$x_{i,Norm} = \frac{x_i - x_{i,min}}{x_{i,max} - x_{i,min}} \quad x_{i,Norm} \in [0, 1], \tag{7}$$

with x_i being the respective value of the currently observed parameter, $x_{i,min}$ being the lowest and $x_{i,max}$ being the highest value of the parameter within the data set.

Equation 8 resulted from the linear regression for the measured data with a maximum deviation of 8.1%

$$X_{CO} = 19.51 + 25.26\, X_{\tau_{mod}} + 13.20\, X_{\frac{H_2}{CO}} + 29.34\, X_T. \tag{8}$$

Using Equation 8, the required reactor temperature was calculated depending on the feed conditions and the target CO conversion. The required reactor temperature to reach a certain CO conversion can be picked from a corresponding plot if τ_{mod} and the H_2/CO ratio are known. This tool was crucial for the planning of experiment E, where an increase in the conversion level based on the temperature should be achieved with quickly reducing residence times and vice versa. The contour plot based on Equation 8 is shown in Figure 5 for a fixed syngas ratio of 2 (Case 2). It was used to determine the conversion throughout experiment D and to calculate the needed temperature for 70% of CO conversion in experiment E.

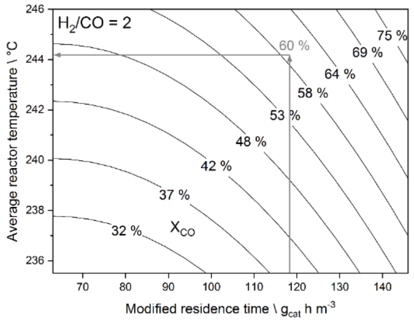

Figure 5. Contour plot derived from Equation 8 with curves of constant CO conversion levels ranging from 32–75% as function of τ_{mod} and the average reactor temperature at a syngas ratio of 2.

The desired temperature was induced proactively by changing the water pressure used for evaporation cooling, see part 1 of our study [38].

3.2. Step Change Experiments—Results

The outcome of the step change experiments is shown in Figures 6–8. The average reactor temperature is shown in Figures 6a and 6b. The methane byproduct formation is depicted in Figures 7a and 7b and the composition of the liquid phase is represented by Figures 8a and 8b, for experiment A and B respectively. Temperature could be measured instantaneously at the reactor. Gas and liquid phase signals are delayed by a time shift of about 17.5 min compared to the moment when the gas concentration was changed, see part 1 of this work [38]. This shift is more apparent in the shorter time steps (Figures 7b and 8b).

Figures 6a and 6b show the effect of different gas concentration change times on reaction temperature without external temperature control. The first plateau in experiment A led to a generally lower reactor temperature due to a longer time period at lower flow before the experiment. Thus, the slope of temperature increase in experiment B is consequently higher, leading to an increased maximum temperature after half of the experiment. Those effects could be countered by temperature manipulation, which was not conducted in these experiments.

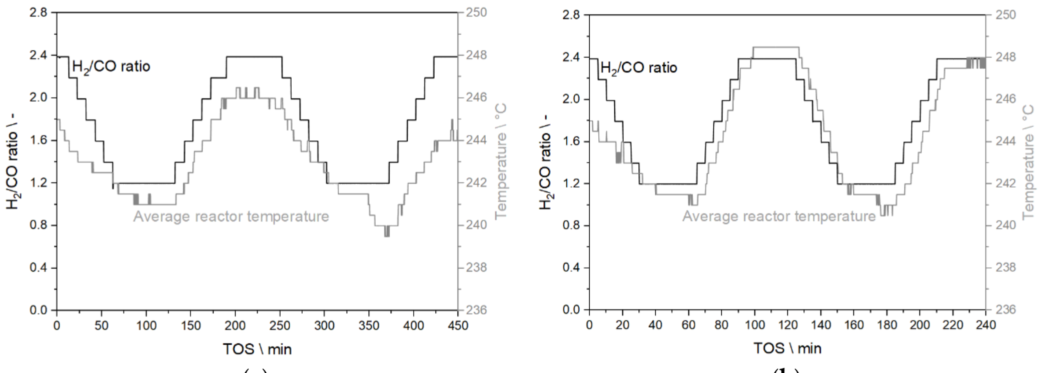

(**a**) (**b**)

Figure 6. Average reactor temperature as function of time in step change experiments A (**a**) and B (**b**).

A high syngas ratio strongly favors methane formation [47–49]. At higher temperatures, its formation is further increased, as Figures 7a and 7b show convincingly. The highest concentration gradient observed in both experiments was around Δc_{CH4} = 10%$_{abs}$. Both experiments show quite similar concentration curves including similar delay of the methane signal. Some signal interruptions and relatively large signal noise are caused by the gas measurement via the Quick Sampling site which is frequently disconnected during liquid phase sampling, see part 1 of the study.

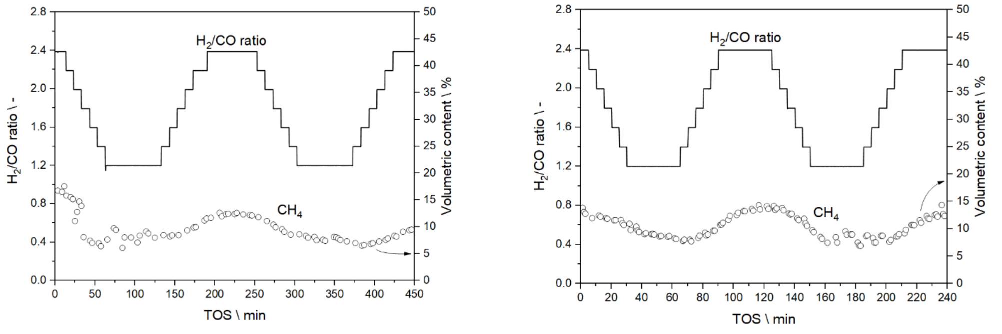

(**a**) (**b**)

Figure 7. Methane concentration as function of the time in step change experiments A (**a**) and B (**b**).

Figures 8a and 8b show the relative content of alkanes, alkenes and the sum of iso-alkanes and alcohols in the liquid phase. Saturation of molecules with hydrogen is dependent on the applied syngas ratio [50] and is visible as a shift between the alkanes' and alkenes' share in the experiments. The amounts of iso-alkanes and alcohols are quite constant despite significant changes of residence time and syngas ratio. The share is not influenced by temperature, as observed previously [38]. The progression of the curves is again similar for both time scales.

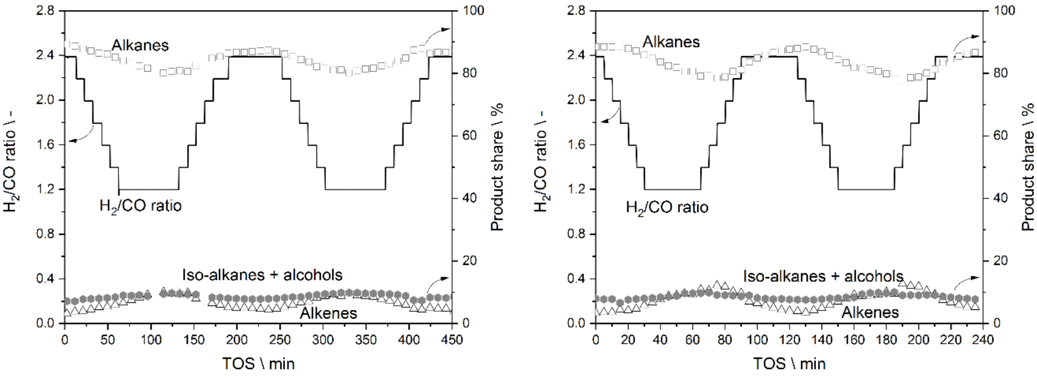

(**a**) (**b**)

Figure 8. Liquid phase composition regarding alkanes, alkenes and sum of iso-alkanes and alcohols in step change experiments A (**a**) and B (**b**).

3.3. Experiments Based on the PV Profile—Results

3.3.1. Results from Experiments without Temperature Manipulation

Experiment C is directly linked to the step change experiments as all are conducted with a constant CO flow. This, as explained earlier, simulates a BtL route without hydrogen buffer. Case 2 represents a PtL application without temperature manipulation (experiment D). Here, the existence of a CO_2 buffer storage is assumed as prerequisite for a dynamic operation of syngas production and utilization. Figures 9–11 show the data on temperature, methane concentration, and liquid product composition in analogy to Figures 6–8.

The reactor temperature in Figure 9a for experiment C shows similar behavior to the trend observed in experiments A and B. The average temperature inside the reactor increases with the available total gas flow and the hydrogen to CO ratio. The maximum average temperature change of the reactor in experiment C over the course of the experiment was ΔT_{max} = 8 °C, which is similar to the observed temperature change in step change experiments, see Section 3.2. The reactor is thus able to buffer fast changes in the 1 min regime while varying the residence time and syngas ratio; this is also valid with regard to a negligible T-gradient along the bed during the experiment. The reactor continued to run autothermally, and the cooling medium was never overheated. Neither did a thermal runaway happen.

Case 2, experiment D, is shown in Figure 9b. The maximum temperature of the reactor change is smaller, i.e., ΔT_{max} = 6 °C. This indicates that the influence of the residence time on the local temperature is much greater than that of the syngas ratio. The pronounced changes in volume flow can be counteracted by temperature manipulation, see next section. Regarding back-mixing of the products before the measurement unit and the general limitations in analysis time, no quantification of conversion could be performed at this point. This emphasizes the need of a prediction model like the one presented in Section 3.1.

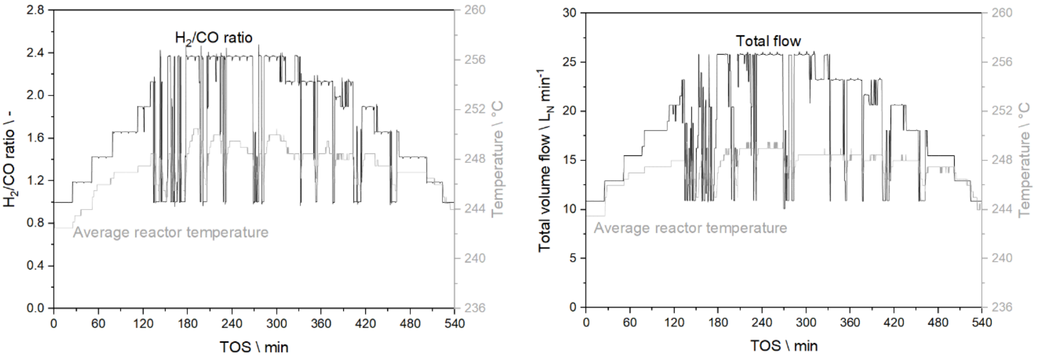

(**a**) (**b**)

Figure 9. Average reactor temperature as function of time for experiments C (**a**) and D (**b**), the latter with a constant syngas ratio of 2.

Methane production in experiment C also followed the behavior observed in step change experiments. Figure 10a demonstrates that a higher available syngas ratio and the increasing reactor temperature resulted in an increased production rate for methane. The highest concentration gradient accounted for $\Delta c_{CH4,max} = 4.5\%_{abs}$, which is only half the value from the step change experiments. Short changes seem to reduce the methane byproduct formation. Methane concentration was more constant in experiment D, as shown in Figure 10b. $\Delta c_{CH4,max}$ is $3.5\%_{abs}$. Interestingly, the methane concentration is the inverse of the concentration in experiment C. At a lower total volume flow, the residence time of the feed gas increases and with it the conversion levels. With a higher conversion, the content of CH_4 in the product gas increases accordingly. Keeping a steady syngas ratio has positive effects on uniform methane production.

Figure 11a shows that the liquid composition is significantly influenced by the available syngas ratio in the catalyst bed, compare experiments A and B with C. The variation of the product shares of alkanes and alkenes is distinctly wider in experiment C compared to experiment D (Figure 11b) with constant syngas ratio. The iso-alkane and alcohol production seem mostly unaffected by the drastic changes applied. Even product properties are crucial for downstream operations such as distillation and hydrotreating. Keeping a constant syngas ratio is thus recommended. Therefore, the PtL case is advantageous compared to hydrogen-boosted BtL with regard to product upgrade.

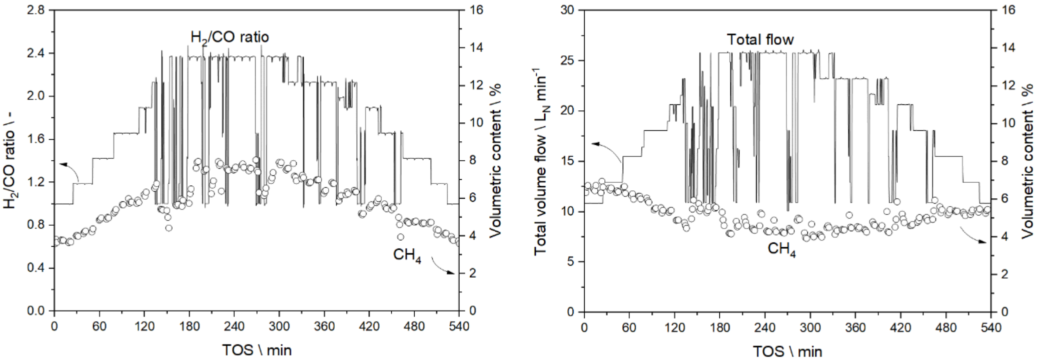

(**a**) (**b**)

Figure 10. Methane concentration as function of time for experiments C (**a**) and D (**b**), the latter with a constant syngas ratio of 2.

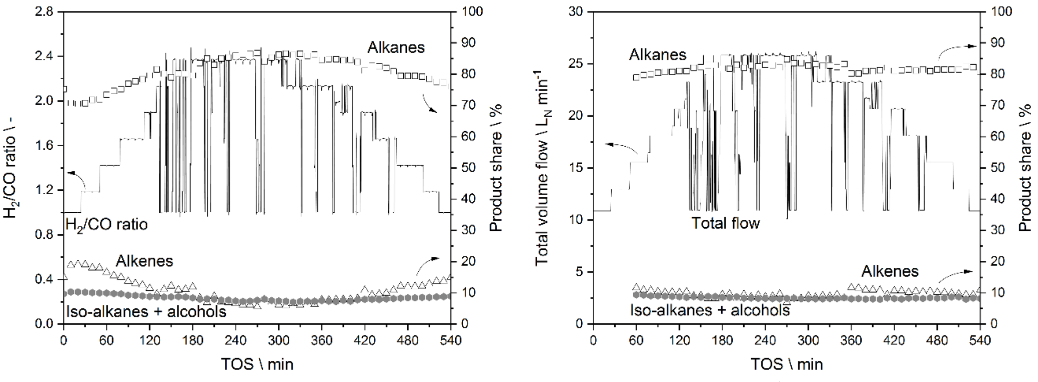

(**a**) (**b**)

Figure 11. Liquid phase composition regarding alkanes, alkenes and the sum of iso-alkanes and alcohols as function of time for experiments C (**a**) and D (**b**), the latter with a constant syngas ratio of 2.

3.3.2. Results from Temperature Adaptation to Reach Targeted Conversion Levels

Experiment E also corresponds to the PtL route including a storage for CO2 and a dynamically operated RWGS unit before the FTS. The reactor temperature is manipulated to aim for a CO conversion of 70+% at every time. The target temperature was calculated from the linear regression equation explained in Section 3.1. The required temperature setpoints as function of time were derived from the plot in Figure 9b as a base case and adapted by changing the water pressure in the cooling cycle per manual operation. The corresponding water pressure could be calculated with the Antoine equation for liquid water [51]. This manipulation was previously explored in part 1 of this study [38].

In Figure 12a, the required average reactor temperature for 60% CO conversion in experiment D is plotted against the measured value. Figure 12b shows the plot of required average reactor temperature for 70% CO conversion and the obtained average reactor temperature by manipulation of the cooling cycle pressure in experiment E. The upper plateau of the measured temperature is a consequence of reaching the evaporation state in the cooling cycle. Lower temperatures exist due to the effect that the reaction heat is not sufficient to reach the evaporation state and the reactor cools down due to heat loss to the environment. The reactor temperature could finally reach the setpoint of the water inlet temperature.

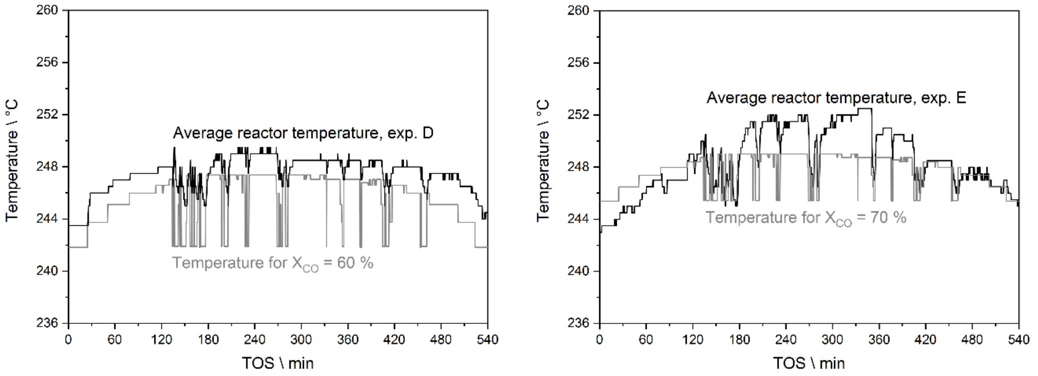

(**a**) (**b**)

Figure 12. Required average reactor temperature by linear regression to reach a certain conversion (grey solid line) and measured average reactor temperature (black solid line) as function of time. (**a**) experiment D with aimed 60% CO conversion; (**b**) experiment E with aimed 70% CO conversion.

According to the linear regression model, experiment D without temperature manipulation already resulted in more than 60% CO conversion at any time during the experiment. Within experiment E, 70% of CO conversion should be reached at any time. It was possible to narrow the observed temperature profile and even to exceed the required temperature levels in some cases. The temperature was too low only during the first 120 min of the experiment. Starting at a low volume flow, the available reaction heat is limited, so less heat is available to increase the average temperature. Nevertheless, water pressure manipulation was in general an effective tool to reach high temperatures and thus high conversion. Above 75% conversion, the developed linear regression model leaves its validated parameter range so it is not possible to plot the conversion in the high temperature range obtained in experiment E.

With temperature control in experiment E, methane formation was even more uniform than in experiment D, see Figure 13. $\Delta c_{CH4,max}$ was further decreased to $2.5\%_{abs}$. This highlights the superior performance of inherently temperature-flexible microstructured fixed bed reactors with regard to minimizing product deviations in dynamic load changes.

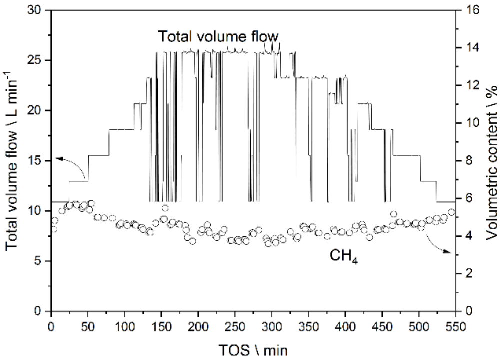

Figure 13. Methane concentration as function of time in the course of experiment E where the total applied feed flow was varied with a constant H_2/CO ratio of 2 and concurrent temperature manipulation.

3.4. Preliminary Analysis of Effects on Catalyst Stability during the Studies

Long-term stability of the catalyst is crucial for any operation with economical interest. The effects from fluctuation in gas concentration and temperature on the FTS catalyst are yet unknown for most reactors, especially for microstructured reactors. The following analysis is preliminary as a continuous operation under load-flexible or dynamic conditions is to be performed on longer time scale.

Different criteria can be chosen to evaluate the state of the catalyst. Easiest to test is conversion and selectivity towards different product classes on a regular basis. This will not give sophisticated information on the state of the catalyst surface, specifically the active sites. In order to get a glimpse of surface effects, in-situ, or better, operando measurements are necessary. In the case of FTS, this is not a simple operation to perform. Process parameters like elevated pressure and temperature usually mean rough conditions for the equipment. Many reaction cells are designed to withstand the required temperature but are vulnerable to pressure. A complementary analysis of the metal surface and the reaction products allows for a more accurate interpretation of the observed phenomena. The methods of choice for operando analysis would be X-ray absorption (XAS) techniques, X-ray diffraction (XRD), and a coupled GC-MS analysis. [19,52–54]. Those studies have been performed in an accompanied study and are subject of another publication under review [55].

In this work, catalyst activity was only evaluated by GC analysis. In Figure 14, the CO conversion and selectivity towards methane (S_{C1}) and liquid products (S_{C5+}) are shown. The same experimental condition was tested multiple times to determine the given values. The figure shows the respective value changes from data points 15–18 of Table 2 (identical parameters: $H_2/CO = 2.2$, ~ 240 °C, 30 bar_{abs}, 94.5 g_{cat} h m^{-3}). Between the measurement of data point 15 ('before experiments') and setup 16 ('after experiment C'), around 1000 h of operation elapsed, during which many different other data were collected from the reactor. In order to isolate the effect of the dynamic cycles on the catalyst from those trials, this data point should have been assessed right before experiment C. However, since this test was not executed, it is difficult to formulate a final assumption on when the catalyst actually deactivated.

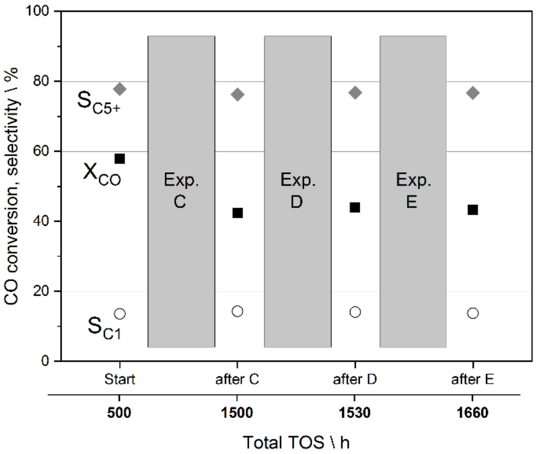

Figure 14. CO conversion and selectivity towards methane (S_{C1}) and liquid products (S_{C5+}) over total experimental TOS. Four setups (15–18 from Table 2) are represented for the sake of activity measurement. Grey rectangles mark the experimental campaigns presented in this work (experiments C–E).

Nevertheless, the CO conversion drop from around 58% to 42.4% within 1000 h of TOS may be correlated much more to the TOS than to experiments A, B and C themselves. This is supported by further constant values for all following experiments (more experiments were conducted that are not the subject of this study). It thus may be concluded that experiment D and E had no effect on catalyst performance. Complementary measurements are, nevertheless, needed for final statements.

4. Conclusions

In part 2 of this study, the challenges of a fluctuating energy supply are tackled. Sector coupling via dynamic operation of a microstructured packed bed reactor for FTS according to step changes and a real PV profile are assumed. From this study, it may be concluded that storage of fluctuating energy on minute- to season-scale via generation of chemical compounds seems feasible with the applied micro-technology. This claim is supported by the superior load flexibility of microstructured reactors. Even though it seems that intermediate hydrogen buffering can be omitted to large extent, economic considerations need to be performed to provide the realistic scenario at which time-scale load flexibility is actually required. It is also unclear how long the catalyst system would persevere in such specific scenarios. From this study, it may be concluded that dynamic operation is feasible in microstructured reactors without considerable influence on degradation. System changes in that time-scale are only possible due to the previously described, increased heat and mass transfer within those reactors and the application of pressure changes via evaporation cooling.

Available PV data from KIT's solar park were translated into time-resolved hydrogen or syngas flow assuming near instantaneous conversion by electrolysis and reverse water-gas shift. The data was discretized to adjust to manageable setpoint changes in a pilot FTS test rig. Two base cases were developed, on which further experiments were performed. Case 1: a small-scale BtL plant where hydrogen is co-fed according to the PV power availability without a hydrogen buffer, leading to feed flow and H_2/CO ratio fluctuations. Case 2: a PtL plant without hydrogen buffer but a CO_2 storage leading to only feed flow fluctuations. Some facts have been neglected, such as the product gas from the RWGS would always include a dilution by inert gases such as CH_4 or CO_2. Nevertheless, effects from high dilution on the catalyst were investigated before [18].

Initial step change experiments were carried out to test the discretized steps from which it could be concluded that the system can buffer simultaneous syngas ratio and residence time changes with regard to thermal behavior and product quality. No obvious changes were found when varying the timeframe of the steps. Experiments with PV data were executed without and with temperature manipulation to emphasize the importance of evaporation cooling as the main tool to even product quality with fluctuating feed. Case 1, the BtL case, yielded unfavorable higher concentration differences along the fluctuation. Case 2 (PtL) showed a much steadier performance, as demonstrated by plots of methane concentration, as well as alkane and alkene content of the liquid product as a function of time.

It could be proven that highly dynamic, load flexible operation in microstructured FT reactors with multi-parameter changes in the one-minute regime are feasible and fully controllable. No runaway or blowout was found during fast changes of experimental conditions. The development of a regression model for adapting the reactor temperature without the need for measuring the product composition—i.e., only on basis of the knowledge of syngas ratio and residence time—led to almost even product quality. Constant product quality is important for product post-processing such as distillation and hydrotreating and highlights the importance of such methods. Keeping the CO conversion level by temperature manipulation seems to be a suitable approach for PtL plants as determined in this study. With a fixed H_2/CO ratio, reaching the goal of a target conversion of 70% by temperature manipulation via the pressure in the evaporating cooling cycle was experimentally verified as good strategy.

Due to the fact of relatively small total flows in the pilot scale FTS test rig, it was difficult to increase system temperature on demand from all starting points. This observation would improve with larger reactors. Consequently, autothermal operation will be possible with even lower relative loads, leading to more hours of operation without considerable hydrogen storage.

Changes in the test rig were done manually, which can be optimized. Last but not least, no apparent signs of catalyst damage were found through dynamic experiments. Nevertheless, operando technology would enable a deeper look onto the catalyst's active sites to determine if the applied process caused negative effects on long-term activity.

Author Contributions: Conceptualization, M.L., M.R., and P.P.; Methodology, M.L. and P.P.; Software, M.L. and M.R.; Validation, M.L. and P.P.; Formal Analysis, M.L. and M.R.; Investigation, M.L. and M.R.; Resources, M.L.; Data Curation, M.L.; Writing—Original Draft Preparation, M.L.; Writing—Review and Editing, M.L., M.R., and P.P.; Visualization, M.L. and M.R..; Supervision, P.P.; Project Administration, M.L. and P.P.; Funding Acquisition, P.P. All authors have read and agreed to the published version of the manuscript.

Funding: We gratefully acknowledge funding from the Vector Stiftung under the project acronym DynSyn.

Acknowledgments: We kindly thank the Vector Stiftung for financially supporting this work. Many thanks go to the colleagues from KIT's Institute of Electrical Engineering and the Battery Technical Center (BATEC) for providing valuable data for us to work with.

Conflicts of Interest: The authors declare no conflict of interest.

References

1. UN Climate Change. Historic Paris Agreement on Climate Change: 195 Nations Set Path to Keep Temperature Rise Well Below 2 Degrees Celsius. Available online: http://newsroom.unfccc.int/unfccc-newsroom/finale-cop21/ (accessed on 3 April 2018).
2. BMU. Hendricks startet Dialog zum Klimaschutzplan 2050. Available online: https://www.bmu.de/pressemitteilung/hendricks-startet-dialog-zum-klimaschutzplan-2050/?tx_ttnews%5BbackPid%5D=3915 (accessed on 12 February 2020).
3. Le Quéré, C.; Andrew, R.M.; Friedlingstein, P.; Sitch, S.; Hauck, J.; Pongratz, J.; Pickers, P.A.; Korsbakken, J.I.; Peters, G.P.; Canadell, J.G.; et al. Global Carbon Budget 2018. *Earth. Syst. Sci. Data* **2018**, *10*, 2141–2194, doi:10.5194/essd-10-2141-2018.

4. Dittmeyer, R.; Boeltken, T.; Piermartini, P.; Selinsek, M.; Loewert, M.; Dallmann, F.; Kreuder, H.; Cholewa, M.; Wunsch, A.; Belimov, M.; et al. Micro and micro membrane reactors for advanced applications in chemical energy conversion. *Curr. Opin. Chem. Eng.* **2017**, *17*, 108–125, doi:10.1016/j.coche.2017.08.001.
5. Maitlis, P.M., de Klerk, A. *Greener Fischer–Tropsch Processes for Fuels and Feedstocks;* Eds.; Wiley-VCH: Weinheim, Germany, 2013; ISBN 3527329455.
6. Verein Deutscher Ingenieure (VDI). *VDI-Statusreport Regenerative Energien*. Available online: https://www.vdi.de/ueber-uns/presse/publikationen/details/vdi-statusreport-regenerative-energien (accessed on 11 April 2020).
7. SAPEA—Science Advice for Policy by European Academies. *Novel Carbon Capture and Utilisation Technologies*, Available Online: https://www.sapea.info/wp-content/uploads/CCU-report-web-version.pdf (accessed on 11 April 2020).
8. International Energy Agency (IEA). *World Energy Outlook 2016*. Available online: https://webstore.iea.org/world-energy-outlook-2016 (accessed on 11 April 2020).
9. Vaillancourt, K.; Bahn, O.; Roy, P.O.; Patreau, V. Is there a future for new hydrocarbon projects in a decarbonizing energy system? A case study for Quebec (Canada). *Appl. Energy* **2018**, *218*, 114–130, doi:10.1016/j.apenergy.2018.02.171.
10. Ridjan, I.; Mathiesen, B.V.; Connolly, D. Terminology used for renewable liquid and gaseous fuels based on the conversion of electricity: A review. *J. Clean. Prod.* **2016**, *112*, 3709–3720, doi:10.1016/j.jclepro.2015.05.117.
11. Li, W.; Wang, H.; Jiang, X.; Zhu, J.; Liu, Z.; Guo, X.; Song, C. A short review of recent advances in CO2 hydrogenation to hydrocarbons over heterogeneous catalysts. *RSC Adv.* **2018**, *8*, 7651–7669, doi:10.1039/C7RA13546G.
12. Reuß, M.; Grube, T.; Robinius, M.; Preuster, P.; Wasserscheid, P.; Stolten, D. Seasonal storage and alternative carriers: A flexible hydrogen supply chain model. *Appl. Energy* **2017**, *200*, 290–302, doi:10.1016/j.apenergy.2017.05.050.
13. Kotzur, L.; Markewitz, P.; Robinius, M.; Stolten, D. Time series aggregation for energy system design: Modeling seasonal storage. *Appl. Energy* **2018**, *213*, 123–135, doi:10.1016/j.apenergy.2018.01.023.
14. Schmidt, P.; Batteiger, V.; Roth, A.; Weindorf, W.; Raksha, T. Power-to-Liquids as Renewable Fuel Option for Aviation: A Review. *Chem. Ing. Tech.* **2018**, 127–140.
15. De Klerk, A. *Fischer–Tropsch Refining*, 1st ed.; Wiley-VCH: Weinheim, Germany, 2011; ISBN 3527326057.
16. Piermartini, P.; Boeltken, T.; Selinsek, M.; Pfeifer, P. Influence of channel geometry on Fischer–Tropsch synthesis in microstructured reactors. *Chem. Eng. J.* **2017**, *313*, 328–335, doi:10.1016/j.cej.2016.12.076.
17. Myrstad, R.; Eri, S.; Pfeifer, P.; Rytter, E.; Holmen, A. Fischer–Tropsch synthesis in a microstructured reactor. *Catal. Today* **2009**, *147*, 301–304. https://doi.org/10.1016/j.cattod.2009.07.011.
18. Loewert, M.; Hoffmann, J.; Piermartini, P.; Selinsek, M.; Dittmeyer, R.; Pfeifer, P. Microstructured Fischer–Tropsch reactor scale-up and opportunities for decentralized application. *Chem. Eng. Technol.* **2019**, 2202–2214, doi:10.1002/ceat.201900136.
19. Kalz, K.F.; Kraehnert, R.; Dvoyashkin, M.; Dittmeyer, R.; Gläser, R.; Krewer, U.; Reuter, K.; Grunwaldt, J.D. Future Challenges in Heterogeneous Catalysis: Understanding Catalysts under Dynamic Reaction Conditions. *ChemCatChem* **2017**, *9*, 17–29, doi:10.1002/cctc.201600996.
20. Silveston, P.; Hudgins, R.R.; Renken, A. Periodic operation of catalytic reactors-introduction and overview. *Catal. Today* **1995**, *25*, 91–112, doi:10.1016/0920-5861(95)00101-K.
21. Güttel, R. Study of Unsteady-State Operation of Methanation by Modeling and Simulation. *Chem. Eng. Technol.* **2013**, *83*, doi:10.1002/ceat.201300223.
22. Iglesias González, M. Gaseous Hydrocarbon Synfuels from H_2/CO_2 based on Renewable Electricity Kinetics, Selectivity and Fundamentals of Fixed-Bed Reactor Design for Flexible Operation. PhD Thesis, Karlsruhe Institute of Technology (KIT), Karlsruhe, Germany, 2016.
23. Iglesias González, M.; Schaub, G. Fischer–Tropsch synthesis with H_2/CO_2-catalyst behavior under transient conditions. *Chem. Ing. Tech.* **2015**, *87*, 848–854, doi:10.1002/cite.201400137.
24. Eilers, H.; González, M.I.; Schaub, G. Lab-scale experimental studies of Fischer–Tropsch kinetics in a three-phase slurry reactor under transient reaction conditions. *Catal. Today* **2015**, doi:10.1016/j.cattod.2015.11.011.
25. Mutz, B.; Carvalho, H.W.P.; Mangold, S.; Kleist, W.; Grunwaldt, J.-D. Methanation of CO2: Structural response of a Ni-based catalyst under fluctuating reaction conditions unraveled by operando spectroscopy. *J. Catal.* **2015**, *327*, 48–53, doi:10.1016/j.jcat.2015.04.006.

26. Kreitz, B.; Wehinger, G.D.; Turek, T. Dynamic simulation of the CO2 methanation in a micro-structured fixed-bed reactor. *Chem. Eng. Sci.* **2019**, *195*, 541–552, doi:10.1016/j.ces.2018.09.053.
27. Kreitz, B.; Friedland, J.; Güttel, R.; Wehinger, G.D.; Turek, T. Dynamic Methanation of CO 2 – Effect of Concentration Forcing. *Chem. Ing. Tech.* **2019**, *91*, 576–582, doi:10.1002/cite.201800191.
28. Fache, A.; Marias, F.; Guerré, V.; Palmade, S. Optimization of fixed-bed methanation reactors: Safe and efficient operation under transient and steady-state conditions. *Chem. Eng. Sci.* **2018**, *192*, 1124–1137, doi:10.1016/j.ces.2018.08.044.
29. Tauer, G.; Kern, C.; Jess, A. Transient Effects during Dynamic Operation of a Wall-Cooled Fixed-Bed Reactor for CO 2 Methanation. *Chem. Eng. Technol.* **2019**, *42*, 2401–2409, doi:10.1002/ceat.201900367.
30. Theurich, S.; Rönsch, S.; Güttel, R. Transient Flow Rate Ramps for Methanation of Carbon Dioxide in an Adiabatic Fixed-Bed Recycle Reactor. *Energy Technol.* **2020**, *8*, 1901116, doi:10.1002/ente.201901116.
31. Bremer, J.; Sundmacher, K. Operation range extension via hot-spot control for catalytic CO 2 methanation reactors. *React. Chem. Eng.* **2019**, *4*, 1019–1037, doi:10.1039/c9re00147f.
32. Fache, A.; Marias, F.; Guerré, V.; Palmade, S. Intermittent Operation of Fixed-Bed Methanation Reactors: A Simple Relation Between Start-Up Time and Idle State Duration. *Waste Biomass Valorization* **2020**, *11*, 447–463, doi:10.1007/s12649-018-0507-3.
33. Fache, A.; Marias, F.; Chaudret, B. Catalytic reactors for highly exothermic reactions: Steady-state stability enhancement by magnetic induction. *Chem. Eng. J.* **2020**, *390*, 124531, doi:10.1016/j.cej.2020.124531.
34. Fache, A.; Marias, F. Dynamic operation of fixed-bed methanation reactors: Yield control by catalyst dilution profile and magnetic induction. *Renew. Energy* **2020**, *151*, 865–886, doi:10.1016/j.renene.2019.11.081.
35. Bremer, J.; Rätze, K.H.G.; Sundmacher, K. CO 2 methanation: Optimal start-up control of a fixed-bed reactor for power-to-gas applications. *AIChE J.* **2017**, *63*, 23–31, doi:10.1002/aic.15496.
36. Theurich, S. Unsteady-state operation of a fixed-bed recycle reactor for the methanation of carbon dioxide. PhD Thesis, Ulm university, Ulm, Germany, 2019.
37. Adesina, A.A.; Silveston, P.L.; Hudgins, R.R. A Comparison of Forced Feed Cycling of the Fischer–Tropsch Synthesis over Iron and Cobalt Catalysts. In *Catalysis on the Energy Scene*; Elsevier: Amsterdam, Netherlands, 1984; pp. 191–196, ISBN 9780444424020.
38. Loewert, M.; Pfeifer, P. Dynamically Operated Fischer–Tropsch Synthesis in PtL-Part 1: System Response on Intermittent Feed. *ChemEng.* **2020**, doi:10.3390/chemengineering4020021.
39. Sun, C.; Zhan, T.; Pfeifer, P.; Dittmeyer, R. Influence of Fischer–Tropsch synthesis (FTS) and hydrocracking (HC) conditions on the product distribution of an integrated FTS-HC process. *Chem. Eng. J.* **2017**, *310*, 272–281, doi:10.1016/j.cej.2016.10.118.
40. Sun, C.; Pfeifer, P.; Dittmeyer, R. One-stage syngas-to-fuel in a micro-structured reactor: Investigation of integration pattern and operating conditions on the selectivity and productivity of liquid fuels. *Chem. Eng. J.* **2017**, *326*, 37–46, doi:10.1016/j.cej.2017.05.133.
41. Tremel, A. *Electricity-Based Fuels*; Springer International Publishing: Cham, Switzerland, 2018; ISBN 9783319724591.
42. SIEMENS. SILYZER 300-Die Nächste Dimension der PEM-Elektrolyse. Available online: https://assets.new.siemens.com/siemens/assets/api/uuid:abae9c1e48d6d239c06d88e565a25040ed2078dc/version:1524040818/ct-ree-18-047-db-silyzer-300-db-de-en-rz.pdf (accessed on 29 March 2020).
43. Monaco, F.; Lanzini, A.; Santarelli, M. Making synthetic fuels for the road transportation sector via solid oxide electrolysis and catalytic upgrade using recovered carbon dioxide and residual biomass. *J. Clean. Prod.* **2018**, *170*, 160–173, doi:10.1016/j.jclepro.2017.09.141.
44. Montgomery, D.C. *Design and Analysis of Experiments*; Eighth edition; John Wiley & Sons Inc.: Hoboken, NJ, USA, 2013.
45. Stiller, C. *Grundlagen der Mess-und Regelungstechnik;* Shaker: Aachen, Germany, 2006; ISBN 3-8322-5582-6.
46. Mueller, J.P.; Massaron, L. *Machine Learning for Dummies;* John Wiley & Sons, Inc.: New York, NY, USA, 2016; ISBN 978-1-119-24551-3.
47. Todic, B.; Ma, W.; Jacobs, G.; Davis, B.H.; Bukur, D.B. Effect of process conditions on the product distribution of Fischer–Tropsch synthesis over a Re-promoted cobalt-alumina catalyst using a stirred tank slurry reactor. *J. Catal.* **2014**, *311*, 325–338, doi:10.1016/j.jcat.2013.12.009.
48. Van der Laan, G.P.; Beenackers, A.A.C.M. Kinetics and Selectivity of the Fischer–Tropsch Synthesis: A Literature Review. *Catal. Rev.* **1999**, *41*, 255–318, doi:10.1081/CR-100101170.

49. Yates, I.C.; Satterfield, C.N. Hydrocarbon selectivity from cobalt Fischer–Tropsch catalysts. *Energy Fuels* **1992**, *6*, 308–314, doi:10.1021/ef00033a011.
50. Dry, M.E. Practical and theoretical aspects of the catalytic Fischer–Tropsch process. *Appl. Catal. A-Gen.* **1996**, *138*, 319–344, doi:10.1016/0926-860X(95)00306-1.
51. VDI-Gesellschaft Verfahrenstechnik und Chemieingenieurwesen. *VDI Heat Atlas*, 2nd Ed.; Springer: Heidelberg/Neckar, Germany, 2010; ISBN 9783540799993.
52. Rønning, M.; Tsakoumis, N.E.; Voronov, A.; Johnsen, R.E.; Norby, P.; van Beek, W.; Borg, Ø.; Rytter, E.; Holmen, A. Combined XRD and XANES studies of a Re-promoted Co/γ-Al2O3 catalyst at Fischer–Tropsch synthesis conditions. *Catal. Today* **2010**, *155*, 289–295, doi:10.1016/j.cattod.2009.10.010.
53. Grunwaldt, J.-D.; Clausen, B.S. Combining XRD and EXAFS with on-Line Catalytic Studies for in situ Characterization of Catalysts. *Top. Catal.* **2002**, *18*, 37–43, doi:10.1023/A:1013838428305.
54. Rochet, A.; Moizan, V.; Pichon, C.; Diehl, F.; Berliet, A.; Briois, V. In situ and operando structural characterisation of a Fischer–Tropsch supported cobalt catalyst. *Catal. Today* **2011**, *171*, 186–191, doi:10.1016/j.cattod.2011.03.079.
55. Loewert, M.; Serrer, M.-A.; Carambia, T.; Stehle, M.; Zimina, A.; Kalz, K.F.; Lichtenberg, H.; Saraci, E.; Pfeifer, P.; Grunwaldt, J.-D. Bridging the gap between industry and synchrotron: An *operando* study at 30 bar over 300 h during Fischer–Tropsch synthesis. *React. Chem. Eng.* **2020**, DOI: 10.1039/C9RE00493A

PAPER IV

COUPLING OF FISCHER-TROPSCH REACTION KINETICS, ENHANCED VAPOR-LIQUID FLASH CALCULATION AND RESIDENCE TIME DISTRIBUTION MODELING FOR TIME-DEPENDENT PRODUCT DETERMINATION IN LOAD-FLEXIBLE PLANTS

Submitted to Chemical Engineering Journal, 24.02.2020

Accepted and available online: 26.06.2020

`https://doi.org/10.1016/j.cej.2020.126032`

Paper IV

Coupling of Fischer-Tropsch reaction kinetics, enhanced vapor-liquid flash calculation and residence time distribution modeling for time-dependent product determination in load-flexible plants

Marcel Loewert, Victor Zaghini Francesconi, Lucas Tim Brübach, Ing. Peter Pfeifer

PII:	S1385-8947(20)32160-4
DOI:	https://doi.org/10.1016/j.cej.2020.126032
Reference:	CEJ 126032
To appear in:	*Chemical Engineering Journal*
Received Date:	24 February 2020
Revised Date:	15 June 2020
Accepted Date:	20 June 2020

Please cite this article as: M. Loewert, V. Zaghini Francesconi, L. Tim Brübach, Ing. Peter Pfeifer, Coupling of Fischer-Tropsch reaction kinetics, enhanced vapor-liquid flash calculation and residence time distribution modeling for time-dependent product determination in load-flexible plants, *Chemical Engineering Journal* (2020), doi: https://doi.org/10.1016/j.cej.2020.126032

Title:

Coupling of Fischer-Tropsch reaction kinetics, enhanced vapor-liquid flash calculation and residence time distribution modeling for time-dependent product determination in load-flexible plants

Author names and affiliations:

Marcel **Loewert**[a], Victor Zaghini **Francesconi**[a], Lucas Tim **Brübach**[a], Prof. Dr.-Ing. Peter **Pfeifer**[a*]

[a] Institute for micro process engineering (IMVT), Karlsruhe Institute of Technology (KIT), 76344 Eggenstein-Leopoldshafen, Germany

* corresponding author, +49-721-608-24767; peter.pfeifer@kit.edu

Additional email-addresses:

Marcel Loewert: marcel.loewert@ineratec.de
Victor Zaghini Francesconi: uhesz@student.kit.edu
Lucas Tim Brübach: lucas.bruebach@kit.edu

Abstract:

Fischer-Tropsch synthesis may be a solution for converting volatile renewable energies into storable liquid fuel. Microstructured reactors have been proven to cope with varying operation conditions and are able to adapt to fluctuations in this circumstance. In this regard, a suitable kinetic model for chemical synthesis is essential for the prediction of reactor and catalyst behavior. The assessment and description of the reactor and plant response during dynamic operation must also be considered to develop a control system for varying operating conditions. In this work, a time-resolved model for the description of relevant processes inside a pilot scale microstructured Fischer-Tropsch reactor and the associated test rig including the product condensation stages is presented. A residence time distribution model describes flow and mixing behavior for all system components. Time and temperature-dependent product concentration in the product traps is determined by vapor-liquid-equilibrium calculation. Phase equilibria models with ideal and real phase behavior assumptions are compared. A micro-kinetic model was adapted with good agreement to a variety of experimental data. When coupled, the overall model is able to predict time-resolved product characteristics based on process conditions and feed only. This mathematical description may be of use for decentralized plants in the future.

Keywords: Fischer-Tropsch synthesis; microstructured reactors; vapor-liquid flash calculation; reaction kinetics; residence time distribution; dynamic synthesis

1. Introduction

Crude oil, natural gas and coal are still main sources of energy for transportation, industrial production and heat supply [1]. The resulting CO_2 emissions contribute to anthropogenic climate change. For this reason, it is imperative that energy generation becomes CO_2-neutral in the future by use of renewable energy sources.

Wind and solar power are temporally and spatially distributed. Thus, solutions for an efficient and flexible energy system are required beyond smart grids. In order to enable sector coupling, Power-to-X technology (PtX) represents a promising concept and may foster the role of electrical energy as primary energy [2]. PtX summarizes technologies that allow energy storage in forms of chemical compounds such as hydrocarbons and supply of other sectors.

Amongst P2X approaches, the Power-to-Liquid (PtL) process produces liquid energy carriers. In the short and medium term, it may not be possible to fully decarbonize the mobility and heat sectors, i.e. to decouple them from the use of fossil fuels and to cover national or global energy requirements entirely on an electrical basis [1]. On the long term, long-distance traffic will depend on liquid fuels with high energy density. According to recent studies, transport will depend due to economic and grid stability with around 50 % on P2X in Germany in 2050 [3].

One possible process pathway for PtL is the Fischer-Tropsch Synthesis (FTS). It is a strongly exothermic, heterogeneously catalyzed process for the generation of liquid hydrocarbons from synthesis gas (hydrogen and carbon monoxide). Hydrogen can be obtained from electrolysis, while CO can be derived from various regenerative and thus CO_2-neutral sources. Examples are biomass digestion or gasification and CO_2 direct air capture. CO_2 must be reduced to CO, which is possible by reverse water gas shift (RWGS) or an electrochemical process. The target products are typically liquid fuels such as gasoline, kerosene and diesel, but also industrial intermediates such as alkenes (olefins) and paraffinic waxes. Fuels produced in the chain length range of diesel have a high Cetane number and improved combustion properties. They are free of aromatics and other heteroatoms such as sulfur and nitrogen which leads to lower soot formation and overall emissions upon combustion [4].

In order to provide an efficient reactor technology for FTS and other reaction processes, microstructured reactors have been developed, investigated and optimized. Due to thin fluid layers in such microstructures, heat transfer and mass transfer in the reaction zone are intensified. This results in a considerably improved energetic and material efficiency as well as a lower space requirement. Higher per-pass conversion in a single reactor can be achieved and almost 100 times higher volumetric space-time yield (1600 – 1800 kg m^{-3} h^{-1}) compared to industrial FTS reactors (20 kg m^{-3} h^{-1}) can be reached. Higher specific performances, increased safety and optimal process control also lead to significant cost reductions and resource efficiency. Together with compactness and modularity of these reactors, implementation of decentralized plants seems feasible in the framework of the energy transition. [5]–[13]

Another advantage of microstructured reactors is the possibility of a dynamic operation [14],[15]. The response time of the reactor is tremendously shortened by its compactness with regard to temperature, concentration and feed flow. Thus, process parameters can be changed quickly in microstructured systems. This is extremely relevant, if an FTS plant would solely depend on volatile renewable energy, i.e. the produced hydrogen. The operating conditions of the reactor must be adaptable in short period to react to these fluctuations. The only alternative would be the provision of a correspondingly large, expensive buffer for hydrogen.

For economical and safe operation, knowledge about conversion and selectivity in the reactor as well as heat integration and material flows in the plant are required information. Dynamic process simulation is able to calculate species distribution, heat flows and product composition at any time at any location inside the plant. In the case of the complex Fischer-Tropsch product composition, the species distribution is hardly to assess experimentally; lots of effort is required to determine the product composition every minute[14],[15] . One issue is a suitable kinetic model for chemical synthesis for the prediction, design and optimization of microstructured reactor behavior [5]. Furthermore, residence time distribution and correct description of the phase equilibria in the two-phase flow of the FT product at product condensation traps are required for description of plants.

This contribution is devoted to deliver the three major elements: kinetics, residence time distribution and the strategy for phase description – all experimentally verified from a pilot scale test rig. The strategy could be applied to larger FT plants to derive the mean composition of the product depending on the input, i.e. wind or solar energy and their respective location. From an economic point of view, it has already been verified in previous contributions that at constant H_2/CO ratio a constant conversion manipulated by the reactor temperature could lead to rather constant product distribution over a real-time photovoltaics energy profile [14],[15]. Heat flows are not yet considered but may be addressed in upcoming further publications.

2. Material and methods

2.1 Experimental setup

The core components of the plant are: mass flow controllers for gas feeding, an evaporation-cooled microstructured packed bed FT reactor, a hot trap (HT) and a micro heat exchanger (µHE) for product condensation before a cold trap (CT); details see elsewhere [14],[16]. The boiling point of the cooling water cycle is controlled by pressure regulation so that the desired reactor temperature can be adjusted in autothermal reactor operation; heat cartridges are used to preheat to ignition temperature of the reaction (approx. 190°C). The product leaving the reactor is mainly gaseous and is fed to the HT via a heated pipeline. In order to condense hydrocarbons which are solid at ambient conditions, the product stream is cooled to approx. 170 °C in the HT. This product fraction will be called “wax”. The remaining gas flow leaves the HT and flows through the µHE into the CT. The gas is cooled to approx. 10 °C and the liquid products, which consist of an oil phase and a water phase, are condensed. The remaining gas from the CT is analyzed in a gas chromatograph (GC) for product analysis. If necessary, gas is directed to a mass spectrometer (MS) via a needle valve during sampling at a Quick Sampling site before the cold trap; details see elsewhere. [14]–[16]

2.2 Experimental data for fitting kinetics

Different experimental campaigns were conducted, analyzed and included into the reactor description via a microkinetic model. An overview of the used process parameters can be found in Table 1.

Table 1: Experimental data and results for 20 steady-state experiments with the microstructured pilot scale reactor.

Experiment	$\dot{V}$	H_2/CO	Dilution	*WHSV*	*T*	p_{total}	X_{CO}	X_{H2}	S_{C1}	S_{C5+}
#	L $\mathrm{min^{-1}}$	ratio -	%	$\mathbf{g_{gas}\,g_{cat}^{-1}\,h^{-1}}$	°C	MPa	%	%	%	%
1	17.526	2.20	2.70	5.23	239.0	3.0	43.29	48.56	13.74	76.71

2	15.528	1.96	3.04	4.91	238.0	3.0	40.53	48.75	12.98	77.77
3	16.263	1.96	17.65	6.20	225.0	3.0	29.11	35.26	10.84	80.38
4	14.309	1.49	20.00	6.08	235.0	3.0	42.06	63.94	9.82	81.86
5	15.290	1.48	18.75	6.15	235.0	3.0	43.55	54.26	11.12	80.27
6	17.249	2.19	16.67	6.27	235.5	3.0	50.24	56.85	13.21	77.11
7	16.272	1.96	17.65	6.21	235.5	3.0	47.74	57.15	12.48	78.23
8	16.360	1.96	17.65	6.24	235.5	2.5	43.98	53.01	13.41	76.71
9	16.492	1.96	17.65	6.29	235.0	2.0	35.86	43.59	13.54	75.88
10	14.304	1.49	20.00	6.08	245.0	3.0	46.28	71.70	20.03	64.16
11	15.281	1.73	18.75	6.14	245.5	3.0	55.98	77.75	14.20	74.76
12	17.273	2.18	16.67	6.28	245.0	3.0	75.40	79.26	16.03	74.20
13	16.297	1.95	17.65	6.22	244.8	3.0	69.73	79.55	13.96	77.16
14	16.360	1.96	17.65	6.24	245.0	2.5	58.52	68.96	14.87	75.08
15	13.745	1.96	3.45	4.37	244.5	3.0	67.37	80.22	13.60	77.45
16	14.692	2.18	3.23	4.42	241.5	3.0	63.49	68.12	14.56	76.36
17	17.747	1.98	2.68	5.43	245.0	3.0	65.25	69.81	13.98	77.21
18	22.913	2.11	2.10	6.96	244.5	3.0	49.05	58.83	14.60	74.90
19	25.574	2.00	1.89	7.74	244.5	3.0	41.58	49.16	14.25	74.90
20	17.788	1.98	2.68	5.45	235.5	3.0	36.06	43.47	13.30	76.55

Experiments were executed on a commercial 20 wt.-% Co-alumina catalyst with 0.5 wt.-% Re promotor. The catalyst has been aged by a multitude of experiments [14],[15] to provide a sound basis of parameter combinations with regard to catalyst activity and selectivity. The loaded particle diameter was 50-200 µm. To guarantee negligible effect of catalyst deactivation, the operation was limited to the following conditions: temperature from 225 to 245.5 °C, a total pressure from 2.0 to 3.0 MPa, a weight hourly space velocity (*WHSV*) from 4.37 to 7.74 h^{-1}, a nitrogen dilution from 1.89 to 20.00 % and a syngas ratio from 1.48 to 2.20. Since the overall results are influenced by the kind of catalyst and its state, i.e. the time on stream (TOS) and previous experiments, the obtained characteristics are only valid for this specific catalyst state. In order to increase model accuracy also for real plant operation, experiments including time dependency of catalyst activity would be required.

2.3 Dead time experiments

The dead time measurements performed with the MS are detailed in a previous work [14]. These measurements have been applied to fit the residence time model according to sections 2.4. CO_2 was used as a tracer with 5 vol.-% of the dosed gas content in non-reactive gas flow. It replaced 5 vol.-% of N_2 to keep the total gas flow. In Table 2, the experimental conditions are shown.

Table 2: Experimental conditions during dead time determination in non-reactive flow [14].

Setup	$\dot{V}$ L min-1	H_2 content vol.-%	N_2 content vol.-%	CO content vol.-%	CO_2 content vol.-%	T °C	p_{total} MPa
CO_2 on/off	20	95	5 / 0	0	0 / 5	225	3

The required time to measure 5 vol.-% of CO_2 in the gas flow was defined as the total dead time after individual parts of the test rig. An overview of different volumes, applied temperature levels and determined dead times is shown in Table 3. The trap temperatures were chosen in order to obtain appropriate hydrocarbon cuts in each respective trap.

Table 3: List of volumes, applied temperatures and the total dead time after the main components of the test rig.

System component	V L	T °C	Total dead time min
Reactor	0.15	220–250	1.4
HT / µHE	4.8	170	17.5
CT	25	10	82.2

Discrepancy between measured dead times and hydrodynamic residence time τ_{hyd} of a component is result of back-mixing and other effects [16]. The dead time before the reactor, i.e. that of the analytics, accounts to 0.4 min and needs to be subtracted from all values. Since the distance between the HT and the µHE is considerably short, the resulting dead time after both components was very similar.

2.4 Residence time distribution

The description of the residence time distribution (RTD) is an important part for the simulation of a chemical plant [18]. It indicates the average residence time of a species in specific plant components.

F(t) is the residence time sum function. It indicates the share of molecules that has left the reactor up to time t. It can be determined directly from a displacement marking experiment as described in section 2.3. The mean residence time τ_{mean} is the first moment μ_1 of the residence time density function *E(t)*:

$$\tau_{mean} \equiv \mu_1 = \int_0^{\infty} t\, E(t)\, dt = \int_0^{1} t\, dF(t) \qquad (1)$$

In order to compare the RTD for different applications, the dimensionless time variable θ can be introduced:

$$\theta = t/\tau_{hyd} \qquad (2)$$

2.4.1 Choice of residence time model for the FT reactor

Model reactors are ideal reaction systems with clearly defined system properties [17]. The ideal plug flow reactor (PFR) model for gas phase applications may describe microstructured reactor systems quite well, even though laminar flow is the predominant regime. This is because radial diffusion is occurring fast over the small radius and evens out the residence time distribution imposed by the parabolic velocity profile.

2.4.2 Tanks-in-series model

In this work, all plant components are described with regard to the residence time distribution by the tanks-in-series (TIS) model. The TIS is based on a cascade of interconnected CSTRs with a volume V_n, which is the respective component volume V_{total} divided by N, the number of CSTRs. With increasing number $N \rightarrow \infty$ the cascade approaches a PFR character. Non-ideal reactors can be described by a combination of several TIS models in parallel. For the TIS, the following equation is valid for a reactor component:

$$\tau_{hyd} = V_{total}/\dot{V} = \frac{1}{\dot{V}}\sum_{n=1}^{N} V_n = C_0 \sum_{n=1}^{N} \Delta X_n/-r_n \qquad (4)$$

with V_{total}: Total component volume [m³],

N: Total number of CSTR in series [-],

n: Number of CSTR in series [-],

V_n: Volume of one CSTR [m³],

C_0: Input concentration [mol m^{-3}],

ΔX_n: Conversion difference obtained in CSTR number n [-],

r_n: Reaction rate in CSTR number n [mol m^{-3} s^{-1}].

In non-reactive flow, the residence time sum function can be expressed via the number of CSTRs as follows:

$$F(\theta) = 1 - \exp(-N\theta) * \left[1 + N\theta + \frac{(N\theta)^2}{2!} + \cdots + \frac{(N\theta)^{N-1}}{(N-1)!} + \cdots\right] \qquad (5)$$

With this equation the CO_2 tracer experiments described in section 2.3 can be fitted by varying N.

2.4.3 RTD modelling and determination of the CSTR number *N* for all test rig components

As described in section 2.4.2 the experimentally determined *F*-curves of each individual component were fitted to equation 5. Figure 1 shows the *F*-curves determined from CO_2 tracer experiments, as well as their description with the TIS models and the corresponding CSTR numbers for the different system components.

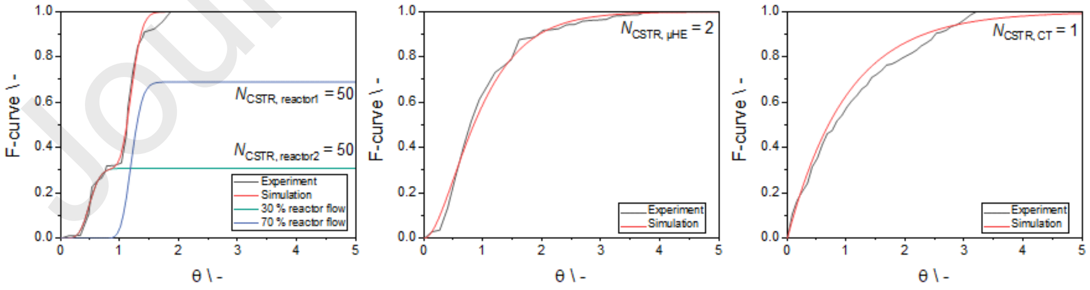

(a) (b) (c)

Figure 1: *F*-curve measurements and TIS modelling of selected system components. Black curves show the experimentally determined CO_2 response, the red curves show the TIS fit. a) FT reactor

adapted by two parallel TIS models with divided volume flow (green and blue curves); b) HT / µHE; c) Cold trap.

Two TIS models fit the experimentally determined CO_2 response of the reactor because of the observed step. The first section of the plot is described by is a cascade of 50 CSTRs for 30 % of the volume flow. The second section is adapted with a cascade of 50 CSTRs for 70 % of the volume flow. A CSTR number of 50 corresponds to a Bodenstein number of 100, which is equivalent to a PFR behavior. Reasons for the observed step could originate from either inhomogeneously packed microstructures and/or back-mixing in the connecting flanges.

The HT could be described by a series connection of two CSTRs, while the CT behaves almost like an ideal CSTR as shown in Figure 1c.

2.5 Reaction kinetics

The reaction mechanism of the FTS is a debate in literature. There is no simplified mechanism that can predict the entire product spectrum [18]. Therefore, it is typically assumed that different reaction routes exist during the reaction, which run in parallel and thus lead to complex product distribution. The FTS is reported to begin with the formation of a CH_2 monomer, which grows to longer hydrocarbon chains via a polymerization reaction [19].

The elementary steps of the FTS can be summarized as follows:

1. adsorption and eventually dissociation of H_2 and CO,
2. chain initiation by formation of the CH_2 monomer at the surface,
3. chain growth by addition of C-species,
4. chain termination by full hydrogenation of a terminal C-atom or dehydrogenation of a C-C bond,
5. desorption of the products.

In detail, literature distinguishes between the carbide, alkyl, CO insertion and enol mechanism [19]–[27]. In macrokinetic approaches, products are grouped together for simplicity (lumping of species).

This is only applicable if the rate-determining step is the formation of monomers and the resulting products do not influence monomer formation [19].

Without discussion and detailed assessment on the real mechanism, we decided to use an adapted microkinetic model based on the alkyl mechanism, developed by Kwack et al. [19], which was able to describe the reactor behavior with good preciseness. This model was also appropriate to describe data from microstructured FT lab reactors in similar circumstance [18],[28].

2.6 Reactor modelling

Appropriate assumptions must be made for a realistic description of the reactor. Based on the criteria of Mears and Weisz-Prater [29]–[31], various boundary conditions and reaction conditions were examined and found to fulfill the absence of mass transport limitation. Transport limitations through the liquid film in and around single particles was also considered to be absent; this is proven in earlier work [28] and supported by modelling done for small catalyst particles [32] as applied in our work. Thus, a pseudo-homogeneous stationary reactor model was chosen. Since a Bodenstein number of 100 was determined from the acquired residence time distribution, ideal plug flow (PFR) was set for the description of conversion and selectivity in the packed microstructures. A step-wise stationary description in this circumstance seems also valid because the mean residence time in the reactor is negligible compared to the rest of the test rig and because reaction follows condition changes immediately [14],[15]. The reactor is described isothermal (see also [8],[16]) and isobaric. Pressure losses over the catalyst bed was determined to be negligible with Δp_{total} < 0.5 bar at 30 bar, i.e. < 2 % change.

Figure 2 shows the principle of the PFR description as applied in the software Matlab®.

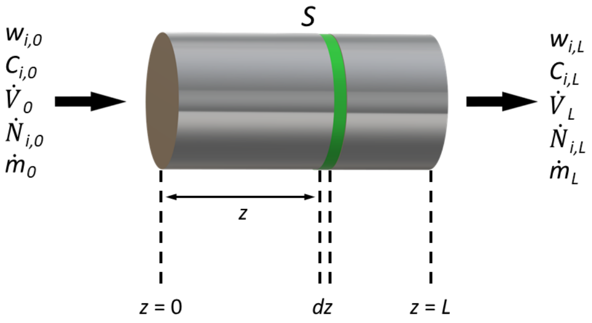

Figure 2: Schematic of the PFR model for description of the microstructured interior reaction process.

A cell model discretizing the reactor was used. Temperature, pressure and volume flow of the reactants are input variables. The mass balance equations are solved for each individual cell in a loop, in which the material properties are continuously updated and applied as input for the calculation of the next cell. For a small volume element (*S dz*) the PFR equation is written as follows:

$$\frac{dm_i}{dt} = (\dot{m}w_i)_z - (\dot{m}w_i)_{z+dz} + M_i r_i S dz \tag{6}$$

With the assumption of $\dot{m}_0 = \dot{m}_L = \dot{m} = constant\ (stationary)$ it can be written as

$$\frac{dm_i}{dt} = 0 \rightarrow (\dot{m}w_i)_z - (\dot{m}w_i)_{z+dz} = -M_i r_i S dz. \tag{7}$$

Replacing ($w_i = M_i C_i/\rho$), ($\dot{m} = \dot{V}\rho$), ($\dot{V} C_i = \dot{N}_i$) and ($Sdz = dV$) gives

$$(\dot{N}_i)_z - (\dot{N}_i)_{z+dz} = -r_i dV. \tag{8}$$

In differential notation this is

$$-d\dot{N}_i = -r_i dV. \tag{9}$$

Finally, the molar change of the species i in a cell is

$$d\dot{N}_{i,\mathrm{cell}} = dV_{cat} \cdot r_{i,cell}(z + dz). \tag{10}$$

To be grid-independent, the cell size was reduced in the iteration until the conversion change in each step was less than 1 % and the difference between the mole flows for H_2 and CO of the input and output of a cell were less than 10^{-12} mol s^{-1}. Figure 3 visualizes the algorithm as a flowchart.

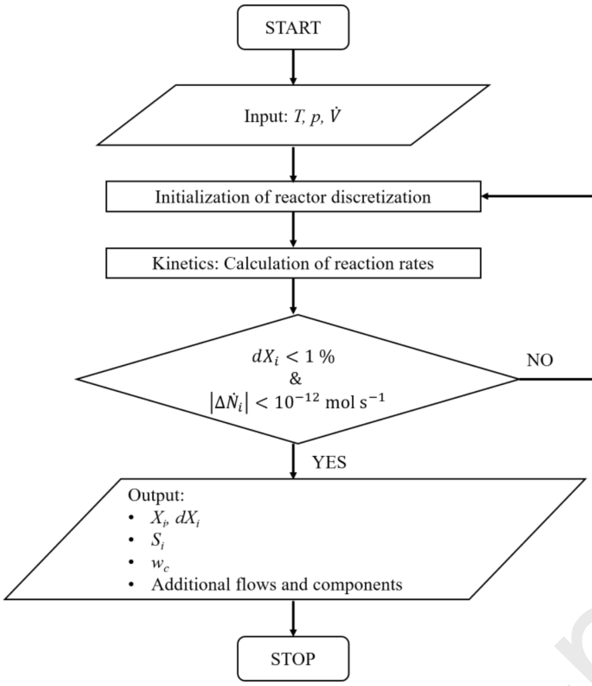

Figure 3: Flowchart for discretizing the reactor during calculation of conversion and selectivity.

2.7 Vapor-liquid equilibrium (VLE) description of the product condensation

VLE modelling of Fischer-Tropsch product is a challenging topic due to the broad variety of components including polar, nonpolar, supercritical and subcritical components. Here, we propose the use of the group contribution-based volume-translated Peng-Robinson equation of state VTPR-GCEOS. It was developed for asymmetric multicomponent mixtures containing polar and nonpolar components and should thus yield reliable results for VLE calculations of Fischer-Tropsch related processes [33]–[35]. The use of an equation of state has the great advantage that the whole product spectrum can be described consistently with one equation.

The basic equation is a volume-translated form of the Peng-Robinson EOS (eq. 13) where the temperature dependent interaction parameters are based on group interaction parameters as in modified UNIFAC. For the α function the exponential approach developed by Twu et al. [36] is used. The concept of volume translation was neglected in this work since it was of no interest to calculate liquid densities. The volume translation parameter *c* does not affect equilibrium calculations [37].

$$p = \frac{RT}{v + c - b} - \frac{a(T)}{(v+c)(v+c+b)+b(v+c-b)} \qquad (11)$$

The calculation routines in MATLAB were adapted and validated from published example MATHCAD sheets [36]. Pure component property data (critical temperature, critical pressure and Twu *α* parameter) was taken from Twu et al. [36] and Bell et al. [38]. For long-chain hydrocarbons (more than 20 carbon atoms) the critical data was estimated using group contribution methods [36],[39] and Twu *α* parameters were fitted to a vapor pressure correlation of Marano and Holder [40]. The acentric factor was calculated from Twu *α* parameters to guarantee internal consistency.

In the HT, a liquid and a gaseous phase are formed. Thus, a two-phase flash based on the Rashford-Rice flash equation [40] was implemented. For the CT, a three-phase flash calculation based on a generalized Rashford-Rice equation was used to account for the immiscible oil and water phases. In each calculation all hydrocarbons were assumed to be n-alkanes.

2.8 Model application in MATLAB®

Differential equations were solved with the *ode45* solver. The optimization algorithm *lsqnonlin*, suitable for nonlinear problems was used to create a fit for experimental data. The *sobolset* function was used to determine the initial values during parameter optimization.

Reaction kinetics and the RTD model interact with each other and deliver coupled results for modelling of the FTS plant. Time-dependent product concentrations and properties such as conversion, selectivity, mass distribution and product formation in different fractions are predicted. Figure 4 gives a schematic of the modelling approach.

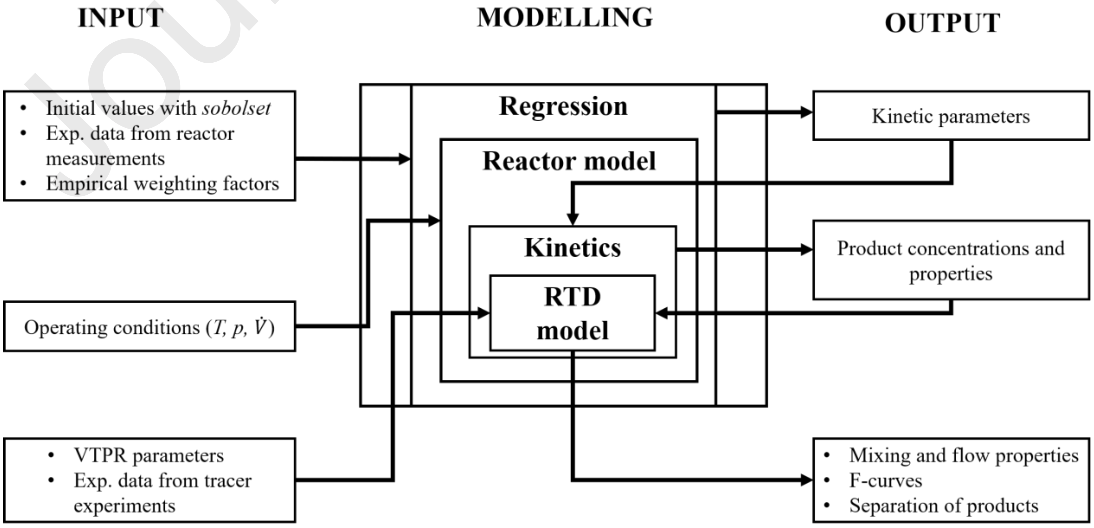

Figure 4: Overview of the modelling approach.

Based on the developed RTD model, mixing and flow properties can be predicted. To calculate flow mixing, two different operating conditions can be used as an input. A mixing ratio of both sets of conditions can be given between 0 and 1, from which a product distribution will be calculated. Alternatively, a mixing time for both sets of conditions can be specified, from which the product distribution will be calculated.

For each separator and for each method of mixing, a *p*-*T* flash is performed to calculate the VLE. An input stream is immediately separated into a liquid and a vaporous product.

If a process parameter changes, product quality is also shifting. Mixing of two fluids was thus implemented in the routine. Figure 5 shows a schematic representation of the calculation of the mixing states. Flow properties and product concentrations are calculated separately for different operating conditions using the VLE. If the mixing ratio is specified, a θ-value is determined based on the *F*-curve of the respective system component. Since the volume and flow rate of the system components are known, an average residence time and thus the elapsed mixing time can be determined to calculate the concentrations in the mixed flow. If the mixing time is specified, a θ-value is determined using equation 4. This allows determination of the *F*-value of the respective component. This *F*-value then corresponds to the mixing ratio with which the two flows of each operating conditions are mixed.

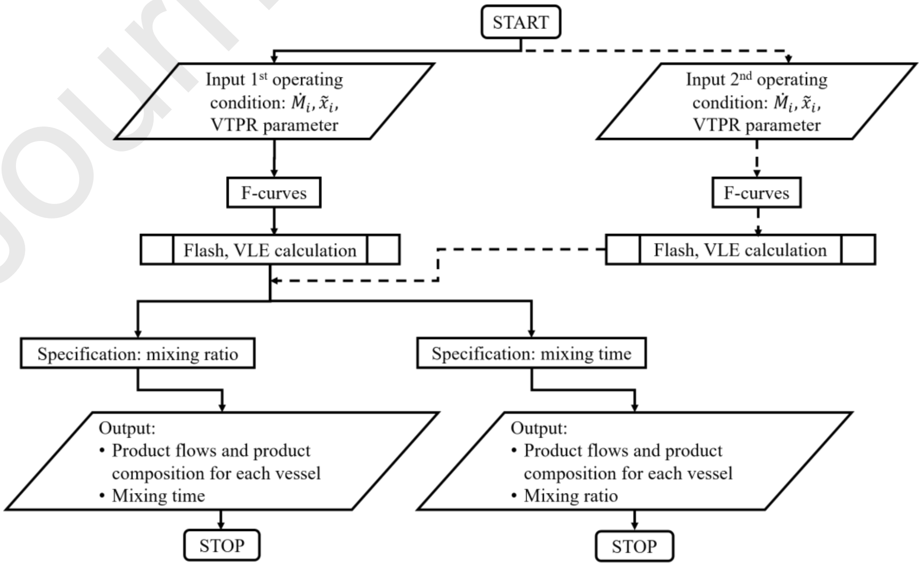

Figure 5: Program flowchart for the calculation of mixing states.

The gaseous phase can be described in each component via the determined *F*-curves (section 2.4.3). For the liquid phase this cannot be assumed. However, if the liquid is formed almost immediately when entering a specific component, the *F*-curve of the gaseous phase of the preceding component can be applied. Figure 6 illustrates this approach.

Since both separators are not continuously discharged but manually emptied in time intervals, the available volume of the separators differs slightly for the gas phase over time. The effect of filling level of liquid was nevertheless neglected as influence on the RTD of the gas phase due to maximum levels below 20 %.

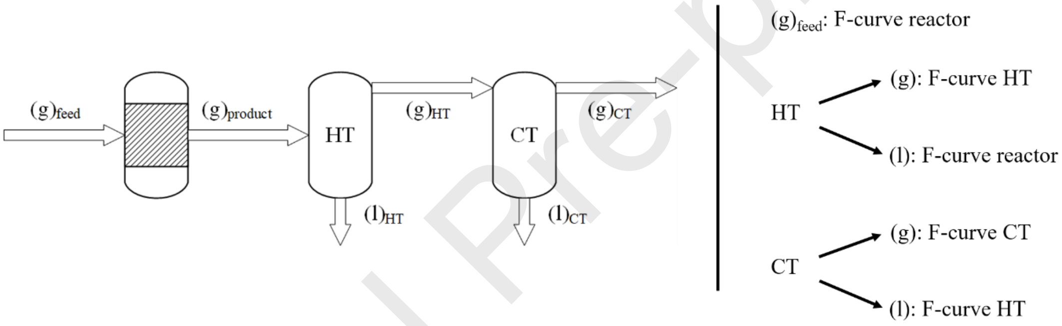

Figure 6: Approach of applied *F*-curves for gas and liquid. “(g)” stands for the gaseous phase, “(l)” for the liquid phase.

3. Model validation

3.1 Validation of the kinetic model

To validate the kinetics and the reactor model, simulated mass distributions, conversions and each selectivity were compared with experimental data. Table 4 shows the results of the nonlinear regression for the determination of the kinetic parameters, as well as provided values from literature along with the model [18],[19]. Two adsorption constants are determined ($K_{H_2}^{ad}$ and $k_{CO}K_{CO}^{ad}$) for the reactants. In addition, five velocity coefficients (k_{IN}, k_G, k_{CH_4}, k_2, k_i) were adjusted, describing phenomena such as chain initiation, growth and termination, as well as the formation of methane and ethane. Two activation energies (E_{IN}, E_G) were adjusted for chain start and chain growth.

Table 4: Adjusted kinetic parameters for the developed reaction model by Kwack et al. [19] – comparison of own values with literature values.

Mechanism	Parameter	Unit	Determined value	Literature value
	$\boldsymbol{K_{H_2}^{ad}}$	bar^{-1}	$2,98 \cdot 10^{-5}$	^{*b} $3,91 \cdot 10^{-5}$
	$\boldsymbol{k_{CO} \cdot K_{CO}^{ad}}$	$mol \cdot kg^{-1} \cdot s^{-1} \cdot bar^{-1}$	$2,15 \cdot 10^{-2}$	^{*b} $5,82 \cdot 10^{-2}$
	^{*a} $\boldsymbol{k_{IN}^0}$	$mol \cdot kg^{-1} \cdot s^{-1}$	$1,03 \cdot 10^{0}$	^{*b} $3,73 \cdot 10^{-1}$
	^{*a} $\boldsymbol{k_{G}^0}$	$mol \cdot kg^{-1} \cdot s^{-1}$	$6,64 \cdot 10^{-1}$	^{*b} $4,33 \cdot 10^{-1}$
	$\boldsymbol{k_{CH_4}}$	$mol \cdot kg^{-1} \cdot s^{-1}$	$5,35 \cdot 10^{1}$	^{*b} $1,89 \cdot 10^{1}$
	$\boldsymbol{k_2}$	$mol \cdot kg^{-1} \cdot s^{-1}$	$2,56 \cdot 10^{0}$	^{*b} $1,46 \cdot 10^{0}$
	$\boldsymbol{k_i}$	$mol \cdot kg^{-1} \cdot s^{-1}$	$5,47 \cdot 10^{0}$	^{*b} $1,21 \cdot 10^{1}$
	$\boldsymbol{E_{IN}}$	$J \cdot mol^{-1}$	$1,28 \cdot 10^{5}$	^{*c} $7,99 \cdot 10^{4}$
	$\boldsymbol{E_G}$	$J \cdot mol^{-1}$	$8,87 \cdot 10^{4}$	^{*b} $9,95 \cdot 10^{4}$

^{*a} $k = k^0 \cdot \exp(-E_a/R \cdot (1/T - 1/T_{ref.}))$, $T_{ref.} = 513.15$ K,

^{*b} value from Kwack et al. [19].

^{*c} value from Sun et al. [18].

Almost all kinetic parameters are in the same order of magnitude as the literature values. Deviations from literature are due to different operating conditions and catalysts, e.g. Kwack et al. performed their experiments at 20 bar, a temperature of 230 °C and a H_2/CO ratio of 2 [19]. Good agreement is generally obtained with previous work from Sun et al. [18] where a much smaller microreactor has been applied but with oil cooling and not with evaporation cooling as in our case.

Figure 7 shows the parity plots of selectivity for C_1 and C_{5+} product phases – experiment versus simulation for all operating conditions of Table 1. It can be seen that the selectivity to the chosen fraction in the simulation are in good agreement with experimental data.

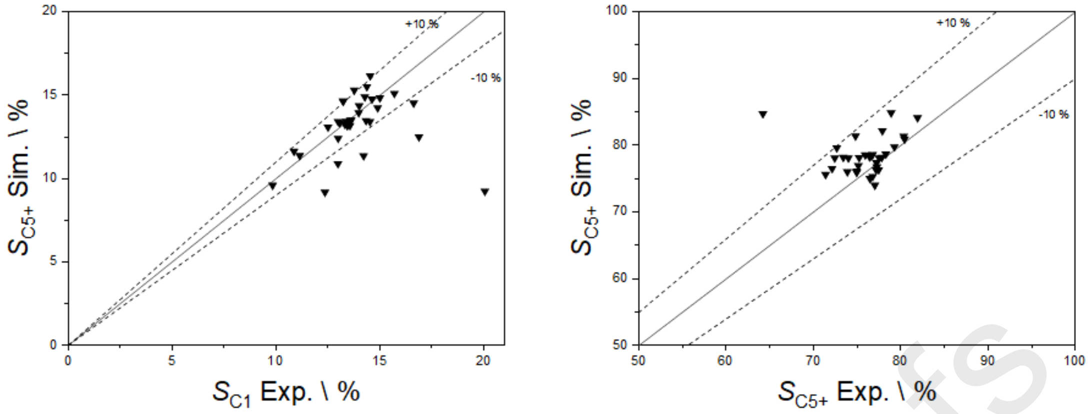

(a) (b)

Figure 7: Parity plots for simulated selectivity over experimentally determined selectivity from all experimental data provided in Table 1; (a) selectivity to methane; (b) selectivity to liquid products (C_{5+}).

It must be noted that the selectivity to the C_{5+} fraction is an integral value. Therefore, differences between simulation data and experiments are less apparent than when comparing the selectivity of a single species such as methane. A maximum deviation of 10 % for most results is obtained.

Figure 8 shows the simulation and experimental mass distributions at two exemplary operating conditions. Inaccurate representations of the mass distribution in the C_3-C_8 range has mainly the reason that two GC data sets are summed up – the gas and liquid phase analysis; in combination, nitrogen as internal standard and the total amount of formed liquid are used to compare the two measurements.

In addition, the model only considers hydrocarbons up to a chain length of 50. Iso-alkanes and alkenes are also not considered in the simulation. These simplifications were done because the mass fraction of the C_{50+} fractions is on average less than two percent and thus negligible. The mass fraction of alkenes and iso-alkanes is between five and ten percent each, so that this may be an additional source of error if these molecules behave as intermediates and not unreactive products [41].

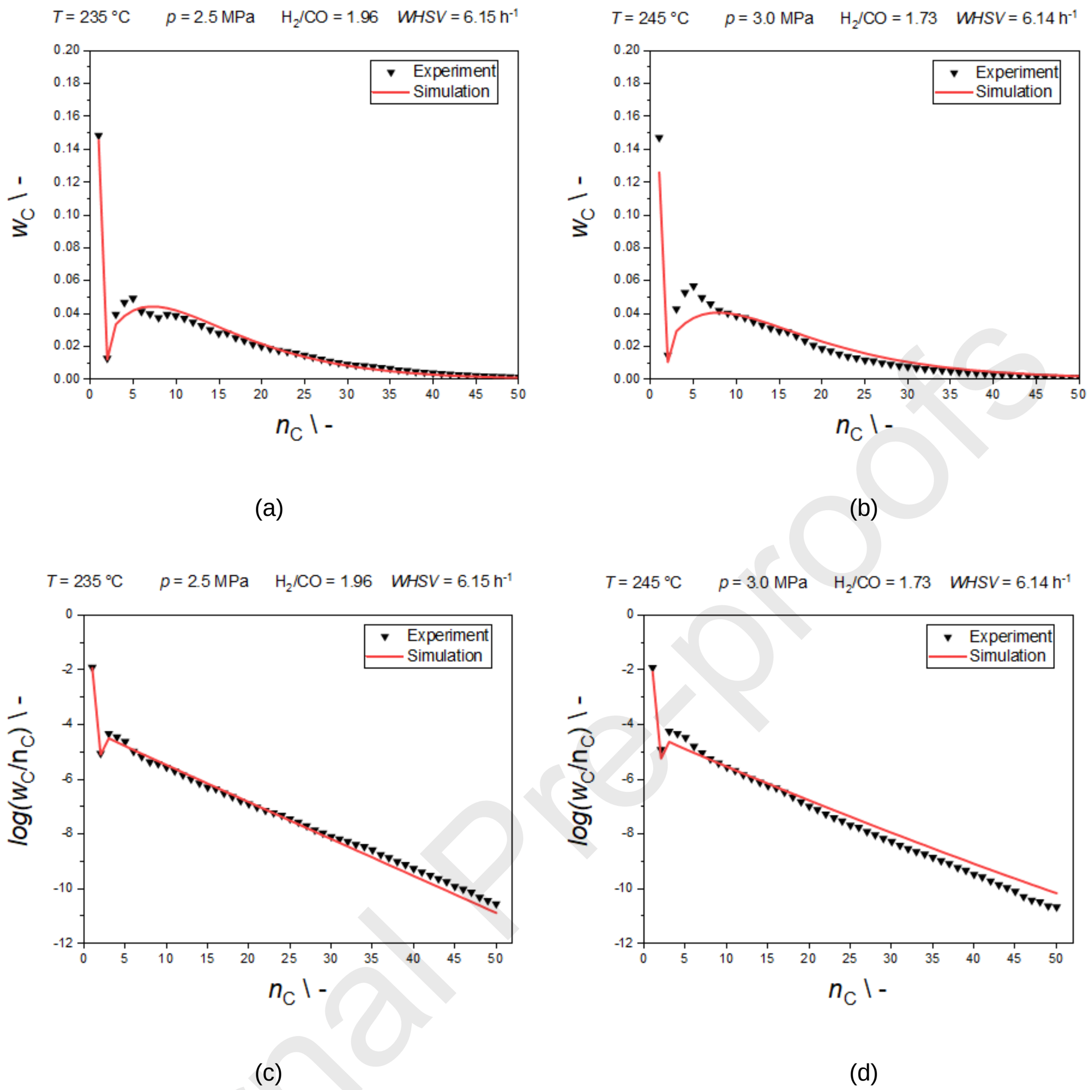

(a) (b)

(c) (d)

Figure 8: Comparison of mass fraction of species in the FT product as function of carbon number obtained from simulation and experiment ((a) and (b)) and comparison of Anderson-Schulz-Flory plots of simulation and experiment ((c) and (d)). Both setpoints were chosen for model validation and are thus not listed in Table 1.

Figure 9 shows the comparison of experiment and simulation with regard to CO and H_2 conversion.

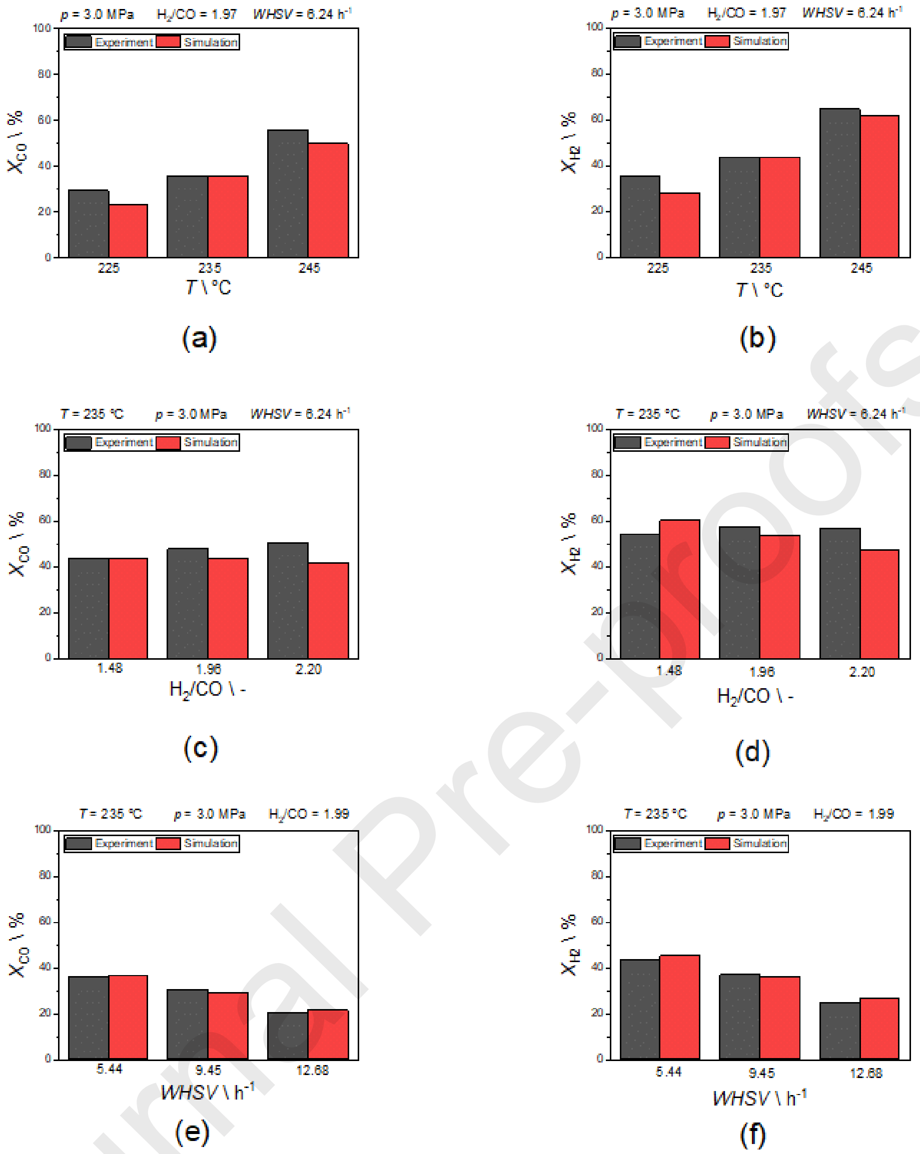

Figure 9: Comparison of CO (left) and H_2 conversion (right) from simulation (red bar) and experiments (black bar). (a),(b) variation of temperature; (c),(d) variation of the H_2/CO ratio; (e),(f) variation of the *WHSV*.

Figures 9 a) and b) show that conversion increases with higher temperature for simulation and experiments, which corresponds to known kinetic effects. Between 230 - 240 °C the model shows its highest validity. In Figures 9 c) and d) opposite trends of simulation and experiment can be observed. At a fixed *WHSV*, the CO partial pressure determines possible product flow. Thus, for increasing H_2/CO ratio (without nitrogen balance) the total volume flow must be adjusted. By this approach, the residence time in the reactor decreases. Accordingly, the conversion could also decrease. As a contradicting effect, an increased H_2/CO ratio results in a higher partial pressure of H_2, which could increase conversion. Experimental results show that the effect of the increased hydrogen partial pressure predominates. In the simulation, however, the residence time decrease seems to dominate. Figures 9 e) and f) illustrate the effect of a decreasing residence time at constant H_2/CO ratio. Conversion decreases with lower residence time for simulation and experiment. Parity plots (not shown) exhibit a satisfactory representation of the conversion within 10 % for 70 % of all data sets.

Apart from the reported deviations in the C_3-C_8 range due to potential experimental error, other sources of error could occur from the homogeneous, ideal PFR description although from RTD experiments two CSTR cascades with N = 50 were required to describe the residence time distribution. Further work should be paid on the applied microkinetics, which seem to influence the opposite trends observed in Figure 9 c) and d).

3.2 Validation of model coupling

To validate the coupling of the individual subroutines for reactor description and flash calculation, steady-state experimental data of the individual analysis of gas, liquid and wax phase was compared to simulation with ideal [28] and EOS model. Feed for the flash calculation was generated by the reactor description subroutine. Figures 10 a-c) show the comparison of the individual mass flow distribution of liquid in the HT and CT and of the residual gas phase, respectively.

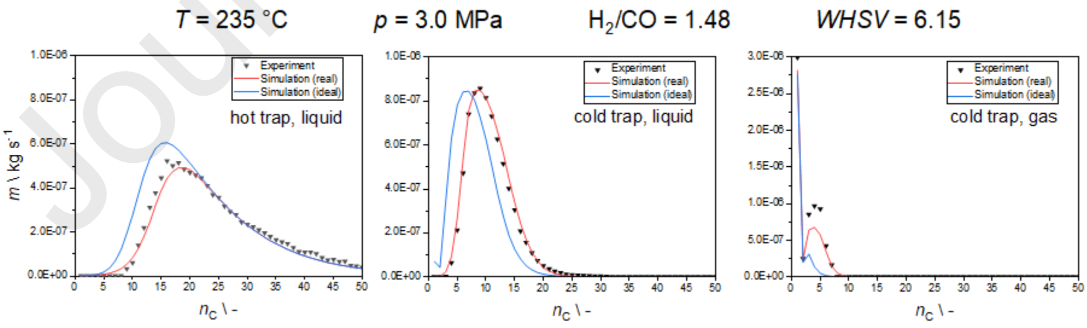

(a) (b) (c)

Figure 10: Comparison of mass flow distributions with ideal and EOS flash model versus experiment for (a) liquid phase in the HT (wax), (b) liquid phase in the CT (oil) and (c) residual gas phase. Feed for separation is generated by the reactor description subroutine.

The experimental mass distribution of the oil in the CT and the wax in the HT is in good agreement with the EOS model. Slight deviations can originate from the determination of the actual temperature inside the HT; only one temperature sensor is located at the outer wall and there might be a local temperature gradient inside. For the CT, slight deviations may occur in the measurement due to volatility of components from C_4 to C_8 when emptying the trap; liquids are stored at operating pressure and are drained versus ambient conditions in a sample container. The carbon mass balance, however, always resulted in 95 – 97 % of the initial carbon flow. The deviation between EOS simulation data and experiments is highest in in the gas phase since the formation of short hydrocarbons is underestimated by the kinetic subroutine. Nevertheless, the EOS model is superior over the calculation of mass flow distribution via the VLE with ideal assumptions, which differs significantly from the experimental data.

Coupling of kinetics, RTD and flash calculation is tested to describe load changes i.e. dynamic operation of an FT-unit in the following. Figures 11 a-c) show the calculated individual mass flow distribution as function of the mixing ratio *a* between two different reaction conditions for liquid in the HT and CT and for the residual gas phase, respectively. The mixing ratio *a* is a value between 0 and 1. *a* = 1 equals 100 % of the operating conditions of setpoint A. *a* = 0 means 100 % of the second operating conditions of setpoint B. For intermediate values of *a*, the flows obtained from the two operating conditions are multiplied by this mixing ratio. This approach has no physical meaning but tests if the routines are working correct and that the mass flow distributions change accordingly for a transition between two different operating conditions.

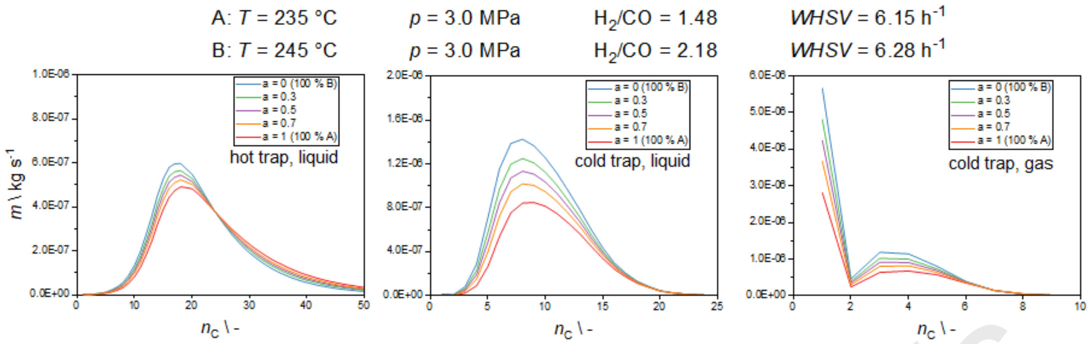

(a) (b) (c)

Figure 11: Mass flow distributions according to the EOS flash model for (a) liquid phase in the HT (wax), (b) liquid phase in the CT (oil) and (c) residual gas phase for reaction conditions A and B and a transitions between both conditions applying the mixing ratio *a*.

Physical meaning is reached, when the mixing time is calculated from the actual volume flow through the test rig. The mixing time indicates how much time elapses for gas mixing in the respective component after the gas composition at the reactor inlet and thus at the reactor outlet changes. Still, the model assumes instantaneous liquid phase formation upon component entry.

For the gas phase in the HT, mixing times between 60 and 150 seconds for a = 0.3 and mixing times between 400 and 800 seconds for a = 0.7 are calculated depending on the overall flow rate. Thus, it can be concluded that the HT needs at least 800 seconds to reach a near steady-state gas composition after changing the reaction conditions. From results in section 2.4.3, the mean RTD of the gas phase in the HT is about 1000 seconds. Thus, the calculation of the mass flow distribution with the overall model provides realistic results. Mixing times of 10 to 30 seconds are calculated for the liquid phase in the HT, since a change in operating conditions quickly affects the reactor and results in a fast change of the concentration in the liquid phase of the HT (see section 2.8).

For the gas phase in the CT, mixing times between 1000 and 2000 seconds for a = 0.3 and mixing times between 4000 and 6000 seconds for a = 0.7 are calculated depending on the overall flow rate. Thus, the CT needs at least 6000 seconds to establish a steady-state gas composition after changing operating conditions for the reactor. According to results from section 2.4.3, the mean RTD of the gas phase in the CT is approximately 5000 seconds. Mixing times of 400 to 800 seconds were determined for the liquid phase. The product mixture must pass the HT and µHE until condensation can take place in the CT, which is again in line with the mean RTD of the HT.

Figures 12 a-c) show the calculation of the individual mass flows distributions as function of the mixing time between two different reaction conditions for liquid in the HT and CT and for the residual gas phase, respectively. The graphs demonstrate the above-mentioned observations. With this data the product composition over time can be calculated for the different traps and integrated to give an overall indication of the product quality at the end of a plant, which is operated in dynamic mode. In the future, the actual calculated product composition can further be used to determine the optimum process conditions in each load state and to change reactor temperature to reach optimum product composition. Other possibilities of control mechanisms are laid in our previous work [15].

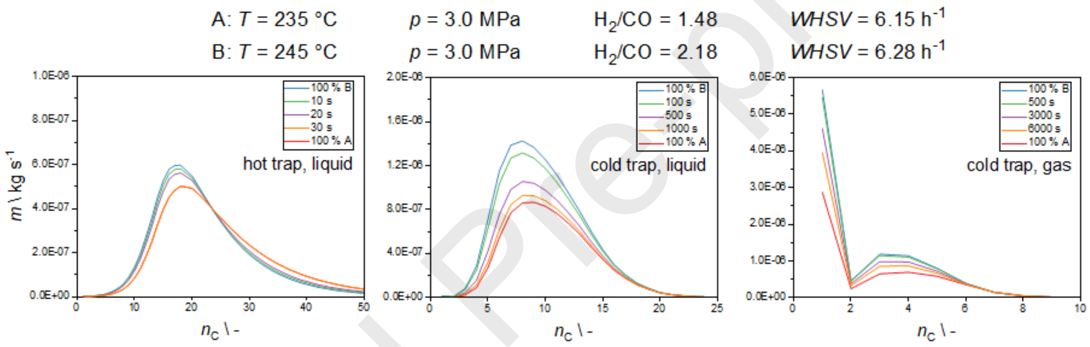

Figure 12: Mass flow distributions according to the EOS flash model for (a) liquid phase in the HT (wax), (b) liquid phase in the CT (oil) and (c) residual gas phase for reaction conditions A and B and transitions between both conditions, applying the respective mixing time.

4. Conclusions

Within this work, a reactor model for a pilot scale microstructured fixed-bed reactor was adapted and approved to cover the main tendencies of the Fischer-Tropsch product composition.

Reaction kinetics were fitted with MATLAB®. With the help of a nonlinear regression, rate and activation coefficients were in good agreement with previous work in smaller reactors highlighting the safe scale-up even at changing the heat removal from oil cooling to evaporation cooling. The reaction kinetics subroutine provided a satisfactory representation of experimental results. There is still potential for improvement, especially in the prediction of H_2 and CO conversion. The kinetic model could also be extended by implementing the formation of alkenes and iso-alkanes to describe processes, such as alkene re-adsorption, to be able to also describe their content in the overall model describing the pilot-scale setup.

A residence time model for the pilot-scale test rig was developed from non-reactive residence time experiments. A model based on the total residence time function (*F*-curve) for each system component was developed. This enabled time resolved calculations of product distribution in gas and liquid phase in all major parts of the test rig after condensation.

With an equation of state (VTPR-GCEOS), a significantly more reliable prediction of the phase equilibrium could be achieved, compared to ideal phase behavior assumptions. This was shown based on the coupling of reaction kinetics and flash calculation for description of the product separation in the different traps in steady state conditions compared with experimental results. The coupling of the reaction kinetics, flash and the RTD model was successfully implemented. By specifying input variables such as temperature, pressure and volume flow of the reactants, the prediction of reaction products, *F*-curves, fractional product separation, as well as flow and mixing properties could be achieved.

The determination of the VLE by means of EOS has contributed to considerable improvements in the modelling of the product in the traps. This is a further step towards the simulation of a load-flexible, dynamic operation FTS process. Further improvement would be the description of a time-resolved product separation from the traps, so that the quantity of products in the hot and cold trap can be determined at any time by varying the operating conditions.

The developed overall MATLAB® program provides satisfactory results and can be used as a first basis for controlling the operation of the FTS system in dynamic mode. A transferability to other reactor sizes and trap sizes is easily possible by adaptation of boundary conditions. Describing feed-flexible reaction, phase changes, condensation and changing pressure and temperature steps in general are important assets in any plant network. The presented model could be an important step to meet the challenges of a decentralized PtL application with regard to volatile energy input.

Funding source declaration:

The Vector Foundation is acknowledged for financial support of parts of this work within the DynSyn project. Mr. Loewert was funded from this project during his PhD.

Declarations of interest conflicts: none.

References

[1] J.M. Cullen, J.M. Allwood, The efficient use of energy: Tracing the global flow of energy from fuel to service, Energ. Policy 38 (2010) 75–81.

[2] Bundesministerium für Bildung und Forschung: Kopernikus Projekte, https://www.kopernikus-projekte.de/projekte/power-to-x, accessed 15 February 2020.

[3] F. Bauer, M. Sterner, Power-to-X im Kontext der Energiewende und des Klimaschutzes in Deutschland, Chem-Ing-Tech 92 (2020) 85–90.

[4] G.P. van der Laan, A.A.C.M. Beenackers, Kinetics and Selectivity of the Fischer–Tropsch Synthesis: A Literature Review, Cataly. Rev. 41 (1999) 255–318.

[5] Institut für Mikroverfahrenstechnik (IMVT), https://www.imvt.kit.edu, accessed 15 February 2020.

[6] R. Myrstad, S. Eri, P. Pfeifer, E. Rytter, A. Holmen, Fischer-Tropsch synthesis in a microstructured reactor, Catal. Today (2009) 301–304.

[7] W. Bier, W. Keller, G. Linder, D. Seidel, K. Schubert, H. Martin, Gas to gas heat transfer in micro heat exchangers, Chem. Eng. Process. (1993) 33–43.

[8] R. Dittmeyer, T. Boeltken, P. Piermartini, M. Selinsek, M. Loewert, F. Dallmann, H. Kreuder, M. Cholewa, A. Wunsch, M. Belimov, S. Farsi, P. Pfeifer, Micro and micro membrane reactors for advanced applications in chemical energy conversion, Curr. Opin. Chem. Eng. 17 (2017) 108–125.

[9] P. Piermartini, T. Boeltken, M. Selinsek, P. Pfeifer, Influence of channel geometry on Fischer-Tropsch synthesis in microstructured reactors, Chem. Eng. J. 313 (2017) 328–335.

[10] F.V. Vázquez, J. Koponen, V. Ruuskanen, C. Bajamundi, A. Kosonen, P. Simell, J. Ahola, C. Frilund, J. Elfving, M. Reinikainen, N. Heikkinen, J. Kauppinen, P. Piermartini, Power-to-X technology using renewable electricity and carbon dioxide from ambient air: SOLETAIR proof-of-concept and improved process concept, J. CO2 Util. 28 (2018) 235–246.

[11] S. LeViness, S.R. Deshmukh, L.A. Richard, H.J. Robota, Velocys Fischer–Tropsch Synthesis Technology—New Advances on State-of-the-Art, Top. Catal. 57 (2014) 518–525.

[12] S. LeViness, Opportunities for modular GTL in North America, Energy Frontiers International 2012, 2012.

[13] S. LeViness, Velocys Fischer-Tropsch Synthesis Technology Comparison to Conventional FT Technologies, San Antonio, Texas, 2013.

[14] M. Loewert, P. Pfeifer, Dynamically Operated Fischer-Tropsch Synthesis in PtL-Part 1: System Response on Intermittent Feed, ChemEng. (2020).

[15] M. Loewert, M. Riedinger, P. Pfeifer, Dynamically Operated Fischer-Tropsch Synthesis – Part 2: Response on Photovoltaics Data, ChemEng (2020).

[16] M. Loewert, J. Hoffmann, P. Piermartini, M. Selinsek, R. Dittmeyer, P. Pfeifer, Microstructured Fischer-Tropsch reactor scale-up and opportunities for decentralized application, Chem. Eng. Technol. (2019) 2202–2214.

[17] H.S. Fogler, Elements of chemical reaction engineering, 4. ed., 12. print ed., Prentice Hall international series in the physical and chemical engineering sciences, Pearson Education Internat, Upper Saddle River, NJ, 2011.

[18] C. Sun, Direct syngas-to-fuel: integration of Fischer-Tropsch synthesis and hydrocracking in micro-structured reactors, Dissertation, Karlsruher Institut für Technologie (KIT), Institut für Mikroverfahrenstechnik (IMVT), Karlsruhe, 2018.

[19] S.-H. Kwack, M.-J. Park, J.W. Bae, K.-S. Ha, K.-W. Jun, Development of a kinetic model of the Fischer–Tropsch synthesis reaction with a cobalt-based catalyst, Reac. Kinet. Mech. Cat. 104 (2011) 483–502.

[20] H. Eilers, Flexibler Betrieb der Fischer-Tropsch-Synthese - Katalysator- und Reaktorverhalten mit Co in der 3-Phasen-Blasensäule, Dissertation, Karlsruher Institut für Technologie (KIT), Institut für Mikroverfahrenstechnik (IMVT), Karlsruhe, 2018.

[21] H. Pichler, H. Schulz, Neuere Erkenntnisse auf dem Gebiet der Synthese von Kohlenwasserstoffen aus CO und H2, Chem-Ing-Tech 42 (1970) 1162–1174.

[22] R.C. Brady, R. Pettit, Mechanism of the Fischer-Tropsch reaction. The chain propagation step, J. Am. Chem. Soc. 103 (1981) 1287–1289.

[23] W. Chen, I.A.W. Filot, R. Pestman, E.J.M. Hensen, Mechanism of Cobalt-Catalyzed CO Hydrogenation: 2. Fischer-Tropsch Synthesis, ACS Catal. 7 (2017) 8061–8071.

[24] M. Zhuo, K.F. Tan, A. Borgna, M. Saeys, Density Functional Theory Study of the CO Insertion Mechanism for Fischer−Tropsch Synthesis over Co Catalysts, J. Phys. Chem. C 113 (2009) 8357–8365.

[25] J. Schweicher, A. Bundhoo, N. Kruse, Hydrocarbon chain lengthening in catalytic CO hydrogenation: evidence for a CO-insertion mechanism, J. Am. Chem. Soc. 134 (2012) 16135–16138.

[26] P.H. Emmet, J.T. Kummer, H.H. Podgurski, W.B. Spencer, Mechanism Studies of the Fischer-Tropsch Synthesis. The Addition of Radioactive Alcohol, J. Am. Chem. Soc. (1951) 564–569.

[27] P.H. Emmett, J.T. Kummer, Fischer-Tropsch Synthesis Mechanism Studies. The Addition of Radioactive Alcohols to the Synthesis Gas, J. Am. Chem. Soc. (1953) 5177–5183.

[28] C. Sun, Z. Luo, A. Choudhary, P. Pfeifer, R. Dittmeyer, Influence of the Condensable Hydrocarbons on an Integrated Fischer-Tropsch Synthesis and Hydrocracking Process: Simulation and Experimental Validation, Ind. Eng. Chem. Res. 56 (2017) 13075–13085.

[29] D.E. Mears, Diagnostic criteria for heat transport limitations in fixed bed reactors, J. Catal. 20 (1971) 127–131.

[30] D.E. Mears, Tests for Transport Limitations in Experimental Catalytic Reactors, Ind. Eng. Chem. Proc. DD. 10 (1971) 541–547.

[31] H. Hofmann, Chemical Reactor Analysis and Design, 2nd ed. 63, John Wiley & Sons, New York - Chichester, 1991.

[32] D. Vervloet, F. Kapteijn, J. Nijenhuis, J.R. van Ommen, Fischer–Tropsch reaction–diffusion in a cobalt catalyst particle: aspects of activity and selectivity for a variable chain growth probability, Catal. Sci. Technol. 2 (2012) 1221.

[33] J. Ahlers, J. Gmehling, Development of a Universal Group Contribution Equation of State. 2. Prediction of Vapor−Liquid Equilibria for Asymmetric Systems: Industrial & Engineering Chemistry Research, Ind. Eng. Chem. Res. 41 (2002) 3489–3498.

[34] J. Ahlers, J. Gmehling, Development of a Universal Group Contribution Equation of State III. Prediction of Vapor−Liquid Equilibria, Excess Enthalpies, and Activity Coefficients at Infinite Dilution with the VTPR Model: Industrial & Engineering Chemistry Research, Ind. Eng. Chem. Res. 41 (2002) 5890–5899.

[35] J. Ahlers, J. Gmehling, Development of an universal group contribution equation of state I. Prediction of liquid densities for pure compounds with a volume translated Peng-Robinson equation of state, Fluid Phase Equilibr. 191 (2001).

[36] C.H. Twu, J.E. Coon, J.R. Cunningham, A new generalized alpha function for a cubic equation of state Part 1. Peng-Robinson equation, Fluid Phase Equilibr. 105 (1995) 49–59.

[37] J. Gmehling, B. Kolbe, M. Kleiber, J.R. Rarey, Chemical thermodynamics for process simulation, Wiley-VCH-Verl., Weinheim, 2012.

[38] I.H. Bell, M. Satyro, E.W. Lemmon, Consistent Twu Parameters for More than 2500 Pure Fluids from Critically Evaluated Experimental Data, J. Chem. Eng. Data 63 (2018) 2402–2409.

[39] Y. Nannoolal, J. Rarey, D. Ramjugernath, Estimation of pure component properties, Fluid Phase Equilibr. (2007) 1–27.

[40] J.J. Marano, G.D. Holder, Characterization of Fischer-Tropsch liquids for vapor-liquid equilibria calculations, Fluid Phase Equilibr. 138 (1997) 1–21.

[41] H. Schulz, Short history and present trends of Fischer–Tropsch synthesis, Appl. Catal. A-Gen. 186 (1999) 3–12.

Highlights

- FT reaction kinetics were adopted to description of a pilot-scale microchannel reactor.
- Product condensation was matched by non-ideal vapor-liquid equilibrium calculations.
- Residence time distribution models were developed for all FTS plant components.
- Time-dependent product composition under dynamic FTS operation are described.

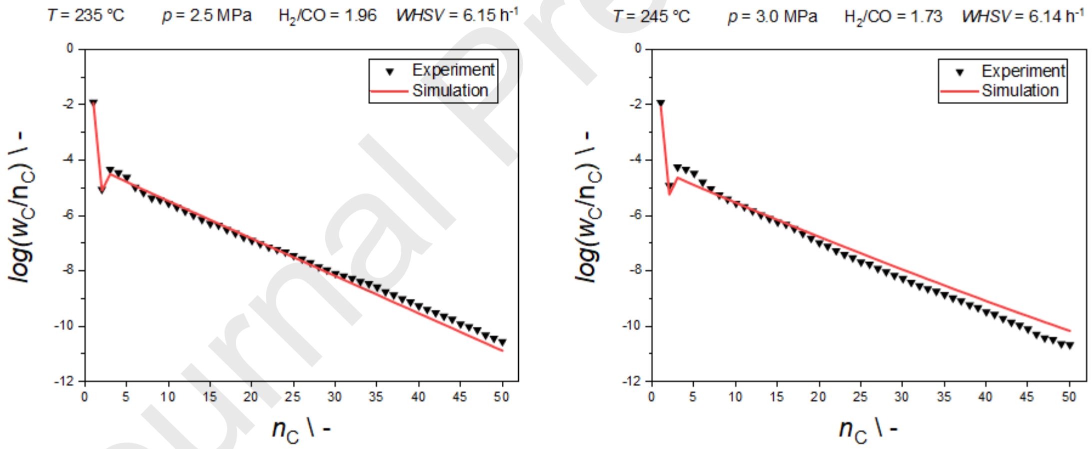

Declaration of interests

☒ The authors declare that they have no known competing financial interests or personal relationships that could have appeared to influence the work reported in this paper.

☐The authors declare the following financial interests/personal relationships which may be considered as potential competing interests:

PAPER V

BRIDGING THE GAP BETWEEN INDUSTRY AND SYNCHROTRON: *operando* STUDY AT 30 BAR OVER 300 H DURING FISCHER-TROPSCH SYNTHESIS

Submitted to Reaction Chemistry & Engineering, 28th of December 2019

Published: 08.04.2020

`https://doi.org/10.1039/C9RE00493A`

Paper V

Reaction Chemistry & Engineering

ROYAL SOCIETY OF CHEMISTRY

PAPER

View Article Online
View Journal | View Issue

Check for updates

Cite this: *React. Chem. Eng.*, 2020, 5, 1071

Bridging the gap between industry and synchrotron: an *operando* study at 30 bar over 300 h during Fischer–Tropsch synthesis†

M. Loewert, ‡[a] M.-A. Serrer,‡[bc] T. Carambia,[a] M. Stehle, [c] A. Zimina,[bc]
K. F. Kalz,[bc] H. Lichtenberg,[bc] E. Saraçi,[bc] P. Pfeifer[a] and J.-D. Grunwaldt *[bc]

Received 28th December 2019,
Accepted 8th April 2020

DOI: 10.1039/c9re00493a

rsc.li/reaction-engineering

In order to reduce CO_2 emissions, it is necessary to substitute fossil fuels with renewable energy using CO_2 as a carbon feedstock. An attractive route for synthetic fuel production is the Fe- or Co-catalysed Fischer–Tropsch process. A profound knowledge of the catalyst deactivation phenomena under industrial conditions is crucial for the process optimisation. In this study, we followed the structural changes of a Co–Ni–Re/γ-Al_2O_3 catalyst for >300 hours at 30 bar and 250 °C during the Fischer–Tropsch synthesis *operando* at a synchrotron radiation facility. The advanced setup built for *operando* X-ray diffraction and X-ray absorption spectroscopy allows simultaneous and robust monitoring of the catalytic activity even over 300 h time on stream. We found three activity regimes for the Co–Ni–Re/γ-Al_2O_3 catalyst during 310 h of operation. Fast decline in activity was observed during the initiation phase in the first hours of operation due to liquid film formation (mass transport limitations). Furthermore, solid state reactions and carbon depositions were found while continuing the exposure of the catalyst to harsh temperature conditions of 250 °C. By using this advanced setup, we bridged the gap between industrially oriented catalysts and fundamental studies at synchrotron radiation facilities, opening up new possibilities for *operando* characterisation of industrial processes that rely on conditions of up to 450 °C and 50 bar.

Introduction

In recent years, climate change and global energy demands led to a distinct increase in the research on efficient renewable energy storage aiming at a CO_2 neutral approach. The use of CO_2 would, furthermore, provide renewable feedstocks for industry or long-distance transport in the course of electrification and abandonment of fossil fuel resources. Promising "Power-to-X"[1] storage technologies for renewable energy are the methanation of CO_2 using advanced catalysts[2–6] and the Fischer–Tropsch synthesis[7–11] (FTS), *e.g.* coupled with CO_2/H_2O co-electrolysis.[12] The low-temperature Fischer–Tropsch synthesis (LT-FTS) is operated at 200–240 °C and at elevated pressure of 10 to 30 bar.[13–15] Various hydrocarbons of different chain length can be synthesised from synthesis gas ("syngas": H_2 and CO). An overview on the involved reaction pathways is given in eqn (1)–(4).

$$\text{Alkenes: } n\mathrm{CO} + 2n\mathrm{H_2} \rightarrow \mathrm{C}_n\mathrm{H}_{2n} + n\mathrm{H_2O} \quad (1)$$

$$\text{Alkanes: } n\mathrm{CO} + (2n+1)\,\mathrm{H_2} \rightarrow \mathrm{C}_n\mathrm{H}_{2n+2} + n\mathrm{H_2O} \quad (2)$$

$$\text{Methane: } \mathrm{CO} + 3\mathrm{H_2} \rightarrow \mathrm{CH_4} + \mathrm{H_2O} \quad (3)$$

$$\text{Alcohols: } n\mathrm{CO} + 2n\mathrm{H_2} \rightarrow \mathrm{C}_n\mathrm{H}_{2n+1}\mathrm{OH} + (n-1)\,\mathrm{H_2O} \quad (4)$$

FTS can be understood as a polymerisation reaction in which the probability of desorption of hydrocarbon chains and of chain propagation is influencing the product distribution. At optimised operation conditions for certain chain growth probabilities, the largest product fraction provides similar properties as fossil fuels. The FTS products can, therefore, be used as a heteroatom- and aromatics-free fuel substitute, not only in cars or trucks but also in ships and planes where batteries are not applicable. Typical catalysts for the FTS are based on Ru, Co, Ni and Fe or combinations thereof.[14,16] Co- and Fe-based catalysts are the main catalysts used in industrial processes. Elemental Co is the active surface species for FTS aiming at higher average product chain lengths.[17,18] Re can be added as structural promotor to enhance the cobalt dispersion and catalytic activity.[19–21] The addition of Ni as second promotor can further enhance the catalytic activity and

---

[a] *Institute for Micro Process Engineering (IMVT), Germany*
[b] *Institute of Catalysis Research and Technology (IKFT), Germany. E-mail: grunwaldt@kit.edu*
[c] *Institute for Chemical Technology and Polymer Chemistry (ITCP), Karlsruhe Institute of Technology (KIT), Germany*

† Electronic supplementary information (ESI) available. See DOI: 10.1039/c9re00493a

‡ Both authors contributed equally to this manuscript.

attrition stability of the catalyst.[22] The overall syngas conversion can be increased by finely dispersing the active components on supports with a high specific surface area, such as γ-Al_2O_3.[14,23]

Although the FTS is a well-known and widely used catalytic process, the structural changes of the catalysts and their impact on the activity and selectivity under industrial reaction conditions have not been sufficiently characterised and are still under discussion.[24–27] During FTS *e.g.* carbides or oxides can be formed resulting in a declined catalytic activity.[24,28] For the rational design of a future generation of FTS catalysts it is crucial to unravel the surface and bulk chemistry of well-established systems and to correlate it to their catalytic activity. In this respect, advanced synchrotron radiation-based methods like *operando* X-ray absorption spectroscopy (XAS) and X-ray diffraction (XRD) can be used to evaluate the chemical state and atomic arrangement of the active species.[26,29–31] As catalysts are highly dynamic systems[29] and their structure can distinctly change due to external stimuli, studies under conditions (*i.e.* pressure, temperature and space velocity) close to industrial ones are preferred. Hence, an optimal *operando* reactor cell for the industrially relevant study of HT- and LT-FTS catalysts should be able to operate at temperatures up to 400 °C, at a pressure of up to 30 bar and should provide good heat and mass transfer properties.[39] The catalyst loading in the cell must be sufficient to apply space velocities in a realistic range and to produce analysable amounts of liquid products at the given conversions. However, in synchrotron radiation experiments reported so far on Co-based FTS catalysts (Table 1), several drawbacks related to the *in situ* cell design were found, *e.g.* pressure limitations of 18–20 bar,[26,27,30,34–38] low catalyst mass[26,34] and time-on-stream (TOS),[26,27,30,34–38] as well as insufficient product formation for analysis.[26,27,30,34–38] Furthermore, it has to be considered that in the most commonly used quartz μ-capillary reactors (200–500 μm diameter, see Table 1), a pronounced inhomogeneity of temperature distribution may occur due to the local heating by a hot air gas blower.[40,41]

In this study, we aimed at bridging the gap between reaction engineering (long TOS, commercial catalyst sample, realistic reaction conditions) and fundamental XAS studies (mobile high-pressure *operando* infrastructure) by performing for the first time an *operando* spectroscopic study over more than 300 h of FTS on a Co-based catalyst at 250 °C and 30 bar with real product analysis to determine activity and selectivity simultaneously. For this purpose, an advanced setup was designed for the application of industrially relevant FTS at synchrotron radiation facilities. This setup includes a high-pressure gas dosing system, an *operando* cell for combined XAS and XRD analysis, as well as online product analysis units (mass spectrometer (MS) and μ-gas chromatograph (μ-GC)) (Fig. 1). The specially designed reactor cell was used to monitor the structural changes at the Co K-edge and catalytic activity of a commercial Co–Ni–Re/γ-Al_2O_3 (ref. 7 and 33) catalyst at 250 °C and 30 bar over 300 h at the CAT-ACT beamline[42] at the KIT light source (Karlsruhe, Germany). After 310 h long-term FTS, the catalyst was further characterised by conventional XRD, Raman spectroscopy, and thermogravimetry. The setup presented here opens unique possibilities for X-ray based *operando* characterisation of catalysts at synchrotron radiation sources under realistic reaction conditions, not only for the FTS, but for a wider range of industrially relevant reactions that are operated at elevated pressure and temperature.

Experimental

High-pressure setup for *operando* XAS & XRD

The entire mobile setup (Fig. 1) is designed in a way that it fits completely in a dedicated fume-hood installed inside the experimental hutch (Fig. S1 in the ESI†). The gas composition was adjusted *via* 5 mass flow controllers (Bronkhorst, Germany) calibrated using a DryCal flow calibrator (Mesa Labs, Germany). The pressure was regulated by two pressure regulators (Schuster Creative Systems; N802 motors by GULEX, Germany) controlled by two process controllers (PMA KS 90-1). All inlet and outlet lines of the reactor cell were heated (190 °C) up to the hot (120 °C) and cold (5 °C) separator using heating cords and insulation (HORST, Germany). The cold trap was cooled by a cryostat (F250 by Julabo, Germany). The high-pressure liquid phase separators were designed and constructed in our lab using Swagelok

Table 1 Comparison of the conditions and product analysis for a microstructured reactor (italic) for decentralised Power-to-X applications to our *operando* XAS studies (bold) and previous *in situ* XAS experiments on Co-based catalysts during FTS

Catalyst	Pressure [bar]	Temperature [°C]	TOS [h]	Total catalyst mass (reactor type) [mg]	Quantitative gas/liquid analysis (GC)	Ref.
Co–Re–Ni/Al_2O_3	*20–30*	*215–240*	*25–270*	*1800 (microstructured reactor)*	*Yes/yes*	32, 33
Co–Re–Ni/Al_2O_3	**30**	**250**	**300**	**83 (newly designed cell)**	**Yes/yes**	***Current study***
Co–Re/Al_2O_3	18	210	6	- (μ-capillary)	No/no	30
Co–Re/Al_2O_3	18	220	32	~8 (μ-capillary)	No/no	26
Co–Re/Al_2O_3	18	220	24	- (μ-capillary)	No/no	27
Co–Pt/Al_2O_3	20	220	2.5	5–10 (μ-capillary)	Yes/no	34
Co/CNT	15	220	10	- (μ-capillary)	No/no	35
Co–Pt/Al_2O_3	20	220	8.5	- (μ-capillary)	Yes/no	36
Co(–Re)/Al_2O_3	1	210	6	- (*in situ* cell)	No/no	37
Co/Al_2O_3	18	250–280	12	- (*in situ* cell)	No/no	38

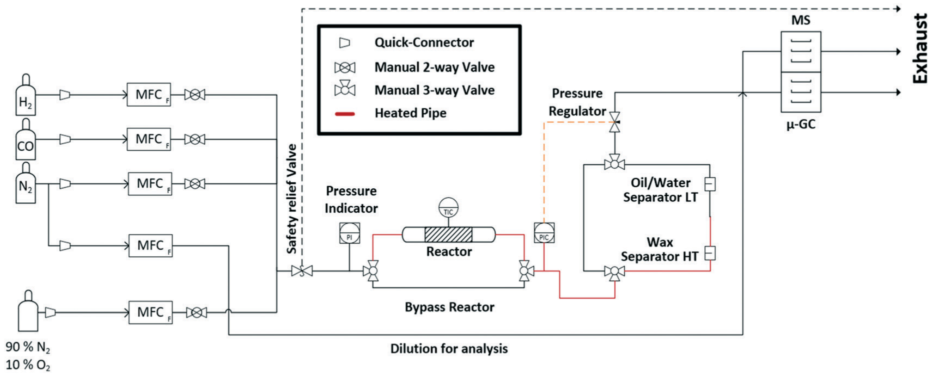

Fig. 1 Scheme of the experimental setup for the long-term high-pressure FTS experiments at the CAT-ACT beamline (KIT light source).

parts and enable online sampling of the liquid phases without inducing a pressure drop in the whole system.

A novel high-pressure cell for simultaneous XAS and XRD measurements was designed and constructed of stainless-steel with large solid angle openings (schematics, *cf.* Fig. 2, details in the ESI†). Notably, up to 85 mg of catalyst with a sieve fraction of 100–200 μm can be loaded into the reactor cell. The upper and bottom sides of the catalyst bed are fixed with 1.5 mm thick PF-60 Be foils (Materion, USA) sealed with graphite foils. The X-ray beam can pass through a 10 mm × 2 mm slit cut on the "outer" part of the cell, probe the catalyst bed and exit on the opposite side. The position of the slit enables spatially resolved measurements (*e.g.* inlet, middle, outlet). The reactive gases are passed through the cell *via* a distributive inlet and outlet to assure a homogeneous gas distribution in the catalyst bed. The gas flow direction is top down to assist the transport of the liquid products which is important for long term stability. The cell is heated by two 160 W heating cartridges (HORST, Germany). The temperature is controlled by a HT MC11 temperature regulator (HORST, Germany) and measured by a NiCr/Ni (type K) thermocouple mounted close to the reactor bed inside the stainless-steel body.

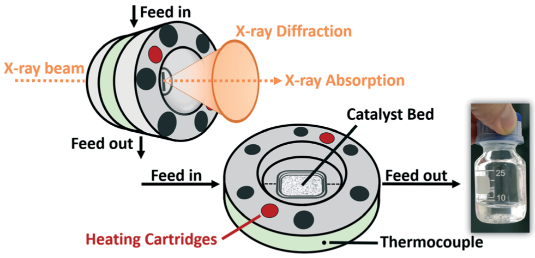

Fig. 2 Scheme of the high-pressure cell for combined X-ray absorption spectroscopy and -diffraction at temperatures up to 450 °C and up to 50 bar pressure and the total FTS wax-phase products obtained during 310 h operation.

For safety reasons, the cell was mounted in a surrounding box made of aluminium and equipped with polyimide windows and continuously flushed with N_2. Particle filters were installed at the gas in- and outlet to prevent Be contamination in the event of bursting. Note, that this experiment includes the use of relatively high pressure which requires equipment with the appropriate pressure rating and operation by experienced personal.

Product analysis

The gas phase was analysed on-line at atmospheric pressure after liquid-phase separation using a ThermoStar™ GSD 320 T1 mass spectrometer (Pfeiffer Vacuum, Germany) equipped with a C-SEM/Faraday detector and an Agilent 490 micro gas chromatograph (μ-GC; channel 1: 10 m PoraPLOT Q, 0.25 mm diameter, carrier gas He; channel 2: 10 m mole sieve column with 5 Å, 0.25 mm diameter, carrier gas Ar). Prior to the experiments, the μ-GC was calibrated for the gases in Table S1 in the ESI.†

CO conversion and selectivity to CH_4 were calculated using N_2 (dosed after the pressure valve) as internal standard:

$$\text{Conversion:}\ X(\mathrm{CO}) = \left(1 - \frac{\mathrm{CO_{out}}\cdot \mathrm{N_{2,in}}}{\mathrm{N_{2,out}}\cdot \mathrm{CO_{in}}}\right) \times 100\% \qquad (5)$$

$$\text{Selectivity:}\ S(\mathrm{CH_4}) = \frac{Y(\mathrm{CH_4})}{X(\mathrm{CO})} \times 100\% \qquad (6)$$

The liquid-phase product samples were taken from the respective traps during the reaction. A previously developed liquid products (C_{5-28}) analysis[7,43] was implemented by using an offline Agilent 7820A GC equipped with a DB-2887 column and a flame ionization detector (FID).

Operando X-ray absorption and diffraction at the synchrotron

The 310 h LT-FTS studies were performed at the CAT-ACT beamline[42] at the Karlsruhe light source. CAT-ACT provides a unique infrastructure for such *operando* studies. The safety-box including the *operando* cell was mounted on a HexaPod motion controller for sample positioning. The beam was cut to 0.5 mm × 0.5 mm and adjusted to the middle of the catalyst bed. The wavelength of the X-rays was selected by a Si (111) double crystal monochromator (DCM) and slightly detuned to improve the stability of the beam intensity and to suppress distracting glitches from the DCM.

The intensities of the incoming and transmitted monochromatic X-rays were measured with nominally high energy ionization chambers (Ohyo Koken Kogyo Co. Ltd., Japan, N_2 filling, 1 bar, 800 mV) before and after the cell. XAS spectra were recorded at the Co K-edge edge (7709 eV). Energy calibration was made on a Co metal foil by assigning the energy of the absorption edge to the tabulated value. One X-ray absorption near edge structure (XANES) scan took around 3.5 minutes, and an extended X-ray absorption fine structure (EXAFS) scan around 30 minutes. The XAS data was analysed using the IFEFFIT/Demeter package[44] (version 0.9.25). Absorption data of Co_3O_4, CoO and $Co(OH)_2$ pellets were recorded as references. A Co_2C reference was made *in situ* by carburisation (exposure) of the catalyst in pure CO (ref. 45 and 46) at 250 °C and 30 bar after the long-term experiments.

XRD measurements were performed using a fixed wavelength of 1.08 Å (11.5 keV). The diffraction patterns were recorded on a circular orbit around the high-pressure cell with a MediPix detector.[47] One XRD measurement took about 10 minutes. The data was calibrated to the NIST LaB_6 standard.

Materials and activation in hydrogen

For the experiments under LT-FTS conditions, a commercial Co–Ni–Re/γ-Al_2O_3 catalyst (Ni and Re as promotors; Re content <0.5 wt%) with a total metal loading of about 26 wt% was used as received (20 wt% nominal load). The catalyst was diluted 1 : 4 with γ-Al_2O_3 to ensure optimal absorption for the XAS experiments. The diluted catalyst was further granulated to a sieve fraction of 100–200 μm to prevent any blocking or pressure drops along the catalyst bed. The Co–Ni–Re/γ-Al_2O_3 catalyst was activated by reduction in hydrogen (see next section).

Fischer–Tropsch long-term studies

The amount of diluted catalyst filled in the cell was 83.8 mg. Prior to the experiments the catalyst was activated in 15 ml min^{-1} pure H_2 for 5 h at ~350 °C (1 K min^{-1}) and atmospheric pressure. Before recording EXAFS and XRD the catalyst was cooled down to 50 °C.

The *operando* cell was heated in pure H_2 to 140 °C and the pressure was increased to 30 bar. Afterwards, the gas feed was switched to the reaction mixture consisting of 10 ml min^{-1} H_2 and 5 ml min^{-1} CO. After reaching a steady state, the cell was heated to ~250 °C with a ramp of 5 K min^{-1} to initiate the Fischer–Tropsch reaction. We chose to perform the LT-FTS at 250 °C in order to promote deactivation. Structural changes were monitored directly upon changing to FTS conditions by XANES (continuously) as well as EXAFS and XRD (every 2 h). The reaction products were analysed simultaneously *via* the on-line μ-GC (cont.), offline-GC (~every 12 h) and MS (cont.) for the first 60 h time on stream (TOS). The X-ray beam was interrupted for 250 h while the reaction was still continuously followed by μ-GC, offline-GC and MS.

After the steady state experiment transient conditions were applied: the H_2 : CO ratio was varied from 2.4 to 1.0. Furthermore, hydrogen was removed from the feed, with and without small amounts of O_2. Subsequently, the catalyst was reduced, and LT-FTS conditions were applied. No major influence of these transient experiments on the catalytic performance was found compared to the state after the long-term study (~3% less X_{CO}). Hence, possible changes that occurred during the long-term experiment were still present. Therefore, the Co–Ni–Re/γ-Al_2O_3 catalyst was investigated *ex situ via* XRD and Raman spectroscopy. Additionally, thermogravimetric measurements combined with mass spectrometry (TG-MS) were performed. Details are given in the ESI.†

Results and discussion

Structural studies during catalyst activation and *operando* characterisation in its initial state during FTS

In order to monitor the activation process of the fresh Co–Ni–Re/γ-Al_2O_3 catalyst, the reduction in hydrogen was followed by *in situ* XANES as function of temperature (Fig. 3a). The reduction from Co_3O_4 to CoO was observed starting from 260 ± 10 °C. The reduction from CoO to Co^0 occurred above 340 ± 10 °C and was completed at about 450 ± 10 °C.

Fig. 3b displays the Co K-edge XANES region before and after the activation. Linear combination analysis (LCA) of the Co K-edge XANES region was realised using Co_3O_4, CoO and a Co-foil as standards (*cf.* Fig. 3b). The LCA demonstrated that the catalyst was in a nearly completely oxidised state (91 ± 0.5 mol% of Co(II, III)-species) before the activation in H_2. The shape of the Co K-edge XANES spectrum of the catalyst after the activation resembled almost that of the Co-foil (about 94 mol% Co^0, rest CoO according to LCA). The slightly different shapes of the reduced Co-K edge compared to the Co foil reference might be due to the different Co morphologies of these samples.

This is also observed in the Fourier transformed extended X-ray absorption spectra (EXAFS) in Fig. 3c, which can be used to derive the changes in the interatomic distances (Δ*R*), as well as coordination numbers (CN). The first shell fit of the Co–Co backscattering peak at about 2.2 Å resulted in a coordination number of 9.1 ± 0.6 which was lower compared to the Co reference foil with a coordination number of 12. The decreased coordination number might be due to the presence of Co nanoparticles or remaining CoO resulting in a

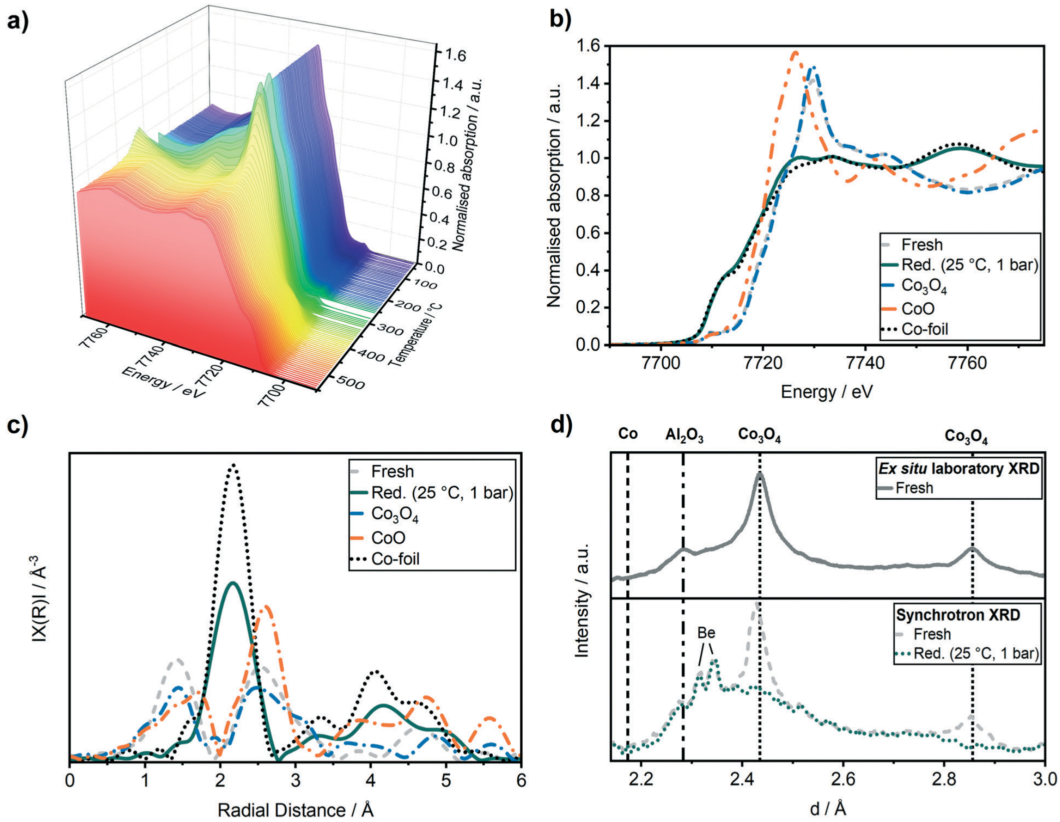

Fig. 3 (a) Co K-edge XANES spectra during H_2-TPR (5 vol% H_2 in He) in a capillary reactor. (b) Co K-edge XANES spectra before and after the H_2-TPR (H_2, 5 h, 380 °C SP) in the *operando* cell. (c) k^2-Weighted Fourier transformed EXAFS of the Co K-edge spectra, (d) *in situ* XRD compared to the *ex situ* laboratory XRD of the Co–Ni–Re/γ-Al_2O_3 catalyst. Before (grey) and after (green) the H_2-TPR, Co reference foil (black dotted), Co_3O_4 (blue) and CoO (orange) reference pellet.

lower coordination of the cobalt atoms compared to a pure Co metal foil. The activation of the catalyst was followed simultaneously by XRD using synchrotron radiation and compared to a conventional laboratory XRD (Cu K_α) in Fig. 3d. The whole recorded range is given in Fig. S2 in ESI.† All reflections could be assigned to the γ-Al_2O_3 support ((311) at d = 2.28, 2.41) and to Co_3O_4 ((311) at d = 2.43 Å and (200) at d = 2.86 Å). After the reduction, the reflections for Co_3O_4 at d = 2.43 Å and d = 2.86 Å disappeared and no Co reflection at d = 2.18 Å appeared, supporting the formation of the active Co^0 species, which are nano-crystalline or amorphous Co particles (no detectable reflections in the XRD).

Fig. 4 provides the catalytic data during operation on the conversion and the C-balance, the C_{5+} selectivity, which includes possible carbon deposition as it has been calculated from the C-balance, and the liquid product selectivity, respectively. Overall, during 310 h TOS, we observed 3 activity regimes. The highest activity and C_{5+} selectivity were observed directly after reaching the reaction temperature of 250 °C (50 vol% CO/H_2, 30 bar). In the first 8 h TOS, where the catalyst typically equilibrates, a fast drop from ~90% to 66% in CO conversion was observed. At this early stage of reaction, the catalyst gave the highest CO conversion, but no liquid products were found in the condensers due to liquid product deposition on the catalyst bed and on the piping in the first ~70 h (Fig. 4c). To our knowledge this is the first time that such extensive on-line analysis of FT-products during a synchrotron experiment has been conducted.

It is important to closely observe the catalyst in this active state separately, since it is often referred to as a "conditioning phase".[48] Selected Co K-edge XANES, EXAFS of the reduced catalyst after activation and during reaction are shown in Fig. 5. Some further spectra are given in Fig. S3 in the ESI.†

In the XANES spectra, we did not observe any changes of the catalyst after 2 h TOS (dark blue line) compared to the freshly reduced catalyst (green dotted line). In addition, the EXAFS spectra also did not give any indication of cobalt–oxygen backscattering at around 1.4 Å. In previous studies on Al_2O_3 supported Co-based model catalysts, the formation of

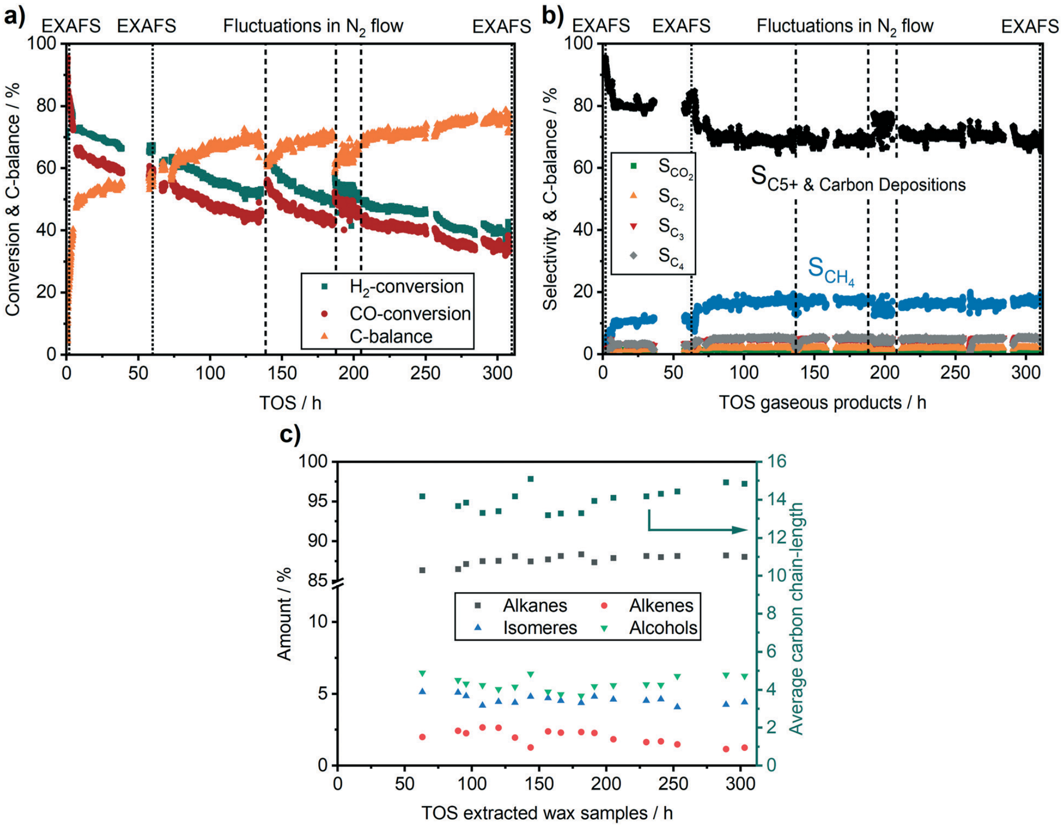

Fig. 4 (a) Conversion of the gaseous products, (b) selectivity of the gaseous products and C_{5+} & carbon depositions selectivity and (c) selectivity of the liquid products during 310 h FTS; m_{cat} = 83.8 mg, T = 250 °C, p = 30 bar in 10 ml min^{-1} H_2, 5 ml min^{-1} CO.

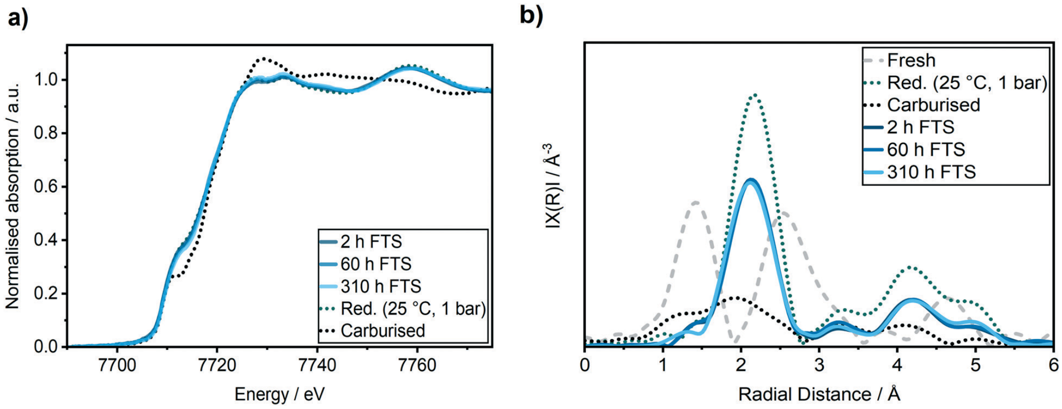

Fig. 5 (a) Co K-edge XANES spectra, (b) k^2-weighted Fourier transformed EXAFS at the Co K-edge obtained from the Co–Ni–Re/γ-Al_2O_3 catalyst in its fresh (grey dotted line) and reduced state after H_2-TPR (green dotted line), after carburization (black dotted line), after 2 h TOS (dark blue), 60 h TOS (blue) and 310 h (light blue) in FTS.

$CoAl_2O_4$ was observed during the FTS by an increase in the peak at 7717 eV in the first derivative of the XANES spectra that is displayed in Fig. 6b.[26,27] Thus, we do not observe any formation of $CoAl_2O_4$ during the first hours of FTS.

Analysis of the Fourier transformed Co K-edge EXAFS spectra (Fig. 5b) revealed that the coordination number was only slightly decreased from 9.1 ± 0.6 after the H_2-TPR to 8.8 ± 0.8 after the first 2 h TOS (details see ESI†). This demonstrates that no major particle sintering or restructuring occurred in the active state of the Co–Ni–Re/γ-Al_2O_3 catalyst. Thus, together with the results of the XANES analysis, we can conclude that in this most active catalyst state the structure is similar to the one directly after activation.

Operando characterisation during long-term Fischer–Tropsch studies (up to 300 h)

A second regime with a linear catalyst deactivation was observed from 2 h up to 80 h TOS (Fig. 4a–c). After the CO conversion dropped from 66% to about 55% in this second time regime. Furthermore, the selectivity to C_{5+} products was declined while the selectivity to CH_4 was increased. Similar deactivation trends can be found in literature.[49] A slight change was observed in the XANES spectra, as seen from the increase in the features at 7730 eV and 7742 eV that are typical for Co_3O_4 (Fig. 5a). This change might additionally be due to Co_2C (carbon deposition), CoO (oxidation) or $CoAl_2O_4$ formation (solid-state reaction). In case of Co_2C formation, it is expected that the white line intensity would increase simultaneously at 7731 eV and 7742 eV in the XANES difference spectra of the reduced and carburised catalyst in Fig. 6b. The formation of Co_2C would be also visible as a Co–C coordination peak at about 1.1 Å and a Co–Co coordination peak shift to about 1.9 Å accompanied by an overall decrease in the peak intensity[50,51] in the Fourier transformed EXAFS data (Fig. 5b). Such changes were not observed after 60 h TOS (blue). Further, the formation of CoO can be excluded, since no feature was observed at about 7730 eV in the XANES difference spectra (blue) in Fig. 6b. However, in the first derivative of the Co K-edge XANES spectra after 60 h TOS (Fig. 6a, blue), we observed the formation of a peak at 7717 eV that can be assigned to the formation of $CoAl_2O_4$.[26,27] Else, no detectable restructuring and sintering was observed, as the determined coordination number of 8.7 ± 0.8 after 60 h TOS did not significantly change compared to the active catalyst state after 2 h TOS.

In a third deactivation regime from 80 h to 310 h, the CO conversion level was continuously flattening from 55% to 33%, as depicted in Fig. 4a. Respective selectivity levels reached a steady state, resulting in ~70% for C_{5+} and 18% for CH_4 in the gas phase (Fig. 4b). Around 88% of alkanes were detected in the liquid samples with an average carbon chain length of 14 (Fig. 4c). In the time period from 60–310 h TOS, we observed a slight decline in the pre-edge feature at 7714 eV accompanied by an increase at 7731 eV and 7742 eV in the Co K-edge XANES (Fig. 6b, light blue). These changes represent the formation of Co_2C, as indicated by the carburised reference catalyst sample. Furthermore, the appearance of a small peak at around 1.1 Å in the Fourier transformed EXAFS spectrum (Fig. 5b) was observed at the same position as of the carburised sample. The coordination number of Co decreased to 8.3 ± 1.2 accompanied by an increase in the *R*-factor of the EXAFS fit (see ESI†). These changes can occur when carbon penetrates into the Co structure because it distorts the cobalt lattice and weakens the backscattering of more distant Co atoms.[50,51] Hence, there is an indirect prove of Co–C species similar to Co_2C. In the time period from 80–310 h, no additional formation of $CoAl_2O_4$ was found, as no further increase of the peak at 7717 eV in the first derivative of the Co K-edge XANES spectra

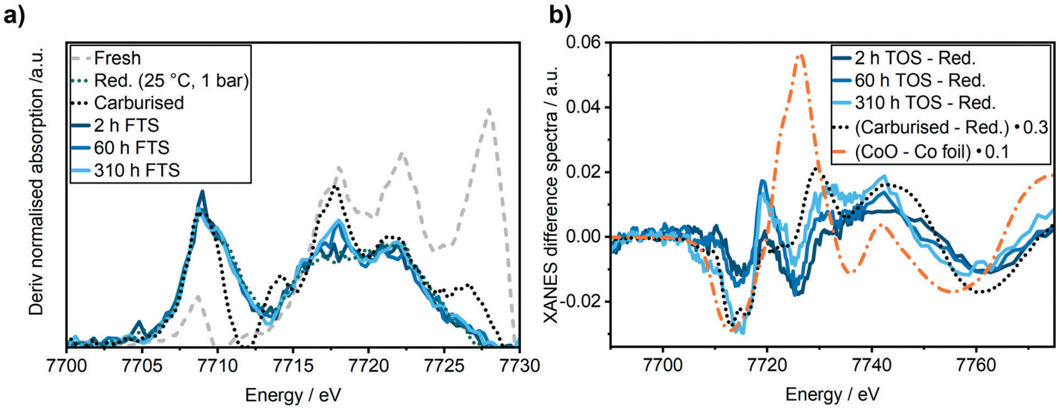

Fig. 6 (a) First derivative of the XANES spectra and (b) difference spectra of the XANES regions of the reduced Co–Ni–Re/γ-Al_2O_3 catalyst and its state after 2 h TOS (dark blue), 60 h TOS (blue) and 310 h (light blue) in FTS. For comparison, the fresh (grey dotted line) and reduced (green dotted line) Co–Ni–Re/γ-Al_2O_3 catalyst, CoO (orange dotted line) and the carburized (black dotted line) sample have been added.

(Fig. 6a) was observed in comparison to the period between 8–60 h TOS.

Analysis after the long-term FTS experiment

The catalyst was characterised after the long-term studies by XRD to investigate whether significant changes occurred during the experiments that could not be followed by the applied *operando* methods, *e.g.* carbon or wax depositions. Although the catalyst was exposed to air after it was removed from the *operando* cell, no formation of crystalline oxidic cobalt species were observed by XRD (Fig. 7a) after all experiments. Instead, a small reflection for Co was found at *d* = 2.18 Å. This indicates the formation of a wax phase on the cobalt particles that protected them from reoxidation under air. To get further details on carbonaceous species, we performed *ex situ* Raman spectroscopy in the range of 1000–1800 cm^{-1} (Fig. 7b). Three pronounced bands were observed in the Raman spectrum that can be attributed to the D_4 (1170 cm^{-1}), D_1 (1319 cm^{-1}) and G (1603 cm^{-1}) band of carbon. According to Sadezky *et al.*,[52] the D_4 band originates from the disordered graphitic lattice, the D_1 band from both the disordered graphitic lattice and/or from the graphitic lattice vibration mode with A_{1g} symmetry and the G band from the ideal graphitic lattice. The absence of the D_2 bands indicates that mainly poorly ordered structures of graphite were formed.[46] This was confirmed by the relatively broad shapes of the D_1 and the G bands which are sensitive to the extent of two-dimensional graphitic ordering, which might be a hint for a large degree of interstitial disorder along the *c*-axis between the in-plane direction.[53] In addition, the microcrystalline planar size $L_a = 44(I_G/I_D)$, that shows a linear relationship with the ratio of the integrated intensity of G *vs.* D band, provides with $L_a \approx 3.1$ nm evidence for a large degree of disorder suggesting the presence of a very poorly graphitised structure.[54]

The carbon and wax depositions were further characterised *ex situ* by combined TG-MS during H_2-TPR and a subsequent O_2-TPO (Fig. 8). Note, that the *ex situ* results might be influenced by the treatment/transport of the catalyst after the long-term experiments, *e.g.* exposure to air (*cf.* experimental section). Nevertheless, they give complementary insight into our *operando* characterisation. The H_2-TPR (Fig. 8a) revealed the formation of two significant methane peaks at 280 °C and 650 °C. The first peak at 280 °C corresponds to a loss of 3% total mass and can be assigned to the hydrogenation of atomic carbon, surface carbides and hydrocarbons. The second peak at 650 °C with a total mass-loss of 2% is likely caused by the hydrogenation of graphitic carbon deposits.[55] The H_2O peak at about 100 °C is due to desorption of surface H_2O, while the second rise of the H_2O signal at around 475 °C is caused by the reduction of oxidised metal species (Co or Ni). In total, around 10% of the sample mass was lost due to hydrogenation, about 5% due to hydrogenation of carbon species and about 5% due to water evaporation and reduction of oxidised cobalt species.

The consecutive O_2-TPO (Fig. 8b) showed one distinct CO_2 peak at around 350 °C. This peak formation is due to hydrogen-resistant carbon species, *i.e.* carbon that cannot be hydrogenated. The mass loss of the catalyst due to oxidation of the hydrogen-resistant carbon species is difficult to quantify in this case, as the increase in mass due to re-oxidation of the catalyst was overlapping with the mass-loss during the oxidation of carbonaceous species. The progressive loss in mass at temperatures above 550 °C without a CO_2 signal might be due to an ongoing $NiAl_2O_4$ or $CoAl_2O_4$ formation. This would be in a good agreement with the blue colour of the catalyst after the TPR/TPO experiment (see ESI†).

Discussion on the origin of deactivation

During the long-term FTS experiment performed in this study various structural changes on the catalyst can occur,[24,29] resulting in the observed deactivation. The possibilities considered in this study are schematically summarised in

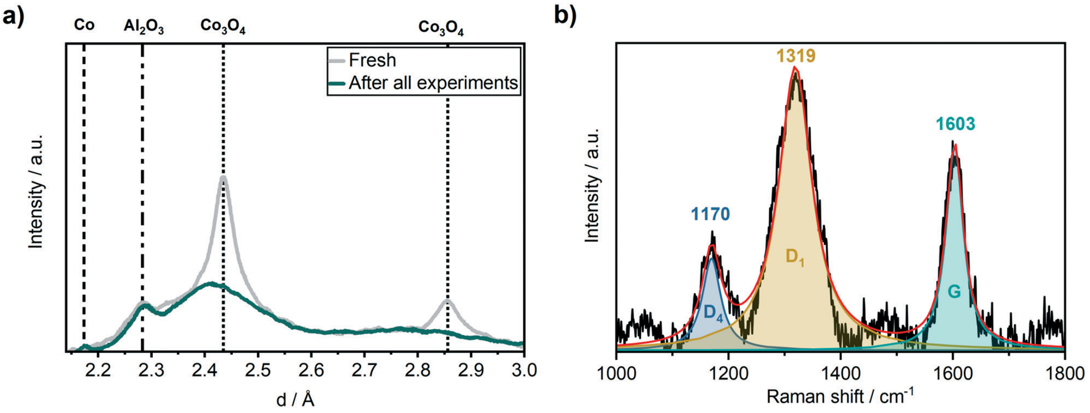

Fig. 7 (a) *Ex situ* XRD before (grey) and after (green) the 310 h long-term FTS experiment and (b) *ex situ* Raman spectroscopy after the 310 h long-term FTS experiment of the Co–Ni–Re/γ-Al_2O_3 catalyst.

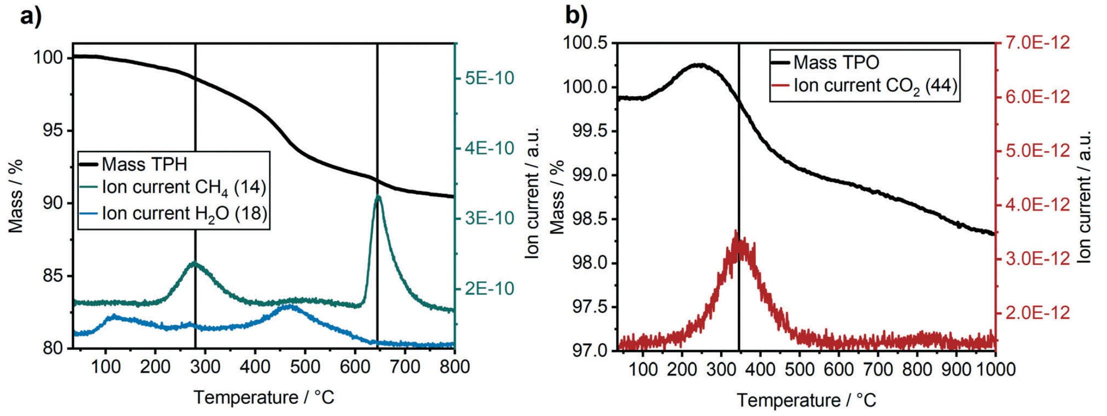

Fig. 8 *Ex situ* TG-MS analysis of the Co–Ni–Re/γ-Al_2O_3 catalyst after the 310 h long-term FTS experiment. (a) H_2-TPR with relative sample mass ("Mass TPH"), as well as CH_4 and H_2O ion currents. (b) O_2-TPO with relative sample mass ("Mass TPO"), as well as CO_2 ion current.

Fig. 9 (a good overview is given in ref. 24). Sulphur poisoning can be systematically excluded during our *operando* studies, as we used gases of high purity. However, sulphur poisoning might still be a critical step for industrial plants that are using synthesis gas *e.g.* from biomass. Oxidation, solid-state reactions, such as the formation of $CoAl_2O_4$, restructuring and sintering were not observed during our *operando* studies, even not in the first 2 h of operation during the initiation phase. Hence, the industrial catalyst provided a much better stability compared to model catalysts typically used for *operando* studies at synchrotron radiation sources.[26,27,56]

Hence, the strong change in the catalyst's performance during the initiation phase in the first 8 h TOS was probably due to changes in the mass transport limitations caused by the formation of a liquid layer (Fig. 9), which was confirmed by the low C-balance in the gaseous products.

In the second reaction regime from 8 h to 60 h TOS a deactivation was observed but the changes were not as fast as during the first 8 h. The only structural change observed by *operando* XAS and XRD was traced back to the formation of $CoAl_2O_4$. This indicates that during this time mostly solid-state reactions (Fig. 9) contributed to the catalyst deactivation. However, these changes were not very pronounced and can therefore not be the only reason for the deactivation. As the rise in the product selectivity to CH_4 and the decrease in the selectivity to C_{5+} did still not reach a steady state, the changes in the mass-transport properties due to liquid phase formation in the pores and developing concentration gradients might still play a role. Hence, formation of hydrocarbons in the pores/carbon deposition were presumably the major reason for the observed deactivation during the first 80 h of FTS.

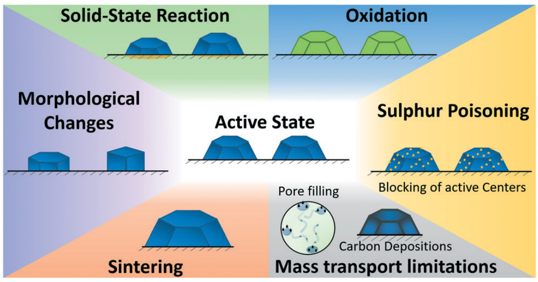

Fig. 9 Overview on the investigated catalyst deactivation mechanisms during Fischer–Tropsch synthesis (*cf.* discussion in text).

In the last 250 h of the long-term experiment, the selectivity levels of the gaseous, as well as the liquid products reached a steady state. This demonstrates that only after 80 h of operating the FTS at 250 °C and 30 bar at the synchrotron, the catalyst reached steady state. However, although the respective selectivity did not further change, some catalyst deactivation was still ongoing. We found hints for the formation of carbide species based on the XAS data. The existence of carbonaceous species was confirmed by Raman spectroscopy and thermogravimetric experiments (TPR&TPO), as the wax was not removed from the catalyst by other means. We observed the conversion of surface carbon, surface carbides, hydrocarbons, and graphitic carbon depositions during TPR. Furthermore, hydrogen resistant carbon species were present in the subsequent TPO. In addition to elucidating the deactivation-causing species on the catalyst surface, these results provide evidence that a reactivation procedure only by H_2-TPR would not be sufficient to retain the initial active state of the catalyst.

Discussion of the newly designed setup for *operando* and long-term high-pressure experiments at synchrotron radiation facilities

The setup presented in this study has been successfully used to perform a combined XAS & XRD synchrotron experiment during FTS over more than 300 h TOS at 250 °C and 30 bar pressure including formation and analysis of liquid FTS products.

Up to now, *in situ* reactors for combined XAS & XRD measurements,[26,27,30,34–38] to monitor complementary changes in both the crystalline and amorphous structure, during FTS usually used less sample, had pressure limitations and were not applied over a long-term including liquid sampling (*cf.* Table 1). A few higher pressure rated spectroscopic reactors were restricted to only one of these X-ray techniques.[38,41] To monitor structural changes under elevated pressure and temperature it is most applicable to use a reactor which is heated by an oven completely enclosing it.[57,58] In such a setup incoming X-rays were straight-forward transmitted through two slits but diffracted X-rays were blocked by the oven. In order to circumvent this issue, we integrated heating cartridges (Fig. 2, red) directly into the stainless-steel cell body and designed the slits for the outcoming beam in a conical way (Fig. 2). This design allows recording X-ray diffraction (Fig. 3d, S2 and S4†) and X-ray absorption data (Fig. 5 and 6) simultaneously. In addition, the larger cell allows recording catalytic data including liquid FTS products.

The temperature of conventional μ-capillary reactors is usually controlled by a hot-air gas blower which may lead to temperature gradients, especially when the gases are not pre-heated.[41] The stainless steel body of our cell ensures an enhanced heat transfer by an up to ten times higher thermal conductivity compared to quartz glass.[59,60] During control experiments, the temperature in the slit over the catalyst bed and the setpoint (~220 °C) differed by 30 °C, which was considered when selecting the temperature setpoints for the measurements. Further prevention of temperature gradients was achieved by pre-heating the inlet lines, as well as by passing the gases through a ~1 cm heated inlet homogeneously distributing the gases in the entire catalyst bed *via* 9 micro-channels.

For an optimised absorption of X-rays most of the catalysts must be diluted, resulting in insufficient yields of liquid products during *in situ* FTS studies (*cf.* Table 1).[26,27,30,34–38] In the cell presented here, we kept the penetration length of X-rays through the catalyst bed in the range of 1–1.5 mm, slightly more than μ-capillary reactors, while increasing the total amount of catalyst, which resulted in a cuboid-shaped catalyst bed. With this design, up to 85 mg of catalyst with defined sieve fraction can be loaded in the new cell while providing good data quality and an absorption step of around 1.0 in the Co K-edge XAS spectra.

This stable catalyst bed finally allows a long-term study with enhanced outflow of liquid and wax-based products by applying a vertical design and top to bottom flow through the catalyst bed. This might have been a critical factor, *e.g.* when performing long-term studies in a horizontally mounted reactor, as it is the case for many conventional μ-capillary reactors (*cf.* Table 1).[26,30,34] Notably, this arrangement prevented any possible pressure drop over the reactor during our >310 h experiment and thus allowed us to produce, collect and analyse liquid FTS products during a synchrotron experiment.

Conclusions

The approach outlined in the present study shows that X-ray based techniques can help to bridge the gap between reaction engineering oriented applied catalytic and fundamental structural studies. This was demonstrated here by performing a long-term *operando* XAS study on a realistic, commercial FTS catalyst over more than 300 h under conditions as close as possible to pilot-scale plants. For this purpose, an advanced *operando* setup for combined X-ray absorption spectroscopy and X-ray diffraction at elevated pressure (up to 50 bar) and temperature (up to 500 °C) was designed and used. To our knowledge, this was the first *operando* study at a synchrotron radiation facility that was operated over 300 hours under harsh FTS conditions (250 °C, 30 bar) including the formation and the detailed analysis of the resulting liquid products.

We observed three different regimes of catalyst activity. In its most active state with a CO conversion of 90%, no changes were found on the cobalt catalyst compared to the state after the activation. During the initiation phase in the first 8 h of FTS, we observed a fast drop in CO conversion from 90% to 66% without detecting any pronounced structural changes on the catalyst. As the C_{5+} selectivity was quite high and the CH_4 selectivity low, we conclude that especially the formation of a liquid film on the catalyst particles lead to decreasing catalytic activity due to mass transport limitations.

The second regime of the catalyst activity was found in the time period from 8–80 h TOS, where CO conversion decreased from 66% to 55%. The deactivation proceeded with a lower rate compared to the first 8 h TOS. The changes in the Co K-edge XANES spectra evidenced the formation of $CoAl_2O_4$. Furthermore, the ongoing increase in CH_4 selectivity accompanied by the decline in C_{5+} selectivity indicated that the filling of the catalyst pores by liquid products was still ongoing. Thus, we conclude that in the second activity regime from 8–80 h the deactivation originated from a combination of changes in mass transport and solid-state reactions.

In the third activity regime, the CO conversion decreased from 55% to 33% during 80–310 h TOS. However, a steady state was reached in the product selectivity indicating that the liquid film formation was completed after 80 h TOS. Furthermore, no additional $CoAl_2O_4$ was formed during this time period. Nevertheless, we observed the formation of carbon depositions on the Co particle surface. The formation of disordered, poorly structured as well as the ideal graphitic carbon depositions on the catalyst was proven by Raman spectroscopy after the long-term experiments. Furthermore, thermogravimetric analysis unravelled the existence of various carbonaceous species, *e.g.* atomic carbon, surface carbides and hydrocarbons, as well as graphitic deposits, which could partially originate from the carburisation procedure. We conclude, that only after 80 h of operating the FTS at 250 °C and 30 bar the commercial catalyst reached its industrially relevant state.

This *operando* XAS and XRD study on FTS over more than 300 h TOS at 250 °C and 30 bar on a commercial catalyst provides an important step forward to bridge the gap between fundamental studies at synchrotron radiation sources and industrial reaction conditions. With the dedicated *operando* setup presented here, we have successfully overcome some drawbacks of conventional reactors commonly applied in X-ray based studies at synchrotron radiation facilities. The results of this study demonstrate that by using spectroscopic reactors that allow to perform *operando* studies with an adequate amount of catalyst and realistic space velocities, the catalytic performance can be well derived directly at a synchrotron radiation facility. This opens new possibilities for the clarification of structure-activity relationships not only in the FTS, but also in other industrial reactions requiring high pressure and temperature.

Conflicts of interest

There are no conflicts to declare.

Acknowledgements

The authors would like to thank the Institute for Beam Physics and Technology (IBPT) for the operation of the storage ring, the Karlsruhe Research Accelerator (KARA). KIT and the BMBF project "Kopernikus-P2X" are gratefully acknowledged for funding this study, as well as KIT and DFG for financing the Raman spectrometer (INST 121384/73-1) and the thermogravimetric setup (INST 121384/70-1). M. Loewert further acknowledges a grant by the Vector Foundation in the project DynSyn with regard to studying the FTS and deactivation under dynamic conditions. Furthermore, we would like to thank Dr. Tim Prüßmann (IKFT/KIT) and Michael Riedinger (IMVT/KIT) for their support during the beamtime and Angela Deutsch (ITCP/KIT) for performing the TG-MS experiments. Jan Pesek (ITCP/KIT) and Holger Karau (IKFT/KIT) are gratefully acknowledged for their support in constructing the mobile gas-dosing unit. Finally, we acknowledge discussion within the SPP2080 by DFG.

References

1 M. Sterner, *Erneuerbare Energien und Energieeffizienz - Renewable Energies and Energy Efficiency*, Kassel University Press GmbH, Kassel, 2009.
2 M.-A. Serrer, K. F. Kalz, E. Saraçi, H. Lichtenberg and J.-D. Grunwaldt, *ChemCatChem*, 2019, **11**, 5018–5021.
3 T. Burger, F. Koschany, O. Thomys, K. Köhler and O. Hinrichsen, *Appl. Catal., A*, 2018, **558**, 44–54.
4 B. Mutz, M. Belimov, W. Wang, P. Sprenger, M.-A. Serrer, D. Wang, P. Pfeifer, W. Kleist and J.-D. Grunwaldt, *ACS Catal.*, 2017, **7**, 6802–6814.
5 D. Pandey and G. Deo, *Chem. Eng. Commun.*, 2016, **203**, 372–380.
6 S. Rahmani, M. Rezaei and F. Meshkani, *J. Ind. Eng. Chem.*, 2014, **20**, 4176–4182.
7 M. Loewert, J. Hoffmann, P. Piermartini, M. Selinsek, R. Dittmeyer and P. Pfeifer, *Chem. Eng. Technol.*, 2019, **42**, 2202–2214.
8 E. Iglesia, *Appl. Catal., A*, 1997, **161**, 59–78.
9 H. Schulz, *Appl. Catal., A*, 1999, **186**, 3–12.
10 J. P. den Breejen, J. R. A. Sietsma, H. Friedrich, J. H. Bitter and K. P. de Jong, *J. Catal.*, 2010, **270**, 146–152.
11 N. Fischer, E. van Steen and M. Claeys, *J. Catal.*, 2013, **299**, 67–80.
12 S. R. Foit, I. C. Vinke, L. G. J. de Haart and R.-A. Eichel, *Angew. Chem., Int. Ed.*, 2017, **56**, 5402–5411.
13 M. E. Dry, *J. Mol. Catal.*, 1982, **17**, 133–144.
14 M. E. Dry, *Catal. Today*, 2002, **71**, 227–241.
15 J. van de Loosdrecht, B. Balzhinimaev, J. A. Dalmon, J. W. Niemantsverdriet, S. V. Tsybulya, A. M. Saib, P. J. van Berge and J. L. Visagie, *Catal. Today*, 2007, **123**, 293–302.
16 W. Chen, T. Lin, Y. Dai, Y. An, F. Yu, L. Zhong, S. Li and Y. Sun, *Catal. Today*, 2018, **311**, 8–22.
17 B. Jager and R. Espinoza, *Catal. Today*, 1995, **23**, 17–28.
18 E. Rytter, N. E. Tsakoumis and A. Holmen, *Catal. Today*, 2016, **261**, 3–16.
19 S. Vada, A. Hoff, E. Ådnanes, D. Schanke and A. Holmen, *Top. Catal.*, 1995, **2**, 155–162.
20 C. J. Bertole, C. A. Mims and G. Kiss, *J. Catal.*, 2004, **221**, 191–203.
21 S. Storsæter, Ø. Borg, E. A. Blekkan and A. Holmen, *J. Catal.*, 2005, **231**, 405–419.
22 E. Rytter, T. H. Skagseth, S. Eri and A. O. Sjåstad, *Ind. Eng. Chem. Res.*, 2010, **49**, 4140–4148.
23 Ø. Borg, S. Eri, E. A. Blekkan, S. Storsæter, H. Wigum, E. Rytter and A. Holmen, *J. Catal.*, 2007, **248**, 89–100.
24 N. E. Tsakoumis, M. Rønning, Ø. Borg, E. Rytter and A. Holmen, *Catal. Today*, 2010, **154**, 162–182.
25 A. M. Saib, D. J. Moodley, I. M. Ciobîcă, M. M. Hauman, B. H. Sigwebela, C. J. Weststrate, J. W. Niemantsverdriet and J. van de Loosdrecht, *Catal. Today*, 2010, **154**, 271–282.
26 N. E. Tsakoumis, A. Voronov, M. Rønning, W. V. Beek, Ø. Borg, E. Rytter and A. Holmen, *J. Catal.*, 2012, **291**, 138–148.
27 N. E. Tsakoumis, J. C. Walmsley, M. Rønning, W. van Beek, E. Rytter and A. Holmen, *J. Am. Chem. Soc.*, 2017, **139**, 3706–3715.
28 E. Rytter and A. Holmen, *Catalysts*, 2015, **5**, 478–499.
29 K. F. Kalz, R. Kraehnert, M. Dvoyashkin, R. Dittmeyer, R. Gläser, U. Krewer, K. Reuter and J.-D. Grunwaldt, *ChemCatChem*, 2017, **9**, 17–29.
30 M. Rønning, N. E. Tsakoumis, A. Voronov, R. E. Johnsen, P. Norby, W. van Beek, Ø. Borg, E. Rytter and A. Holmen, *Catal. Today*, 2010, **155**, 289–295.

31 J.-D. Grunwaldt and B. S. Clausen, *Top. Catal.*, 2002, **18**, 37–43.

32 R. Myrstad, S. Eri, P. Pfeifer, E. Rytter and A. Holmen, *Catal. Today*, 2009, **147**, S301–S304.

33 P. Piermartini, T. Boeltken, M. Selinsek and P. Pfeifer, *Chem. Eng. J.*, 2017, **313**, 328–335.

34 M. Sadeqzadeh, H. Karaca, O. V. Safonova, P. Fongarland, S. Chambrey, P. Roussel, A. Griboval-Constant, M. Lacroix, D. Curulla-Ferré, F. Luck and A. Y. Khodakov, *Catal. Today*, 2011, **164**, 62–67.

35 T. O. Eschemann, W. S. Lamme, R. L. Manchester, T. E. Parmentier, A. Cognigni, M. Rønning and K. P. de Jong, *J. Catal.*, 2015, **328**, 130–138.

36 H. Karaca, O. V. Safonova, S. Chambrey, P. Fongarland, P. Roussel, A. Griboval-Constant, M. Lacroix and A. Y. Khodakov, *J. Catal.*, 2011, **277**, 14–26.

37 Ø. Borg, N. Hammer, S. Eri, O. A. Lindvåg, R. Myrstad, E. A. Blekkan, M. Rønning, E. Rytter and A. Holmen, *Catal. Today*, 2009, **142**, 70–77.

38 A. Rochet, V. Moizan, C. Pichon, F. Diehl, A. Berliet and V. Briois, *Catal. Today*, 2011, **171**, 186–191.

39 J.-D. Grunwaldt, M. Caravati, S. Hannemann and A. Baiker, *Phys. Chem. Chem. Phys.*, 2004, **6**, 3037–3047.

40 S. R. Bare and T. Ressler, in *Adv. Catal.*, Academic Press, 2009, vol. 52, pp. 339–465.

41 D. E. Doronkin, H. Lichtenberg and J.-D. Grunwaldt, in *XAFS Techniques for Catalysts, Nanomaterials, and Surfaces*, ed. Y. Iwasawa, K. Asakura and M. Tada, Springer International Publishing, Cham, 2017, pp. 75–89, DOI: 10.1007/978-3-319-43866-5_6.

42 A. Zimina, K. Dardenne, M. A. Denecke, J.-D. Grunwaldt, E. Huttel, H. Lichtenberg, S. Mangold, T. Pruessmann, J. Rothe, R. Steininger and T. Vitova, *J. Phys.: Conf. Ser.*, 2016, **712**, 012019.

43 C. Sun, T. Zhan, P. Pfeifer and R. Dittmeyer, *Chem. Eng. J.*, 2017, **310**, 272–281.

44 B. Ravel and M. Newville, *J. Synchrotron Radiat.*, 2005, **12**, 537–541.

45 M. Claeys, M. E. Dry, E. van Steen, E. du Plessis, P. J. van Berge, A. M. Saib and D. J. Moodley, *J. Catal.*, 2014, **318**, 193–202.

46 K. H. Cats and B. M. Weckhuysen, *ChemCatChem*, 2016, **8**, 1531–1542.

47 R. I. de Vries, S. Weijers, K. Bethke, V. Kogan, J. Vasterink, A. Kharchenko, M. Fransen and J. Bethke, *Nucl. Instrum. Methods Phys. Res., Sect. A*, 2007, **576**, 164–168.

48 H. Schulz, Z. Nie and F. Ousmanov, *Catal. Today*, 2002, **71**, 351–360.

49 P. J. van Berge and R. C. Everson, in *Stud. Surf. Sci. Catal.*, ed. M. de Pontes, R. L. Espinoza, C. P. Nicolaides, J. H. Scholtz and M. S. Scurrell, Elsevier, 1997, vol. 107, pp. 207–212.

50 J. C. Mohandas, M. K. Gnanamani, G. Jacobs, W. Ma, Y. Ji, S. Khalid and B. H. Davis, *ACS Catal.*, 2011, **1**, 1581–1588.

51 Y. Liu, D. Wu, F. Yu, R. Yang, H. Zhang, F. Sun, L. Zhong and Z. Jiang, *Phys. Chem. Chem. Phys.*, 2019, **21**, 10791–10797.

52 A. Sadezky, H. Muckenhuber, H. Grothe, R. Niessner and U. Pöschl, *Carbon*, 2005, **43**, 1731–1742.

53 J. Llorca, N. Homs, J. Sales and P. R. de la Piscina, *J. Catal.*, 2002, **209**, 306–317.

54 F. Tuinstra and J. L. Koenig, *J. Chem. Phys.*, 1970, **53**, 1126–1130.

55 D. J. Moodley, J. van de Loosdrecht, A. M. Saib, M. J. Overett, A. K. Datye and J. W. Niemantsverdriet, *Appl. Catal., A*, 2009, **354**, 102–110.

56 N. E. Tsakoumis, R. E. Johnsen, W. van Beek, M. Rønning, E. Rytter and A. Holmen, *Chem. Commun.*, 2016, **52**, 3239–3242.

57 J.-D. Grunwaldt, M. Caravati and A. Baiker, *J. Phys. Chem. B*, 2006, **110**, 9916–9922.

58 A. Rochet, V. Moizan, V. Briois and C. Pichon, *Diamond Light Source Proc.*, 2011, 1.

59 I. M. Abdulagatov, S. N. Emirov, T. A. Tsomaeva, K. A. Gairbekov, S. Y. Askerov and N. A. Magomedova, *J. Phys. Chem. Solids*, 2000, **61**, 779–787.

60 E. Schramek, K. Albers and H. Amberg, *Recknagel Taschenbuch für Heizung+ Klimatechnik*, München, Oldenburg Verlag, 2001.